NOVEL QUANTUM DOT AND NANO-ENTITY PHOTONIC STRUCTURES

by
Miltiadis Vasileiadis

Thesis for the degree of Doctor of Philosophy

University of Patras
Department of Materials Science

Patras 2014

Novel Quantum Dot and Nano-Entity Photonic Structures

by

Miltiadis Vasileiadis

Thesis for the degree of Doctor of Philosophy

University of Patras

Department of Materials Science

Patras 2014

Co-financed by Greece and the European Union

Advisory Committee

Nikolaos Vainos
Professor, University of Patras

Ulrike Woggon
Professor, Technische Universität Berlin

Asterios (S) Pispas
Senior Researcher, National Hellenic Research Foundation

Examination Committee

Robert Eason
Professor, ORC-University of Southampton

Demetris Photinos
Professor, University of Patras

Ioannis Koutselas
Assistant Professor, University of Patras

Christina (T) Politi
Assistant Professor, University of Peloponnese

ABSTRACT

This thesis addresses novel nanocomposite materials by incorporating quantum dots (QDs), and other nano-entities, into polymer and sol-gel derived matrices, aiming to produce integrated photonic structures. Its objectives embrace the synthesis and the investigation of photonic materials, together with alternative fabrication methodologies enabling the effective integration of functional nanocomposite photonic structures, such as active waveguides, micro-ring structures and diffractive optical elements for sensing applications.

Design, synthesis and characterization of nanocomposite materials in this context, involves QD incorporation in tailored-made polymers, synthesized using radical polymerization as well as QD embedment in titania matrices synthesized via sol-gel methods. Low cost sol-gel derived silica incorporating $NiCl_2$ –nano-entities was exploited in the proposed scheme of remote point sensing for ammonia detection. Commercially available hybrid organic/inorganic materials of the ORMOCER family are also used for structure fabrication. Further to microscopy, characterization of the materials mainly includes spectroscopic studies and refractive index measurements using reflectance interferometry.

For the demonstration of complex photonic structures by using nanocomposites elaborated studies are presented here focusing on two fabrication methods: a) direct laser ablative microfabrication using ArF excimer radiation at λ=193 nm and, b) soft lithography. To achieve this, a fully automated ArF excimer laser microfabrication

station was established comprising computer controlled nanopositioning and laser beam control, as well as various prototype materials synthesis and fabrication devices. QD/polymer computer generated holograms, waveguides and micro-ring structures were simulated, designed and fabricated. Specific protocols and method were established. A modified solvent-assisted soft lithography method was also used for micropatterning and fabrication of photonic structures using QD/polymer and QD/titania films in conjunction to common UV and thermally curable materials. A solvent vapor smoothing process was found to significantly enhance the quality of the structures as observed with scanning electron microscopy.

QD/polymer computer generated holograms, diffractive optical elements, micro-ring structures, vertical cavity resonators and other advanced photonic structures comprising quantum dot nanocrystals and nano-entities are investigated.

A new photonic sensing scheme is proposed and demonstrated here for remote, spatially-localized sensing. It comprises a low cost diffractive thin film of a sensing material remotely interrogated by use of light beams. A silica/$NiCl_2$ system fabricated via the sol-gel methods and micropatterned using the direct laser ablative microfabrication method is demonstrated, to allow detection of as low as 1 ppm of ammonia.

Finally, the merits of incorporating epitaxially grown quantum dots in highly resonant structures for signal amplification, namely vertical cavity semiconductor optical amplifier and micro-ring semiconductor optical amplifiers, are discussed. Such devices are demonstrated to lack a laser threshold if designed properly allowing for the full exploitation of the fast carrier dynamics of quantum dots by driving them at high currents, for amplification of high-bit-rate signals of up to 100 Gb/s. A rate equation theoretical model was developed which provides both performance prediction of the devices under discussion and design guidelines for threshold-less operation.

This doctoral thesis served, as a whole, its main scope of providing a palette of materials and methods as well as some useful concepts for the fabrication of functional photonic structures and devices based on advanced nanocomposites.

ΣΥΝΟΨΗ

Στην παρούσα διδακτορική διατριβή μελετώνται νανοδομημένα υλικά με ενσωματωμένες κβαντικές ψηφίδες και άλλες νανο-οντότητες σε πολυμερή και ανόργανες μήτρες μέσω της μεθόδου sol-gel, στοχεύοντας στην κατασκευή δομών ολοκληρωμένων φωτονικών κυκλωμάτων. Οι στόχοι της διατριβής επικεντρώνονται στην σύνθεση και μελέτη φωτονικών υλικών και στον συνδυασμό τους με εναλλακτικές μεθόδους κατασκευής φωτονικών δομών. Τα νανοσύνθετα υλικά που μελετήθηκαν παρουσιάζουν μια σειρά από φωτονικές ιδιότητες για την υλοποίηση φωτονικών δομών διαφόρων λειτουργικοτήτων όπως ενεργοί οπτικοί κυματοδηγοί, ενεργοί συντονιστές μικροδακτυλίου και περιθλαστικά οπτικά στοιχεία για φωτονικές εφαρμογές.

Στα πλαίσια της σχεδίασης, σύνθεσης και χαρακτηρισμού αυτών των νανοδομημένων υλικών, κβαντικές ψηφίδες ενσωματώθηκαν σε πολυμερικές μήτρες ειδικά σχεδιασμένες για τον σκοπό αυτό καθώς και σε ανόργανες μήτρες παρασκευασμένων με την μέθοδο sol-gel. Μελετήθηκαν ακόμα υλικά διοξειδίου του πυριτίου εμπλουτισμένα με νανο-οντότητες χλωριούχου νικελίου του για χρήση σε φωτονικούς αισθητήρες. Τα υλικά αυτά συνετέθησαν με μεθόδους χαμηλού κόστους και χρησιμοποιήθηκαν σε καινοτόμες διατάξεις φωτονικών αισθητήρων που περιγράφονται εδώ. Επιπλέον μελετήθηκαν υβριδικά οργανικά/ανόργανα υλικά

ORMOCER για την κατασκευή μιας σειράς φωτονικών διατάξεων. Ο χαρακτηρισμός των υλικών που περιγράφονται εδώ πραγματοποιήθηκε με φασματοσκοπικές μεθόδους ενώ ο δείκτης διάθλασης τους μετρήθηκε με την τεχνική της ανακλαστικής συμβολομετρίας.

Η κατασκευή και επίδειξη σύνθετων νανοδομημένων φωτονικών διατάξεων πραγματοποιήθηκε με δύο μεθόδους: α) την μέθοδο φωτο-εκρηκτικής αποδόμησης με χρήση excimer laser σε μήκος κύματος λ=193 nm και β) με την μέθοδο soft lithography. Για τον σκοπό αυτό αναπτύχθηκε μια πλήρως αυτοματοποιημένη διάταξη μικροκατασκευής με χρήση ArF excimer laser στην οποία τόσο η πηγή laser όσο και η νανομετρική πλατφόρμα για την κίνηση του υπό διαμόρφωση δείγματος ελέγχονται από υπολογιστή. Η διάταξη αυτή χρησιμοποιήθηκε για την κατασκευή διαφόρων διατάξεων σε πολυμερικά υμένια με ενσωματωμένες κβαντικές ψηφίδες όπως υπολογιστικά σχεδιασμένα ολογραμμάτα, κυματοδηγοί και συντονιστές μικροδακτυλίου με γεωμετρικά χαρακτηριστικά που προκύπτουν από θεωρητικές προσομοιώσεις. Ακόμα αναπτύχθηκε μια παραλλαγή της μεθόδου soft lithography για την υποβοηθούμενη από χημικό διαλύτη φωτονικών δομών πολυμερικών μητρών και μητρών τιτανίας με ενσωματωμένες κβαντικές ψηφίδες σε συνδυασμό με κοινά υλικά σχεδιασμένα για την μέθοδο soft lithography και τα οποία διαμορφώνονται με έκθεση σε υπεριώδη ακτινοβολία.

Στην διατριβή αυτή παρουσιάζεται ακόμα μια καινοτόμα σχεδίαση φωτονικών αισθητήρων για την τοπική ανίχνευση διαφόρων χημικών ή φυσικών παραγόντων από απόσταση. Οι αισθητήρες αυτοί αποτελούνται από περιθλαστικές δομές κατασκευασμένες σε υμένα κατάλληλων υλικών, οι οπτικές ιδιότητες των οποίων ανιχνεύονται με τη χρήση δέσμης laser. Ένας τέτοιος περιθλαστικός αισθητήρας αμμωνίας υμενίου διοξειδίου του πυριτίου με ενσωματωμένες νανο-οντότητες χλωριούχου νικελίου παρουσιάζεται εδώ, του οποίου η περιθλαστική δομή κατασκευάστηκε με τη μέθοδο της φωτο-εκρηκτικής αποδόμησης με laser. Ο αισθητήρας αυτός παρουσιάζει εξαιρετική επίδοση και ικανότητα ανίχνευσης αμμωνίας συγκέντρωσης μόλις 1 ppm.

Τέλος, συζητούνται τα πλεονεκτήματα της χρήσης κβαντικών ψηφίδων αναπτυγμένων με επιταξιακές μεθόδους σε δομές οπτικών ενισχυτών ισχυρού συντονισμού, συγκεκριμένα σε οπτικούς ενισχυτές ημιαγωγού κάθετης κοιλότητας και οπτικούς ενισχυτές ημιαγωγού μικροδακτυλίου. Επιδεικνύεται με τη χρήση ενός θεωρητικού μοντέλου που αναπτύχθηκε εδώ πως με τον κατάλληλο σχεδιασμό είναι δυνατόν στις διατάξεις αυτές να αποτρέπεται πλήρως η λειτουργία laser με την απουσία ρεύματος κατωφλίου. Η ιδιαιτερότητα αυτή επιτρέπει την χρήση μεγάλων ρευμάτων και την συνεπακόλουθη εκμετάλλευση της γρήγορης δυναμικής των φορέων στις κβαντικές ψηφίδες για την αποτελεσματική ενίσχυση σημάτων υψηλών ταχυτήτων (μέχρι 100 Gb/s).

Η διδακτορική διατριβη, υπηρετεί συνολικά τον κύριο σκοπό της προσφέροντας μια παλέττα υλικών και μεθόδων για την ανάπτυξη λειτουργικών φωτονικών δομών και διατάξεων βασισμένων σε προηγμένα νανοσύνθετα υλικά.

to Cookie and Aggelos

Table of Contents

Abstract .... **vii**

Σύνοψη .... **ix**

Acknowledgments .... **xix**

List of Abbreviations .... **xxxiii**

Preface .... **xxxvii**

Chapter 1: Introduction **1**

1.1 Introduction to photonics 1
1.2 Brief history of photonics 2
1.3 Photonic devices 6

Chapter 2: Photonic Nanocomposites: Quantum Dots & other Nano-entities **9**

2.1 Introduction to Quantum Dots 9
2.2 Spectroscopic studies of commercially available QDs 14
2.3 Incorporating QD in polymer matrices 19
2.4 Synthesis of polymers 22
2.5 Evaluation of QD nanocomposites of different polymer matrices 25
2.6 Measurement of the refractive index of QD/polymer thin films 34
2.7 Incorporation of QDs and other nano-entities in sol-gel matrices 41
2.8 Hybrid organic-inorganic materials for photonic applications 46
2.9 Sol-gel incorporating nano-entities for sensing applications 52
2.10 Conclusions 55
2.11 Future work 56

Chapter 3: Photonic Structures: Micro/Nanofabrication Routes 57
3.1 Introduction to microfabrication of photonic structures 57
3.2 Direct Laser Ablative Microfabrication 58
3.3 The 193 nm ArF excimer laser microfabrication station 62
3.4 Fine-tuning of the laser microfabrication procedure 67
3.5 Example fabrication of complex photonic structures 72
3.6 Fabrication of polymer waveguides incorporating QDs 75
3.7 Ablated polymer structures - smoothing by solvent vapor treatment 80
3.8 Excimer laser microfabrication of micro-ring resonators 81
3.9 Waveguide fabrication using the soft lithography method and materials of the ORMOCER family 87
3.10 Laser cleaving of OrmoCore/OrmoClad reverse rib waveguides 95
3.11 Implementation of QD/polymer reverse rib waveguides 99
3.12 Soft lithographic replication of complex photonic structures of QD/polymer nanocomposites 99
3.13 Towards the fabrication of low cost QD/polymer and QD/sol-gel Distributed Feedback structures 105
3.14 Conclusions 111
3.15 Ongoing and future work 112

Chapter 4: Sensing the Environment with Nano-entity Photonic Sensors 119
4.1 Introduction to photonic sensors 119
4.2 The Remote Point Sensing scheme 121
4.3 Operating principle of the Remote Point Sensing scheme 126
4.4 Different configurations of the RPS scheme 128
4.5 Nano-entities for ammonia sensing 131
4.6 Microstructuring of diffractive optical elements in thin film sensing materials using ArF direct etching method at 193 nm 132
4.7 Protocols for photonic sensor testing and analysis under the RPS scheme . 133
4.8 Evaluation of ammonia sensors 137
4.9 Ultra-low cost fabrication method of diffractive optic sensors micropatterning by soft lithography.. 143
4.10 Theoretical study for optimum design of the diffraction sensors 149
4.11 Conclusions 157
4.12 Future work.. 158

Chapter 5: Quantum Dots in Highly Resonant Semiconductor Structures ... 161

5.1 Introduction ... 161
5.2 Epitaxially grown quantum dots ... 163
5.3 Vertical cavities photonic structures ... 164
5.4 QD-Vertical Cavity Semiconductor Optical Amplifier modelling ... 167
5.5 Modelling of the QDs inside a vertical cavity ... 170
5.6 Calculation of the mirror losses ... 174
5.7 Results of a QD-VCSOA modelling ... 175
5.8 Comparison of the dynamic response between a QD-VCSOA and a QW-VCSOA ... 178
5.9 QD micro-ring amplifiers ... 183
5.10 Conclusions ... 189
5.11 Future work ... 190

Chapter 6: Conclusions ... 191

Appendix B: Automation of the Excimer Laser Microfabrication Facility ... 195

Appendix A: Temperature Sensor Operating under The RPS Scheme ... 201

Appendix C: Rigorous Coupled-Wave Analysis (RCWA) ... 203

References ... 205

List of Publications ... 227

Acknowledgments

There are a great many people who supported me during my PhD work and writing of the thesis to whom I am grateful to. First of all, I would like to thankmy supervisor Prof. Nikos Vainos who offered me not only the opportunityto accomplish these research activities presented here but also his teaching and guidance. I am grateful to the members of my Advisory Committee Dr Stergios Pispas from the National Hellenic Research Foundation (NHRF) in Athens and Prof. Dr Ulrike Woggon from the Technische Universität Berlin for their guidanceand support. Furthermore, Prof. Dimitirs Alexandropoulos whose friendship and guidance has been invaluable during the years, Prof. Ioannis Koutselas for his immense help, Dr Vaggelis Karoutsos, my good fellow Dr Loukas Athanasekos,Prof. Michael Sigalas, Nikos Aspiotis, Alexandros El Sachat, all researchers at NHRF who offered me their help and knowledge willingly: Dr George Papavassiliou, Dr AnastasiaMeristoudi, Dr George Mousdis, Dr Grigoris Mountrihas,Dr Georgia Pagona, Dr Maria Karagianni, Giannis Manasis and also Anastasia Vasilakopoulou, Varvara Egglezopoulou and all professors, researchers and students I collaborated with at the University of Patras and NHRF. Likewise, I am immeasurable indebted to Dr Nikos Kehagias from Institut Català de Nanocència i Nanotechnologia in Barcelona for his vital help and support, as well as to Prof. Alessio Perrone from the University of Salento, Italy, Prof. Mike Adams

from University of Essex, UK, and also Prof. Michalis Zervas and Prof. Robert Eason both from ORC-University of Southampton, UK, for their invaluable help.

Last and most importantly I am grateful to my family, my mother Betty andmy sisters Vassia and Thekla, as well as to Olga, Nikos, Eleni, Efi, Adam and all my friends for their motivating and unwavering support and love I received throughout all the years of my PhD.

The author is grateful to the Foundation for Education and European Culture, Athens, Greece (IPEP, www.ipep-gr.org) for sponsoring part of the work performed during the first year of his doctoral studies.

This research has been co-financed by the European Union (European Social Fund – ESF) and Greek national funds through the Operational Program "Education and Lifelong Learning" of the National Strategic Reference Framework (NSRF) - Research Funding Program: **Heracleitus II**. Investing in knowledge society through the European Social Fund.

Ευρωπαϊκή Ένωση
Ευρωπαϊκό Κοινωνικό Ταμείο

ΥΠΟΥΡΓΕΙΟ ΠΑΙΔΕΙΑΣ ΚΑΙ ΘΡΗΣΚΕΥΜΑΤΩΝ
ΕΙΔΙΚΗ ΥΠΗΡΕΣΙΑ ΔΙΑΧΕΙΡΙΣΗΣ

ΕΥΡΩΠΑΪΚΟ ΚΟΙΝΩΝΙΚΟ ΤΑΜΕΙΟ

Με τη συγχρηματοδότηση της Ελλάδας και της Ευρωπαϊκής Ένωσης

European Union
European Social Fund

MINISTRY OF EDUCATION & RELIGIOUS AFFAIRS
MANAGING AUTHORITY

EUROPEAN SOCIAL FUND

Co-financed by Greece and the European Union

List of Figures

Figure 1-1: Conceptual outline of the general procedure for the realization of photonic structures. The red arrow outlines the close connection between the fabrication route of the photonic structure and the photonic materials to be used. 7

Figure 2-1: **(a)** A simple illustration of a two bands diagram of a direct gap semiconductor, **(b)** energy levels discretezation due to quantum confinment. 11

Figure 2-2: Photoluminescence spectrum under excitation at 380nm and absorption (UV/VIS) spectrum of the initial QD/toluene solution...15

Figure 2-3: Energy dispersive X-ray spectrum (EDX) of the solvent-free QD nanoparticles deposited on silicon substate outlining the main measures X-ray emission peaks. P/S=P/ZnS=0.29..............16

Figure 2-4: **(a)** Depiction of the structure of the core-shell CdSe/ZnS quantum dot capped with hexadecylamine ligands, the structural and condensed formulas of: **(b)** hexadecylamine (HDA), and **(c)** trioctylphosphine oxide (TOPO). The figure is conceptual and not to scale. 16

Figure 2-5: **(a)** Photoluminescence spectrum for different excitation wavelengths, **(b)** maximum photoluminescence of the QDs versus the excitation wavelength...................17

Figure 2-6: **(a)** Absorption of the QDs solution diluted in toluene with respect to the initial concentration, **(b)** the dependence of the excitonic peak on the relative QD concentration relative to the initial solution and the linear fitting (R^2=0.986). 18

Figure 2-7: The structural formulas of the polymers studied in this chapter and their abbreviations: **(a)** Poly(methyl methacrylate) –PMMA, **(b)** Poly(butyl methacrylate) –PBMA, **(c)** Poly(methyl methacrylate-co-lauryl methacrylate) –P(MMAcoLMA), **(d)** Polystyrene, **(e)** Poly(2,2,2-trifluoroethyl methacrylate) –P3FEMA, **(f)** Poly(dimethylsiloxane) –PDMS. 22

Figure 2-8: Illustration of the radical polymerization procedure. Polymerization occurs inside an oxygen-free flask under stirring at fixed temperature for 12 hours. 24

Figure 2-9: **(a)** Example of photoluminescence of 0.15 g/ml PMMA solutions in toluene at various concentration QD concentrations. **(b)** Gaussian fitting of the photoluminescence peaks (back lines: experimental measurements, red line: Gaussian fittings). 26

Figure 2-10: The dependence of the photoluminescence peak of QD toluene solutions for various concentrations of the nanocrystals. **(a)** PMMA, **(b)** PBMA, **(c)** P(MMAcoLMA) 75-25, and **(d)** Polystyrene. 27

Figure 2-11: The dependence of the photoluminescence peak wavelength of QD toluene solutions for various concentrations of the nanocrystals. 27

Figure 2-12: The dependence of the photoluminescence FWHM of QD toluene solutions for various concentrations of the nanocrystals. **(a)** PMMA, **(b)** PBMA, **(c)** P(MMAcoLMA) 75-25, and **(d)** Polystyrene...28

Figure 2-13: TEM micrographs of CdSe/ZnS QDs embedded in a PMMA matrix.....................29

Figure 2-14: TEM micrograph of CdSe/ZnS QDs embedded in a PBMA matrix 29

Figure 2-15: The photoluminescence peak of polymer/QD films for various QD concentrations for four different polymeric matrices: **(a)** PMMA, **(b)** PBMA, **(c)** P(MMAcoLMA) 75-25, and **(d)** Polystyrene. Solid symbols: excitation 405 nm, open symbols: excitation 375 nm. 31

Figure 2-16: The photoluminescence shift of polymer/QD films for various QD concentrations: The polymer matrix is: **(a)** PMMA, **(b)** PBMA, **(c)** P(MMAcoLMA) 75-25, and **(d)** Polystyrene. Solid symbols: excitation 405 nm, open symbols: excitation 375 nm....................................32

Figure 2-17: The dependence of the photoluminescence FWHM of QD/polymer films on the QD concentration: **(a)** PMMA, **(b)** PBMA, **(c)** P(MMAcoLMA) 75-25, and **(d)** Polystyrene. Solid symbols: excitation 405 nm, open symbols: excitation 375 nm....................................32

Figure 2-18: Normalized decay at various QD concentrations: **(a)** PMMA, **(b)** PBMA, **(c)** P(MMAcoLMA), and **(d)** Polystyrene. The trend of the QD concentration increment is indicated by the arrow in (a)...33

Figure 2-19: Comparison of the normalized decay of the polymeric matrices under study for: **(a)** maximum QD concentration (4.89 μM), and **(b)** half of the maximum QD concentration (2.45 μM). .. 34

Figure 2-20: **(a)** The path of light impinging on a thin film exhibiting multiple reflections, **(b)** measuring configuration of reflectivity, and **(c)** sketch of the fiber optic bundle inside the reflection probe...36

Figure 2-21: Dispersion curves of silicon for **(a)** the real part and **(b)** the imaginary part of the refractive index as found in the literature (red circles/line) and as fitted using the exponential Cauchy formula (black lines). 37

Figure 2-22: Experimentally measured (gray lines) and numerically fitted (red lines) reflectivity spectra of various polymer (left column) and QD/polymer (right column) thin films deposited on silicon substrates: **(a, b)** PMMA, **(c, d)** PBMA, **(e, f)** P(MMAcoLMA), and **(g, h)** Polystyrene. The concentration of the QDs is 4.89 μM.. 40

Figure 2-23: Dispersion curves of QD/polymer nanocomposite for various QD concentrations as predicted by the Bruggeman model: **(a)** PMMA, **(b)** PBMA, **(c)** P(MMAcoLMA), and **(d)** Polystyrene. 42

Figure 2-24: Refractive indices of various QD/polymer thin films vs nanoparticle concentration (filling factor) at λ=632.8 nm as predicted by the Bruggeman model (black solid lines) and as calculated using spectral reflectance measurements (points): **(a)** PMMA, **(b)** PBMA, **(c)** P(MMAcoLMA), and **(d)** Polystyrene. 42

Figure 2-25: Normalized PL spectrum of 5-amino-1-pentanol: a) diluted in isopropanol (green line), and b) in titania matrix (blue line) upon excitation at 404 nm...45

Figure 2-26: Illustration of the encapsulation process of CdSe/ZnS QDs in sol-gel matrix by ligand exchange with a bi-functional molecule: **(a)** the initial form of the nanoparticles with TOPO as ligands, **(b)** the nanoparticle after ligand exchange with aminopentanole and, **(c)** incorporation of the aminopentanole capped QD in titania matrix by the sol-gel process. 45

Figure 2-27: ORMOCERs advantages as a combination of properties of different material families, namely silicones, glasses and organic polymers. (figure from www.ormocer.de website of Fraunhofer Institut für Silicatforschung). 47

Figure 2-28: Brief demonstration of the curing procedure of the ORMOCER materials family.[119] ... 48

Figure 2-29: Example combinations of organic and inorganic monomers and their connecting units for ORMOCERs synthesis. 49

Figure 2-30: Commercially available photoinitiators used with the ORMOCER materials: **(a)** BASF® Lucirin® TPO, and **(b)** Ciba® IRGACURE® 369....................49

Figure 2-31: Precursor monomers of OrmoCore and OrmoClad materials of the ORMOCER family. ..51

Figure 2-32: **(a)** OrmoClad and OrmoCore dispersion curves at 25°C (no hardbake), **(b)** refractive index tuning by mixing OrmoClad and OrmoCore (after hardbake). Data provided by manufacturer.[122]....................51

Figure 2-33: Photoluminescence spectrum of QD encapsulated in dioctyl sodium sulfosuccinate (AOT) micelles embedded in OrmoCore matrix. 52

Figure 2-34: Illustration of the sol-gel process for synthesis of the ammonia sensing material. 54

Figure 2-35: Atomic Force Microscopy (AFM) image of the sol-gel/$NiCl_2$ nanocomposite material surface. 55

Figure 3-1: Photograph of the ArF excimer laser microfabrication facility established at the Photonic Applications, Structures and Materials (PhASMa) laboratory at the Dept. of Materials Science of the University of Patras. 62

Figure 3-2: The excimer laser microfabrication station setup. 63

Figure 3-3: Wiring diagram for the connection of the PC controlled DAQ card to the excimer laser and the stepper motor that rotates the attenuator/compensator pair. 66

Figure 3-4: Evaluating the pulse energy delivered to the sample under processing. 68

Figure 3-5: The laser transmittance from the attenuator-compensator pair at various angles: **(a)** the whole angle range, **(b)** the expanded range of highest attenuation. 69

Figure 3-6: Laser writing protocol on PMMA: **(a, b)** optical microscopy images of craters drilled on a PMMA thin film at different fluence and, **(c)** the etching depth of crater plot for various pulse fluence and the fitted curve for the formula indicated (R^2=0.92). 69

Figure 3-7: SEM micrograph of the ~ 0.5 µm ablated pinhole on the thick (25µm) copper plate. .70

Figure 3-8: The normalized laser intensity distribution diffracted by a pin hole (Airy pattern): **(a)** Relative intensity distribution for the x=ka*sin*(θ) being in the [-12,12] range. The red line denotes a hypothetical ablating threshold of the material under processing while the blue dashed lines indicate the size of the formed crater. The ablating threshold of the substrate is well beyond the peak intensity. **(b)** Photograph of a fluorescence screen (paper soaked with yellow pigment) illuminated by the ArF excimer laser just after the spatial filter. 70

Figure 3-9: **(a)** The laser writing tracing of a cycle exaggerated for a hypothetical stepper motor step of 1.5 µm, and **(b)** laser writing tracing of a cycle for the actual stepper motor step of 80 nm. Smaller steps produces a smoother cycle. 71

Figure 3-10: **(a)** Target design of a "*PhASMA*" logo CGH, **(b)** the optimum unit mask as calculated by the algorithm and, **(c)** the resultant reconstruction of the optimum mask of the CGH as predicted by the algorithm. 73

Figure 3-11: QD-doped polystyrene CGH fabricated using the direct laser writing method: **(a)** microscope image under bright field illumination, **(b)** microscope image under dark field illumination, **(c-d)** SEM micrographs. 73

Figure 3-12: Reconstruction of the CGH fabricated using the direct laser writing method under 532 nm laser illumination. The distance from the CGH to the screen is about 10 cm...73

Figure 3-13: Demonstration of POF microstructuring: **(a)** SEM micrograph of test structure on POF clad, **(b)** light scattering of the same etched structure while waveguiding, **(c)** SEM micrograph of structure formed at the core/shell interface due to different ablation thresholds, **(d)** SEM micrograph of etched holes at different ablation fluences. 74

Figure 3-14: POF microstructuring for applications in photonic sensors, **(a-b)** etch of a groove, **(c-d)** etch of holes. 75

Figure 3-15: Optical microscopy images of microstructures ablated on POF: **(a)** side view of holes, **(b)** deep groove etched right up to the POF axis (500 μm) as an acceptor of sensing material. 75

Figure 3-16: Cross section of α QD-doped polymer waveguide fabricated on top of a thick low refractive index fluorinated polymer (P3FEMA) buffer layer on an oxidized silicon substrate... 77

Figure 3-17: **(a)** The transverse refractive index profile of the QD-doped PMMA/P3FEMA rib waveguide, **(b)** the fundamental mode of the waveguide as computed using the BPM method. The white lines outline the waveguide edges. 78

Figure 3-19: **(a)** SEM micrograph of the QD-doped PMMA/P3FEMA waveguide on silicon fabricated using the direct ablation method prior to solvent vapor smoothing, **(b)** the cleaved edge of the waveguide. 79

Figure 3-20: **(a)** The shape of the ablated groove as defined by the successive laser pulses, **(b)** the tracing line of the groove and, **(c)** the geometry of two successive craters (not to scale). .79

Figure 3-18: **(a-c)** SEM micrographs of grooves ablated on thick (4 μm) P3FEMA polymer films, **(d)** microscope image of filament formation upon single pulse irradiation at 193 nm. .79

Figure 3-21: Illustration of the chloroform vapor procedure for smoothing the polymeric ablated structures. 80

Figure 3-22: **(a)** SEM micrograph of the QD-doped PMMA/P3FEMA waveguide on silicon fabricated after the solvent vapor smoothing treatment, **(b)** the edge of the waveguide...... 80

Figure 3-23: Processing of laser ablated polymeric waveguides with chloroform vapors for smoothing: **(a)** unprocessed waveguide, **(b)** processed at 2.1×10-3 mol/l of chloroform vapor concentration, **(c)** 4.2×10-3 mol/l, **(d)** 6.3×10-3 mol/l, **(e)** 8.4×10-3 mol/l, **(f)** 1.05×10-2 mol/l, **(g)** 1.58×10-2 mol/l and, **(h)** 2.11×10-2 mol/l. In all instances the scale bar corresponds to 10 μm....81

Figure 3-24: Theoretical modeling of a QD/polystyrene ridge waveguide on fused silica substrate: **(a)** Transverse profile of the refractive index, and **(b)** the computed profile of the fundamental mode using the BPM. 82

Figure 3-25: Theoretical modeling of a polystyrene micro-ring resonator of radius R=60 μm on a fused silica substrate : **(a)** Transverse profile of the refractive index, **(b)** the computed profile of the fundamental mode using the PBM. The green arrow depicts the center of the curvature of the structure. 83

Figure 3-26: Microscope images of laser ablated micro-rings: **(a)** bright field images of micro-rings of R=20 μm prior to stripping and, **(b)** dark field image of micro-rings after their complete isolation. 84

Figure 3-27: Microscope close up images of laser ablated polystyrene micro-rings: **(a)** prior to isolation and **(b)** after striping the area around the structure. 84

Figure 3-28: SEM micrographs of laser ablated micro-rings fabricated on QD/polystyrene films: **(a)** a micro-ring prior to solvent vapor smoothing, **(b, c)** micro-ring structures after smoothing and, **(d)** detail of a micro-ring structure (the observed cracks were induced by the electron beam of the SEM). 85

Figure 3-29: SEM micrograph of an ablated polymer micro-ring resonator outlining the main fabrication issues: **(a)** deposition of ablated fragments back on to the structure, **(b)** corrugation of the side walls of the structure due to an insufficiently small step and **(c)** substrate damage due to high laser pulse energy. 86

Figure 3-30: **(a)** A solvent tapered POF in proximity with a QD/polystyrene micro-ring and, **(b)** SEM micrograph of a glass optical fiber etched with hydrofluoric acid. 86

Figure 3-31: **(a)** Microscope image of a micro-ring structure of R=20 μm upon excitation at 405 nm and, **(b)** a micro-ring in proximity with a tapered glass fiber. 87

Figure 3-32: The (tridecafluoro -1, 1, 2, 2-tetrahydroctyl) trichlorosilane molecule structural form (abbreviation F_{13}-TCS). 88

Figure 3-33: **(a)** Depiction of the silicon stamp containing grooves that define the waveguide to be made. The stamp is covered with an antisticking layer. **(b)** PDMS stamp after molding and detaching from the silicon substrate is a negative replica of the initial structure. The figure is not in scale. 90

Figure 3-34: **(a)** Schematic of the UV curing setup, **(b)** the quartz sealed chamber used for the establishment of oxygen free atmosphere during curing under an argon flow. 91

Figure 3-35: **(a)** SEM micrograph of the waveguide grooves on OrmoClad, **(b)** close up of the structure. 92

Figure 3-36: **(a-b)** SEM micrograph of a cross section of an OrmoClad groove prior to filling with OrmoCore. 92

Figure 3-37: **(a)** A water droplet on the cured OrmoClad surface after curing, inhibition layer removal and hard baking, **(b)** a water droplet on the same surface after treatment with piranha solution for 20 min and drying. 93

Figure 3-38: **(a)** SEM micrograph of a cross section of a reverse ridge waveguide of OrmoCore/OrmoClad materials, **(b)** the same micrograph with white lines outlining the edges of the waveguide structure. 94

Figure 3-39: **(a)** The profile of an OrmoClad groove (KLA-Tencor Alpha Step), **(b)** the profile of a fully fabricated waveguide with an OrmoCore layer on top of the initial OrmoClad groove (Bruker DektakXT). 94

Figure 3-40: **(a)** top view of the waveguiding edge, **(b)** the waveguide modes as projected with a 4X microscope objective. 94

Figure 3-41: **(a)** The transverse refractive index profile of the OrmoCore/OrmoClad reverse rib waveguide, **(b)** the fundamental mode of the waveguide as computed using the BPM method. The white lines outline the waveguide edges. 95

Figure 3-42: SEM micrographs of common cleaving problems of waveguides fabricated on silicon substrates: **(a-b)** the deposited film is cleaved at an angle relative to the cleaving facet, **(c)** delamination at the edge region, and **(d)** substrate damage due to the cleaving process. 97

Figure 3-43: (a-c) SEM micrographs and, **(d)** microscope image of OrmoCore/OrmoClad reverse rib waveguides laser cleaving..........97

Figure 3-44: SEM micrographs of patterned surface of OrmoClad by 193 nm ArF excimer laser radiation: **(a,b)** cone formation, **(c)** ablated fringes due to diffraction of the laser radiation by the cones and, **(d)** crystal-like structures on the top of every each cone (red circles) suggest the formation of inorganic particulates that diffract the laser radiation. 98

Figure 3-45: (a) The transverse refractive index profile of the QD-Polystyrene/OrmoClad reverse rib waveguide, **(b)** the fundamental mode of the waveguide as computed using the BPM method. 100

Figure 3-46: (a) Microscope image of the edge of a 2 μM QD-doped polystyrene reverse rib waveguide on OrmoClad where waveguiding can be observed (excitation at 405 nm), **(b)** a waveguide where the geometry does not favor waveguiding and **(c)** top view of the waveguiding structure. An LPF has been used to isolate the QD luminescence from the excitation radiation. 100

Figure 3-47: (a) Schematic illustration of the solvent-assisted micro molding (SAMIM) method and **(b)** schematic of the diffraction grating cross section depicting the inhibition layer. 101

Figure 3-48: (a-c) SEM micrographs of the CGH PDMS stamp at different magnifications levels, **(d)** SEM micrograph of the edge of the CGH PDMS stamp. 102

Figure 3-49: (a) Sketch of the soft lithography apparatus for the transfer of a PDMS stamp design to a thin film deposited on a hard substrate. **(b)** Photograph of the portable custom made apparatus which can be placed on a hot plate, inside an oven or a vacuum chamber. ..103

Figure 3-50: (a-c) SEM micrographs of the QD-doped polystyrene CGH fabricated using the soft lithography method, **(d)** detail of the edge of the CGH. 104

Figure 3-51: Reconstruction of the QD-doped polystyrene CGH using a 532 nm laser source. The distance between the CGH and the screen is about 10 cm. 104

Figure 3-52: SEM micrographs of some common problems faced due to the poor adhesion of the polymeric film on the substrate: **(a)** local defect of the film, **(b)** extensive detachment of the patterned film during stamp separation. 105

Figure 3-53: Conceptual illustration of the DFB structure under consideration..........106

Figure 3-54: SEM micrograph of a soft lithographed QD-doped polystyrene DFB structure with a 1μm where the excess of solvent was not completely removed from the PDMS stamp. 107

Figure 3-55: SEM micrograph of the soft lithographed QD-doped polystyrene DFB structure with a 1μm grating. The white lines depict the position of the buried rib waveguide..........107

Figure 3-56: SEM micrographs of various aspects of the soft lithographed QD-doped polystyrene DFB structure with a 1 μm grating: **(a)** the polymeric film has been intentionally peeled off to reveal the underlying groove on OrmoClad, **(b)** detached and folded polymeric film retaining the micro patterning, **(c)** the edge of the micro pattern polymeric film and, **(d)** cross section of the film at a damaged position of the structure. 108

Figure 3-57: SEM micrographs of the 200 nm grating: **(a)** the silicon master, **(b)** 10:1 PDMS stamps exhibiting line collapse, **(c)** 5:1 PDMS stamp with some line collapse and, **(d)** 5:1 PDMS stamp with no line collapse..........109

Figure 3-58: SEM micrographs of the QD/polymer soft lithographed fine pattern of the 200 nm grating on top of reverse rib waveguides. 109

Figure 3-59: **(a)** The transverse refractive index profile of the QD-TiO_2/OrmoClad reverse rib waveguide, **(b)** the fundamental mode of the waveguide as computed using the BPM method. 110

Figure 3-60: SEM micrographs of the QD-doped TiO_2 DFB structure on OrmoClad grooves: **(a, b)** the top view of the structure, **(c)** the grating structure at a plain area and, **(d)** the QD-TiO_2 film at the patterned by the PDMS stamp edge. The presence of the stamp causes the effective crack-free hydrolysis of the sol-gel material. 111

Figure 3-61: SEM micrographs of the fabricated soda lime wave guides on fused silica substrates: **(a)** the ablated grooves on fused silica, **(b)** the soda lime waveguide after polishing, **(c)** cracking of the waveguide formed during polishing and, **(d)** defect (unfilled area) on the waveguide. 114

Figure 3-62: Photograph of the PLD process where the plume is clearly observed. 114

Figure 3-63: Schematic of the Pulsed Laser Deposition (PLD) set-up used for the fabrication of soda lime waveguides on fused silica substrates. 115

Figure 3-64: Theoretical modeling of a polystyrene micro-ring resonator of radius: **(a, b)** R=30 μm and **(c, d)** R=50 μm embedded on PDMS. The transverse profiles of the refractive indices are shown in (a) and (c) while the profiles of the fundamental mode calculated using the BPM are shown in (b) and (d). The green arrow depicts the center of the curvature of the structures....................116

Figure 4-1: The Remote Point Sensing scheme in **(a)** transmission operation mode, **(b)** reflection mode using a reflective substrate, and **(c)** reflection mode using a retroreflector (cube-corner reflector or prism) to guide the monitor beam. 122

Figure 4-2: Principle of operation of the Remote Point Sensing Scheme....................127

Figure 4-3: Transmittance spectrum of a 1 μm thin film on a soda lime glass substrate (n_{sub}=1.52) as calculated using equation for two different values of the refractive index of the film material: n_{film}=1.55 (black line) and n_{film}=1.55 (red line). 129

Figure 4-4: Principle of the Remote Point Sensing scheme using a diffractive optic sensor head in transmission and reflection mode. 130

Figure 4-5: **(a)** SEM micrograph of the sol-gel/$NiCl_2$ diffraction grating photonic sensor, **(b)** the profile of the surface relief structure measured using a KLA-Tensor Alpha Step profilometer. .. 134

Figure 4-6: SEM micrographs of: **(a-c)** the edges of the ablated regions of the sol-gel/$NiCl_2$ diffractive structure, **(d)** the untreated surface of the film.................... 134

Figure 4-7: **(a)** Photograph of the vacuum chamber used to evaluate the photonic sensors operating under the RPS scheme, **(b)** a testing setup comprising a laser source, a photodiode receiver and a mobile sensing film fixed on top of a retroreflector. 135

Figure 4-8: Schematic illustration of the experimental setup used for the evaluation of the nano-entity diffractive optic photonic sensors. 136

Figure 4-9: Temporal evolution of the real time responsivity of a thin film sensor exhibiting exposure at different concentrations of ammonia vapors. The dotted lines indicate the instant of ammonia insertion at known values into the chamber and consecutive evacuation by air flow to restore ambient, ammonia-free environment. 139

Figure 4-10: **(a)** Temporal response of the first diffraction order diffraction efficiency of consecutive cycles at various ammonia levels followed by evacuation down to the ambient environments and **(b)** the corresponding responsivity, R(%). 139

FIGURE 4-11: Responsivity curve of a sol-gel $SiO_2/NiCl_2$ planar thin film photonic ammonia sensor: **(a)** over a wide ammonia levels range up to sensor saturation region, and **(b)** a blow up at low ammonia concentrations. The response of the 1st order of a diffractive structure fabricated on the same film is also shown in **(a)** for comparison. 140

FIGURE 4-12: Temporal responsivity of **(a)** zero order, **(b)**, **(c)** ± 1 order to 150 ppm of ammonia and **(d)** the temporal concentration of ammonia. 141

FIGURE 4-13: Responsivity of the diffraction grating sensor to various ammonia concentrations of zero order and ± 1 order. The response of the unprocessed planar sensor thin film sensor is shown in the same figure for comparison. **(a)** Overall responsivity and **(b)** low ammonia level responsivity. 142

FIGURE 4-14: Repeatability recordings of diffractive optic sensor tested...............................143

FIGURE 4-15: **(a)** Schematic illustration of the molding in capillaries (MIMIC) fabrication method, **(b)** schematic of the inhibition layer free cross section of the diffraction grating. 146

FIGURE 4-16: Microscopy images of diffraction grating using the MIMIC procedure. **(a)** A close up of the diffractive pattern, **(b)** unevenly filled channels at the edges of the diffraction grating 147

FIGURE 4-17. Profilometry measurements of **(a)** the PDMS stamp and **(b)** a diffractive optic sensor fabricated using the MIMIC method. 148

FIGURE 4-18: **(a)** Photograph of the diffraction pattern of the structure shown in Figure 4-16 illuminated with a HeNe laser at 632.8 nm and **(b)** the power distribution for orders from +4 to the -4 diffraction orders expressed in diffraction efficiency η. 148

FIGURE 4-19: The $+1^{st}$ diffraction order responsivity of three different diffraction grating ammonia sensors fabricated using the MIMIC method with different sensing materials: **(a)** $CuCl_2$ nanoclusters in silica matrix sol-gel (TMOS) matrix, **(b)** (a) $NiCl_2$ nanoclusters in silica matrix sol-gel (TMOS) matrix, and **(c)** block copolymer SPS-b-PtBS. 149

FIGURE 4-20: The SRG geometry used for theory and design...151

FIGURE 4-21: Variation in the diffraction efficiency as a function of grating depth, h, for various refractive indices and corresponding change with refractive index, n, for various grating depths of: **(a-b)** the first diffraction order and **(c-d)** the second diffraction order. The other characteristics of the diffraction grating are: period a = 100 µm and duty cycle = 0.5. 153

FIGURE 4-22: Change in the diffraction efficiency as a function of grating period, a, for various refractive indices and corresponding change with refractive index, n, for various grating periods of **(a-b)** the first diffraction order and **(c-d)** the second diffraction order. The other characteristics of the diffraction grating are: grating depth h = 1.4 µm and duty cycle = 0.5.. 154

FIGURE 4-23: Change in the diffraction efficiency as a function of grating duty cycle for various refractive indices and corresponding change with refractive index, n for various duty cycles of **(a-b)** the 1st diffraction order and **(c-d)** the 2nd diffraction order. The other characteristics of the diffraction grating are: grating depth h = 1.4 µm and period = 100 µm......................155

FIGURE 4-24: Variation in the diffraction efficiency with the angle of the incident beam –θ for various refractive indices and corresponding change with refractive index, n, for various angles of **(a-b)** the 1st diffraction order and **(c-d)** the 2nd diffraction order. The other characteristics of the diffraction grating are: grating depth h = 1.4 µm, grating period a = 100 µm and duty cycle = 0.39..156

FIGURE 4-25: Experimentally measured diffraction efficiency of the **(a)** first and **(b)** second diffraction orders of a SGR with a = 100 µm, h = 1.39 µm, and duty cycle = 0.39. 156

Figure 5-1: Density of state function of energy for bulk semiconductor materials and successively reduced dimension semiconductor structures: quantum wells (2D quantum confinement), quantum wires (1D quantum confinement), and quantum dots (0D quantum confinement). .162

Figure 5-2: Section schematic of a Vertical Cavity Surface Emitting Laser (VCSEL). 165

Figure 5-3: Illustration of the two operating mode of a VCSOA structure: **(a)** reflection mode and **(b)** transmission mode. 166

Figure 5-4: Schematic of a QD-VCSOA and the refractive index profile. 166

Figure 5-5: **(a)** Schematic of a VCSOA structure with the precise placement of the QD layer stacks. **(b)** The 3λ/2 length VCSOA cavity has been replaced by a FP cavity with hard mirrors using the penetration depths. The red line indicates the antinodes of the oscillating optical field inside the cavity where the QD layer stacks has been placed. The distortion of the optical field inside the DBR mirror is not shown for simplicity. 169

Figure 5-6: Schematic of the energy states diagram of a quantum dot also depicting the characteristic times of the carrier dynamics...170

Figure 5-7: Illustration of the homogeneous and inhomogeneous broadening of quantum dots and the energy discretization for the numerical solution of the equations. The figure is not to scale. 172

Figure 5-8: **(a)** The threshold current versus surface QD density of a 3×5 layers QD-VCSOA, and **(b)** the time evolution of the GS occupation probability of two QD-VCSOA, one exhibiting a threshold current operating at $I=0.95\times I_{thr}$ and one threshold-less device driven at 40 mA. ..176

Figure 5-9: **(a)** Gain curves of a threshold-less 3×5 QD-VCSOA in reflection mode of QD density $N_D=5.5\times10^{10}$ cm^{-2} driven at various currents in a wide range of 1.5 mA to 300 mA. The arrow indicates the trend for increasing current. **(b)** The saturation gain as a function of the current for the same device. 177

Figure 5-10: Gain curves of a 3x5 QD-VCSOA driver at I=25 mA for various surface QD densities. .178

Figure 5-11: **(a)** The maximum achievable gain of a 3×5 QD-VCSOA driven at I=25 mA as a function of the surface QD density, and **(b)** the dependence of the saturation input power of the same device on the surface QD density. 178

Figure 5-12: The amplification spectrum of a 3×5 QD-VCSOA of QD density $N_D=5.5\times10^{10}$ cm^{-2} driven at I = 25 mA for two carrier induced refractive index change values: **(a)** dn/dN=0, **(b)** $dn/dN=-2.8\times10^{-26}$ m^{-3}. 179

Figure 5-13: Detuning of the 3×5 QD-VCSOA ($N_D=5.5\times10^{10}$ cm^{-2}, I = 25 mA) gain spectrum maximum from the cavity resonance wavelength (λ_{cavity}=1300 nm) as a function of the carrier induced refractive index change value dn/dN. 179

Figure 5-14: Gain curves of a QW VCSOA amplifier pumped at various currents. The threshold current of the device is I_{thr}=8.9 mA...181

Figure 5-15: Dynamical response of a 3×5 QW-VCSOA exhibiting a threshold of I_{thr}=8.9 mA driven at **(a-c)** $I=0.90\times I_{thr}$, and (d-f) $I=0.95\times I_{thr}$: **(a & d)** gain change due to carrier depletion, **(b & e)** input and output signal waveforms at 100 Gb/s and, **(c & f)** eye diagrams of the input and output waveforms. 182

Figure 5-16: Dynamical response of a 3×5 QD-VCSOA of $N_D=6.5\times10^{10}$ cm^{-2} exhibiting a threshold of I_{thr}=16.9 mA driven at $I=0.90\cdot I_{thr}$: **(a)** gain change due to carrier depletion, **(b)** input and output signal waveforms at 100 Gb/s and, **(c)** eye diagrams of the input and output waveforms. 183

Figure 5-17: Dynamical response of a 3×5 threshold-less QD-VCSOA of N_D=5.5×10^{10} cm^{-2} driven at I=30 mA: **(a)** gain change due to carrier depletion, **(b)** input and output signal waveforms at 100 Gb/s and, **(c)** eye diagrams of the input and output waveforms. 184

Figure 5-18: **(a)** 2D and, **(b)** perspective schematic illustrations of a QD micro-ring resonator in the all pass configuration, **(b) 2D** and, **(d)** perspective schematics of a cross section. 185

Figure 5-19: The dependence of the threshold current of a QD micro-ring amplifier of on the QDs surface density. 187

Figure 5-20: Gain curves of a threshold-less QD micro-ring amplifier pumping at different currents. 188

Figure 5-21: Gain curves of a QD micro-ring amplifier for various coupling constants κ. 188

Figure 5-22: Gain curves of QD micro-ring amplifier for various QD surface densities N_D. ... 188

Figure 5-23: Gain spectrums of QD micro-ring amplifier exhibiting a differential refractive index of dn/dN=-2.8× 10^{-26} m^{-3} for various coupling constants κ. 189

Figure 5-24: Gain spectrum of a QD micro-ring amplifier for various coupling exhibiting a hysteresis loop. 189

Figure A-1: The main control window for operating the laser, the picomotors movement and the attenuator angle separately...196

Figure A-2: The external writer window for inserting a txt file containing the writing instruction that has been calculated externally. 196

Figure A-3: The “Raster Design” window for inserting a jpg image file containing black.......197

and white pixels. The black pixels indicate the spots to be laser etched. The number..........197

pitch distances between pixels to be written and the force/number of pulses at each 197

pixel are defined. 197

Figure A-4: The “Diff. Grating Writing” window for the fabrication of diffraction grating either using the fast writing method of the more precise stop-and-shoot method. 197

Figure A-5: The “Line Writer” window where individual steps and their repeats can be programmed. 198

Figure A-6: The “μRing Designer” window for the fabrication of micro-ring resonators. 198

Figure A-7: The “Laser Writing Protocol” window for the evaluation of the material ablation procedure at different conditions (pulse energy, number of pulses, repetition rate and z position-focus). 198

Figure A-8: The “Pulse Energy Meas.” window in histogram mode for the measurement of the pulse energy distribution and calculation of the mean value and standard error. 199

Figure A-9: The “Power Meas.” window for measuring the power of the laser pulse train at a given repetition rate and angle of attenuator. 199

Figure A-10: The “Pulse Energy Meas.” window in time trace mode for monitoring the laser stability. .. 200

Figure A-11: The “Force/Angle Energy” window for measuring the pulse energy on different angles of the attenuator. 200

Figure B-1: Schematic illustration of the structure design and SEM micrograph (bottom). ...202

Figure B-2: Measurements of R_0, T_0 and R_{+1} for ascending (↑) and descending (↓) temperatures...202

All illustrations in this thesis were designed by the author with the exception of Figure 2-27.

List of Tables

Table 2-1: Summary of the synthesized polymers measured properties 25
Table 2-2: PL peak increase by increasing the QD concentration from 1 μM to 4.79 μM.......31
Table 3-1: List of the component characteristics of the laser microfabrication station 63
Table 3-2: Summary of the successive process steps for the OrmoClad/OrmoCore waveguide fabrication. 96
Table 5-1: List of parameters of the QD-VCSOA used in calculations...................................174
Table 5-2: List of the fitting parameters for the QW-VCSOA modelling. 180
Table 5-3: List of parameters of the QD-micro-ring used in calculations 187

List of Abbreviations

AFM	Atomic Force Microscopy
AP	5-Amino-1-pentanol
BPM	Beam Propagation Method
CGH	Computer Generated Hologram
CVD	Chemical Vapor Deposition
DAQ	Data Acquisition
DBR	Distributed Bragg Reflector
DE	Diffraction Efficiency
DI	Deionized (purified) water
DLAM	Direct Laser Ablative Microfabrication
DOE	Diffraction Optical Element
DOS	Density of States
DSC	Differential Scanning Calorimetry
EDX (EDS)	Energy-Dispersive X-Ray Spectroscopy
ES	Excited State
EtOH	Ethanol
F_{13}-TCS	(Tridecafluoro-1,1,2,2-tetrahydroctyl) trichlorosilane
FP	Fabry-Pérot
FWHM	Full Width at Half Maximum
GPC	Gel Permeation Chromatography
GS	Ground State
HAZ	Heat Affected Zone

HDA	Hexadecylamine
HR	High Reflectivity
IR	Infrared
LED	Light Emitting Diode
LIDAR	Light Detection and Ranging
LT	Life Time
MBE	Molecular Beam Epitaxy
MIMIC	Micromolding in Capillaries
MOVPE	Metal-Organic Vapor Phase Epitaxy
NC	Nanocrystals
NIL	Nanoimprint lithography
OSA	Optical Spectrum Analyzer
P3FEMA	Poly(2,2,2-trifluoroethyl methacrylate)
PBMA	Poly(butyl methacrylate)
PD	Photodiode
PGMEA	Propylene glycol monomethyl ether acetate
PIC	Photonic Integrated Circuit
PL	Photoluminescence
PLD	Pulsed Laser Deposition
PLMA	Poly(lauryl methacrylate)
PMMA	Poly(methyl methacrylate)
ppm	parts per million
pps	pulses per second
PS	Polystyrene
QD	Quantum Dots
RCWA	Rigorous Coupled-Wave Analysis
RIE	Reactive Ion Etching
rms	root mean square
RPS	Remote Point Sensing
RT	Room Temperature
SAMIM	Solvent-assisted Micro Molding
SEC	Size-Exclusion Chromatography
SEM	Scanning Electron Microscopy
SNR	Signal-to-Noise Ratio

SOA	Semiconductor Optical Amplifier
SPS-b-PtBS	Polystyrene sulfonate-b-tert-butylstyrene
SRG	Surface Relief Grating
S-K	Stranski-Krastanov
TCSPC	Time-Correlated Single Photon Counting
TEM	Transmission Electron Microscopy
TEOS	Tetraethyl Orthosilicate (Tetraethoxysilane)
THF	Tetrahydrofuran
TMOS	Tetramethyl Orthosilicate (Tetramethoxysilane)
TOPO	Trioctylphosphine Oxide
UV	Ultra Violet
VC	Vertical Cavity
VCSEL	Vertical Cavity Surface Emitting Laser
VCSOA	Vertical Cavity Semiconductor Optical Amplifier
VLSI	Very Large Scale Integration
WL	Wetting Layer

Preface

The main objective of this thesis is the demonstration of novel combination of advanced photonic materials with complex photonic structures, with the scope of focusing on alternative fabrication protocols. The experiments presented here were performed in the Photonic Applications, Structures and Materials (PhASMa) Laboratory in the Department of Materials Science, University of Patras, Patras, Greece, and at the Photonics Laboratory and Materials Physical Chemistry Labs of the Theoretical and Physical Chemistry Institute (TPCI) at the National Hellenic Research Foundation (NHRF) in Athens, Greece. In particular, materials synthesis and characterization was performed mainly in NHRF under the guidance of Dr S. Pispas (polymers) and Dr G. Mousdis (sol-gels) as well as in the Molecular Nanomaterials Laboratory in the Dept. of Materials Science, University of Patras, under the guidance of Prof. I. Koutselas. The ArF excimer laser and soft lithography microfabrication was established and performed in the PhASMa Laboratory in Patras, were most of the photonic device experiments were also performed, while photonic sensors characterization was performed in the Photonics Laboratory in NHRF by using the environmental sensor testing facilities. Microscopic analysis (Optical, AFM, SEM, TEM) was performed at Patras. Theoretical studies on diffractive optics sensors were

performed using the rigorous coupled-wave analysis (RCWA) with the help of Prof. M. Sigalas. Finally, theoretical models for the performance prediction of quantum dots highly resonant amplifiers were developed under the guidance of Prof. D. Alexandropoulos.

After a short introduction on the concept of photonics devices design and fabrication, design, synthesis and characterization of nanocomposite photonics materials is presented in chapter 2. This include spectroscopic studies of quantum dots in polymer and sol-gel derived matrices, hybrid organic/inorganic materials for soft lithography and sol-gels incorporating nano-entities for sensing applications.

Chapter 3 of this thesis introduces to the microfabrication of photonic structures focusing on the direct laser ablative microfabrication method and soft lithography. The ArF excimer laser microfabrication station at λ=193 nm is presented and several laser fabrication protocol are discussed. Soft lithographically replication of both UV curable and quantum dots/polymer photonic structures is also discussed. Photonic structures demonstration include active waveguides, computer generated holograms, micro-rings and distributed feedback structures.

The novel remote point-sensing scheme is presented in chapter 4. The operating principles of this sensing configuration is discussed and performance of a silica/$NiCl_2$ diffractive ammonia sensor of low detection limit (1 ppm) is demonstrated. Fabrication protocols of such a photonic structure are discussed and the cases of direct laser ablative microfabrication and soft lithography are demonstrated. A theoretical study of the performance prediction this sensing scheme is also presented to provide design guidelines.

In chapter 5 the merits of using epitaxially quantum dots as the active material in highly resonant structures semiconductors optical amplifiers, namely vertical cavities semiconductor optical amplifiers and micro-ring semiconductor optical amplifiers, are demonstrated.

Finally, a conclusion and an outlook of this thesis is given in chapter

Chapter 1
Introduction

1.1 Introduction to photonics

Photonics is the science and technology of generating, transmitting and manipulating light in order to study nature and accomplish various tasks of technological interest and extreme societal impact. Radiation within a wide region of the electromagnetic spectrum is systematically used to unveil the properties of the materials, by exploiting the many variations of the spectroscopic techniques. Absorbance (UV/VIS) spectroscopy, photoluminescence, time-elapsed, Fourier Transform Infrared (FT-IR) and Raman spectroscopy are among the scientific methods where the advances of photonics are used. At the same time photonics being related to the sense of vision provides a detailed description of the world around us at an enormous range of scales; from micro and nano features via microscopy, to huge structures in the universe such as galaxies from the edge of time with sophisticated telescopes. Moreover, the complicated properties of light have allowed the detection of single atoms in advanced set-ups, e.g. atomic force microscopy (AFM), while interferometers of high precision are exploited in the search of tiny gravitational waves and other fields of fundamental research.

Besides providing a main set of scientific tools, photonics have altered the everyday life of mankind offering technology of the greatest impact ranging from lighting sources to the realization of today's computers and broadband internet. The most prominent example of photonics applications is optical communications which permits ultra-fast data networks connecting the entire globe, and transferring information at enormous data-rates by means of modulated light through billions of kilometers of optical fibers. In addition, manipulation of light provides the main interface between humans and machines with thousands of tiny liquid crystals cells forming pixels in computer or other screens. Very Large System Integration (VLSI) techniques for the fabrication of electronic integrated circuits have become feasible due to the development of lithographic techniques and the accurate manipulation of light for micro and nanofabrication while high power lasers are used for the precise fabrication of large scale structures using laser cutting and laser welding. Photonics is also used in monitoring and detection devices and in high performance sensors for measuring distances from the nano scale to the long range regime, temperature and various other chemical or physical agents. The applications of photonics are ubiquitous, ranging from telecommunications to the construction industry and from microelectronics to the development of photonic computing devices and quantum encryption devices.

Photonics is today a multi-billion Euro industry. In the time period of 2005-2011 photonics contributed to the outgrowth of the global GDP while in 2020 the expected market volume is in the order of 650 billion Euro.[1] The market share of Europe was about 60 to 65 billion Euro in 2011 with the biggest share lying in the laser and lithographic systems (55%) and optical components and systems (40%) segments.

1.2 Brief history of photonics

The nature of light has fascinated human kind since the ancient times. Aristotle (4th century BC), among others, wondered on the nature of light in his texts

proposing that light does not originate from the human eye while also reporting on the occurrence of refraction as the alteration of the linear propagation of light. Euclid (4th century BC) proposed that light only travels in straight lines and Heron of Alexandria formulated the least distance principle for the propagation of light during the 1st century AD. Apart from essays in philosophy, applications of optics in antiquity include the mentioning of burning glass by Aristophanes (4th century BC) in one of his plays while the great mathematician Archimedes (3rd century BC) is reported by historians to have concentrated sun light using mirrors to destroy enemy ships.

The first essay on optics entitled "The Book of Optics" was written in 1015 by the medieval Arab scholar Ibh al-Haytham who was named the "*father of modern optics*" but some historians of science.[2,3] Elaboration of the exact nature of light begun with the advent of modern science. Sir Isaac Newton (1642-1727) proposed in 1665 the existence of corpuscles of light, entities resembling the particles we now call photons, whereas Christian Huygens (1629-1695) argued on the wave nature of light. It was not however until the nineteenth century that a deep understanding of light became feasible mainly due to the work of James Clerk Maxwell (1831-1879) when his set of equations effectively described most of the properties of electromagnetic radiation. The work of Maxwell was a corollary of the work of ingenious scientists like Thomas Young, Augustin Jean Fresnel, Armand Hippolyte Louis Fizeau, Jean Bernard Leon Foucault Joseph Fraunhofer, Gustav Robert Kirchhoff and Heinrich Rudolf Hertz to name just a few. Finally, our understanding of the nature of light was completed with the coming of the quantum physics era, in the dawn of the twentieth century following the work of Max Karl Ernst Ludwig Planck and the explanation he provided for the black body radiation. In this context Albert Einstein in 1905 re-proposed the existence of the "*fundamental particle*" of light to effectively explain the photoelectric effect. During the same year Einstein published his work on Special Relativity to complete the classical interpretation of electromagnetic radiation by expelling the concept of the "*aether*." The name "*photon*" for the quantum of light was

coined by Gilbert Lewis in 1926.[4] Finally, our understanding of the nature of light in the frame of quantum physics was completed by the work of Paul Dirac and Richard Feynman, among others, who established the field of quantum electrodynamics and quantum optics.

Until the first use of the term "*photonics*" by the French scientist Pierre Aigrain[5] in 1967, three main milestones has led to the rapid development of the field, the first being the invention of the laser (Light Amplification by Stimulated Emission of Radiation). Although the main concept had been proposed theoretically by Albert Einstein in 1917, the first laser was demonstrated by Theodore H. Maiman in 1960 following the demonstration of the maser (Microwave Amplification by Stimulated Emission of Radiation) in 1953 by Charles Hard Townes, based on the work of Nikolay Basov and Aleksandr Prokhorov who had proposed the pumping of laser with energy to maintain population inversion. Since then, the availability of directional, monochromatic light sources of high power with well-defined polarization and coherence, the main characteristics of the laser radiation, by low-cost and easy-to-handle sources, allowed for the methodical exploration of the properties and application of light and also promoted the study of light-matter interactions.

The development of photonics was also accelerated by the introduction of semiconductor devices. Due to the great technological importance for the implementation of computational devices, semiconducting devices became the center of intense research activities after the demonstration of the transistor in 1947 by John Bardeen, Walter Brattain, and William Shockley. Phototransistors, initially demonstrated by John N. Shive in 1950, and photodiodes not only offered a beneficial alternative to other light-electricity transducers such as photoresistors and photomultiplier tubes, but also allowed for the integration of electronic and optoelectronics components. Besides semiconducting photodetectors, semiconductor light emitting devices fabricated from gallium arsenide or other binary materials from the III-V elements groups were demonstrated in 1962 by Robert N. Hall. The high efficiency, low cost and small volume of such devices gave birth to the

field of optoelectronics. The close relation between semiconductor electronics and photonics is supported not only by the use of semiconductors in optoelectronics, but also by the use of photonic methods, namely photolithography, for the fabrication of high density integrating microelectronic circuits for the realization of high efficiency processors and memory units widely used today.

Yet another milestone in the development of photonics was the invention of optical fiber in the 1960s. The concept of photonic waveguides exploiting the phenomenon of total internal reflection was initially demonstrated by Daniel Colladon and Jacques Babinet in the early 1840s followed by the studies by John Tyndall in 1850s. In 1910, Demetrios Hondros and Peter Debye proposed the name *"dielectric wires"*[6] and solved for the first time the boundary condition problem of the Maxwell equations inside a waveguide, and derived the waveguiding conditions. However, it was not until the 1970s and the demonstration of low attenuation light guidance (<20 dB/km) over long distances, that effective high speed data transmission was achieved. Optical fibers and the invention of the erbium-doped fiber amplifier in 1986 eventually led to the development of large area computer networks and the internet by replacing copper wires for massive data transmission over very long distances.

Today, although the exact nature of light is not a mystery anymore, photonics remains at the center of scientific research in both academia and industry. The new fields of nanophotonics and plasmonics have expanded the horizons of photonics providing new routes for advanced devices in the nano scale with improved or inherently new properties. Communication and information technology, microelectronics, the defense industry, energy conversion, medicine, environmental and structural monitoring are only a few of the fields that benefit from the advances of photonics, and are expected to be further promoted by exploiting the new era in photonic research.

To recognize the contribution of photonics to the development of the human civilization, on 20 December 2013 the United Nations (UN) General Assembly 68th Session proclaimed 2015 as the International Year of Light and Light-based Technologies (IYL 2015).[7]

1.3 Photonic devices

Every photonic system, or system whose operation partially relies on the properties of light, comprises a set of basic units which accomplish one or more operations including the generation, emission, propagation, amplification, modulation, absorption and detection of light. Such units can be either well separated or closely integrated on the same substrate. In the case of distinct components, each unit can be connected with a form of waveguide (e.g. optical fiber), or otherwise light can propagate in free space, through the atmosphere or other mediums. In all cases apart from the propagation of light in free space, light is generated/propagated/detected or modulated in a medium exhibiting optical properties exploited in favor of the functions of the photonic component. Waveguides, for instance, are made of materials of low optical attenuation (loss) in the operating frequency range while rare earth doped crystals and glasses can provide light generation, thus being exploited in lasers, amplifiers and other light sources. Materials exhibiting nonlinear properties are of great importance for use in light modulators, while materials sensitive to their environment are candidates for use in photonic sensors.

On the other hand, light, being an electromagnetic wave, is affected by the geometry of the photonic structure. This is another key element in any photonic device design, which determines the precise manipulation of light. Confinement in a waveguide is achieved not only via the photonic materials having specific properties, but also by a well-defined geometry, the photonic structure. Further to the common internal reflection notion, diffractive optics and photonic crystals offer some of the best examples of photonic structures having properties defined by their geometry. In a related important family of optical resonators, optical feedback is also provided by the geometry, forcing light to oscillate in the defined region, where, for example, a gain medium may be placed.

In general, starting with the required application, the design of the photonic device lies along two directions: (a) the design, synthesis or growth of the photonic materials to be used, and (b) the design and fabrication of the photonic structure. An illustrative representation of this procedure is shown in Figure 1-1. A crucial factor, however, in the implementation of a photonic structure is the fabrication techniques that need to be followed. The small wavelength of light in the micron regime dictates the necessity for very accurate fabrication of photonic structures with narrow tolerances. Photonic structures are therefore often fabricated using methods initially developed for the microelectronics industry, namely

FIGURE 1-1: Conceptual outline of the general procedure for the realization of photonic structures. The red arrow outlines the close connection between the fabrication route of the photonic structure and the photonic materials to be used.

photolithography, reactive ion etching (RIE), electron beam lithography (EBL) and various deposition methods including spin-coating, chemical vapor deposition (CVD) and molecular beam epitaxy (MBE). These methods are usually effective in the field of optoelectronics where semiconductors are used as photonic materials whereas they often pose limitations in combination with other photonic materials such as polymers or sol-gels. The close connection between the photonic materials to be used in photonic devices and the photonic structure fabrication route is outlined by the red arrow in Figure 1-1.

Apart from VLSI methods, many other fabrication approaches find application in photonic devices. Direct laser writing, laser ablation, two photon polymerization and pulsed laser deposition (PLD) are a few examples based on light–matter interaction, while fiber drawing methods are applied for the manufacturing of fiber optics. A large family of alternative lithographic procedures also include nanoimprint lithography (NIL) and soft lithography approaches. Materials exhibiting self-assembly properties due to their interaction with their chemical and or physical environment, have also been studied for the implementation of advanced photonic structures.

CHAPTER 2

PHOTONIC NANOCOMPOSITES: QUANTUM DOTS & OTHER NANO-ENTITIES

2.1 Introduction to Quantum Dots

Quantum dots (QDs) are considered to be a great confirmation of the famous quotation by Richard Feynman in 1959 when he argued that "*there's plenty of room at the bottom*", essentially foreseeing the coming of nanotechnology. QDs are fluorescing or not nanosized particles of a, normally, semiconducting material, which exhibits -in most cases- spatial quantum confinement for electrons and/or holes in all three dimensions due to lack of periodicity. This attribute alters the available energy states of the semiconductor material, thus affecting the absorption and photoluminescence (PL) spectrum.[8,9] In most cases, these alterations take place when the size of nanoparticle is smaller than the Bohr radius of the exciton of the three dimensional (3D) material.

The history of QDs starts in the early 1960s when quantum effects in ultra-thin layers of materials were studied.[10] The role of the size of small particles in the color of molten glasses is reported was 1981[11] when, during the same year, G. Papavassiliou published his work on the size dependence of the PL spectrum of small chemically synthesized CdS nanoparticles.[12] Surprisingly, the first submission of this work for

publication was rejected and the reviewer suggested there was a malfunction of the spectrometer he used.[13] R. Rossetti, S. Nakahara, and L. Brus in 1983 published their study on CdS crystallites in aqueous solution[8] while A. Ekimov, A. Efros, and A. Onushchenko in 1985 reported on the quantum size effects in semiconductor microcrystals.[14] The term "*quantum dots*" was first used in 1986 in the work of M. Reed et al. on lithographic GaAs/GaAlAs QDs.[15]

The simplest model for the description of the effect of quantum confinement in a QD is the "*particle in a box*" model where, upon the formation of an exciton (an electron hole pair) inside the nanoparticle when excited in either an optical or electrical manner, the wave function of each carrier is forced to be confined inside the nanosized direct gap semiconductor nano-entity surrounded by dielectric or semiconducting material of higher energy gap. Then, by solving the Schrödinger equation with the appropriate boundary conditions, the eigenstates of the carriers are obtained and the new allowed energy states can be calculated. The critical parameters for the occurrence of the quantum confinement is the nanoparticle Bohr radius α_0, given by the formula:[16–18]

$$a_0 = \frac{4\pi\varepsilon_0\hbar^2}{m_e^2 e^2} \tag{2.1}$$

ε_0 being the permittivity of free space, $\hbar$ the reduced Planck's constant, m_e the effective electron rest mass in the semiconductor material and e the elementary charge. The ratio of the exciton Bohr radius to the size of the nanoparticle defines the strength of the quantum confinement: weak confinement regime for QDs of radius on the order of the exciton Bohr radius and strong confinement regime for QD of smaller radii. Quantum confinement leads to the discretization of the energy bands[19,20] and defines the available energy states for the carriers as shown illustratively in Figure 2-1. If confinement occurs in all three dimensions and the nanoparticles exhibit an atom-like energy diagram and the consequent optical properties with an entirely discrete density of states (DOS). The nanoparticle is

then said to be a quantum dot. This is to be contrasted with quantum wells (QWs), 2D dimensional nanoentities, and quantum wires, 1D dimensional nano-entities, where quantum confinement occurs in only one or two dimensions respectively.

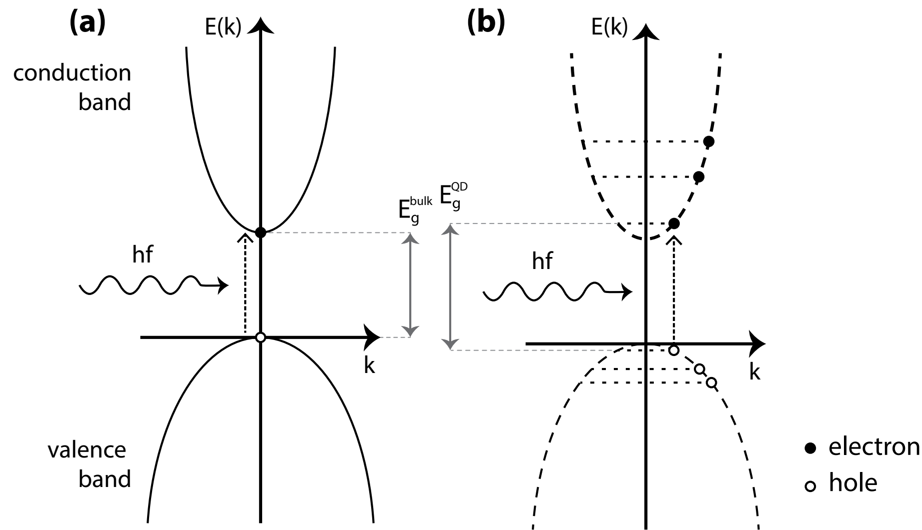

FIGURE 2-1: (a) A simple illustration of a two bands diagram of a direct gap semiconductor, **(b)** energy levels discretezation due to quantum confinment.

The presence of a finite number of well-defined energy levels in a QD instead of the continuum valence and conduction bands of the bulk semiconductors denotes that only discrete electronic transitions are allowed, thus light of only discrete frequencies can be emitted by the nanoparticle. Another consequence of this effect is the dependence of the band edge shift, therefore the emitted light, on the size of the nanoparticle. In 1986, L. Brus provided an analytical approximation for the lowest eigenvalue, hence the first excited electronic state (neglecting Coulomb interactions):[21]

$$E \simeq E_g^{3D} + \frac{\hbar^2 \pi^2}{2R^2}\left[\frac{1}{m_e} + \frac{1}{m_h}\right] + smaller\ terms \qquad (2.2)$$

where E_g^{3D} is the energy gap of the bulk semiconductor (3D), R is the QD radius while m_e and m_h are the electron and hole effective masses. According to this formula, the energy of the first electronic transition shifts due to quantum confinement as R^{-2}. Typical sizes of QDs range in the 1.5-10 nm regime incorporating 10^2 to 10^5 atoms.

Although many fabrication routes for the implementations of QDs have been proposed, chemical synthesis using colloidal chemistry and epitaxial growth using molecular beam epitaxy (MBE) or metallorganic vapor phase epitaxy (MOVPE) are most widely reported. While epitaxial growth, which is discussed in chapter 5, requires complex, high cost facilities, colloidal QDs can be synthesized using relatively simple chemistry in a glass beaker at moderate temperatures.[22–31] The semiconductor precursors are dissolved in an appropriate solvent with the addition of organic surfactants. Upon heating, the precursors are transformed into monomers which initiate the nucleation process and the growth of the nanocrystals under proper conditions. The temperature of the process and the concentration of the precursors and surfactants are critical factors for successful growth. The size of the synthesized QDs exhibits a size distribution due to fluctuations of the growth process which is reflected in the broadening of the PL spectrum of the nanocrystals. Quality synthesis of QDs aims at the monodispersion of the nano-entities in terms of size and shape. Metal-organic precursors are the commonly used raw materials for such synthesis which undergoes pyrolysis at elevated temperatures (120°C–360°C). Extensive studies of the particle nucleation and growth have provided deep understanding of these processes[16,32,33] where three distinct successive steps have been identified: a short initial nucleation, a rapid growth from the solution phase of the monomers and Ostwald ripening, a slow recrystallization process where small nanocrystals are re-dissolved and deposited on the larger ones. Further processing of the colloidal QD can reduce the size of the nanoparticles by controlled etching by exposing them to an etching agent, usually an acid. Typical QDs synthesized using colloidal synthesis include, but are not limited to, both binary and ternary alloys such as cadmium selenide (CdSe), cadmium sulfide (CdS), cadmium telluride (CdTe), cadmium selenide sulfide (CdSeS), zinc sulfide (ZnS), mercury telluride (HgTe), indium arsenide (InAs), indium phosphide (InP) and lead sulfide (PbS) to name just a few of the nanocrystals reported in the literature.

A key characteristic of the chemically-synthesized QD is the usage of ligands as the terminating material of the nanoparticles. Ligands are organic molecules attached to the outer surface of the nanocrystals to electronically and physically isolate the nano-entities from their environment. They stabilize the QDs in solution or in a matrix by providing passivation, prevention of aggregation and protection from oxidation and other degradation mechanisms that can induce quenching of the luminescence. Capping of the QDs with ligands also passivates the surface states of the nanocrystals that can allow non-radiative recombination and thus induce reduction of the quantum yield of the material. Moreover the capping molecules also provide the required interaction of the QDs to the environment of the nanocrystals rendering them soluble in specific solvents. The choice of ligands is accordingly crucial to the incorporation of QDs in various matrices.

Chemically-synthesized QDs are usually initially provided in solution form with toluene, chloroform and hexane as typical solvents. To render them useful in the development of practical integrated photonic structures, it is necessary to encapsulate the nanocrystals in solid matrix without altering their functionality. Much effort has been devoted to the study of such encapsulation. The choice of host materials follows the development of common photonic materials with glasses, polymers and sol-gels being at the center of scientific research.

Today, chemically-synthesized QDs are massively produced in large batches at low cost. It is therefore believed that they will find their way into commercialization during the next years in a broad range of commercial applications in addition to their already intense scientific research, many start-ups already commercially supply QDs. QDs can be exploited in advanced photonic structures,[34] as efficient and versatile gain material in organic light emitting diodes (OLED),[35–38] lasers,[39–44] as fluorescent coatings in lighting applications, in new photovoltaic devices,[45–49] photodetectors,[50–52] flat panels displays,[53,54] for sensing applications,[55–58] as biological reagents, in cellular

imaging of other biotechnology applications.[59–61] Moreover QDs are being studied as effective materials for future emerging fields of quantum computing[62] and quantum cryptography.[63,64]

Chemically synthesized QDs are also to be contrasted to the use of other optically active materials that are widely incorporated in organic and inorganic matrices, mainly dyes. The advantages of QDs include:

- The easily tuning of emission wavelength by the control of the size of the nanoparticles during synthesis in addition to their composition, a property not offered by dyes
- The narrower photoluminescence spectrum
- The broader absorption spectrum of QDs
- The inherent higher stability
- The higher resistance of QDs to photobleaching
- The temperature independent emission

2.2 Spectroscopic studies of commercially available QDs

Commercially available CdSe/Zn core/shell QDs dissolved in toluene under the trademark Lumidot™ have been synthesized by Nanoco Technologies®, a UK-based company, and being purchased through Sigma-Aldrich. The initial solution contains a 5 mg/ml concentration of QDs of average core size of 6.3 nm emitting deep red light at 640 nm upon excitation with a full width at half maximum (FWHM) of the PL spectrum of less than 40 nm. According to the supplier, the solution exhibits a high quantum yield of ≥30% while the boiling point and density coincide with that of the toluene solvent. The PL and absorption spectrum of the diluted initial solution (about 40:1 with toluene) as measured in the National Hellenic Research Facilities (NHRF, Athens) are shown in Figure 2-2.

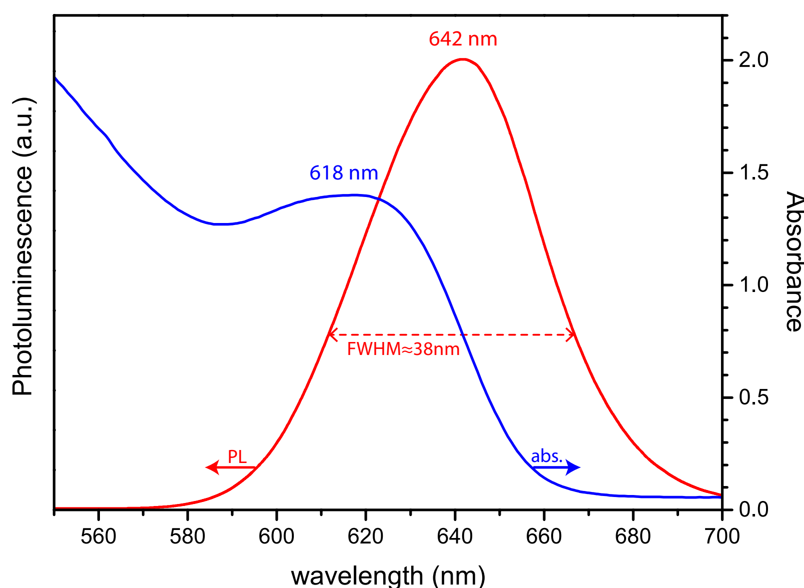

FIGURE 2-2: Photoluminescence spectrum under excitation at 380nm and absorption (UV/VIS) spectrum of the initial QD/toluene solution

The QDs are capped with hexadecylamine (HDA) and trioctylphosphine (TOPO) ligands in order to stabilize them. Energy dispersive x-ray spectroscopy (EDX) measurement was performed using an Oxford Instruments™ 10mm^2 SDD Detector attached to a Zeiss EVO 10 scanning electron microscope (SEM) established in the Department of Materials Science in University of Patras. The EDX spectrum shown in Figure 2-3 reveals the ratio of the elements comprising the nanocrystals. A relatively high ratio of phosphorus and the elements of the shell, (P/Zn=P/S=0.29) indicates the present of excess of TOPO in the solution. From the same measurement the size of the ZnS shell of about 3 Å has been estimated while the total size of the nanoparticle including the ligands sums to a diameter of 8.6 nm. An illustrative depiction of the QD structure and the form of the ligands molecules are shown in Figure 2-4.

To identify the optimum excitation wavelength for maximum photoluminescence, we have recorded a series of PL spectra using a calibrated spectrofluorometer (Horiba FluoroLog®-3) established in National Hellenic Research Foundation (NHRF) in Athens, incorporating a 450 W xenon CW lamp for excitation wavelengths spanning 250 nm to 600 nm as shown in Figure 2-5(a). The peak PL as a function of the excitation wavelength shown in Figure 2-5(b) reveals that the

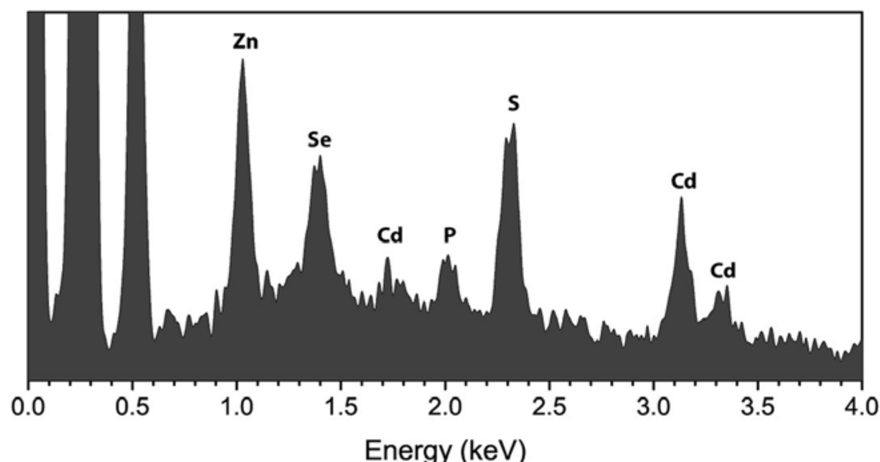

FIGURE 2-3: Energy dispersive X-ray spectrum (EDX) of the solvent-free QD nanoparticles deposited on silicon substate outlining the main measures X-ray emission peaks. P/S=P/ZnS=0.29

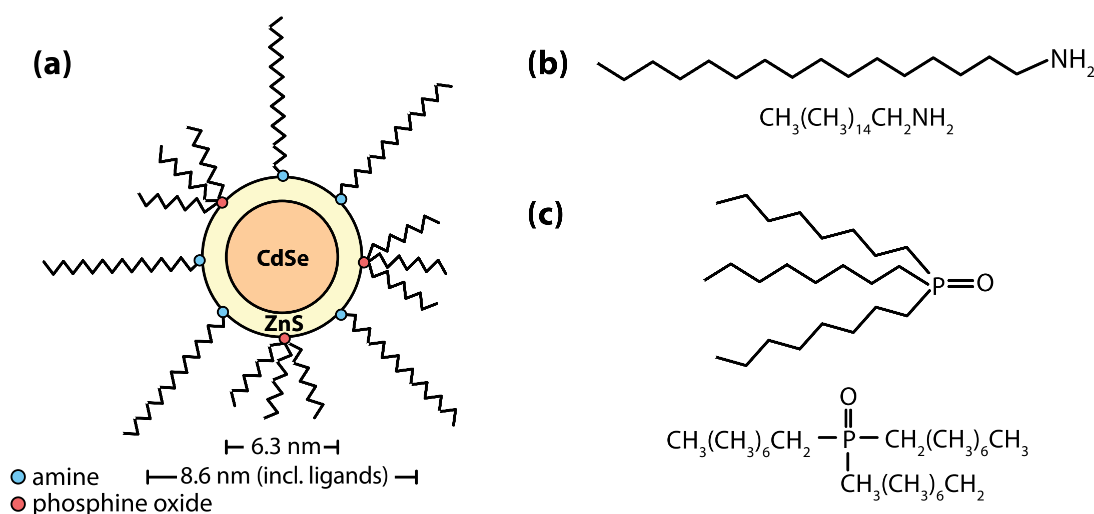

FIGURE 2-4: (a) Depiction of the structure of the core-shell CdSe/ZnS quantum dot capped with hexadecylamine ligands, the structural and condensed formulas of: **(b)** hexadecylamine (HDA), and **(c)** trioctylphosphine oxide (TOPO). The figure is conceptual and not to scale.

maximum amount of light is emitted from the QD solution when illuminated with a 382 nm source. Efficient light sources emitting at 365 nm and 380 nm available today include LED and diode lasers in a wide chose of output power from a few mW up to few W due to the advances in gallium nitride-based optoelectronics. The use however of GaN based diode lasers emitting at 405 nm is favorable in terms of cost offering comparable PL efficiency with a reduction of only a few percent in the efficiency. The low cost of such laser sources emitting up to 150 mW is attributable to their mass production due to their use in the entertainment industry, particularly in blue-ray discs and popular games consoles.

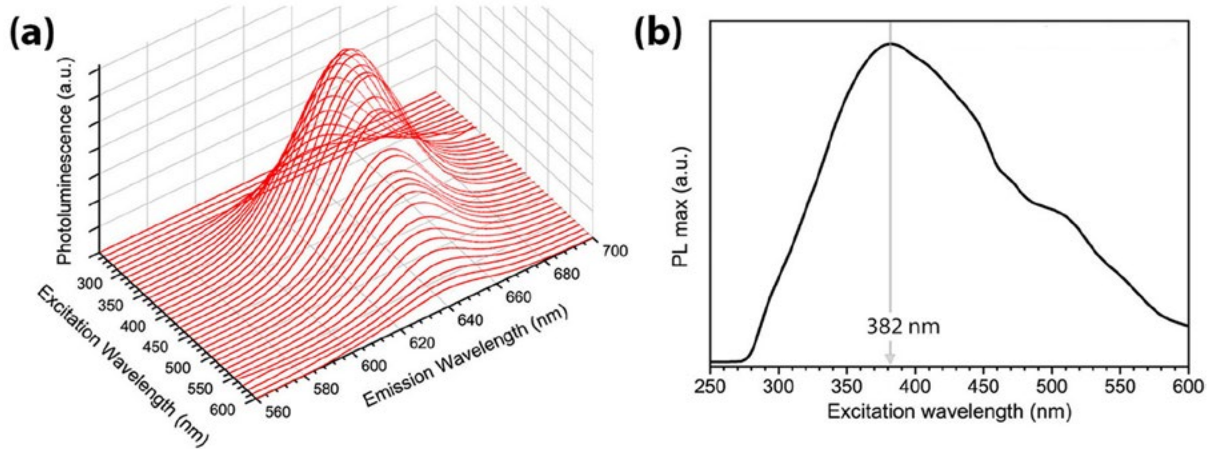

FIGURE 2-5: (a) Photoluminescence spectrum for different excitation wavelengths, **(b)** maximum photoluminescence of the QDs versus the excitation wavelength.

The concentration of the QDs in the initial solution can be roughly calculated from the size of the nanoparticles, the mass concentration provided by the supplier and the densities of the materials. A more accurate method to measure the functional QD concentration in every transparent solvent or matrix is by exploiting the optical characteristics of the material and in particular the extinction coefficient of the nanocrystals. In 2003 the X. Peng group synthesized QD of various sizes and characterized them with precise UV-VIS, transmission electron microscopy (TEM) and atomic absorption measurements to reach a set of fitting equations for the CdSe QD optical properties as a function of their size.[65] The wavelength of the first excitonic peak λ in nm is closely connected to the diameter D_{CdSe} of the nanocrystals in nm, given by the empirical formula:[65]

$$D_{CdSe} = \left(1.6122\times10^{-9}\right)\lambda^4 - \left(2.6575\times10^{-6}\right)\lambda^3 + \left(1.6242\times10^{-3}\right)\lambda^2 - 0.4277\lambda + 41.57 \tag{2.3}$$

while the experimentally determined extinction coefficient ε per mole of particles for CdSe nanocrystals is reported to be given by:[65]

$$\varepsilon_{CdSe} = 5857\times D_{CdSe}^{2.65} \tag{2.4}$$

which is valid for bare CdSe QD. The CdSe/Zn nanocrystals under study exhibit an extinction coefficient of 5.90×10^5 M^{-1} cm^{-1} as provided by the supplier.

The QDs concentration C can be calculated from the Beer-Lambert law by measuring the solution absorbance A at the first excitonic peak:

$$A = \varepsilon l C \tag{2.5}$$

In this formula l is the length of the light path in the solution, i.e. the length of the cuvette used in measurements (1 cm). Such a measurement can be performed only in low QD concentration solutions to avoid re-absorption of the photoluminescent light by the nanocrystals by ensuring that the mean distance between particles is greater than the light wavelength.[66] A set of solutions of various relative volume concentrations in respect to the initial -as purchased- solution have been prepared and shown in Figure 2-6(a), measured using a UV-vis spectrophotometer (Shimadzu UV-1800). The height of the first excitonic peak as a function of the relative volume concentration is shown in Figure 2-6(b), as well as a linear fitting of equation 2.6.

$$\begin{gathered} abs. = a \cdot C + b \\ a = 0.02886 \pm 0.00156 \ \ (per\ \%\ v/v), \quad b = 0.22888 \pm 0.00242 \end{gathered} \tag{2.6}$$

The slope a of the fitting corresponds to the absorbance per relative volume concentration (% v/v) of the initial solution while the intercept b is attributed to the

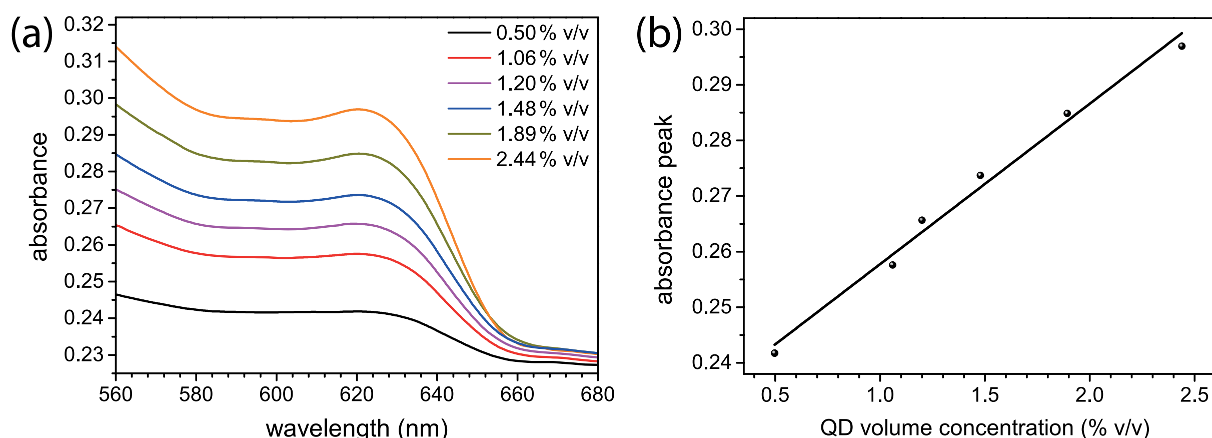

FIGURE 2-6: **(a)** Absorption of the QDs solution diluted in toluene with respect to the initial concentration, **(b)** the dependence of the excitonic peak on the relative QD concentration relative to the initial solution and the linear fitting (R^2=0.986).

background absorbance of the solvent, impurities and measurement flaws. From this calculation it is deduced that a 1% v/v QD/toluene solution in respect to the initial solution has a QD concentration of 0.0489 ± 0.0026 μM, thus concluding that the initial solution has a nanocrystal concentration of 4.89 ± 0.26 μM.

2.3 Incorporating QD in polymer matrices

The benefits of using polymers as photonic materials for the implementation of photonic systems arise not only from the low cost of polymers, but also from the inexpensive, simple and versatile fabrication techniques available for this family of materials. In contrast to semiconductors widely used in optoelectronics such as silicon and gallium arsenide, polymer complex photonic structures can be fabricated using large area manufacturing techniques, e.g. nanoimprint lithography (NIL) and soft lithography, on a wider range of inexpensive, even flexible, substrates. The versatile, low cost chemistry of polymers also allows for the easy alteration of their functionalities and the fabrication of tailor-made polymers for various applications. Furthermore, the much lower and easily tunable refractive index of polymers, of the order of 1.5 in contrast to 3.8 for silicon (at 650 nm), enables the fabrication of photonic structures of larger features size, e.g. photonic crystals, with improved fabrication tolerances and minimum optical loss, also enabling the simple coupling to optical fibers. For all the aforementioned reasons, encapsulation of QD in a polymer matrix is an emerging topic of intense research activities and is related to this work.

Any attempt to incorporate QDs into a polymer matrix is mainly aimed at preservation of the properties of the nanocrystals and prevention of degradation and quenching of the luminescence due to their sensitivity to surface passivation.[67] The proximity of the polymer chains to the QD ligands may alter the effectiveness of surface passivation and allows for the emerging of surface states deleterious to the emission properties. Furthermore, phase separation between the QDs and the

polymer may not only cause degradation of the nanocrystals, but also the increase of optical losses of the final photonic material due to scattering. Ideal dispersion of QDs into a polymer host is translated into a homogeneous distribution of the nanoparticles with the maximum possible distance among them for a given concentration. Various routes have been proposed for the implementation of functional QD/polymer nanocomposites including the use of compatible polymers and QD ligands where the capped nanoparticles are incorporated as-is into the polymer after any ligand exchange procedure if needed,[68–72] and the use of polymers with functional groups that attach to the QD surfaces acting as ligands.[34,73,74] Alternatively the polymerization of monomers or oligomers in the presence of QDs[75,76] and the encapsulation of QDs into polymer micelles, among other methods, have been demonstrated.[77,78]

A series of polymers have been either synthesized or purchased to study the performance of their nanocomposites at various QD concentrations. The selection of the appropriate materials is based on the requirement for high transparency in both the working wavelength range (550-700nm) and the excitation wavelength (375-405 nm) as well as their solubility in toluene, the solvent of the initial QD solution. The polymers studied here include two of the most commonly used polymers for the implementation of photonic structures: poly(methyl methacrylate) –PMMA, an acrylic polymer ("*acrylic glass*"), and polystyrene –PS. Both exhibit excellent transparency in the visible and infrared region allowing for the fabrication of low loss waveguides.[79] Moreover, these polymers are known to be easily and effectively processed for the fabrication of quality photonic integrated circuits. Variations of PMMA have also been designed, synthesized and characterized for better interaction with the QD surface ligands where the crucial point is the properties of the part of the ligands which form the outer shell of the QDs. Both molecules used, hexadecylamine (HDA) and trioctylphosphine oxide (TOPO) are amphiphilic molecules exhibiting a group that attaches covalently on to the ZnS surface of the QD shell (amine and phosphine oxide respectively), and long alkyl chains exposed to the outer region

of the nanoparticles rendering them hydrophobic and soluble in non-polar solvents such as toluene. Although in QD/polymer solutions in toluene the nanoparticles mainly interact with the solvent molecules, by casting and drying to form solid nanocomposites the nanoparticles are forced to be in proximity to the polymer chains. In the case of PMMA the carbon oxygen polar bonds in the ester group (both C–O and C=0) are regions on the polymer chains where the interaction with the alkyl chains is not completely favored. Better compatibility between ligands and polymer chains is expected to improve the dispersion of the nanoparticles in the host and reduce agglomeration and luminescence quenching. In this concept, acrylic monomers with alkyl chains attached to the ester group are used to synthesize polymers and random copolymers. These chains are not part of the polymer backbone, rather they protrude perpendicular to it, being free to interact with the exposed alkyl chains of the QD ligands. Such polymers have been reported indeed in the literature to yield better QD encapsulation into polymer matrices by preventing quenching of the quantum yield of the nanoparticles.[69,72,80] In another approach, different types of ligands have been used to promote compatibility with the polymer.[81,82]

The monomers used here are n-butyl methacrylate–BMA (the abbreviation of BMA instead of nBMA is used for simplicity) featuring a 4 carbon atom linear chain and lauryl methacrylate –LMA, which features a longer, 12 carbon atoms linear alkyl chain. The polymer synthesized and studied are PMMA, PBMA, PLMA and two P(MMA-LMA) copolymers of different monomer weight ratios: P(MMAcoLMA) 50-50 where equal amounts of MMA and LMA were reacted during synthesis, and P(MMAcoLMA) 75-25 where a 3:1 weight ratio of the MMA/LMA monomers was used. Depiction of the polymers under study are shown in Figure 2-7 along with two other polymers discussed later: poly(2,2,2-trifluoroethyl methacrylate) –P3FEMA, a low refractive index[83] fluorinated alternative of PMMA and poly(dimethylsiloxane) –PDMS, an organosilicon compound used for soft lithography fabrication.

2.4 Synthesis of polymers

Synthesis of the polymeric matrices was performed in the polymer laboratory of National Hellenic Research Foundation in Athens (NHRF), under the supervision of Dr. Stergios Pispas. Free radical polymerization has been employed using 2,2'-azobis(isobutyronitrile) –AIBN, an azo compound with the formula $[(CH_3)_2C(CN)]_2N_2$, as the initiator. In such a procedure the initiator is transformed into free radicals under heating, which add monomer units to the growing polymer chain successively by opening a π-bond to form a new growing macroradical.[84] In the case

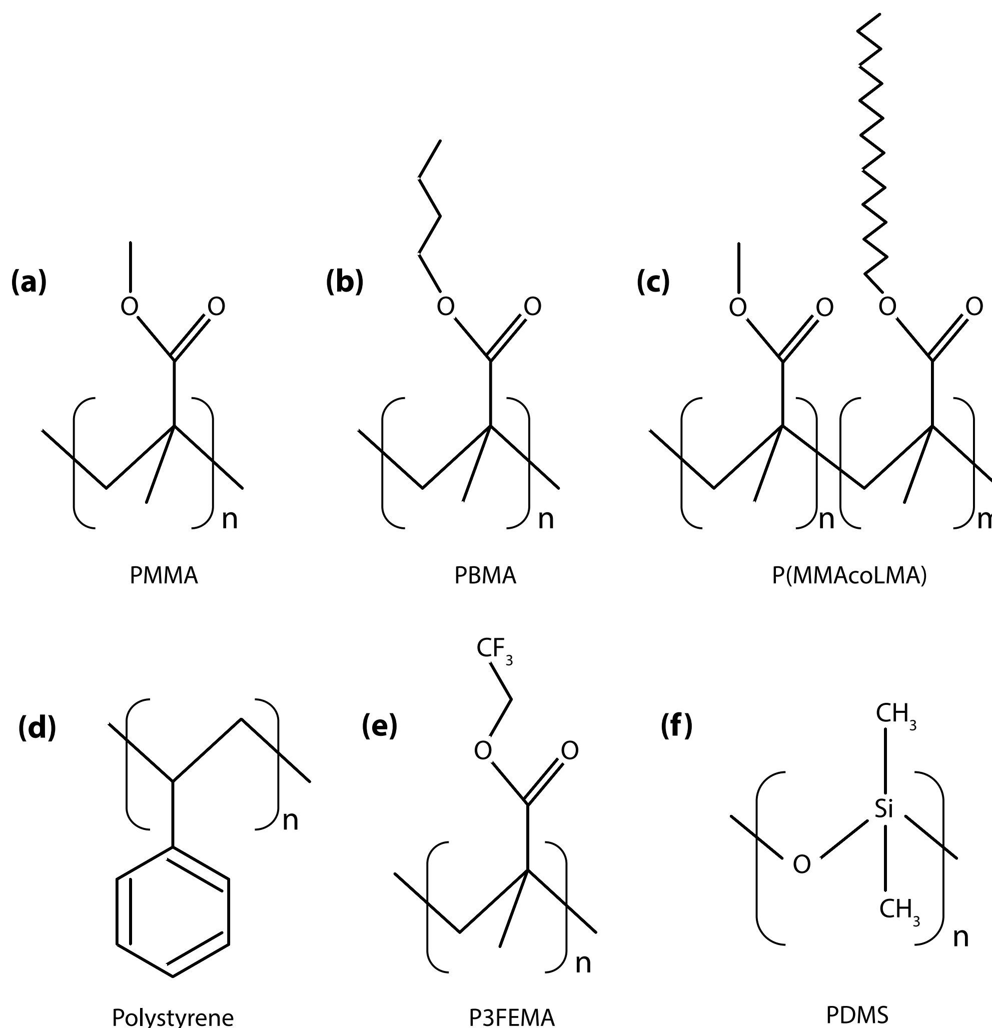

FIGURE 2-7: The structural formulas of the polymers studied in this chapter and their abbreviations: **(a)** Poly(methyl methacrylate) –PMMA, **(b)** Poly(butyl methacrylate) –PBMA, **(c)** Poly(methyl methacrylate-co-lauryl methacrylate) –P(MMAcoLMA), **(d)** Polystyrene, **(e)** Poly(2,2,2-trifluoroethyl methacrylate) –P3FEMA, **(f)** Poly(dimethylsiloxane) –PDMS.

of use of AIBN as the initiator, the azo molecule decomposes, eliminating a nitrogen molecule and forming two 2-cyanoprop-2-yl radicals. This initiator is suitable for vinyl monomers exhibiting carbon-carbon double bonds such as the monomers used for synthesis of acrylic polymers studied here. Initially the free radical interacts with a loose electron of the π-bond of a monomer to form a more stable bond with the carbon atom while the other electron from the π-bond electron pair stay in the second carbon atom and forms another radical. The process is repeated until the population of the monomers is depleted or the polymer chain growth is stopped by deactivation of the reactive center, e.g. by reacting with a contaminant or inhibitor. Alternatively, the reaction can be terminated by intentionally allowing the solution to react with the atmosphere.

Free radical polymerization is a simple, versatile form of polymerization that can be applied to a vast number of monomers. The experimental procedure starts with meticulously dissolving the correct amount of the initiator in part of the total solvent volume, which is toluene in the case under study. The solution is added in a cleaned round-bottom flask filled with the remaining solvent, the monomers to be reacted and a stirring bar. The flask is then sealed with a precision seal septa and degassed by a copious nitrogen flow for at least 15 minutes. The flask is placed in a pre-heated oil bath at a steady temperature of 60°C for 12 hours under stirring. The process is stopped by unfastening the flask and allowing it to interact with the oxygen of the atmosphere. The polymer solution is then precipitated in a non-solvent for the produced polymer, with methanol being used here for the acrylic polymers, in a methanol/polymer solution volume ratio of about 5-10:1. Finally the polymer obtained is dried in vacuum for at least 24 hours. A typical polymer synthesis include a total of 4 g of monomer, 20 ml of toluene and 20 mg of AIBN or other amounts of materials of the same proportions. All polymers synthesized under identical conditions with the exception of the P3FEMA for which the temperature was set at 67°C and the solution was left for 24 hours polymerization. Random copolymers have also

been synthesized by reacting more than one monomer in well-defined weight ratios. A depiction of the polymerization process in presented in Figure 2-8.

All polymers were characterized after synthesis and dried. Differential scanning Calorimetry (DSC, TA Instruments model Q200) was used to measure the glass transition temperature of the materials while the density of the polymers was measured by a specific gravity meter based on a precision balance (Shimadzu AUW120D with SMK-401 specific gravity measurement kit). The molecular weight and molecular weight distribution of each polymer was determined by size exclusion chromatography (SEC, Waters system composed of a Waters 1515 isocratic pump, a set of three μ-Styragel mixed bed columns, with a porosity range of 102 Å to 106 Å, a Waters 2414 refractive index detector, operating at 40°C, and controlled through Breeze software). All measurements are summarized in Table 2-1 with the addition to the polystyrene which was purchased from Sigma-Aldrich. Due to the low glass transition temperature of PLMA (-9.5°C) and P(MMAcoLMA) 50-50 (32.0°C) these polymers was not further studied as fabrication issues are encountered under room temperature conditions.

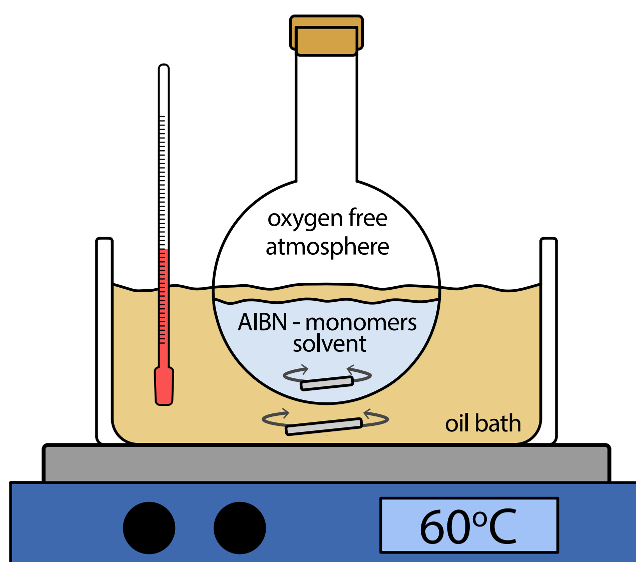

FIGURE 2-8: Illustration of the radical polymerization procedure. Polymerization occurs inside an oxygen-free flask under stirring at fixed temperature for 12 hours.

Table 2-1: Summary of the synthesized polymers measured properties

Polymer	T_g (°C)	d (g/ml)	M_n	M_w	PDI
PMMA	104.3	1.161	40500	64700	1.60
PBMA	32.3	1.051	39700	6300	1.59
P(MMAcoLMA)	40.9	1.044	50300	86300	1.71
P(MMAcoLMA)	32.0	-	45800	77900	1.70
PLMA	-9.5	1.051	-	-	-
Polystyrene	125*	1.049	35000*	-	-
P3FEMA	53.6	-	-	-	-

*Information provided by the supplier (Sigma-Aldrich)

2.5 Evaluation of QD nanocomposites of different polymer matrices

To study the influence of dissolved polymer into QD toluene solutions at various QD concentrations, a series of solutions were prepared and their photoluminescence spectra have been measured. In all cases the polymer concentration was kept steady at 0.15 g/ml altering only the nanoparticle concentration. Figure 2-9(a) shows some typical photoluminescence spectra of QD/PMMA solutions in toluene at different QD concentrations ranging from 1.47 μM to 4.41 μM upon excitation at 405 nm. It is apparent from these measurements that the solution of higher QD concentration exhibits a lower PL peak, an effect attributed to reabsorption of the emitted light within the solution and to intense scattering and screening of the excitation light. Reabsorption is also apparent from the non-symmetrical shape of the PL spectrum of the high QD density solution. Briefly, the low wavelength light emitted from smaller QDs is reabsorbed by larger nanoparticles to excite them, which consequently emit light at higher wavelengths. To precisely measure the position of the PL peak of each spectrum the procedure shown in Figure 2-9(b) is followed: a narrow region around the peak of the recorded spectrum shown with black crooked lines is isolated and fitted with a Gaussian curve by means of a linear transformation. From these Gaussian fittings the peak values and their wavelength position is estimated. To account for the asymmetric form of the PL spectrum however, FWHM values are calculated from the raw data.

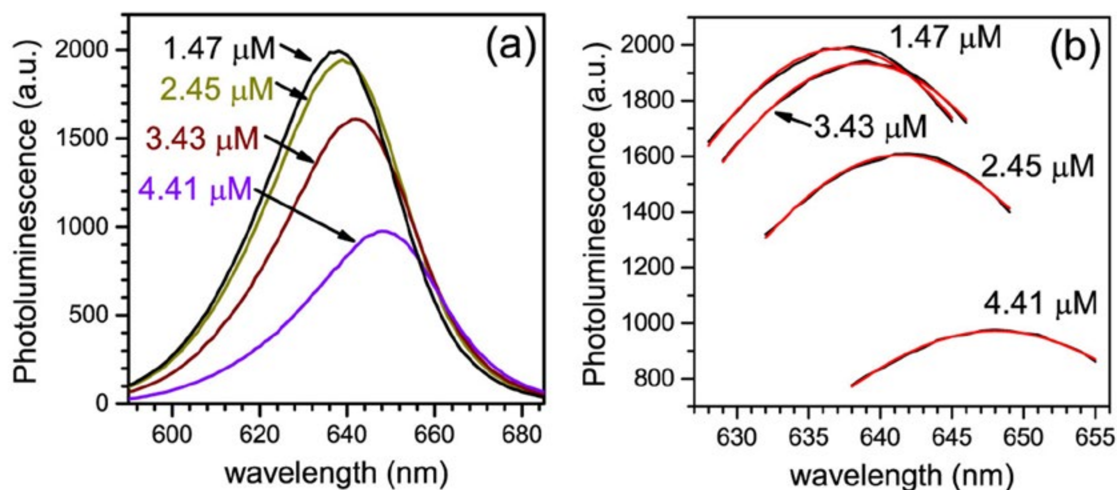

FIGURE 2-9: (a) Example of photoluminescence of 0.15 g/ml PMMA solutions in toluene at various concentration QD concentrations. **(b)** Gaussian fitting of the photoluminescence peaks (back lines: experimental measurements, red line: Gaussian fittings).

The dependence of the maximum PL value on the QD concentration C for the four polymers under study is presented in Figure 2-10. For all spectra of the solutions the emitted light is initially increased to a concentration of up to about 1 µM after which reduction of the PL peak due to reabsorption is observed for all polymer species apart from PMMA which shows a negligible PL reduction up to a C value of about 3.5 µM. It is Interesting that PBMA and P(MMAcoLMA) 75-25 solutions exhibit a small increase of the emitted light after about C=2.5 µM which probably denotes a polymer nanoparticle interaction at high QD concentrations. The shift of the PL peak position as a function of C is shown Figure 2-11. The red shift of about 12 nm at increased QD concentration is also attributed to reabsorption of photons of higher energy emitted by smaller nanoparticles by larger ones that emit photons of low energy. This is the same cause of the small dependence of the FWHM versus C as shown in Figure 2-12.

For the evaluation of the solid QD/nanocomposites in the form of thin films, a similar procedure to the solution measurements has been followed. In particular small amounts of the solutions are spin-coated at 1000 rpm for 60 s on cleaned silicon substrates of about 3×3 cm for the fabrication of thin films of about 1 µm thickness, as measured with a profilometer. The thin films are kept at 80°C for 10 minutes for the solvent to be completed removed. In parallel, thinner thin films

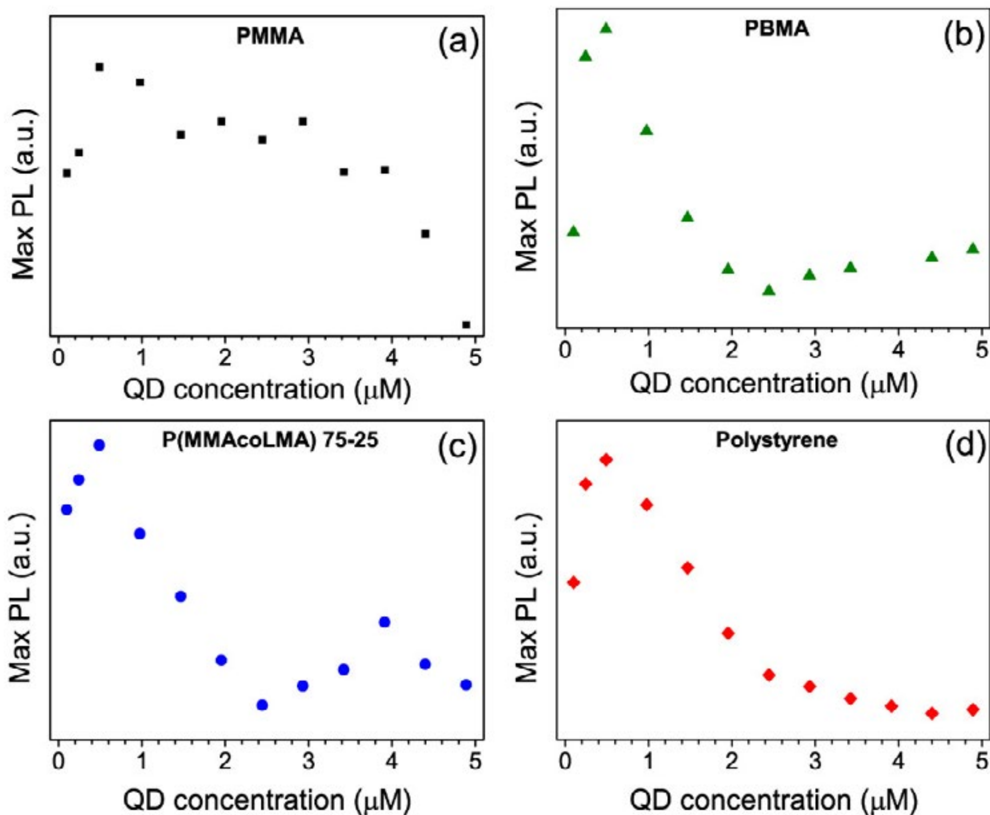

FIGURE 2-10: The dependence of the photoluminescence peak of QD toluene solutions for various concentrations of the nanocrystals. **(a)** PMMA, **(b)** PBMA, **(c)** P(MMAcoLMA) 75-25, and **(d)** Polystyrene.

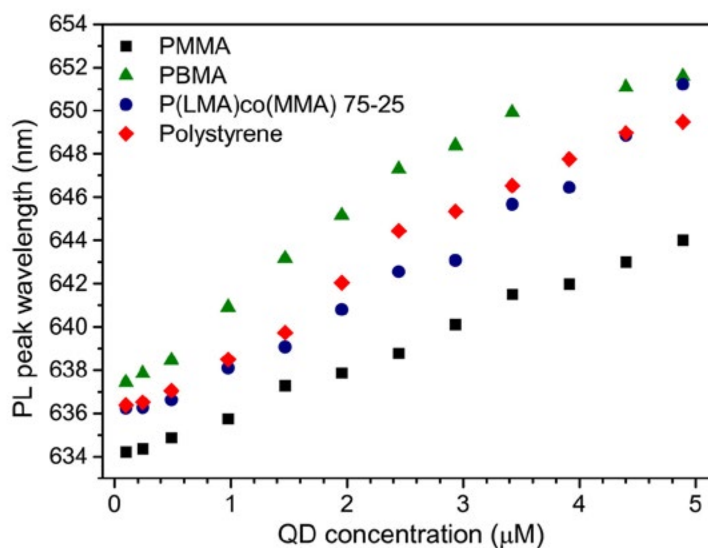

FIGURE 2-11: The dependence of the photoluminescence peak wavelength of QD toluene solutions for various concentrations of the nanocrystals.

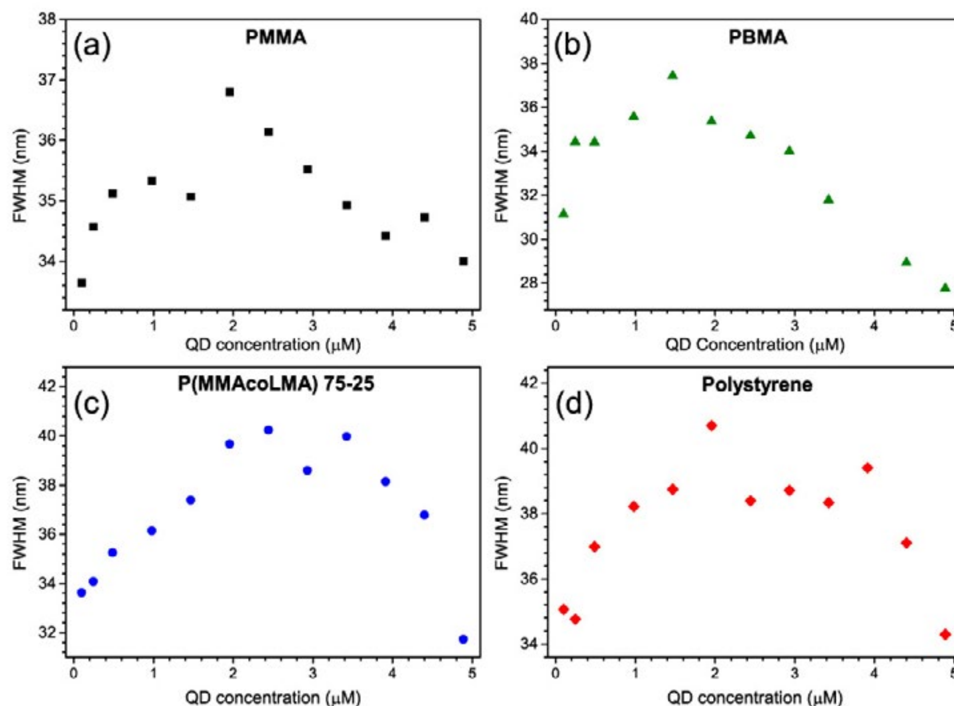

FIGURE 2-12: The dependence of the photoluminescence FWHM of QD toluene solutions for various concentrations of the nanocrystals. **(a)** PMMA, **(b)** PBMA, **(c)** P(MMAcoLMA) 75-25, and **(d)** Polystyrene.

of about 300 nm thickness are spin-coated at 3000 rpm for 60 seconds and dried, for transmission electron microscopy (TEM) measurements. These thin films were detached from their substrates by emerging them in a beaker with ultrapure water under intense sonication. After about 15 minutes large parts of the detached thin film of more than 200×200 μm in size are found to float on the surface of the water and are carefully placed with a fine tweezers on a TEM bare copper grid of 200 lines/inches mesh. The measurements were performed using a JEOL 6300 TEM operating at the reduced voltage of 100 kV to prevent material damage. Agglomerations of QD in PMMA matrix at the higher concentration of the nanoparticles (C=4.89μM) are shown in Figure 2-13 while a TEM micrograph for the PBMA matrix of the same concentration is shown in Figure 2-14. Due to the challenging measurement procedure, micrographs from the other polymer matrices could not be obtained. Aggregates in both PMMA and PBMA matrices indicate lack of full compatibility of the nanoparticles with the host materials and their tendency to avoid contact with the polymer chains by forming agglomerations.

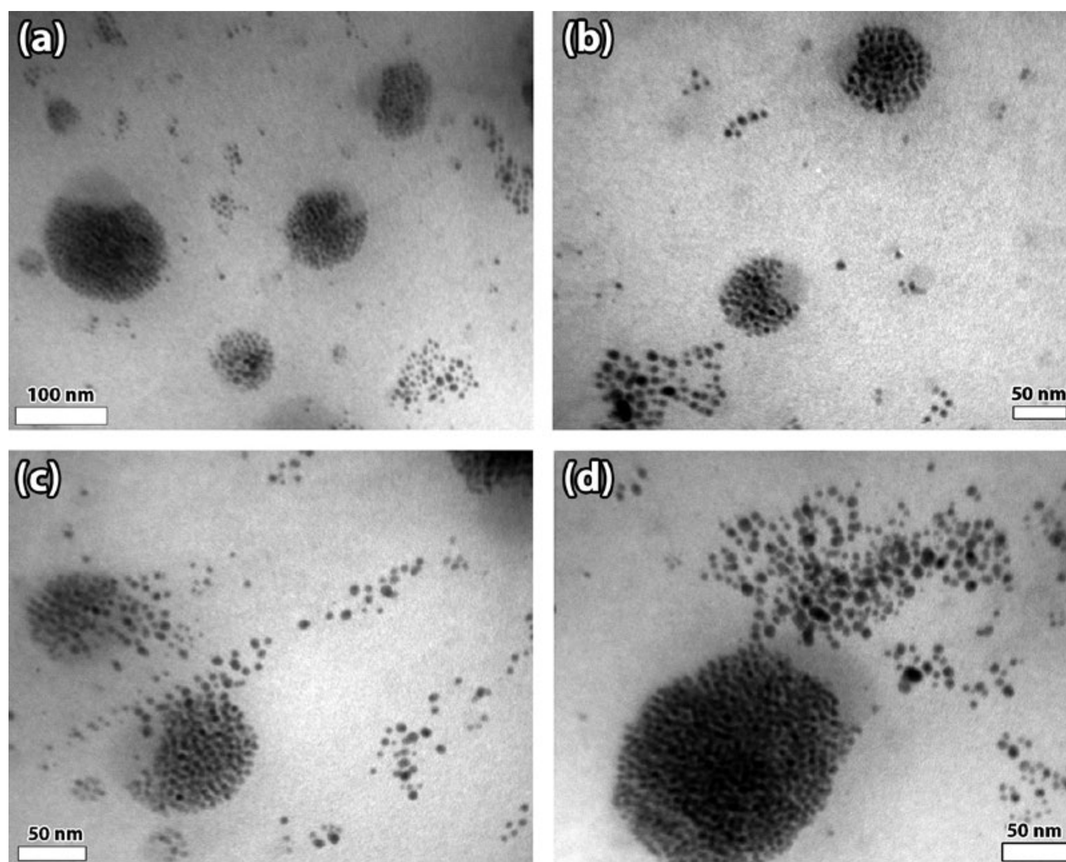

FIGURE 2-13: TEM micrographs of CdSe/ZnS QDs embedded in a PMMA matrix

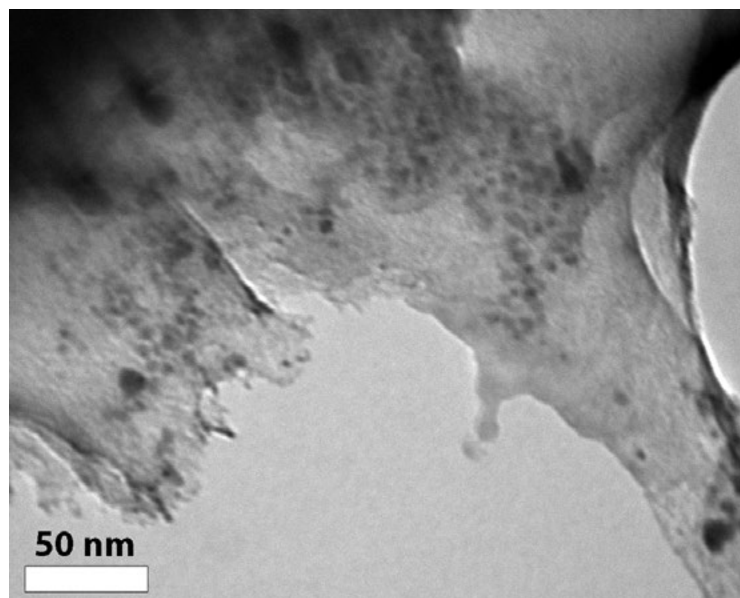

FIGURE 2-14: TEM micrograph of CdSe/ZnS QDs embedded in a PBMA matrix

The PL spectra of the various thin films were measured and analyzed for an incidence angle of the excitation beam at 45° with the same fluorospectrometer under identical conditions. Although measurements from different polymers cannot be compared due to small variations in the film thickness, films of the same polymer matrix are identical since the polymer concentration is always the same and the nanoparticle concentration is not expected to alter the viscosity of the solutions to be spin-coated. Thus, any trends for each measurement set can safely be extracted. In all subsequent spectra two excitation wavelength have been studied: 405 nm measurements are denoted with solid symbols while open symbols are used for excitation at 375 nm.

The PL peak for increased QD concentration C shows no saturation in the thin films exhibiting an almost linear dependence for all polymers as shown in Figure 2-15. To evaluate the performance of the various polymer matrices at incresased QD concentration we compare the PL peak at C=1 μM and at the maximum QD concentration of C=4.89 μM. At low C the nanoparticles are expected to be better distributed inside the matrix with minimum quenching of their PL properties while at increased C they tend to form agglomerations and exhibit reduced quantum yield. In the case of PMMA a ×4.89 increase of the QD concentration results in an about only ×2.52 increase of the PL denoting quenching of the PL of the nanopatricles. The performance of QD/PBMA nanocomposite is better with a ×3.71 increase of the PL while P(MMAcoLMA) 75-25 with the longer alkyl chain exhibits a ×3.22 increase of the PL for the same increase of the QD concentration. Finally, polystyrene exhibits an almost identical to QD concentration increase of ×4.73 the PL peak. It is thus suggested that the last two polymer are better matrices for QD/polymer nanocomposites. All data are summarized in Table 2-2.

In contrast to the measurements in solutions, negligible red shift of the PL spectrum is observed in thin films as indicated in Figure 2-16 with the exception of PMMA, which exhibits a small red shift of about 2 nm. Finally, no alteration to the FWHM of the PL spectrum is observed as shown in Figure 2-17 which is comparable to that of the solutions and initial QD solutions indicating no alteration of the size distribution of the nanoparticles.

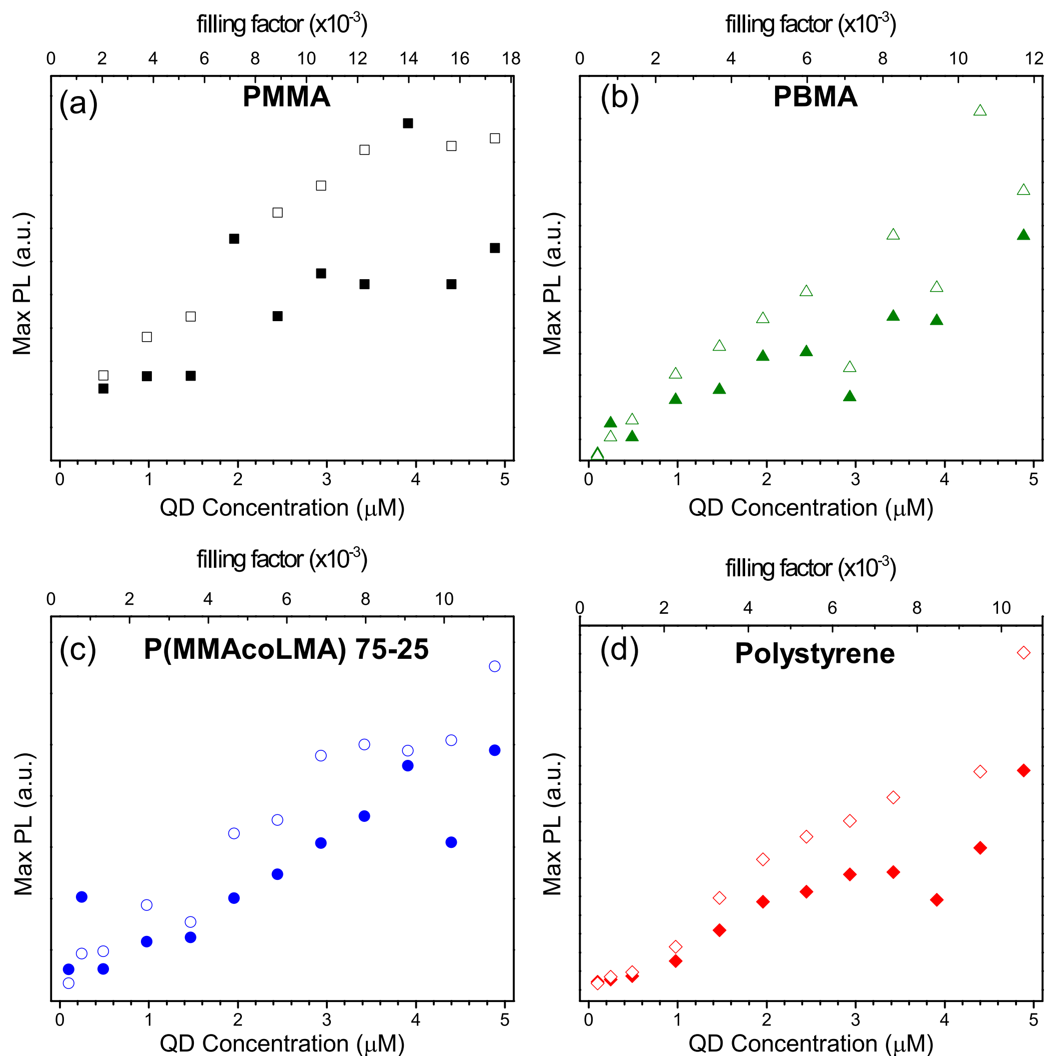

FIGURE 2-15: The photoluminescence peak of polymer/QD films for various QD concentrations for four different polymeric matrices: **(a)** PMMA, **(b)** PBMA, **(c)** P(MMAcoLMA) 75-25, and **(d)** Polystyrene. Solid symbols: excitation 405 nm, open symbols: excitation 375 nm.

TABLE 2-2: PL peak increase by increasing the QD concentration from 1 μM to 4.79 μM

Polymer	**PL peak increase** **QD C =1 μM → 4.79 μM**
PMMA	×2.52
PBMA	×3.71
P(MMAcoLMA) 75-25	×4.22
Polystyrene	×4.73

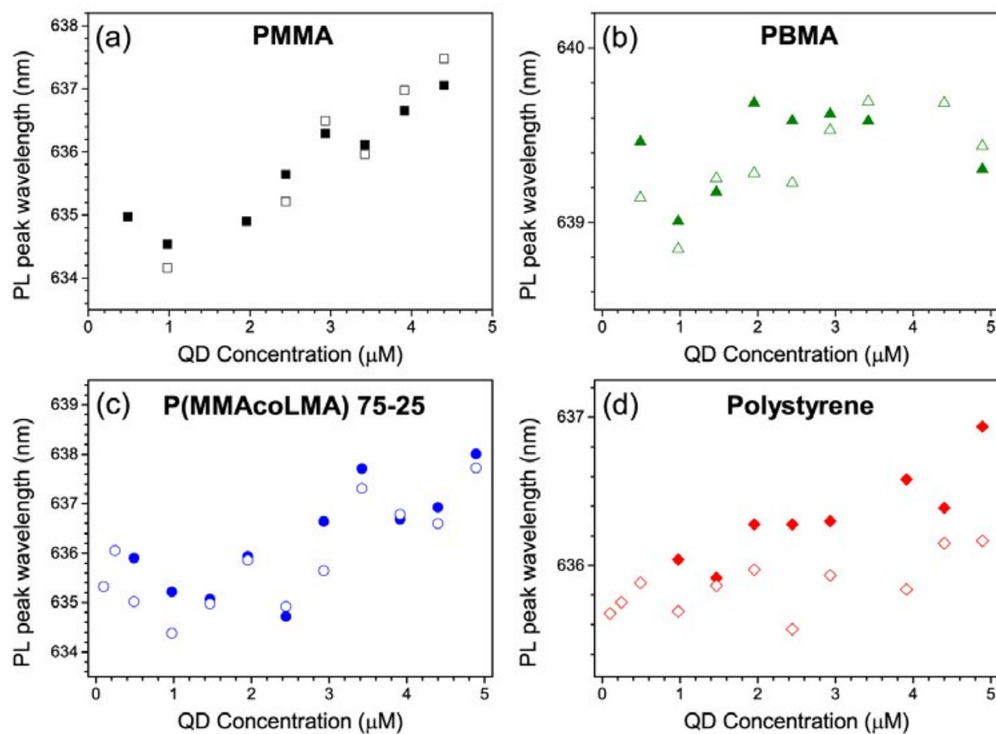

FIGURE 2-16: The photoluminescence shift of polymer/QD films for various QD concentrations: The polymer matrix is: **(a)** PMMA, **(b)** PBMA, **(c)** P(MMAcoLMA) 75-25, and **(d)** Polystyrene. Solid symbols: excitation 405 nm, open symbols: excitation 375 nm.

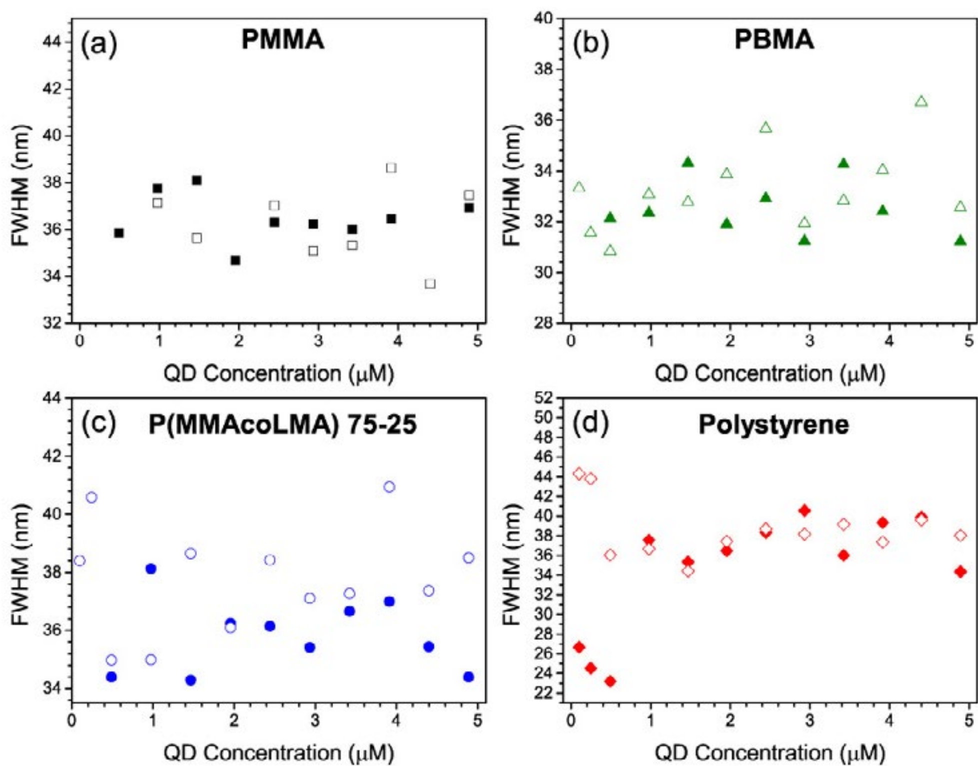

FIGURE 2-17: The dependence of the photoluminescence FWHM of QD/polymer films on the QD concentration: **(a)** PMMA, **(b)** PBMA, **(c)** P(MMAcoLMA) 75-25, and **(d)** Polystyrene. Solid symbols: excitation 405 nm, open symbols: excitation 375 nm.

Life-time measurements of the various QD polymer films have been performed using time-correlated single photon counting (TCSPC) with a Horiba® SPEX® FluoroLog® 3 station equipped with a laser diode light source (NanoLED) emitting at 375 nm with a typical optical pulse duration <100ps and a TBX-04 photomultiplier tube detector. In Figure 2-18 the normalized decay of the films of different QD concentrations is shown where an increase of the life-time of the excited states is apparent for all polymers with increasing QD concentration, apart from the PBMA, which surprisingly shows no such dependence. On the other hand, a comparison of all polymer matrices at maximum (C=4.89 μM) and ≈half the maximum (C=2.45 μM) QD concentrations shown in Figure 2-19 reveals no dependence of the life-times at these concentrations.

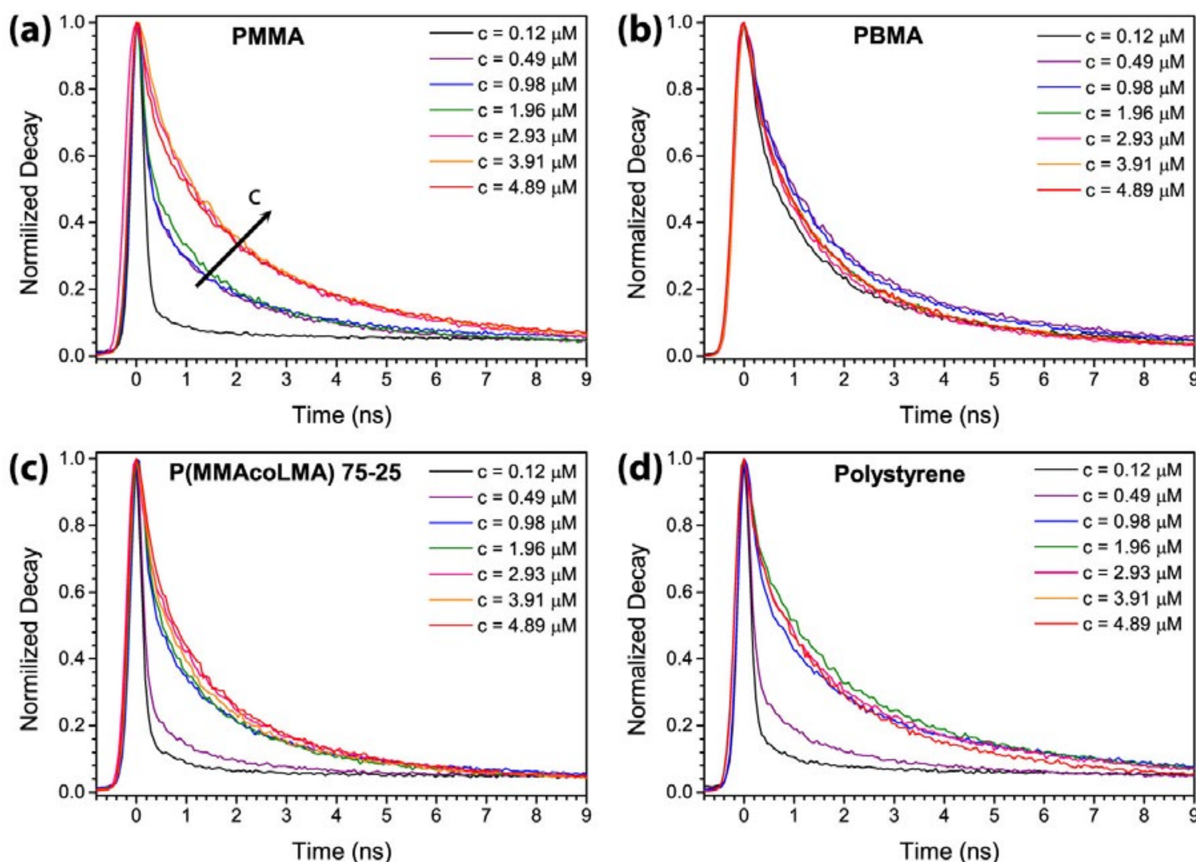

FIGURE 2-18: Normalized decay at various QD concentrations: **(a)** PMMA, **(b)** PBMA, **(c)** P(MMAcoLMA), and **(d)** Polystyrene. The trend of the QD concentration increment is indicated by the arrow in (a).

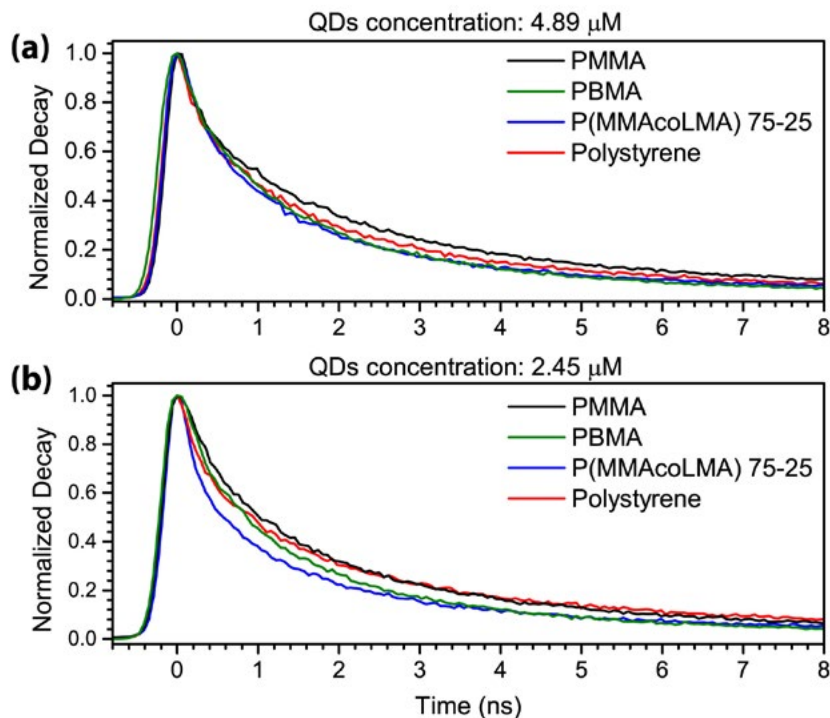

FIGURE 2-19: Comparison of the normalized decay of the polymeric matrices under study for: **(a)** maximum QD concentration (4.89 μM), and **(b)** half of the maximum QD concentration (2.45 μM).

2.6 Measurement of the refractive index of QD/polymer thin films

For the determination of the refractive index of the QD/polymer thin films spin-coated on silicon substrates, the spectral reflectometry technique has been exploited in combination with the independent measurement of the film thickness using a profilometer (Bruker DektakXT) to reduce the unknown variables and increase the accuracy of the calculations. An in-house measurement geometry has been designed and implemented. Moreover, to enhance the accuracy of the method, an in-house data processing algorithm has been developed and used accounting for both the imaginary part of the refractive index of the polymer and the substrate while also including the light losses due to scattering, into the calculations.

The technique is based on numerically fitting the observed reflectivity spectrum of the thin film to extract the optical constants as the fitting parameters. It is noted here that with this technique the refractive index of the thin film material itself is measured in contrast to other methods such as the m-line technique[85] where

the effective refractive index of the slab waveguide is measured. For reflection measurements the sample is illuminated with a broad spectral source and the spectrum of the reflected light is recorded and then compared to the reflectance of a sample of known reflectivity, provided the sensor array operated in the linear range. The reflectivity of the sample is then given by the following formula:

$$R_m(\lambda) = \frac{I_m(\lambda) - I_{dark}(\lambda)}{I_{ref}(\lambda) - I_{dark}(\lambda)} \cdot R_{ref}(\lambda) \qquad (2.7)$$

where $R_m(\lambda)$ is the measured reflectivity, $I_m(\lambda)$ is the intensity of the reflected light, $I_{ref}(\lambda)$ and $R_{ref}(\lambda)$ are the measured intensity of the reflected light and the known reflectivity of a well-characterized reference sample respectively. $I_{dark}(\lambda)$ is the signal recorded when the light source is disconnected from the setup. For fast and accurate measurement a Y-fiber bundle is used to simultaneously illuminate the sample and collect the reflected light to be measured by the spectrometer. The measuring station used was supplied by Theta-Metrisis (model FR-UV/VIS*). It is equipped with a broad transmission (200-1100 nm) fiber optic reflection probe (Ocean Optic UV-SR, core 400 μm) delivering light from a common tungsten halogen lamp (about 4 watts emitting in the 360-2000 nm range). To avoid exciting the quantum dots inside the films, a low pass filter with a cut-off frequency of 570 nm (UQC optics, model OG570) has been used to narrow the illuminating spectrum at longer wavelengths only. The fibers bundle delivers the light to a miniature fiber optic spectrometer (Ocean Optics USB4000 featuring a Toshiba TCD1304AP linear CCD array of 3648 pixels, 16 bit A/D, SNR 300:1) connected to a computer. To enhance the accuracy of the measurements, a modification of the recording geometry was designed and implemented. Since the recorded data is sensitive to the measuring geometry and the placement of the sample relative to the optic fiber probe, the setup shown in Figure 2-20(b) was chosen for stability and consistency. The optic fiber probe is fixed at a position facing upwards while the sample is placed on the probe holder facing downwards. This geometry

* www.thetametrisis.com

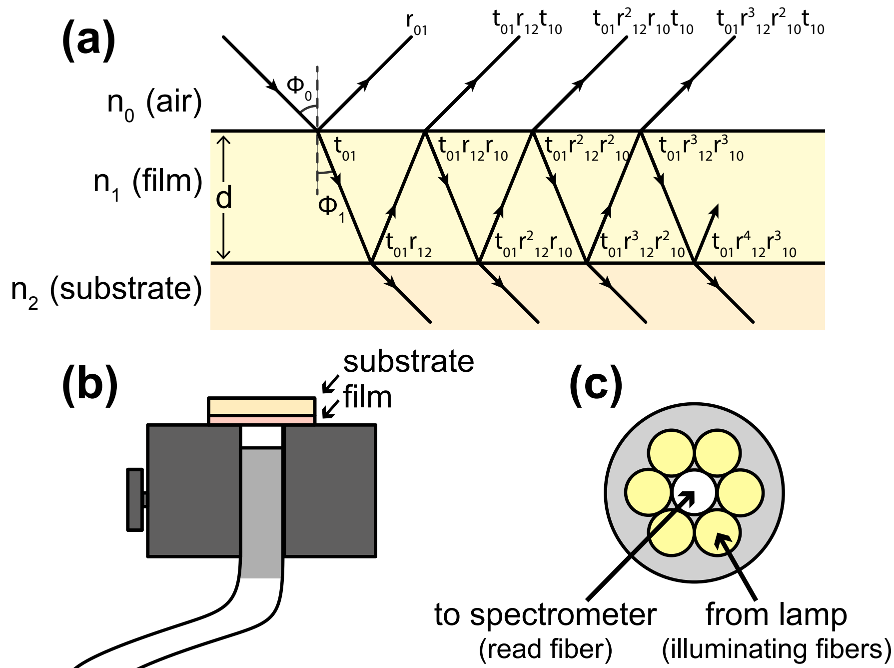

FIGURE 2-20: (a) The path of light impinging on a thin film exhibiting multiple reflections, **(b)** measuring configuration of reflectivity, and **(c)** sketch of the fiber optic bundle inside the reflection probe.

ensures a fixed distance between the sample interface and the probe while isolating the sample from the environmental light. A schematic of the light propagation inside the film and a sketch of the fiber optic bundle are also shown in Figure 2-20.

The refractive index is incorporated into the thin film reflectance formulas by means of empirical formulas which also account for dispersion. Among the various models used the most common are the Cauchy, Sellmeier and Schott formulas.[86] Although the Sellmeier formula usually has better agreement with the experimental data, the advantage of the Cauchy formula is that it can be used for absorbing materials by including the imaginary part of the refractive index (κ). Here, a variation of the Cauchy formula, the exponential Cauchy formula is used:[87]

$$n = A_n + \frac{B_n}{\lambda^2} + \frac{C_n}{\lambda^4} \ , \qquad \kappa = A_\kappa \exp\left(B_\kappa \left(\frac{1239.856115}{\lambda} \right) - C_\kappa \right) \tag{2.8}$$

where
$$n = n_r + i \cdot \kappa, \quad (\kappa < 0) \tag{2.9}$$

The suitability of the formulas is demonstrated in Figure 2-21 where the experimental[88] and fitted values for n and κ for silicon (the substrate material used) are drawn.

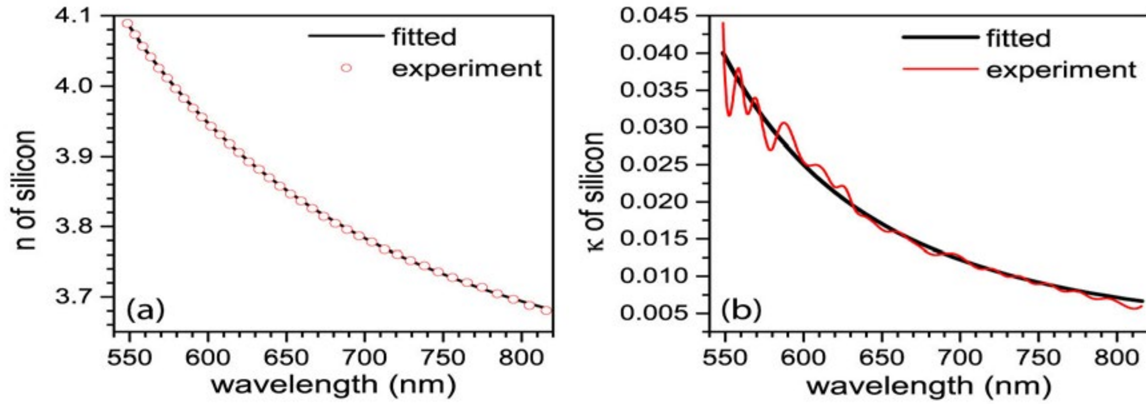

FIGURE 2-21: Dispersion curves of silicon for **(a)** the real part and **(b)** the imaginary part of the refractive index as found in the literature (red circles/line) and as fitted using the exponential Cauchy formula (black lines).

It should be noted here that these formulas are suitable for spectral ranges of normal dispersion only and that they fail to include some minute resonances observed into the extinction coefficient of silicon.

The measured reflectivity is affected by light scattering in the surface of the film due to deviation from the ideal homogeneous profile. The height of the interface irregularities are assumed to follow a Gaussian distribution centered on the mean film thickness with an *rms* value of R_q. A Debye-Waller factor is introduced to the standard Fresnel coefficients to account for this energy loss mechanism. For normal incidence of light onto the film, the modified coefficients now take the following forms:[87,89–91]

$$r_{m-1\,m} = \frac{n_m - n_{m-1}}{n_m + n_{m-1}} \cdot \exp\left(-2(K \cdot n_{r\,m-1})^2\right) \tag{2.10}$$

$$r_{m\,m-1} = \frac{n_{m-1} - n_m}{n_{m-1} + n_m} \cdot \exp\left(-2(K \cdot n_{r\,m})^2\right) \tag{2.11}$$

$$t_{m-1\,m} = \frac{2n_{m-1}}{n_m + n_{m-1}} \cdot \exp\left(-\frac{1}{2}\left(K \cdot (n_{r\,m} - n_{r\,m-1})\right)^2\right) \tag{2.12}$$

$$t_{m\,m-1} = \frac{2n_m}{n_m + n_{m-1}} \cdot \exp\left(-\frac{1}{2}\left(K \cdot (n_{r\,m-1} - n_{r\,m})\right)^2\right) \tag{2.13}$$

where
$$K = \frac{2\pi R_q}{\lambda} \tag{2.14}$$

assuming incidence from the (m-1)th to the mth medium and that scattering is small relatively to the film reflectivity (R_q<<λ). An immediate result of the Debye-Waller

factor is the loss of symmetry between the $r_{m-1\,m}$ and $r_{m\,m-1}$ coefficients not allowing the usual simplification of the reflected amplitude formulas. Summation and arrangement of the multiple components of the amplitude of the electric field as shown in Figure 2-20(a) yields the following formula:

$$R_{ampl} = r_{01} + t_{10} r_{12} t_{01}\, \mathrm{e}^{i\frac{4\pi}{\lambda} n_{r,1}(\lambda)\cdot d}\, e^{\frac{4\pi}{\lambda}\kappa_1(\lambda)\cdot d} \cdot \sum_{m=0}^{\infty} \left(r_{10} r_{12}\, \mathrm{e}^{i\frac{4\pi}{\lambda} n_{r,1}(\lambda)\cdot d}\, e^{\frac{4\pi}{\lambda}\kappa_1(\lambda)\cdot d} \right)^m \qquad (2.15)$$

which can be fitted numerically. In the above formula d is the film thickness. The exponential terms accounts for the phase shifts along the path of the light through the film and the absorption of light inside this layer. The terms in the infinite geometric sum fulfills the criterion of $|z| < 1$, where z is the term in the sum of the mth power, thereby the infinite summation converges to $1/(1-z)$ and the formula reduces to:

$$R_{ampl} = r_{01} + \frac{t_{10} r_{12} t_{01}\, \mathrm{e}^{i\frac{4\pi}{\lambda} n_{r,1}(\lambda)\cdot d}\, e^{\frac{4\pi}{\lambda}\kappa_1(\lambda)\cdot d}}{1 - r_{10} r_{12}\, \mathrm{e}^{i\frac{4\pi}{\lambda} n_{r,1}(\lambda)\cdot d}\, e^{\frac{4\pi}{\lambda}\kappa_1(\lambda)\cdot d}}, \qquad (\kappa_1 < 0) \qquad (2.16)$$

Finally, the reflectivity of the film is given by:

$$R = n_0 R_{ampl} R_{ampl}^{*} \qquad (2.17)$$

Given a reflection spectrum, the aforementioned formula includes 8 unknown variables: the Cauchy coefficients for the real part of the refractive index of the film $A_{n,1}$, $B_{n,1}$ and $C_{n,1}$, the exponential Cauchy coefficients for the imaginary part of the refractive index of the film $A_{n,2}$, $B_{n,2}$ and $C_{n,2}$, the film roughness R_q and the film thickness d. R_q and d can be measured separately using a profilometer to reduce the number of the unknown parameters and increase the fidelity of the fitting. To fit the model described by the formulas and to the experimentally recorded reflectivity data, nonlinear regression analysis is used and the required optical constants can be determined. The evaluation of each fitting step is calculated by use of a figure-of-merit function that measures the agreement between the data and the fitting function.

The parameter used is the quantity chi-square χ^2 as a goodness-of-fitting test:

$$\chi^2 = \sum_i \left(\frac{R_i - R_{\mathrm{model}}\left(A_{n,1}, \mathrm{B}_{n,1}, C_{n,1}, A_{\kappa,1}, \mathrm{B}_{\kappa,1}, C_{\kappa,1}\right)}{\sigma_i} \right)^2 \quad (2.18)$$

for R_i being the recorded data at each wavelength, R_{model} the calculated reflection at the same wavelength and σ_i being the standard deviation. To find the χ^2 minimum various methods can be used including downhill simplex algorithm,[87,92,93] the Levenberg-Marquardt algorithm[87,93] or the trust–region optimization method.[93] Here the commercially available mathematical platform MATLAB™ has been used (embedded function *lsqcurvefit*) utilizing the *trust-region-reflective* method. Recorded and fitted reflectivity spectra for various polymeric films (plain and with embedded QDs at maximum concentration of 4.89 μM) spin-coated on silicon substrates are shown in Figure 2-22. From these figures the excellent fitting is apparent of the function presented in to the experimental data.

The refractive index of nanocomposites can be also estimated theoretically by use of effective medium approximations accounting for different contributions of the matrix and the nanoparticles to the effective index of the nanocomposite medium. The key parameter for such an approximation, apart from the refractive indices of the different materials is the filling factor of each material defined as the average volume fraction occupied by the nanoparticles:

$$f_i = \frac{N_i V_i}{V}, \qquad f_{matrix} = 1 - \sum_i f_i \quad (2.19)$$

N_i being the number of the i-type nanoparticles of average volume V_i embedded in total volume V of the nanocomposite. Various effective medium formulas have been proposed while those most often used are the Maxwell Garnett formula[94] and the Bruggeman ansatz.[87,95,96] The general form of the last one gives the effective dielectric constant ε_{eff} as:

$$\sum_n f_n \cdot \frac{\varepsilon_n - \varepsilon_{eff}}{\varepsilon_n + 2\varepsilon_{eff}} = 0 \quad (2.20)$$

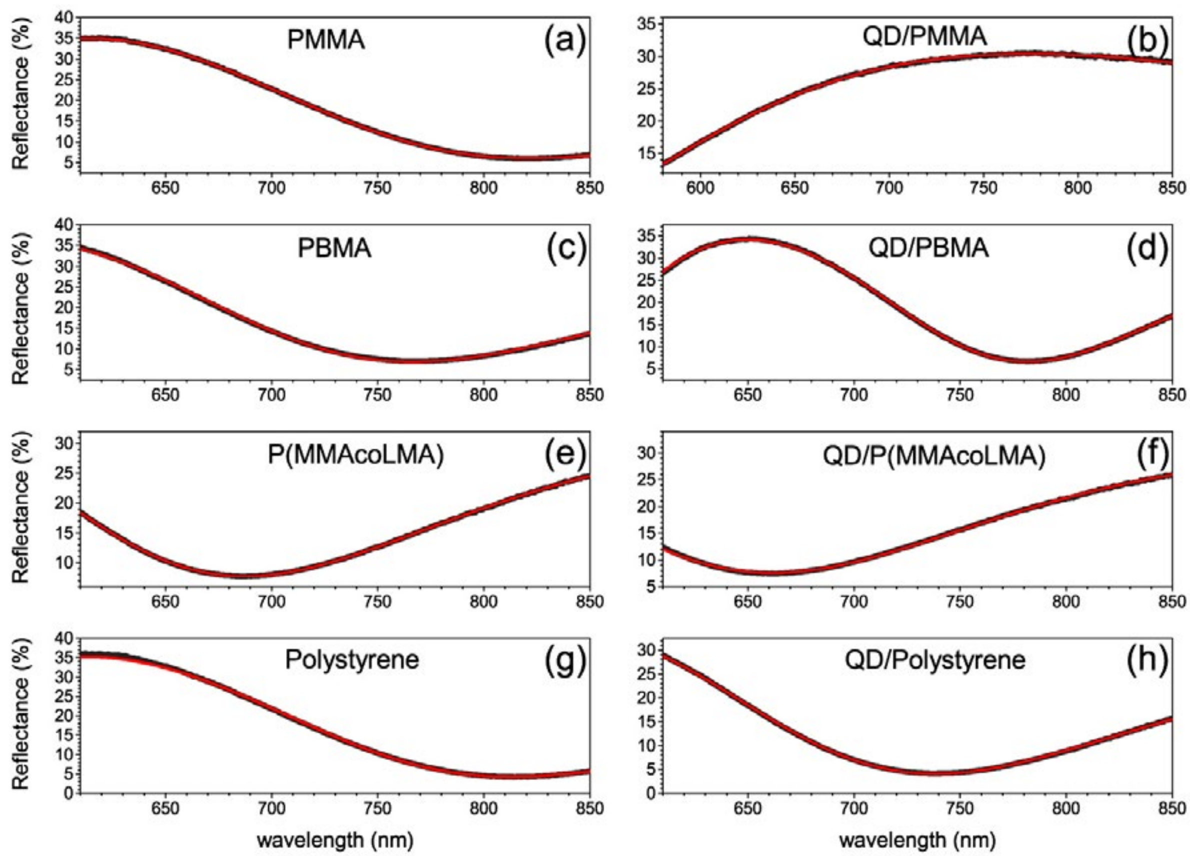

FIGURE 2-22: Experimentally measured (gray lines) and numerically fitted (red lines) reflectivity spectra of various polymer (left column) and QD/polymer (right column) thin films deposited on silicon substrates: **(a, b)** PMMA, **(c, d)** PBMA, **(e, f)** P(MMAcoLMA), and **(g, h)** Polystyrene. The concentration of the QDs is 4.89 μM.

where ε_n is the dielectric constant of each material comprising the nanocomposite. This model is valid for low concentrations where the inclusions are well separated. Conversion between the dielectric functions and the refractive index is provided by the standard Maxwell formulas:

$$\varepsilon_1 = n^2 - \kappa^2, \quad \varepsilon_2 = 2n\kappa \tag{2.21}$$

$$n = \sqrt{\frac{\varepsilon_1}{2} + \frac{1}{2}\sqrt{\varepsilon_1^2 + \varepsilon_2^2}}, \qquad \kappa = \sqrt{-\frac{\varepsilon_1}{2} + \frac{1}{2}\sqrt{\varepsilon_1^2 + \varepsilon_2^2}} \tag{2.22}$$

In the calculations the nanocomposite is assumed to be comprised of three components, namely the CdSe core of the QDs, the ZnS shell and the polymeric matrix. Other compounds present in the material such as the ligands (HDA and TOPO), possible residues of monomers/oligomers, the polymerization initiator, impurities etc.

are neglected. From these, the main contribution is attributed to the ligands which have refractive indices close to that of the polymeric materials (~ 1.45) combined to their small filling factor are not expected to yield a significant contribution. The volume occupied by each of the CdSe and ZnS portions is calculated by their average ratio in the QD volume multiplied by the QD concentration in the solution while the volume of the polymeric matrix is calculated by the w/v concentration of the polymer in the solution and the density of the polymer in solid form. For QD concentrations in the range up to 4.89 μM the filling factors are calculated to be up to 1.22×10^{-2} for PMMA, 1.10×10^{-2} for PBMA, 1.18×10^{-2} for P(MMAcoLMA) 75-25, and 1.10×10^{-2} for Polystyrene. Dispersion curves for various QD concentrations are shown in Figure 2-23 while the dependence of the refractive index of the nanocomposite at λ=632.8 nm on the QD concentration is shown in Figure 2-24. In the same figure, the values measured using the spectral reflectance method are also shown indicating a good agreement between the Bruggeman model and the experimentally obtained data. It should be noted here that the main uncertainty of the measured values stems from the deviation of the real QD concentration of the thin films due to the formation of small amounts of sediments in the polymer/QD/toluene solution prior to spin-coating. This effect reduces the actual QD concentration in the thin films. As already mentioned, the polymer/nanoparticles sediment is re-dissolved into the solution when diluting towards smaller QD concentrations at the same concentration of the polymer.

2.7 Incorporation of QDs and other nano-entities in sol-gel matrices

By the term sol-gel we usually refer not only to the process of synthesizing metal alkoxides by hydrolysis and condensation, but also to the materials produced. The versatility and cost reduction of this low temperature wet chemistry of the sol-gel process has led to intense research activities in the field as an alternative to the production of glass and ceramic materials by the high temperature methods. The process usually starts with the conversion of precursors into colloidal solution

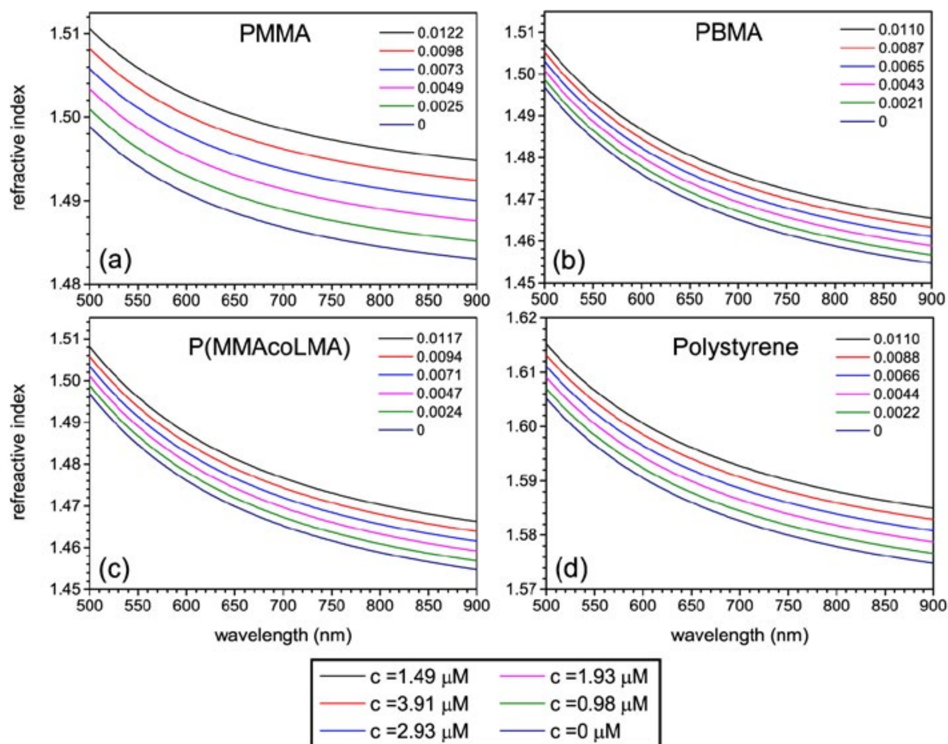

FIGURE 2-23: Dispersion curves of QD/polymer nanocomposite for various QD concentrations as predicted by the Bruggeman model: **(a)** PMMA, **(b)** PBMA, **(c)** P(MMAcoLMA), and **(d)** Polystyrene.

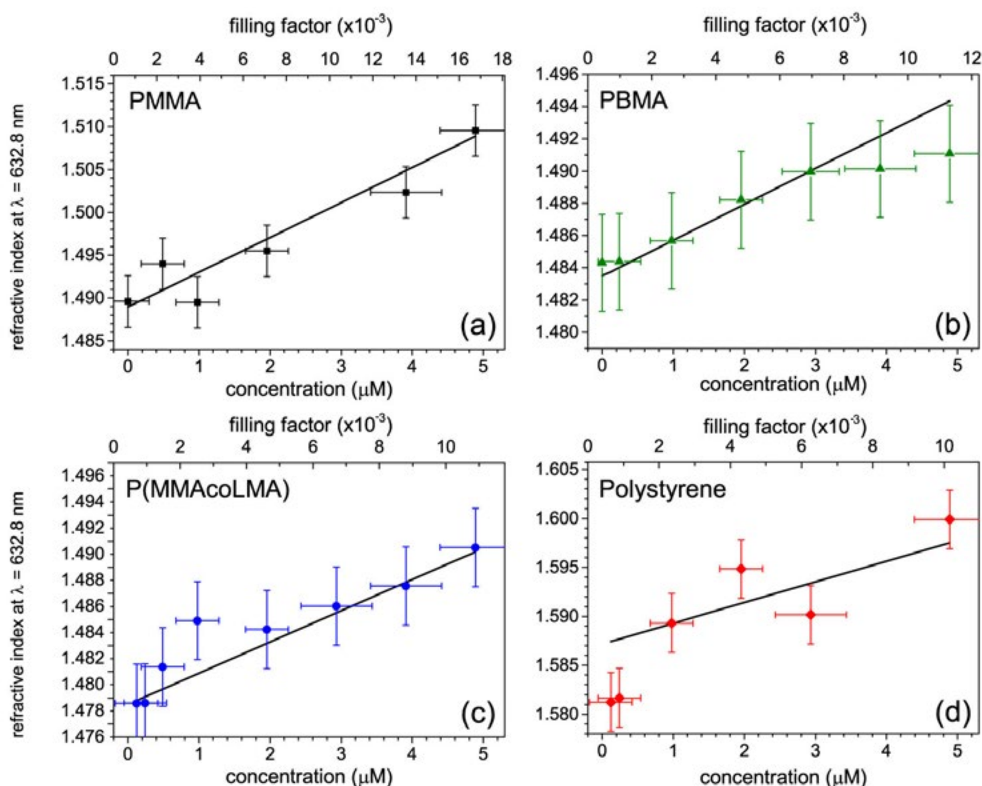

FIGURE 2-24: Refractive indices of various QD/polymer thin films vs nanoparticle concentration (filling factor) at λ=632.8 nm as predicted by the Bruggeman model (black solid lines) and as calculated using spectral reflectance measurements (points): **(a)** PMMA, **(b)** PBMA, **(c)** P(MMAcoLMA), and **(d)** Polystyrene.

and the subsequent formation of a network.[97,98] Precursors used mainly include metal alkoxides, metal or metalloid atoms attached to organic ligands with the intervention of an oxygen atom, for the synthesis several materials, the most common being silica (SiO_2), titania (TiO_2), zirconia (ZrO_2) and alumina (Al_2O_3). Another choice for the sol-gel method is the use of hybrid organic/inorganic precursors which are discussed in the next paragraph. Apart from the simple, low cost fabrication, other advantages of the sol-gel method include the ability to fabricate high quality thin films and coatings for corrosion protection and other applications, as well as materials of complex shapes. Moreover, due to the "*in a bottle*" nature of the process, additives, e.g. nanoparticles or dyes, can be easily combined into the precursor mix prior to hydrolysis and subsequently incorporated into the final solid. The properties of the synthesized materials can also be easily tailored by varying the molecular network, e.g. by controlling the porosity which also defines the refractive index. The use of the sol-gel method for optical material begins back in 1845[99] and common fields include optical coatings[100] (antireflection coatings, high reflection band pass filters, dichroic mirrors etc.), integrated photonic circuits,[101] optical elements including contact lenses[102] and photonic sensors.[103]

Due to the hydrophobic nature of the QDs synthesized using the usual hot injection method attributed to the alkyl chains of the commonly used ligands (TOPO, oleic acid, alkyl amines etc.), incorporating of the nanocrystals in sol-gel matrices is a challenging process. Most sol-gel recipes encompass alcohols and water in the solution as the result of the hydrolysis process. A successful approach for synthesis of QD/sol-gel nanocomposites was introduced by Sundar et al. which involves a ligand exchange step (tris-hydroxylpropylphosphine) to render the nanoparticles hydrophilic and demonstration of QD incorporation into silica microspheres via the Stöber method.[104] Petruska et al. proposed the use of 5-amino-1-pentanol (AP) for the ligand exchange with interesting results.[105] By such a procedure, the initially TOPO molecules capping the nanoparticles are replaced by AP, a bi-functional

ligand enabling solubility of the nanocrystals to alcohols without formation of agglomeration. The AP ligand contains an amine group which is covalently bonded to the ZnS shell of the CdSe/ZnS surface while a hydroxyl on the other edge of a 5 carbon atom alkyl chain provides the solubility to alcohols.

For the implementation and study of this ligand exchange process, 1.5 ml of the initial CdSe/ZnS QD solution dispersed in toluene are precipitated from solution with an excess of methanol. After about 2 hours the nanocrystals are collected by removing the supernatant toluene which also includes the excess of TOPO of the initial solution. The precipitation is then dried under vacuum and about 5 mg of nanoparticles are obtained which are re-dispersed in a small amount (20 μl) of tetrahydrofuran (THF). Then 10 mg of 5-amino-1-pentanol diluted in 200 μl of isopropanol are added to the solution which was stirred for several hours. After more than one month the nanoparticles remained fully diluted in isopropanol without any apparent precipitation or agglomeration, emitting strong red light upon excitation. A typical photoluminescence spectrum of the AP-capped QDs in isopropanol upon excitation at 405 nm is shown in Figure 2-25 where a blue shift of about 20 nm with respect to the initial QD solution in toluene is apparent.

Incorporation into a sol-gel matrix, is achieved by mixing the QD/alcohol solution with a metal alkoxide precursor. Titanium isopropoxide (TIPP) with chemical formula $Ti(OCH(CH_3)_2)_4$ was used for synthesis of the titania matrix while the zirconia isopropoxide can be used for the synthesis of a zirconia nanocomposite. It was proposed that capping the nanoparticles with AP not only renders them soluble in alcohols but also allows for their integration into the final metal oxide network[106] as shown illustratively in Figure 2-26.

A main issue in the fabrication of thin films using via the sol-gel process is the formation of cracks[99,107,108] that destroy all useful optical properties of the material. Due to the fast hydrolysis and condensation steps, the alkoxide solution homogeneity and transparency are decreased and there is need to be stabilized for controlled,

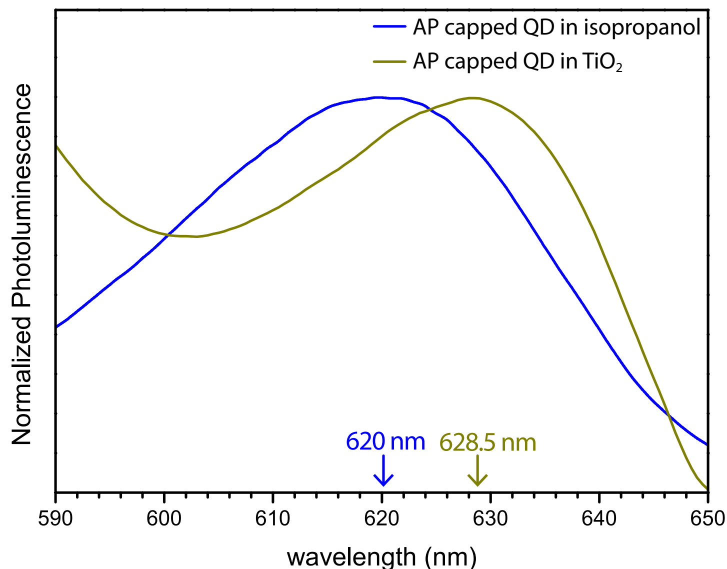

FIGURE 2-25: Normalized PL spectrum of 5-amino-1-pentanol: a) diluted in isopropanol (green line), and b) in titania matrix (blue line) upon excitation at 404 nm.

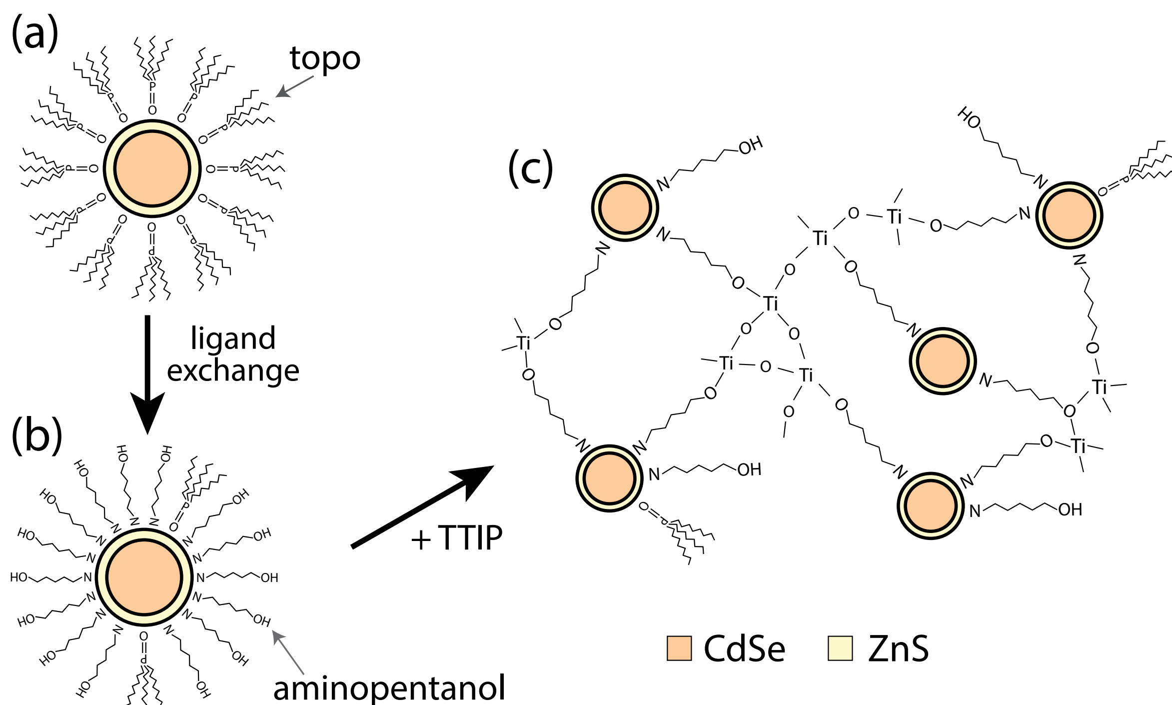

FIGURE 2-26: Illustration of the encapsulation process of CdSe/ZnS QDs in sol-gel matrix by ligand exchange with a bi-functional molecule: **(a)** the initial form of the nanoparticles with TOPO as ligands, **(b)** the nanoparticle after ligand exchange with aminopentanole and, **(c)** incorporation of the aminopentanole capped QD in titania matrix by the sol-gel process.

slow formation of the inorganic network. Usually this is achieved by controlling the pH of the solution by insertion of an acid or in some cases a base. However, such an environment would be deleterious for the properties of the QDs which tend

to lose their ligands and subsequently their luminescence properties. A chelation agent, usually a nucleophilic species, can be used instead.[41,108–110] These molecules act as bidentate ligands to bond on to the sol-gel precursor and reduce its reactivity. Acetylacetone, a β-ketone, is used here which attaches to titanium isopropoxide to form titanium acetylacetonates and render the precursor mixture stable. A total of 1 ml of titanium isopropoxide was mixed with 0.36 ml of acetylacetone for a 1:1 mole ratio which was then added to the QD/isopropoxide solution for the final QD/titania precursor solution, the photoluminescence spectrum of which is shown in Figure 2-25. The weak emitting spectrum however and the emission of light at lower wavelengths suggests the partial successful ligand exchange and the subsequent quenching of the quantum yield of the QDs.

2.8 Hybrid organic-inorganic materials for photonic applications

ORMOCERs®[†] (Organically MOdified CERamics) are silicate-based inorganic-organic hybrid polymer materials that combine the benefits of both worlds: the inorganic materials synthesized via the sol-gel method and the organic polymers. ORMOCERS can be designed to exhibit properties associated with three main material families, namely silicones, glasses and organic polymers as shown illustratively in Figure 2-27. The properties of the materials can be tuned accordingly to the specific application by the choice of the relative proportions of the structural elements that determine the material properties. ORMOCERs find application in various types of anti-reflective coating, corrosion protection, decorative coating, passivation layers etc., as well as in sensors, polymer ionic conductors, medical, dentistry and ophthalmology, microelectronics and adhesives to name just a few of their various usages.[111,112] Two other interesting properties of ORMOCERs are their ability to be tuned for precise micro/nanofabrication and their excellent optical properties. Combined

† ORMOCER® is a registered trademark of the *Fraunhofergesellschaft zur Förderung der Angewandten Forschung* in Deutschland e.V.

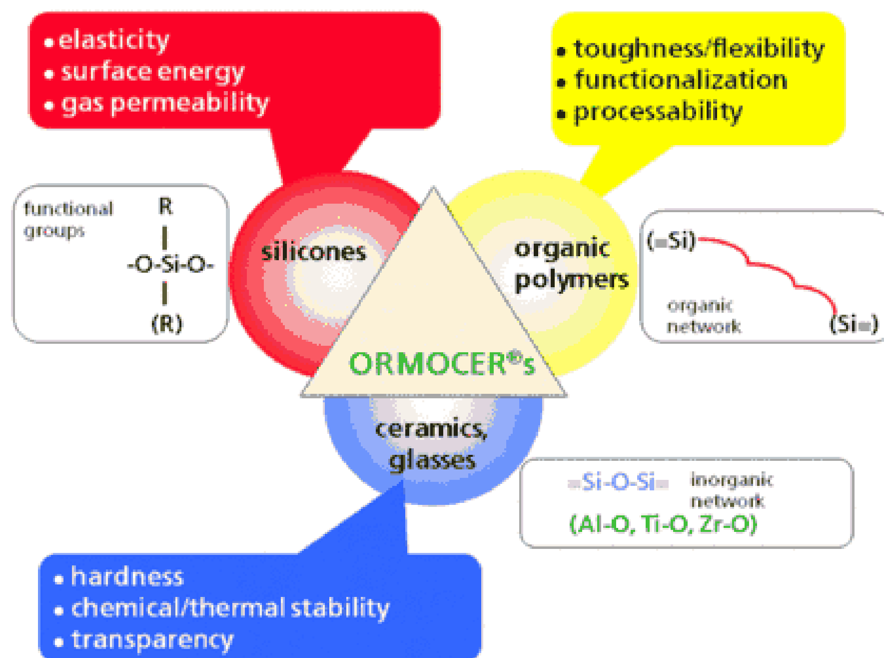

FIGURE 2-27: ORMOCERs advantages as a combination of properties of different material families, namely silicones, glasses and organic polymers. (figure from www.ormocer.de website of Fraunhofer Institut für Silicatforschung).

together ORMOCERs provide a powerful toolset for the implementation of photonic structures of advanced functionalities.[113–116]

In general, the manufacturing process of ORMOCERs consists of synthesis of an inorganic network which is built up through controlled hydrolysis and condensation of organically modified Si alkoxides. The precursors include organo-substituted silisic acid esters of the formula, $R_n^{'}Si((OR)_{4-n}$, $R^{'}$ being any organofunctional group that can be either a non-hydrolysable group (e.g. $-Si-CH_3$) or can be bonded together to form a network.[99,111,117,118] In either case the organofunctional groups can provide a plethora of physical properties to the material, including mechanical stability and optical properties, or functionalities such as polymerization upon UV exposure or heating for the formation of a dense organic/inorganic network. A brief demonstration of the formation of such complex hybrid network procedure[119] is illustrated in Figure 2-28 while example combinations of organic and inorganic monomers and their connecting units for ORMOCERs synthesis[111,120] are shown

in Figure 2-29. For the polymerization of the organic part of the hybrid material, a photoinitiator is added into the solution in conjunction with the appropriate organic part, e.g. (meth)acrylic monomers which can react by radical polymerization.[111] Commercially available photoinitiators used[113,121] are BASF® Lucirin® TPO and Ciba® IRGACURE® 369 shown schematically in Figure 2-30.

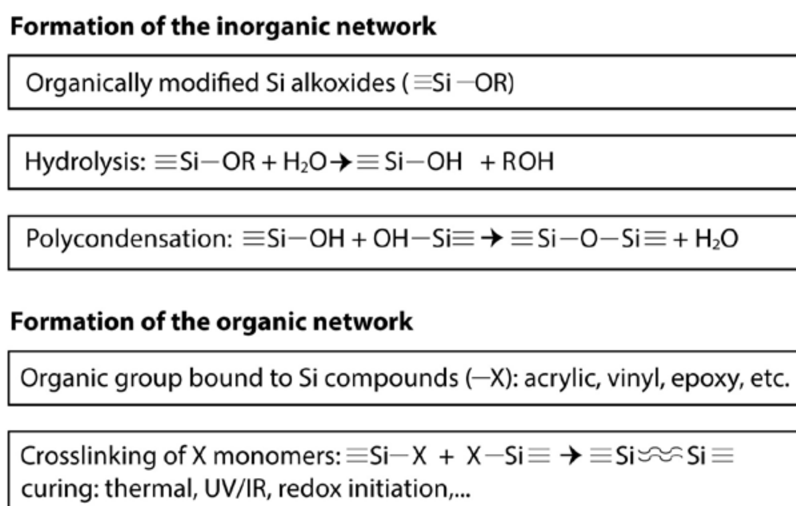

FIGURE 2-28: Brief demonstration of the curing procedure of the ORMOCER materials family.[119]

Hybrid organic-inorganic materials studied here for the implementation of photonic structures are the UV polymerizable OrmoCore®, OrmoClad®‡ supplied by *micro resist technology GmbH* (Berlin, Germany).[122] Both belong to the ORMOCER family (OrmoCore is ORMOCER b59 while OrmoClad is ORMOCER b66[123,124]) initially developed by the Fraunhofer Institute for Silicate Research (ISC) in Würzburg, Germany, and are specially design for application in directly UV patterned planar optical waveguides. Another material from the same supplier is OrmoStamp® used for the replication of hard stamps for the soft lithography technique. The precursors of OrmoClad and OrmoCore[125] are shown in Figure 2-31. The choice the precursor is based on an overall low content of Si-OH and aliphatic content by use of diphenylsilanes to ensure low absorption in the near infrared region.[114]

‡ OrmoCore®, OrmoClad® and OrmoStamp® are trademarks of *micro resist technology GmbH* (Berlin, Germany).

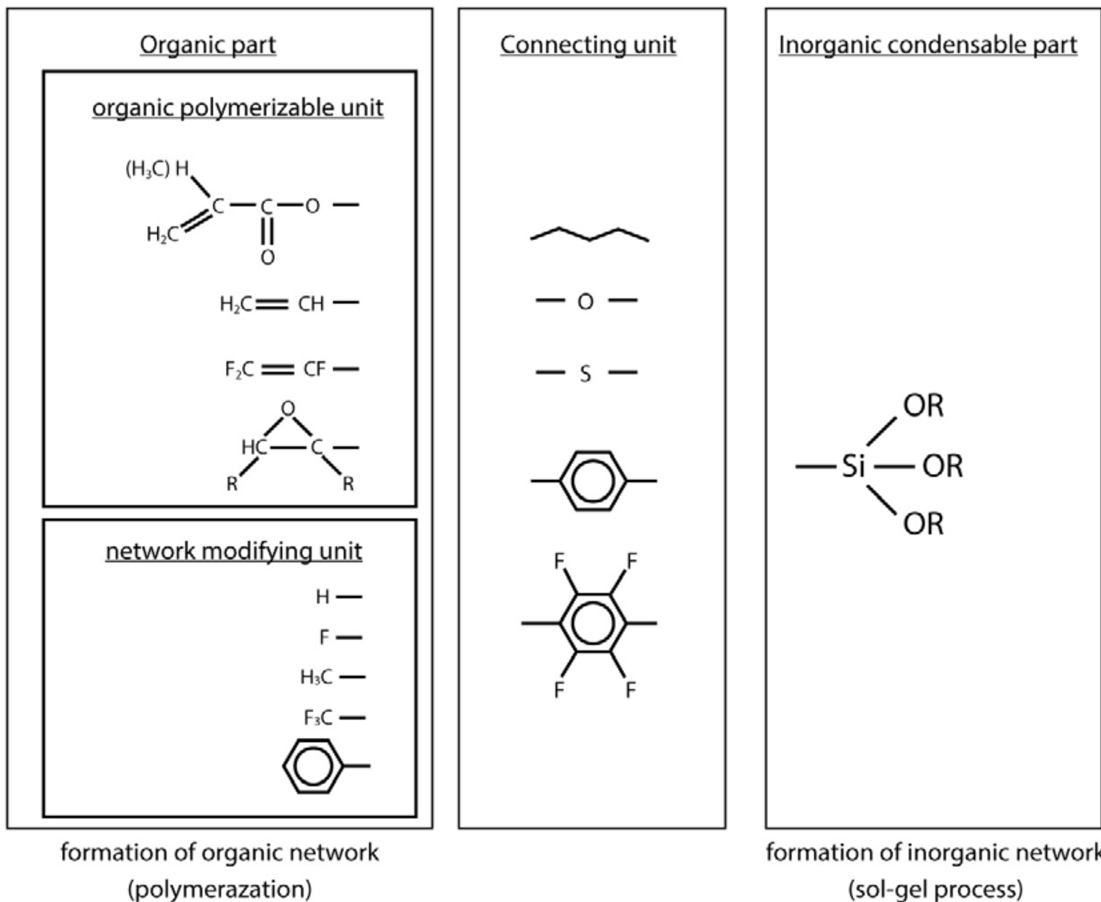

Figure 2-29: Example combinations of organic and inorganic monomers and their connecting units for ORMOCERs synthesis.

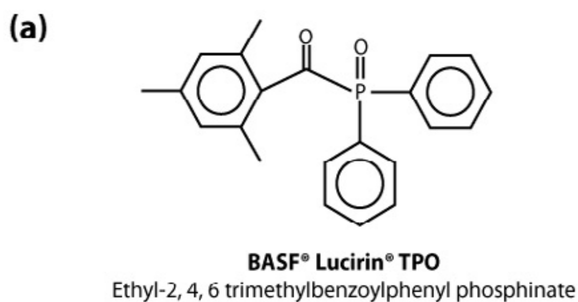

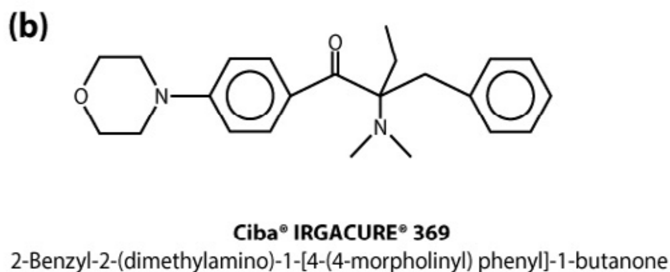

Figure 2-30: Commercially available photoinitiators used with the ORMOCER materials: **(a)** BASF® Lucirin® TPO, and **(b)** Ciba® IRGACURE® 369.

Both OrmoCore and OrmoClad are highly transparent to radiation above 450 nm and have very low optical losses in the visual range, of ≤0.1 dB/cm at 633 nm and relatively low losses at the telecom windows, 0.23 and 0.26 dB/cm at 1310 nm respectively and 0.5-0.6 and 0.48 dB/cm at 1550 nm where the lower values for OrmoClad are due to the lower C-H content.[114] The materials are supplied pre-hydrolyzed in liquid, a highly viscous form, and are cured upon UV radiation in the UVA and UVB region with their maximum sensitivity around the i-line of the mercury lamp (365 nm). A strong photoluminescence at around 500 nm observed when illuminated with UV light is probably attributed to the presence of the photoinitiator. Although the initial materials are solvent-free, their viscosity can be adjusted by dilution with propylene glycol monomethyl ether acetate (PGMEA) if needed for spin-coating of thin films.

The main difference between OrmoClad and OrmoCore is their refractive index which has a difference of about 0.013 at the wavelength of 650 nm which allows them to be used, as their names implies, as clad and core in photonic waveguides. This difference is attributed to the presence of a low refractive index partially fluorinated alkyloxide in OrmoClad as shown in Figure 2-31. OrmoCore and OrmoClad exhibit a refractive index in the range of 1.555-1.531 and 1.545-1.515 in the visual and near infrared region respectively shown in Figure 2-32(a). Conveniently, the refractive index of the material used can be precisely tuned in a linear manner by simply mixing the appropriate amount of OrmoCore and OrmoClad as indicated in Figure 2-32(b).

Incorporation of QDs directly into hybrid polymers has failed since the nanoparticles completely lose their luminescence properties when mixed with either OrmoCore or OrmoClad even when the initial TOPO ligands are replaced with shorter molecules that are expected to adhere more strongly to the nanoparticles, e.g. zinc acetate. Possible explanations for such QD degradation include stripping of the nanoparticle ligands by the presence of active species in the solution such as the activated photoinitiator or additives present for pH control. Photodestruction

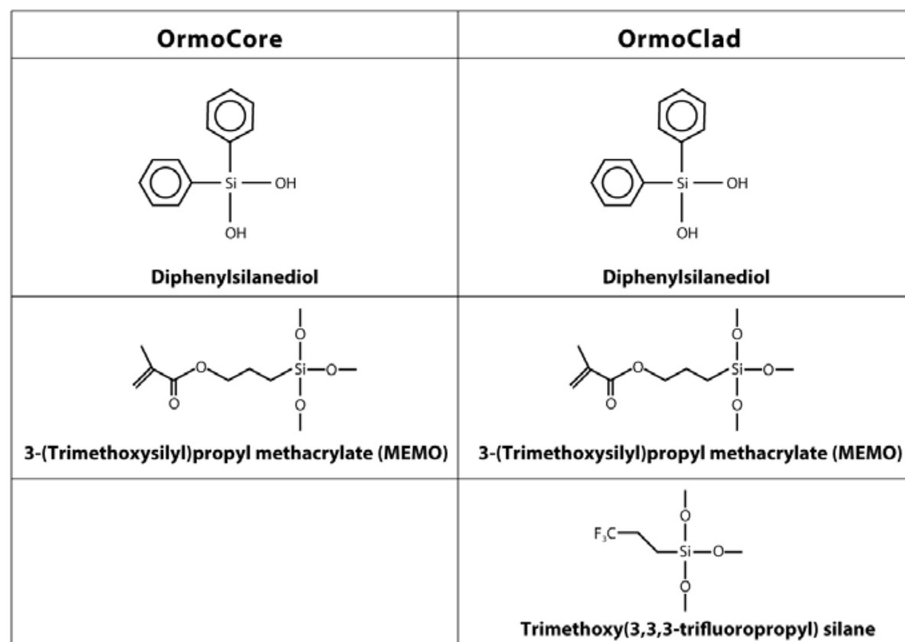

FIGURE 2-31: Precursor monomers of OrmoCore and OrmoClad materials of the ORMOCER family.

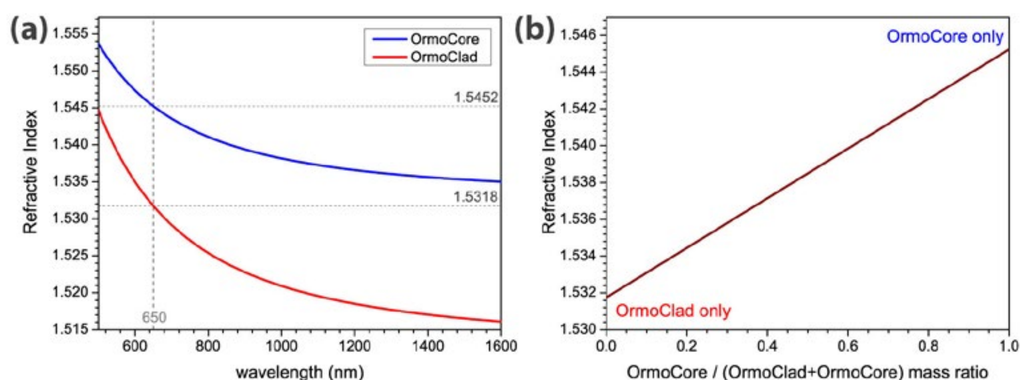

FIGURE 2-32: **(a)** OrmoClad and OrmoCore dispersion curves at 25°C (no hardbake), **(b)** refractive index tuning by mixing OrmoClad and OrmoCore (after hardbake). Data provided by manufacturer.[122]

of the nanocrystals upon exposure to the intense UV radiation during curing has been eliminated as a possible cause by using low power UV radiation from a LED emitting source at 375 nm at elevated curing times with no success. The initial QD solution has also been exposed under the same conditions and have been found to be unaffected by the UV radiation. Mixing of hydrophilic QDs diluted in isopropanol by the ligand exchange process described in the previous paragraph also resulted in no light emission from the QDs. Furthermore, attempts to embed QDs/titania sol-gel stabilized with acetylacetone into the matrix of the hybrid materials similarly to the procedure previously shown in Figure 2-26 resulted in well-separated materials

upon solidification and curing. This is attributed to the fact that the materials are purchased pre-hydrolyzed, being apparent from their high viscosity, and only their organic parts undergo polymerization upon curing. It is suggested here however that by mixing the AP-capped nanoparticles during the first steps of the hybrid materials synthesis prior to hydrolysis, QD incorporation into the inorganic part of the ORMOCER material could be feasible. Indeed, embedding of QD into hybrid sol-gel matrices after capping with the appropriate ligands has been reported in the literature.[126,127] Limited success has been achieved only by encapsulating the nanoparticles into polymer micelles by use of the sulfosuccinate (AOT) surfactant. The weak photoluminescence signal of the hybrid is shown in Figure 2-33.

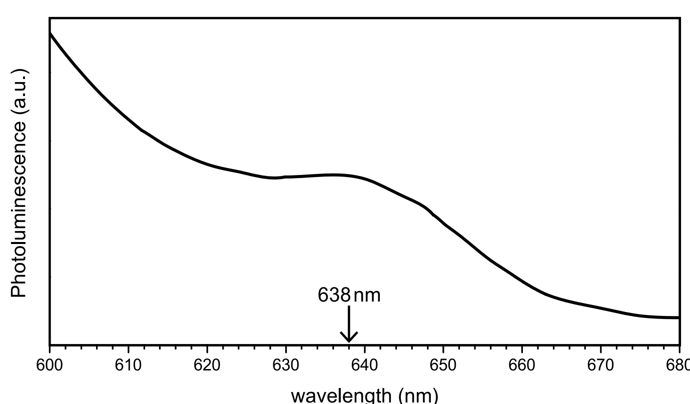

FIGURE 2-33: Photoluminescence spectrum of QD encapsulated in dioctyl sodium sulfosuccinate (AOT) micelles embedded in OrmoCore matrix.

2.9 Sol-gel incorporating nano-entities for sensing applications

Apart from the various applications as coatings and for the implementation of photonic structures, sol-gels are also excellent materials for sensing applications.[103,128] Sol-gel sensors have been demonstrated for chemical and biochemical sensing[129,130] and gas sensing[131,132] among others. In another approach sol-gel matrices can host nanoentities for collective sensing properties,[133–136] a property enhanced by the ability to control the porosity of the sol-gels and thus their interaction with the environment via the large surface area of these materials.

For the demonstration of a low cost, high performance photonic sensor operating under the remote point scheme presented later in chapter 4, an oxide nanocomposite material of silica matrix produced via the sol-gel method incorporating $NiCl_2$ cluster nanoentities has been used. This nanocomposite has been studied previously in the National Hellenic Research Foundation and the University of Patras yielding excellent results for ammonia sensing. The choice of this material is attributed not only to its high performance as a chemical sensor but also to its low cost, simple and fast synthesis, its ability to produce spin-casted thin films of good optical quality, the adequate selectivity to ammonia but also to the importance of ammonia detection in the industrial environment. The $SiO_2/NiCl_2$ nanocomposite material exploited here is synthesized by use of tetramethyl orthosilicate (TMOS) mixed with deionized water, HCl 0.1M, and isopropanol with the addition of stoichiometric equivalent of $NiCl_2 \bullet 6H_2O$ in order to obtain a 5 % w/v solution. The solution was left for 3 days under stirring and consequently was aged for few days at room temperature to ensure complete hydrolysis and polymerization before spin-coating on pre-cleaned (with chromosulphuric acid, acetone and isopropanol) glass substrate. Spin-coating at 3000 rpm for 60 seconds yields uniform films of good optical quality with thickness of about 1.65 μm as measured with a KLA Tencor Alpha Step profilometer. The nickel salt concentration and other parameters of the aforementioned synthesis were adjusted to ensure crack-free films of optical transmittance typically exceeding 75 % in the whole visible spectrum. An outline of the synthesis route of these materials is depicted in Figure 2-34.

The $SiO_2/NiCl_2$ films were characterized using atomic force microscopy (AFM, model: Veeco Multimode) shown in Figure 2-35 where an even distribution of the $NiCl_2$ nanoentities with size ranges from 30 to about 250 nm is revealed. Moreover the silica matrix exhibits regular porosity and nanograin morphology. Possible densification of the matrix by heat treatment not only is expected to deteriorate the sensing performance but also complex procedures are needed to avoid formation of large cracks in the film. Thus, the nanoporous silica nanocomposite thin film is not subjected to any baking step.

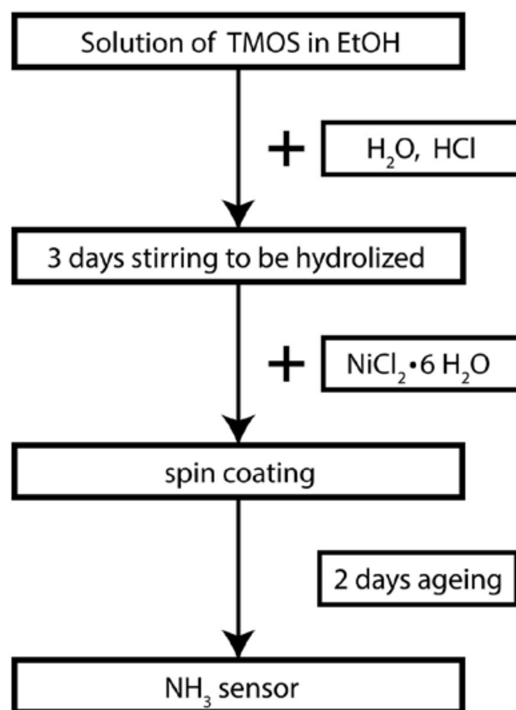

FIGURE 2-34: Illustration of the sol-gel process for synthesis of the ammonia sensing material.

Sensing is achieved by the interaction of ammonia gas with the salt nanoentities. The presence of the ammonia in the nickel salt clusters produces complexation and enables the exchange between captured water and diffused ammonia molecules. This entirely reversible effect gives rise to variation of the effective refractive index of the material and probably volume fraction changes that affect the geometry, and results in the change of the relative optical path therefore enabling sensing. The important role of the $NiCl_2$ nanoentities is supported by the fact that the undoped silica matrix exhibits no response to ammonia. It is stated here that no color change or preferential shift in the optical transmission spectrum of the material is detected upon exposure to ammonia. The use of tetraethyl orthosilicate (TEOS), another common precursor for silica sol-gel matrices has also being studied and found to yield similar results. Ammonia sensing measurements from photonic sensors made of $SiO_2/NiCl_2$ films are demonstrated in chapter 4.

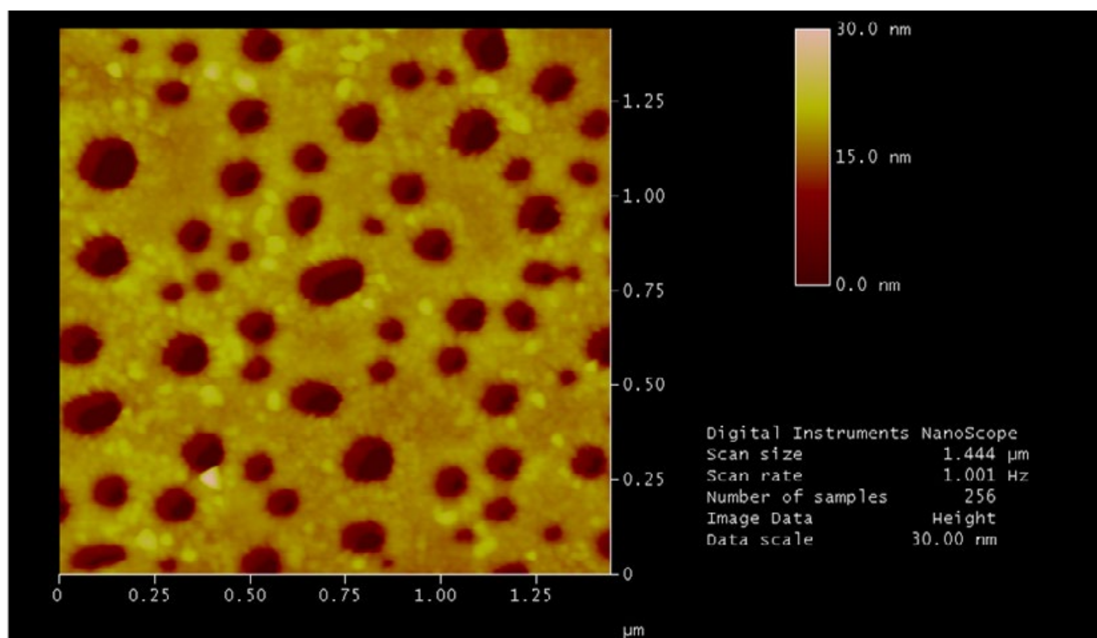

FIGURE 2-35: Atomic Force Microscopy (AFM) image of the sol-gel/$NiCl_2$ nanocomposite material surface.

2.10 Conclusions

In this work, properties of QDs were analyzed together and methods for their incorporation into various solid matrices were developed aiming to the fabrication of solid nanocomposites. Polymer and sol-gel derived matrices have been synthesized and characterized, in their pure and hybrid form, with a view to be used in the photonic device fabrication procedures described in the following chapters.

In particular, custom tailored-made polymers were designed and synthesized for the effective interaction between the QD ligands and the polymer chains. PMMA and some PMMA variations with long alkyl chains (PBMA and PMMA-PLMA copolymers) were studied for the embedment of QDs with their initial ligands. Interference reflectometry methods were used for the measurement of the refractive index of the derived nanocomposite thin films. Theoretical modeling has been developed for the present purposes. The enhancement of the QD/polymer nanocomposites for the case of PBMA over PMMA was confirmed mainly by the lack of observation of any PL peak shift at increased QD concentrations. The low

refractive index of the QD/PBMA nanocomposite measured (1.48-1.49) limits its use in some application. Indeed, QD/polystyrene exhibiting a higher refractive index, in the 1.58-1.60 range, was used for the fabrication of complex devices as will is discussed in the next chapter.

The case of sol-gel derived matrices as hosts for QDs was also explored using recipes found in the literature. Titania was the case of study. As will be demonstrated, such nanocomposite exhibits a good compatibility with the flexible soft lithographic fabrication techniques for the fabrication of complex photonic structures of good quality. In this context, hybrid organic/inorganic material, from the ORMOCER family, were also studied. This nanocomposites exhibit excellent optical properties, tailored for soft lithographic processes.

Finally, a custom-made silica/$NiCl_2$ sensing material derived using the sol-gel process was demonstrated. This material incorporates nanoentities exhibiting a reversible response to ammonia and is to be explored for the design, fabrication and evaluation of diffractive photonic sensors operating under the newly proposed remote point scheme discussed in chapter 4.

2.11 Future work

The nanocomposite materials discussed in this thesis incorporates a QD concentration of up to 5 µM for the initial solution from which thin films were coated, or equivalently a filling factor of up to about 1.2 % for the final thin films. This concentration range is lower than that this reported in the literature for the fabrication photonic structures exhibiting optical gain enabling the demonstration of chemically-synthesized QD lasers (e.g. 80 µM of CdSe/CdZnS/ZnS in sol-gel zirconia matrix[44]). The QD concentration for the synthesis of the nanocomposite was dictated by the availability of the initial QDs for the studies presented here. In higher nanoparticles concentration, the merit of using the specially designed matrices is expected to be more prominent.

CHAPTER 3
PHOTONIC STRUCTURES: MICRO/NANOFABRICATION ROUTES

3.1 Introduction to microfabrication of photonic structures

Fabrication techniques of planar photonic structures and integrated photonic circuits (PICs) have followed the advent of very large-scale integration (VLSI) schemes developed for the microelectronics industry. They typically involve the use of lithographic techniques followed by etching and growth methods. In this context, the substrate (or wafer) is coated with a sensitive layer (resist) and exposed to light, electrons or ions in order to be polymerized or decomposed as appropriate in a designed pattern. Following processing the written pattern is revealed and serves as the mask for subsequent processing by applying etching (wet, dry, ion) methods, or post-growth schemes towards the fabrication of the designed device.

In the above context, the use of laser radiation is not limited to the conventional lithographic techniques but offer new tools allowing flexible and direct processing. Direct laser ablative microetching (DLAM) discussed here can be used as a microfabrication technique based on the selective ablative removal of material. In addition two-photon polymerization provides a flexible fabrication route for the realization of complex 3D structures.[137,138]

Alternative structuring techniques such as nano-imprinting lithography (NIL) and soft lithography are also found in literature. For NIL patterning of polymer thin films, a "*hard*" pre-patterned stamp usually made of silicon, glass or metal, is applied on to spin-coated polymer under controlled pressure and temperature followed a gradient cooling. An antisticking treatment of the stamp is required for the successful detachment of the stamp without damaging the film. On the contrary, common soft lithography does not imply any pressurization, since UV of heat curable materials in liquid form are used. OrmoCore and OrmoClad are indicative examples of such materials. The pattern is initially transferred from a "*hard*" master stamp (usually silicon), to a "*soft*" stamp made of an elastomeric material, usually polydimethylsiloxane –PDMS. The benefits of using PDMS as the stamp material stems not only from its low cost, easy handling and excellent mechanical properties, but also from its high transparency in the UV, allowing UV curing of the underlying material under processing. The requirement of processing curable materials places a severe constraint to the application of such a technique since not all materials can be rendered UV or heat curable. An alternative approach for the implementation of polymer film patterning using soft lithography is successfully demonstrated here.

3.2 Direct Laser Ablative Microfabrication

The term direct laser ablative microfabrication is used here to describe materials processing by a tightly focused laser beam incident on a workpiece producing an "*ablative photo-decomposition*" process, as named by R. Srinivasan[139,140] in 1986.

The first investigation of laser modification of materials and laser fabrication was reported just after the invention of the laser in 1960. The term direct laser ablative microfabrication (DLAM) is used here to describe the removal of a localized portion of the material under processing via an "*ablative photo-decomposition*" process, by focusing a laser beam on the surface of the material. The term "ablation" is to

be contrasted to the "*direct laser writing*" which usually relates to the modification of optical properties by use of continuous wave laser radiation and in some cases results in engraving, polymerization or other photochemical modification. In recent literature may also refers to the multiphoton lithographic techniques.[141]

When focused intense laser radiation is absorbed near the solid surface, several effects may occur depending on laser wavelength, laser intensity and nature of material. An energetic photon (e.g. UV) may induce electronic transitions into excited states, photo-ionize the atoms, dissociate molecules and initiate photochemical reactions, with minimal thermal effects to the bulk. In contrast, relatively long wavelength radiation (e.g. IR) can be absorbed by free and bound electrons which transfer by collisions the energy to the lattice increasing rapidly the temperature to reach some 1000's ^{o}K in a very short time scale (ns-μs). In both exemplar cases, the absorbed energy is high enough (more than the binding energy) and the material decomposes, or becomes photo-ablated, producing ejection of plasma under non-equilibrium thermodynamic conditions.[137,140,142] Several models are reported in literature for the ablation process which involve photophysical and photochemical processes including pyrolytic and photolytic dissociation, thermal and mechanical effects, plasma formation and ionized and neutral species ejection.[142] It should be noted, however, that to date no model can effectively describe all coupled, thermal, photophysical, photomechanical and photochemical complex mechanisms evolving during ablation.[137] The effects are strongly dependent on the materials nature, and the laser radiation characteristics, including laser wavelength (from deep UV to IR) pulse energy and duration, which are translated to laser fluence (J/cm^2) and intensity (W/cm^2) on target.

UV laser radiation, such as radiation emitted by excimer lasers mainly induce direct photo-dissociation effects while radiation in the infrared region (e.g. from Nd:YAG lasers and Ti-sapphire lasers) transfer the laser energy on the substrate, produces rapid heating and causes photothermal dissociation.[137]

The requirements for high quality ablative structures for the fabrication of photonics structures are briefly summarized here. PICs usually operate in the near infrared and visible spectra ranges (roughly free-space wavelengths of λ=400 nm-2000 nm). The short wavelength of light implies the requirement for fabricating structures of very small minimum features (~ hundreds of nanometers or less) and of very low fabrication tolerances (less than some tens of nanometers). Features of that size can be fabricated by tightly focusing the laser beam. In this case, short wavelength radiation is beneficial as indicated by the simplest approach of a Gaussian beam, where the diameter of the focused spot is given by:[143]

$$d_0 \approx \frac{4f}{\pi D}\lambda \tag{3.1}$$

λ being the radiation of light, f and D the focal length and the aperture (or equivalently the laser beam spot size on lens) of the lens used. In this context, the use of laser sources of a short wavelength in the UV region can provide an effective route for miniaturization.

Another important factor for ablative fabrication is the material damage of the area around the ablated hole. This area, defined as the heat affected zone (HAZ), can severely deteriorate the quality of the fabricated structure. Such an effect is attributed to the diffusion of the laser produced heat on the material. The extend of this HAZ is defined by the thermal diffusion length, L_{th}:[137]

$$L_{th} = 2\sqrt{D_{th}\tau} \tag{3.2}$$

where D_{th} is the thermal diffusion coefficient and τ is the laser pulse duration. Moreover, at high intensities a re-solidification area may be also formed around the crater due to processes such as alloying and vitrification.[137] Deterioration of the not-ablated material area near the ablated crater can be avoided by use of one of two routes: a) the use of laser radiation of ultra-short pulses and, b) the use of laser radiation of highly energetic photons. Ultra-short pulses lasers of femtosecond pulse duration are indeed used for fabrication of structures of high quality.[144]

Their benefits are based on the ultra-fast delivery of energy on the workpiece, not allowing the heat to be diffused away from the ablated area and the minimization of the HAZ as indicated from equation 3.2. On the other hand, laser radiation of highly energetic photons induces photochemical only processes delivering negligible heat to the non-ablated areas.[137,140] A qualitative explanation of this effect is the following: upon laser radiation interaction with the material, the energy of the photons induces the breaking of molecular bonds while any remaining energy is removed from the sample in the form of kinetic energy of the ablated photofragments.

Excimer lasers (from **exc**ited di**mer**) are rare-gas-halides lasers where the radiation is produced by stimulated emission from excited dimers induced by an electrical discharge. Common excimer lasers are ArF for emission at 193 nm, KrF at 248 nm, XeCl at 308nm, XeF at 351 nm and, KrCl at 222 nm with the recent addition of F_2 emitting at 157 nm. The most widely used excimer lasers today are ArF (193 nm) and KrF (248 nm), although the shorter wavelength from the commonly available excimers is the 157 nm, F_2 excimer laser. In this latter case the extremely short wavelength induces severe difficulties in the microfabrication process. In particular due to the absorbance of this radiation from the atmosphere, the entire procedure including the laser source and the sample under processing needs to take place under vacuum. Moreover, the lack of high performance refractive optics of moderate cost for such laser radiation is another prohibitive for F_2 microfabrication. Indeed, fused silica optics widely used for 193 nm and other deep UV laser sources exhibits high absorbance in such a wavelength, thus MgF_2 and CaF_2 are the only available options for refractive optics at 157 nm. ArF radiation on the other hand does not suffer from these limitations. Commercially available fused silica optics include lenses, high magnification objectives and high reflectance mirrors. Furthermore, the laser beam can propagate in nitrogen with minimum losses or even in the atmosphere for short propagation distances if the attenuation induced is of no concern. In terms of safety, special care is taken to evacuate all ozone produced by the interaction of the beam with the oxygen of the atmosphere.

3.3 The 193 nm ArF excimer laser microfabrication station

The deep UV (λ=193 nm) ArF excimer laser microfabrication fully automated station used in this work for the patterning of the desired structures on samples of various geometries is established in the Photonic Applications, Structures and Materials (PhASMa) laboratory of the Department of Materials Science in Patras and is shown in Figure 3-1 and schematically depicted in Figure 3-2. The laser micromachining station is based on an ArF excimer laser (Neweks PSX-501) delivering laser radiation at λ=193 nm with pulse energy up to 7.5 mJ with typical 5 nanosecond pulse at a maximum repetition rate of 300 pulses per second (pps). The laser beam is manipulated by a set of high purity fused silica optics including an attenuator/compensator pair, mounted on a computer controlled rotary mount, a 3.7X objective lens in conjunction to a high laser power pinhole and a planar convex lens of focal length f=114.8 mm at the laser radiation for spatial filtering the laser beam, and a 15X objective for focusing the laser beam on to the sample. The path of the laser beam is defined by two high reflectivity (HR) multicoated mirrors at the laser wavelength. The sample under processing is mounted on x-y-z nanopositioning translation stages of 80 nm minimum step

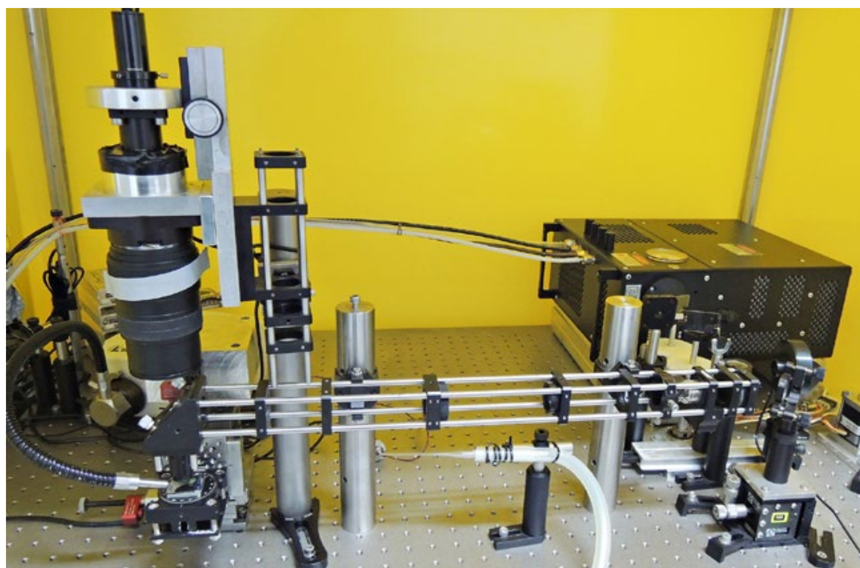

FIGURE 3-1: Photograph of the ArF excimer laser microfabrication facility established at the Photonic Applications, Structures and Materials (PhASMa) laboratory at the Dept. of Materials Science of the University of Patras.

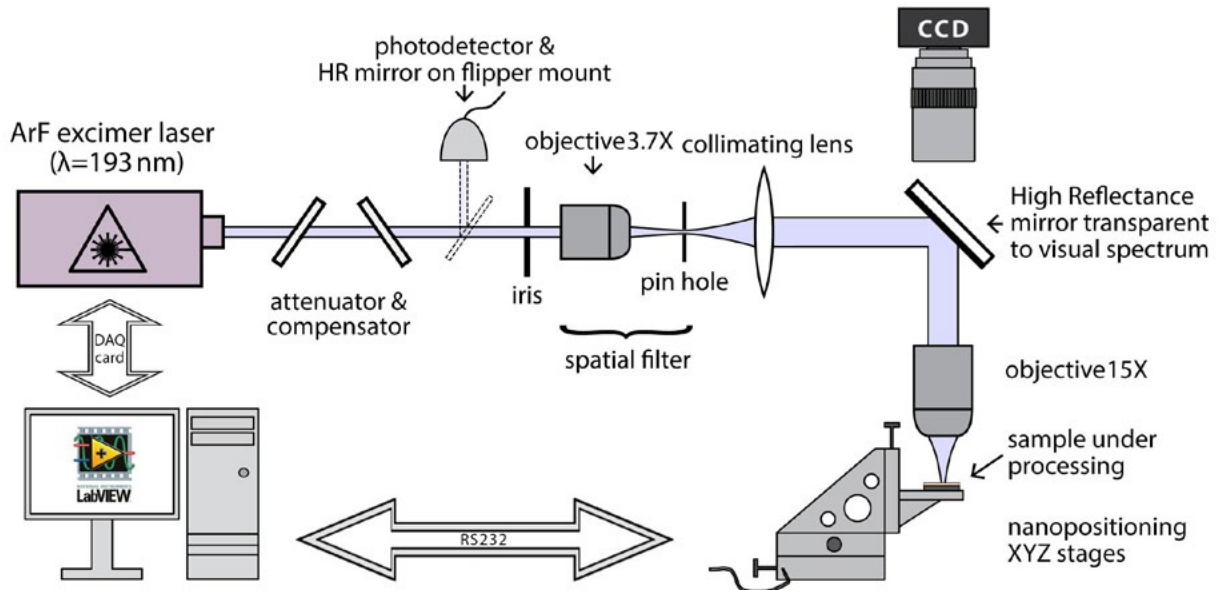

FIGURE 3-2: The excimer laser microfabrication station setup.

equipped with optical feedback for high precision movement driven by a closed loop controller. A detailed list of the components comprising the laser microfabrication station is shown in Table 3-1.

TABLE 3-1: List of the component characteristics of the laser microfabrication station

ArF laser	
Model	Neweks PSX-501
Wavelength	λ=193nm
Emergent beam size	4×3 mm
Beam divergence (V×H)	2.0x6.0 mrad
Maximum pulse energy	7.5 mJ
Maximum average power output	3W
Gas fill lifetime	2.5x10^6 shots
Maximum repetition rate	300 pps
Pulse duration	5 ns (typical)
Pulse-to-pulse stability	3%
Timing jitter	1 ns
Force (output power tuning)	67% - 100 %

x-y-z nanopositioners	
Optically encoded Translation stages model	New focus 9067-COM-E
Resolution	80 nm
Bearings type	Crossed roller bearings
Travel range	5.08 cm
Piezoelectric motors model	New Focus 8303 Picomotors Actuators
Resolution	30 nm
Maximum speed	1.2 mm/min
Driver model	New Focus 8766-Kit
Network controller	New Focus 8752
Connectivity	RS 232
Optical Elements	
15X Objective	Thor Labs LMU-15X-193 MicroSpot Focusing Objective, 192 - 194 nm, NA=0.32
3.7X Objective	Thor Labs RMS4X193 3.7X UV Imaging Microscope Objective Design λ=193 nm
2x HR mirror	CVI – ARF-1025-45-UNP – 193 nm mirror
HR mirror	CVI – KRF-1025-45-VNP – 248 nm mirror
Lens	CVI – PLCX-25.4-64.4-EUV focal length at 193 nm: 114.8 mm
Attenuator – Compensator	Laser Optic – Variable attenuator 0-45° T8-10%, AR 193nm/0°
High Power Pinhole	Thor Labs – P10C Damage threshold: 1 x 10^6 W/mm^2, 10 ns Pulse @ 700 nm
Power detector	
Power & energy meter	Ophir Nova
Power & energy sensor	Ophir 3A-SH, thermal sensor
Spectral range	0.15-20μm

Power range	10 μW – 3W
Energy range	20μJ-2J
Connectivity	RS 232
USB camera	Celestron digital microscope imager
Camera lens	Sigma 55-200mm D 1:4-5.6
DAQ card	National Instrument PCI-6221
Software	National Instrument LabView

An automation control platform of the whole setup based on LabView™ has been developed in the context of thesis research. Details are given in Appendix A. The automation allows control of the laser microfabrication station, the laser source, the nanopositioning translation stages, the attenuator/compensator rotary motor and the energy/power detector. A data acquisition (DAQ) card connected to the computer enables laser triggering and the control of the laser operation power and monitoring of the laser status by the automation platform. An electronic interface between the laser and the DAQ card was developed to accommodate the fact that the laser inputs and outputs are not transistor-to-transistor (TTL) logic signals. In addition to the laser, the DAQ card provides control of a motorized stepper motor and stepper motor control electronics enabling precise control of an attenuator/compensator pair which in conjunction with the computer-controlled power and energy detector enables for the accurate setting of the laser pulse energy delivered to the sample under processing. The electronic connection diagram of the interface between the computer-controlled DAQ card, the laser and stepper motor is depicted in Figure 3-3. The developed LabView™ interface controls the complete process of the laser firing and the translation stages movement for the fabrication of complex structures, the pulse energy and power measurement as well as the laser force output, a term used by the laser manufacturer defined as the output power percentage to the maximum output power of the laser. The use of a HR mirror for

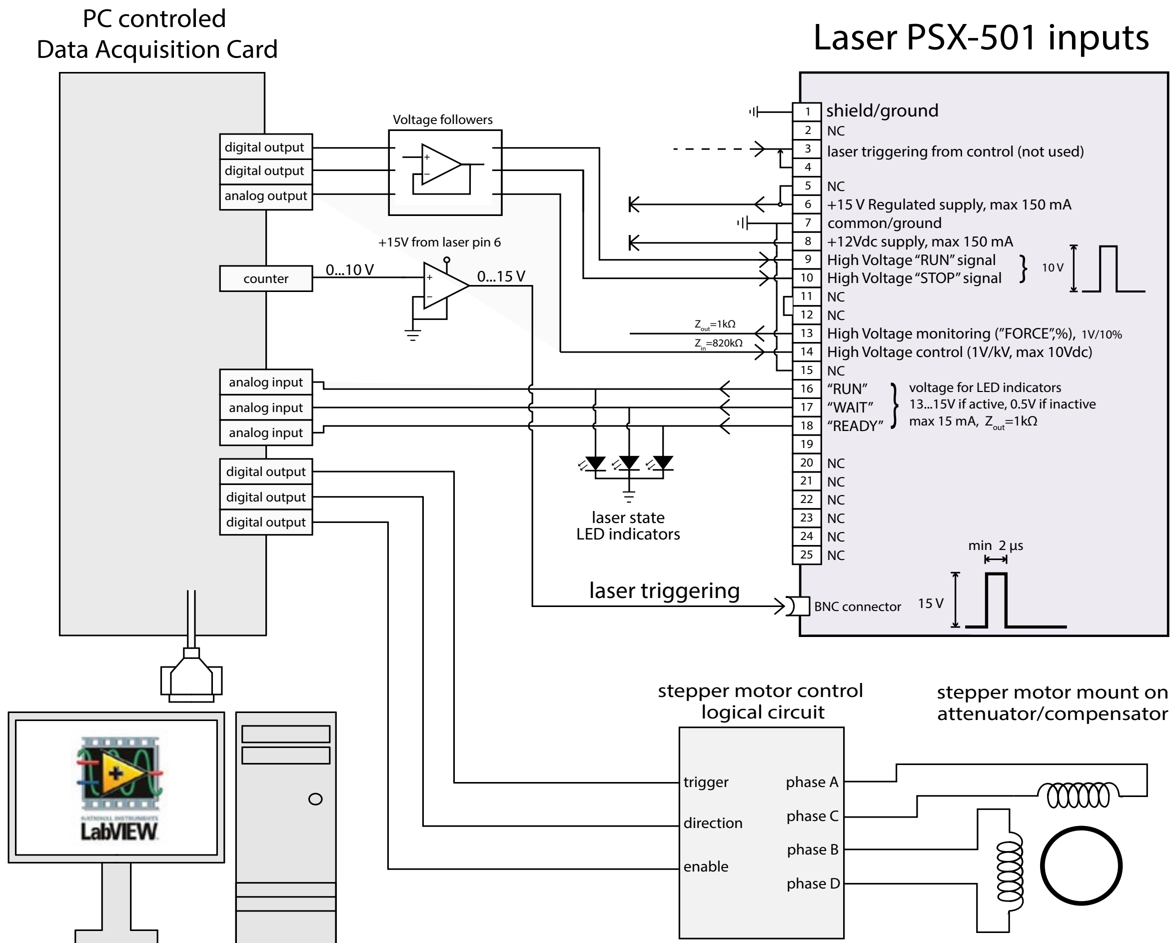

FIGURE 3-3: Wiring diagram for the connection of the PC controlled DAQ card to the excimer laser and the stepper motor that rotates the attenuator/compensator pair.

the 193 nm radiation which is transparent in the visible spectral range allows for the visual inspection of the ablative process with a use of a computer controlled camera and a camera lens. For the fabrication of a structure, the LabView interface is programed by a set of steps entered either by externally providing an array of firing points or calculated by the program. Alternatively, a bitmap picture can be loaded for raster scanning. Laser microfabrication protocols at various pulse energies can also be performed automatically while fabrication of common structures such as diffraction grating and micro-rings can be programmed by simply entering the desired geometry and key parameters. A detailed preview of the various features of the laser microfabrication suite is presented in appendix A.

3.4 Fine-tuning of the laser microfabrication procedure

For the fabrication of complex photonic structures, it is important to define a protocol for tuning the laser microfabrication procedure. The most important factors for such a protocol are the a) precise delivery of the required pulse energy to the sample, b) the shape of the beam and c) the identification of the optimum patterning path of the laser beam.

Power Measurement

To account for the first issue and also for the laser output instability, the following protocol is followed: following a new fill of the laser with gas mixture to ensure the highest possible power stability and while firing at a constant repetition rate (usually 100 pps) for a fixed configuration of the iris and pinhole, the laser output power is measured in two positions, a position just after the attenuator/compensator pair by the interposition of a HR mirror on a flipper mount (position A) and the position of the sample (position B) as shown in Figure 3-4. These two measurements enable us to calculate a ratio of the laser pulse energy or power of the laser beam at the two measuring positions for a fixed configuration. At any subsequent instance the power or pulse energy delivered to the sample can be conveniently calculated by easily deflecting the laser beam to the detector fixed at position A using the flipper mount and thereby deducing the measurement at position A for that of position B. Control of the laser pulse energy is achieved by proper adjustment of the attenuator compensator pair. The presence of the compensator is crucial to redirect the refracted beam from the attenuator, thus enabling the preservation of the exact laser path and the use of the spatial filtering technique.

A laser microfabrication station suite feature has been developed to automatically measure the transmittance of the attenuator at various angles of laser beam incidence, thus providing a pulse energy calibration route. Such a measurement is shown in Figure 3-5. Although it would possible to adjust the laser force which lies

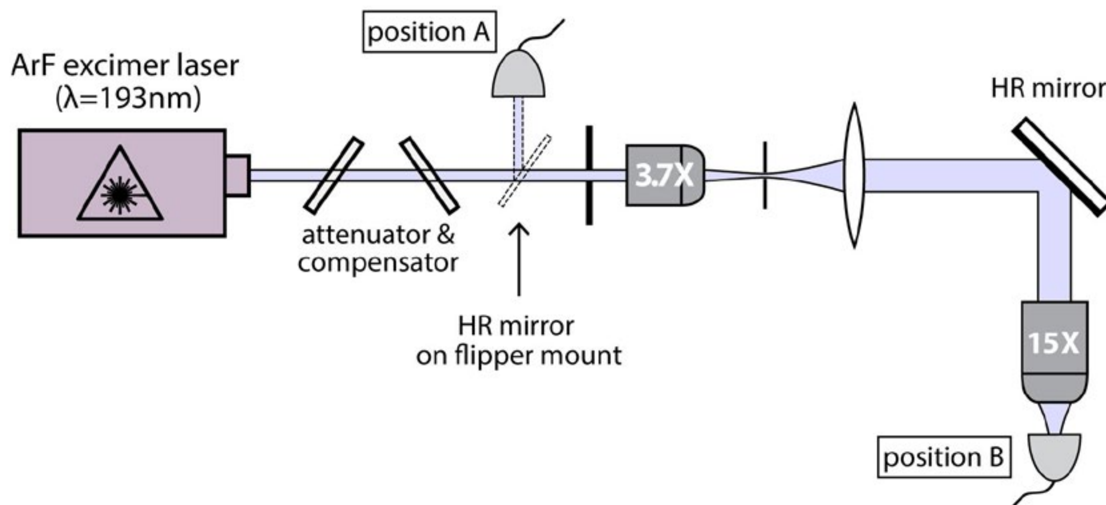

Figure 3-4: Evaluating the pulse energy delivered to the sample under processing.

between 68% and 100% with respect to the maximum possible force, such an option has been found to increase the instability of the laser output, therefore it has been avoided. Automatically controlling the laser energy delivered to the sample enables the implementation of fast laser writing protocols by firing pulses of increased or decreased energy at different positions of the sample for the derivation of etching rates curves and determination of the ablation threshold and incubation regions of various materials. The etching depth d dependence on the pulse fluence F for the case of a PMMA film is shown in Figure 3-6. The measurement points can be fitted by the following expression found in literature:

$$d(\mathrm{F}) = \frac{1}{\alpha_{eff}} \ln\left(\frac{F}{F_{th}}\right) \quad (3.3)$$

for the derivation of the effective absorption coefficient α_{eff} and the threshold fluence F_{thr}.

Spatial Filter

In order to improve the beam quality, a spatial filter is developed. The common spatial filtering technique applied for wavelengths in the visual and infrared windows is difficult for Deep UV radiation since very small (sub-micron) pinholes are required. Moreover, laser radiation tends to ablate and enlarge the pinhole. A simple and straightforward technique that yield satisfactory results is the use of the laser beam to drill a small hole on a copper

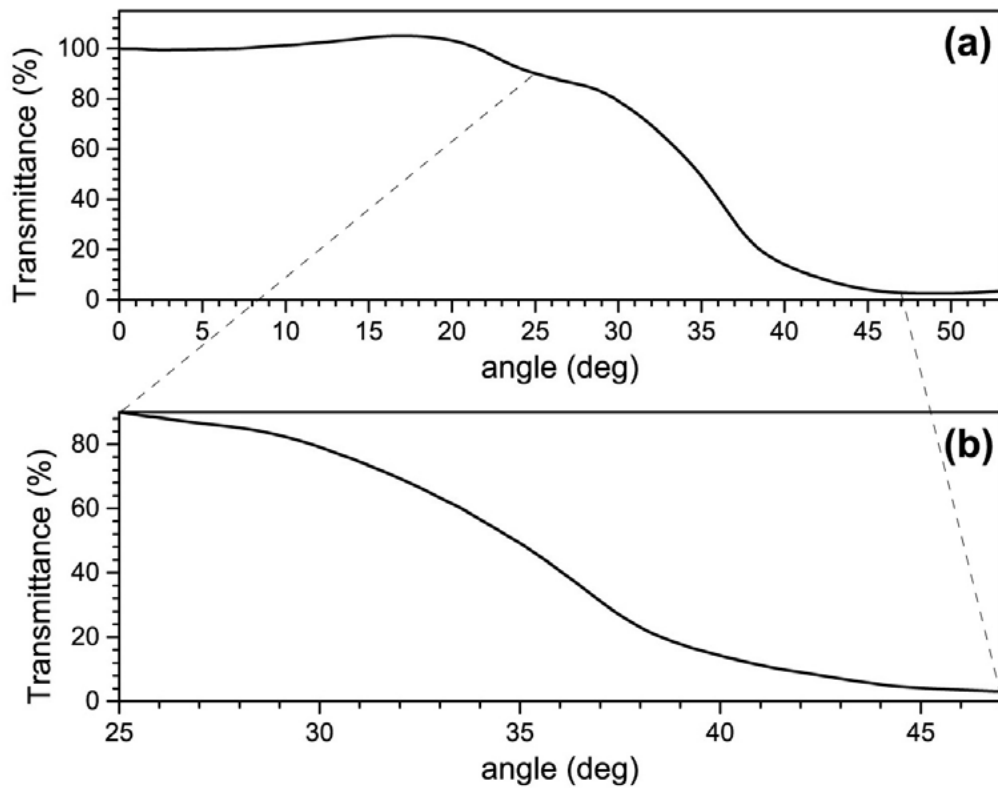

FIGURE 3-5: The laser transmittance from the attenuator-compensator pair at various angles: **(a)** the whole angle range, **(b)** the expanded range of highest attenuation.

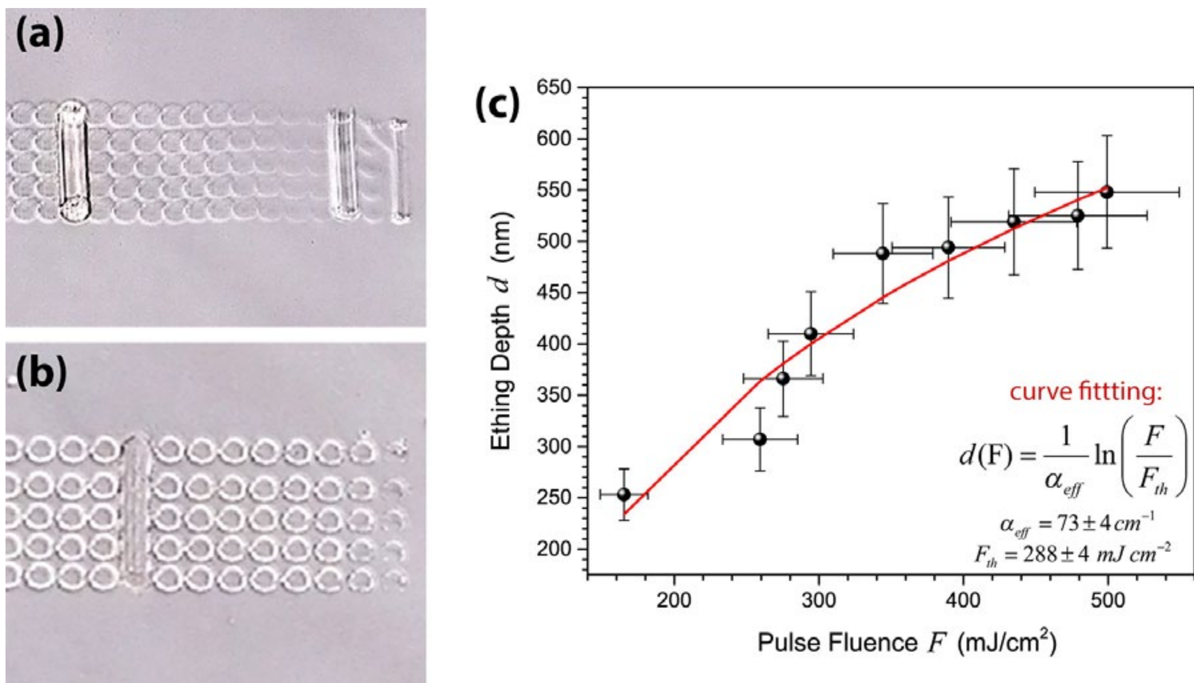

FIGURE 3-6: Laser writing protocol on PMMA: **(a, b)** optical microscopy images of craters drilled on a PMMA thin film at different fluence and, **(c)** the etching depth of crater plot for various pulse fluence and the fitted curve for the formula indicated (R^2=0.92).

pinhole sheet initially designed for high power lasers at the near infrared region, using the 3.7X objective of the spatial filter. Although this technique can be applied only for low pulse energy ablative procedure, it was found to work well for processing of polymer thin films. A SEM micrograph of such an ablated pinhole used in the experiments presented below is shown in Figure 3-7 while the fluorescing pattern of the beam shape after the spatial filter shown in Figure 3-8 clearly indicating an airy pattern.

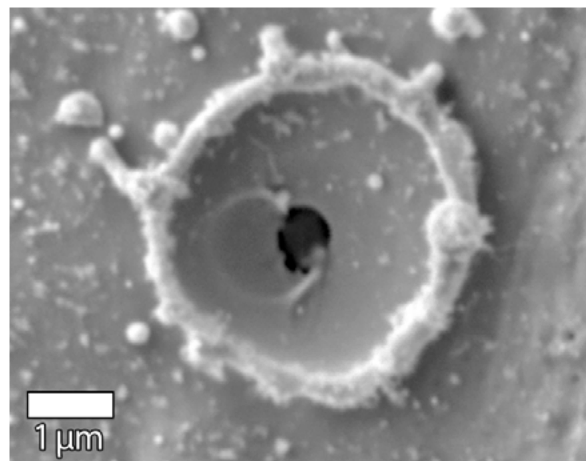

FIGURE 3-7: SEM micrograph of the ~ 0.5 µm ablated pinhole on the thick (25µm) copper plate.

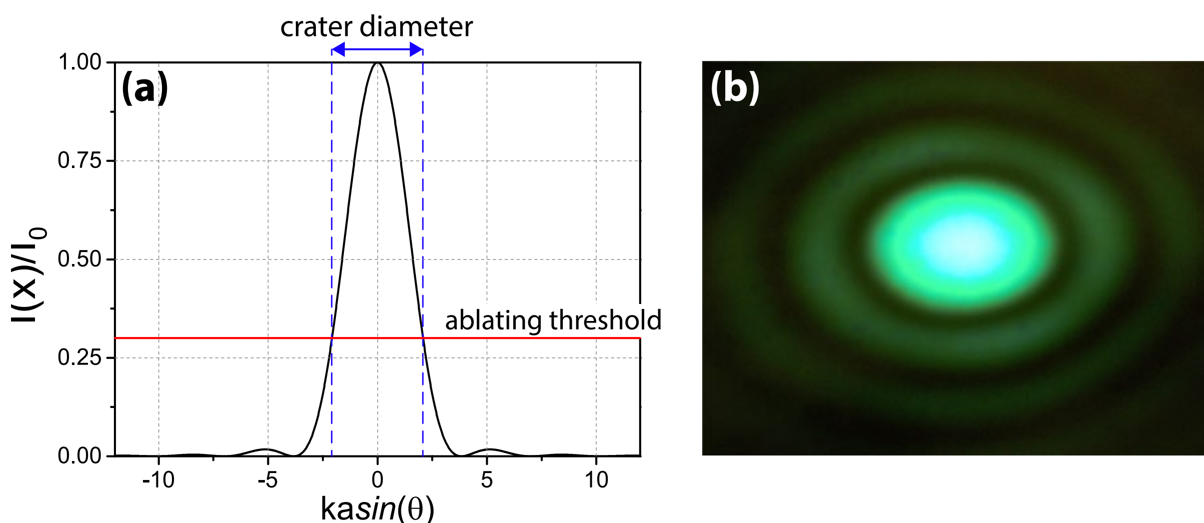

FIGURE 3-8: The normalized laser intensity distribution diffracted by a pin hole (Airy pattern): **(a)** Relative intensity distribution for the x=ka*sin*(θ) being in the [-12,12] range. The red line denotes a hypothetical ablating threshold of the material under processing while the blue dashed lines indicate the size of the formed crater. The ablating threshold of the substrate is well beyond the peak intensity. **(b)** Photograph of a fluorescence screen (paper soaked with yellow pigment) illuminated by the ArF excimer laser just after the spatial filter.

Nanopositioners

The finite step nature of the nanopositioning system used implies that for precision microfabrication of low tolerances photonic structure it is beneficial to use a "*stop and shoot*" technique in contrast to the faster "*vector*" movement of the sample while firing with the laser since the latter technique suffers from fluctuations in the acceleration of the nanopositioners due to static friction of the motors. By a raster scan of the ablation points, the high precision optical feedback system of the translation stages can ensure the correct position by correction of any movement fluctuations. For the design of such an "*ablation points*" map, one must also take into consideration the limitation of the finite step of the nanopositioning system. Nonlinear structures such as polymer micro-ring resonators are implemented with such a procedure as shown in Figure 3-9. Initially the position of the ablation points are calculated by an algorithm for a given size of a single pulse ablated crater on the film and the required smoothness of the structure by simulating the cycle under fabrication by a polygon with the required number of vertices. The exact positions of the actual points are then calculated by rounding the necessary moving steps to

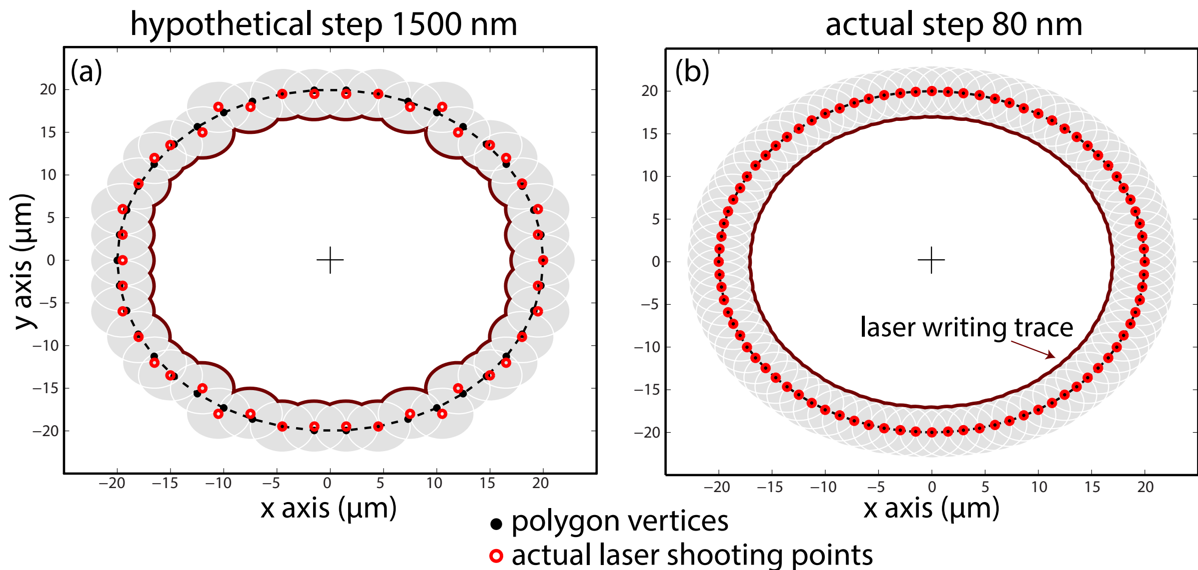

FIGURE 3-9: (a) The laser writing tracing of a cycle exaggerated for a hypothetical stepper motor step of 1.5 μm, and **(b)** laser writing tracing of a cycle for the actual stepper motor step of 80 nm. Smaller steps produces a smoother cycle.

integer multiples of the nanopositioner step. As shown in Figure 3-9 the step size plays a crucial role in the successful implementation of such structures. However, even for small micro-ring resonators of radius of 20 μm a step of 80 nm is adequate.

3.5 Example fabrication of complex photonic structures

To demonstrate implementation of complex photonic structures on polymer films, a binary computer generated hologram (CGH) has been designed using an available algorithm.[‡‡] Figure 3-10 shows the target pattern which is the "PhASMa" logo of our group, the mask as calculated by the algorithm and the predicted reconstruction of the holographic mask. This 50×50 pixels unit pattern is then placed in a 4×4 array for a total of 200×200 pixels bitmap file consisting of black and white pixels. The image file is loaded into the corresponding feature of the laser microfabrication station suite together with the pixel pitches in the x and y axis and the number of pulses per stop value. A polystyrene/toluene solution of polymer concentration of 0.15 g/ml, also incorporating 2 μM of QD for the proof of concept of the procedure, was spin-coated on a clean microscope slide at 2000 rpm for 60 s and heated at 80°C for 10 minutes. A laser writing protocol was used to identify the optimum conditions in terms of focus and total energy delivered on film. A 3 μm diameter (approx.) crater was found to be formed when shoot with 10 numbers for a total energy delivery of about 10 μJ. Then the CGH pitch, defined as the distance between two successive ablated pixels, was chosen to be 4 μm for a total CGH area of 200×4μm=800μm on each side. Microscope images and SEM micrographs of the fabricated structure are shown in Figure 3-11 while the reconstruction of the CGH upon illumination with a 532 nm laser shown in Figure 3-12 confirms the success of the fabrication procedure.

Another example of ablation of complex photonic structures is presented in Figure 3-13, Figure 3-14 and Figure 3-15 where ablation in non-planar topologies is demonstrated. As has been explained previously, the possibility to easily process

‡‡ Holomaster 2, free demonstration version

Figure 3-10: (a) Target design of a "*PhASMA*" logo CGH, **(b)** the optimum unit mask as calculated by the algorithm and, **(c)** the resultant reconstruction of the optimum mask of the CGH as predicted by the algorithm.

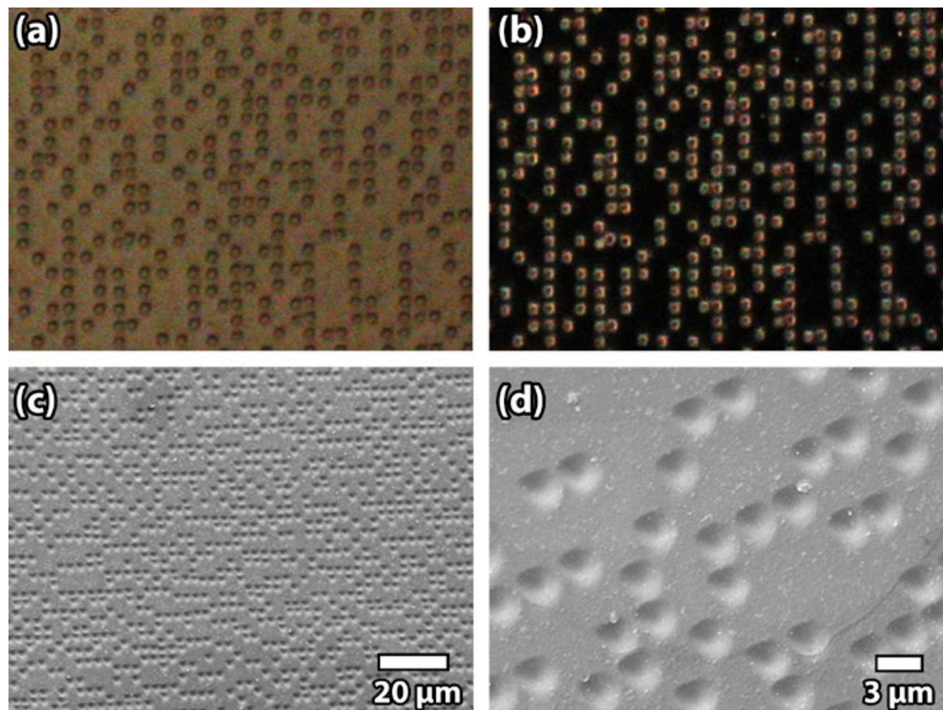

Figure 3-11: QD-doped polystyrene CGH fabricated using the direct laser writing method: **(a)** microscope image under bright field illumination, **(b)** microscope image under dark field illumination, **(c-d)** SEM micrographs.

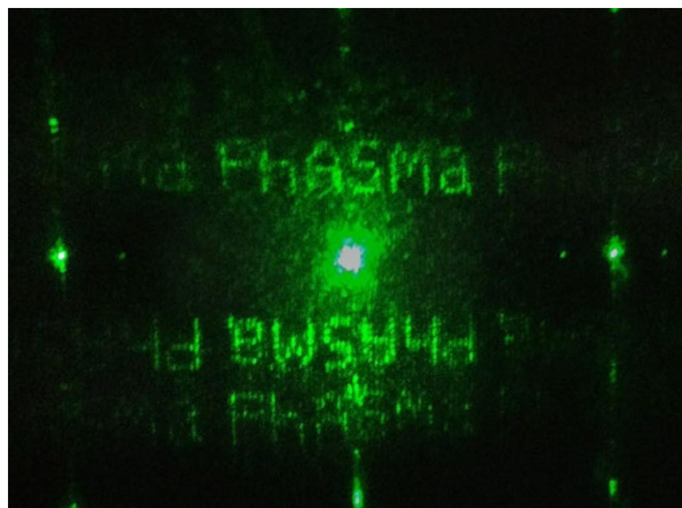

Figure 3-12: Reconstruction of the CGH fabricated using the direct laser writing method under 532 nm laser illumination. The distance from the CGH to the screen is about 10 cm.

non-planar surfaces is an important advantage of laser processing over the more common lithographic techniques. Here ablation of plastic optical fibers (POFs) were patterned in various ways. POFs studied here (ESKA GH-4001P, Mitsubishi-Rayon Co.) consist of a large core of 980 μm diameter made of PMMA covered with a 10 μm thick fluorinated polymer cladding of lower refractive index. The two materials exhibit different ablation thresholds and hence different response upon interaction with 193 nm radiation. The goal of this study was to engrave deep structures on the POF which can be potentially filled with sensing material in order to enhance its interaction with the waveguiding field for application in POF photonic sensors. Interesting results from our group (not shown here for simplicity) show indeed enhanced sensing response over other POF sensor configurations such as casting of the sensing material on a bended POF for evanescent field interaction.

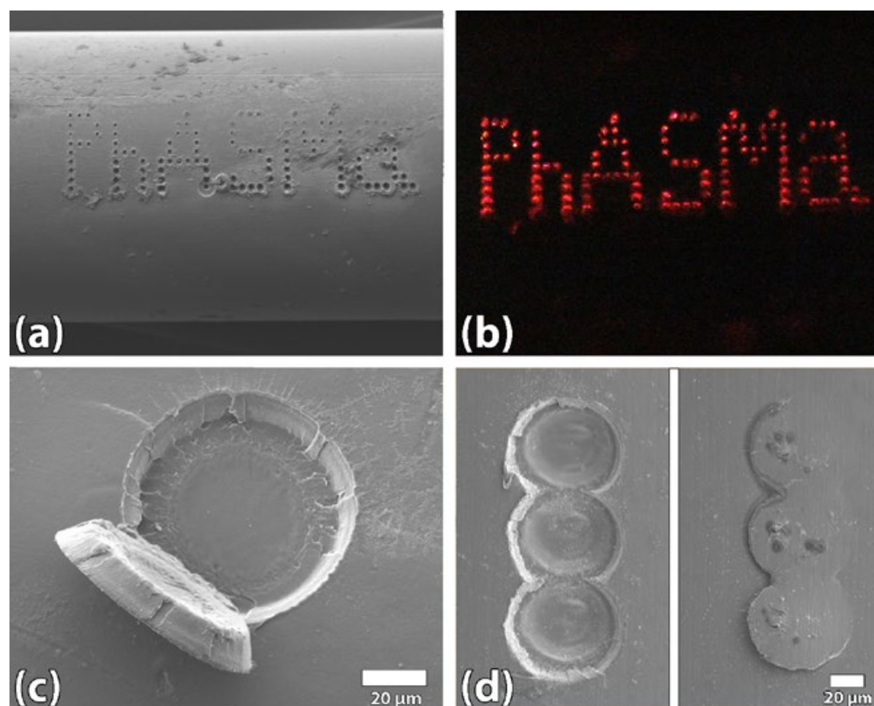

FIGURE 3-13: Demonstration of POF microstructuring: **(a)** SEM micrograph of test structure on POF clad, **(b)** light scattering of the same etched structure while waveguiding, **(c)** SEM micrograph of structure formed at the core/shell interface due to different ablation thresholds, **(d)** SEM micrograph of etched holes at different ablation fluences.

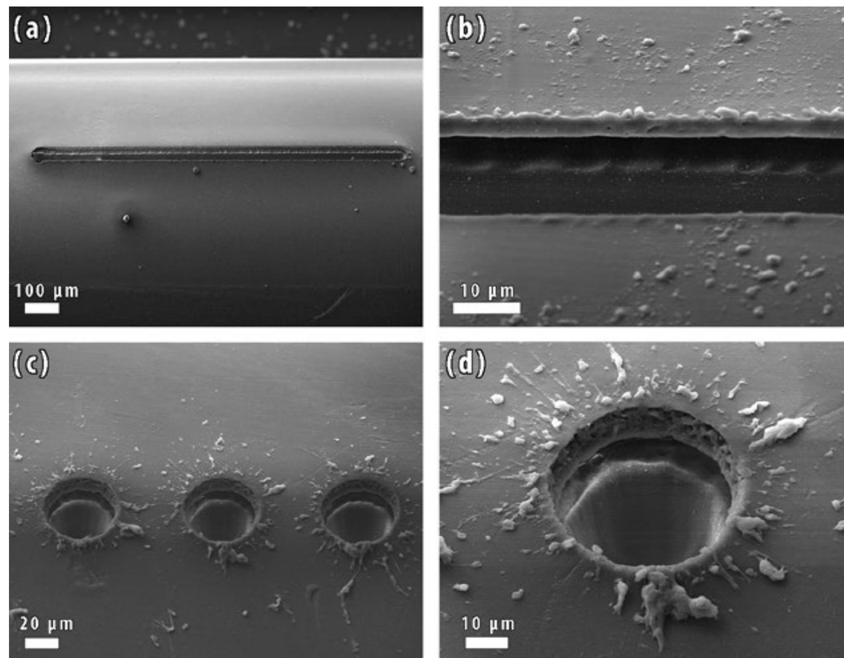

FIGURE 3-14: POF microstructuring for applications in photonic sensors, **(a-b)** etch of a groove, **(c-d)** etch of holes.

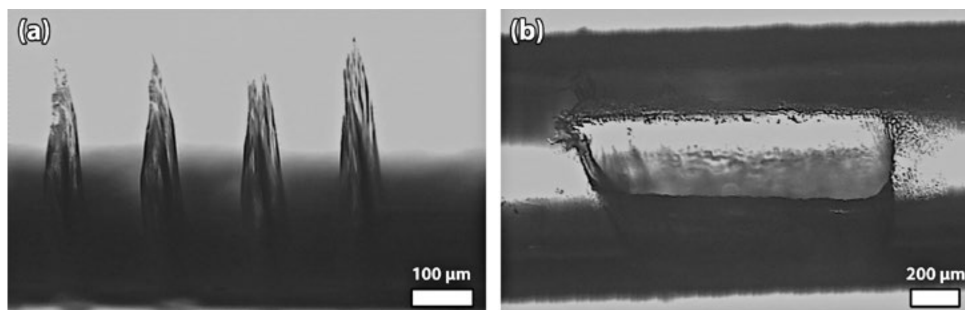

FIGURE 3-15: Optical microscopy images of microstructures ablated on POF: **(a)** side view of holes, **(b)** deep groove etched right up to the POF axis (500 µm) as an acceptor of sensing material.

3.6 Fabrication of polymer waveguides incorporating QDs

Polymer waveguides incorporating QDs have been designed and fabricated on a silicon substrate. The choice of silicon as the substrates material instead of the other lower cost substrate such as polymer or microscope slides was made due to the simple cleaving of such structures along the crystallographic planes of silicon. With the spin-coating technique, the uniform casting of the polymer material near the edges of the substrate is difficult or not feasible. To overcome this limitation, larger substrates are used which are then cut to size. Cleaving of polymer or glass substrates is challenging

and often shows poor reproducibility. On the contrary, precise cutting of thin silicon wafers is very easy by means of a small diamond cutter while the polymer thin films have the tendency to also be cleaved along the silicon cut edge. Moreover, techniques such as surface modification, adhesion promotion or antisticking treatments are available for silicon substrates. The use however of as-is silicon wafers as substrates for polymer photonic integrated circuits (PICs) is not favored due to the high refractive index of silicon (about n_{Si}=3.8 in contrast to values in the range of 1.4-2 for polymers). To bypass such a drawback, a thick SiO_2 layer can be grown or deposited which exhibits the low refractive index of n=1.46 which is ideal for most polymer PICs. This silicon oxide layer can be grown by wet thermal oxidation or can be deposited using chemical vapor deposition (CVD) techniques.

Thermally-oxidized silicon wafers with a thick oxide layer of 1.1 μm have been used here for the demonstration of polymer waveguides fabrication.[§§] Simulations have shown that this thickness does not suffice to prevent light leakage into the substrate, therefore an additional low refractive index layer has been employed. Poly(2,2,2-trifluoroethyl methacrylate) –P3FEMA, is a fluorinated acrylic polymer resembling PMMA with a trifluorinated ethyl attached to the ester group instead of a methyl as was shown in Figure 2-7(e). This polymer exhibits a low refractive index of n=1.42[83] at the wavelength of λ=650 nm rendering it ideal for use as the cladding layer in waveguides. P3FEMA was synthesized using the free radical method described in paragraph 2.4. P3FEMA has a low solubility in toluene, thus chloroform, a chlorinated solvent, was used instead. A solution of 0.15 g/ml in chloroform was prepared and filtered with a 0.25 μm millex filter prior to spin-cast on clean silicon/silica substrates. The substrates were thoroughly cleaned with acetone and isopropanol and baked for two hours at 200°C to completely remove any traces of humidity.

§§ Dr M. Vassilopoulou from The Department of Microelectronics in National Center for Scientific Research-NCSR “Demokritos” is acknowledged for providing thermally oxidized silicon wafers.

For the preparation of relatively thick films, a two-step coating procedure was followed. Dynamic deposition was found to yield films of good quality over an area of more than 1 cm^2. The spin-coating protocol has as follows: A small amount of about 40 µl of solution was rapidly dropped on the substrate while spinning at the low speed of 700 rpm, immediately followed by a 30 s spin at 1500 rpm for uniformity and solidification to be achieved. This process yielded a film of thickness of about 2 µm as measured using a profilometer (Bruker DektakXT). The films were dried at 60°C for 15 minutes and the procedure is repeated for a total of 4 µm of the low refractive index cladding layer. The QD/polymer nanocomposites were then spin-coated on top from a filtered toluene solution of polymer concentration of 0.15 g/ml for the deposition of a 1.5 µm thick layer. Finally, ArF excimer laser micromachining is used to etch waveguides of widths in the range of 2-10 µm. A schematic illustration of the final structure is shown in Figure 3-16 while the transverse fundamental mode of the waveguide was calculated using beam propagation method (BPM) for the calculation of the effective refractive index, is shown in Figure 3-17.

To fabricate QD/polymers waveguides using the direct excimer laser ablation techniques the different ablation thresholds of PMMA and P3FEMA need to be taken into account. It was found that for PMMA a fluence value of at least 60 mJ/cm^2 per single pulse is needed for fabrication of clearly defined holes while P3FEMA exhibits

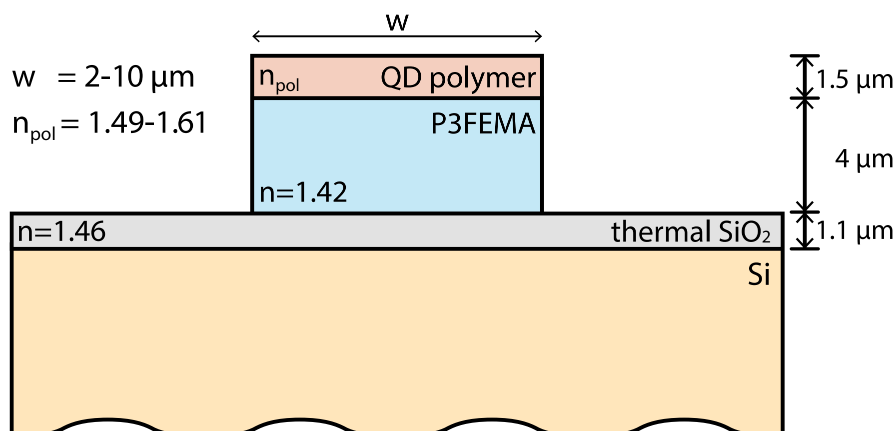

FIGURE 3-16: Cross section of α QD-doped polymer waveguide fabricated on top of a thick low refractive index fluorinated polymer (P3FEMA) buffer layer on an oxidized silicon substrate.

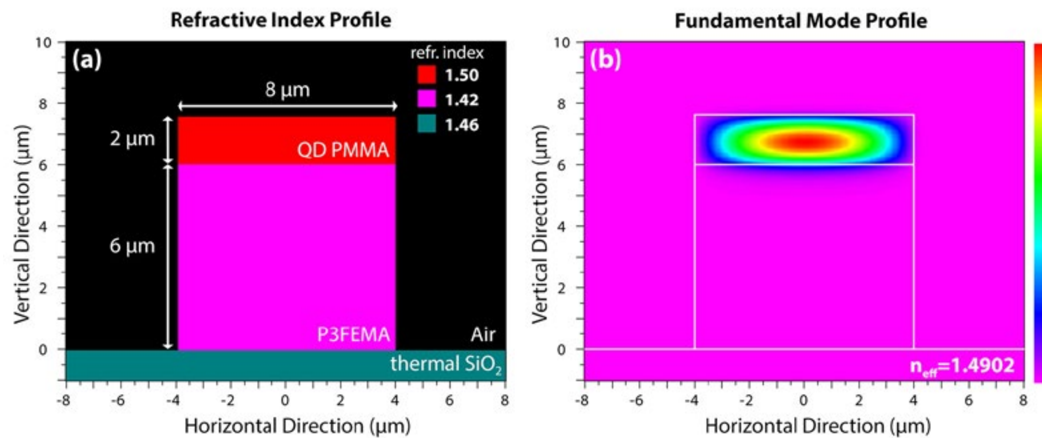

FIGURE 3-17: (a) The transverse refractive index profile of the QD-doped PMMA/P3FEMA rib waveguide, **(b)** the fundamental mode of the waveguide as computed using the BPM method. The white lines outline the waveguide edges.

a higher resistance to laser radiation and a fluence of more than 150 mJ/cm^2 is needed for clear ablation. However, a fluence value of more than 200 mJ/cm^2 is required for the clean microetching of such a material due to its trend to form filaments and incubation effects on the non-ablated material left upon irradiation as shown in Figure 3-18. This material behavior is attributed not only to the higher ablation threshold, but also to the higher transparency of fluorinated materials to deep UV radiation. It should be noted here that these fluence values cannot be safely considered to be the ablation thresholds due to the non-uniform, Gaussian like distribution of the laser beam intensity.

Micromachined waveguides are shown in Figure 3-19 prior to any smoothing treatment. The laser energy delivered is about 0.1 µJ in a circular area of diameter of about 5 µm for each pulse. The laser repetition rate was set at 200 pps while the sample was linearly moved at a speed of about 160 µm/s for an about 2.5 J/cm^2 overall radiation fluence deliveru on the sample. The geometry of the fabricated groove as defined by the laser writing trace is shown in Figure 3-20. The corrugation-free side walls predicted are also confirmed by the SEM micrographs of Figure 3-19. Multiple overlapped lines were successively written on both sides of the waveguiding structure with a 3 µm movement step perpendicular to the structure. The waveguide is cleaved along a crystallographic axis of the silicon substrate and the edge without any further treatment is shown in Figure 3-19(b).

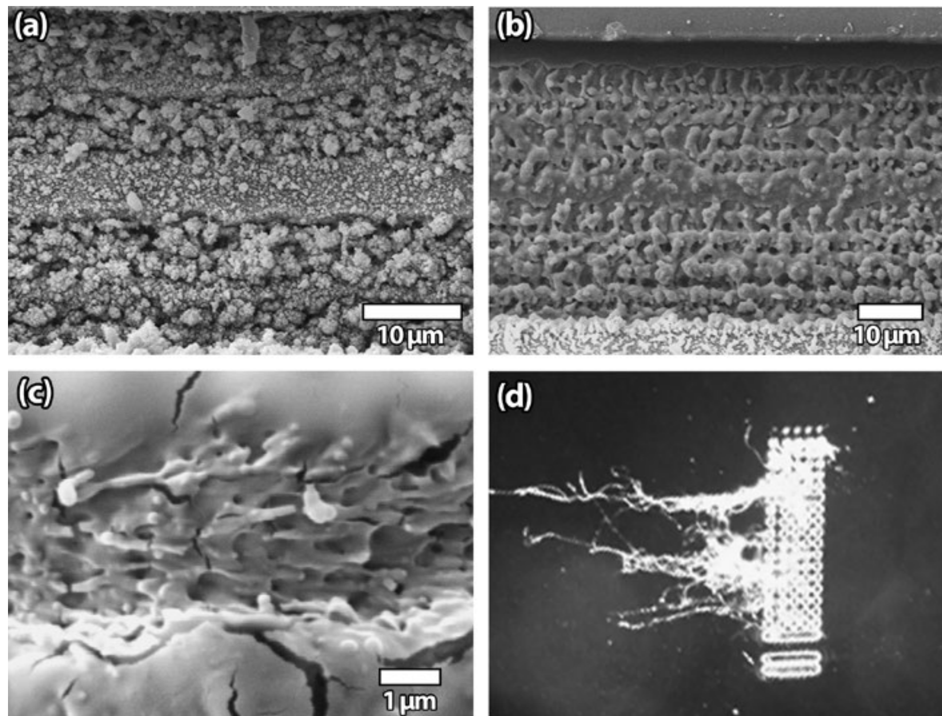

FIGURE 3-18: (a-c) SEM micrographs of grooves ablated on thick (4 µm) P3FEMA polymer films, **(d)** microscope image of filament formation upon single pulse irradiation at 193 nm.

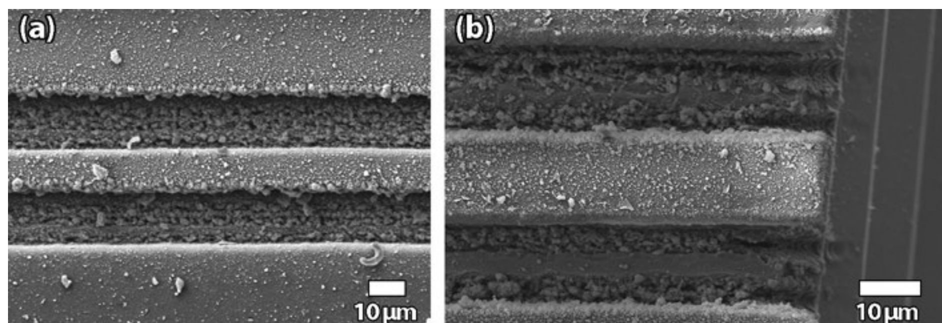

FIGURE 3-19: (a) SEM micrograph of the QD-doped PMMA/P3FEMA waveguide on silicon fabricated using the direct ablation method prior to solvent vapor smoothing, **(b)** the cleaved edge of the waveguide.

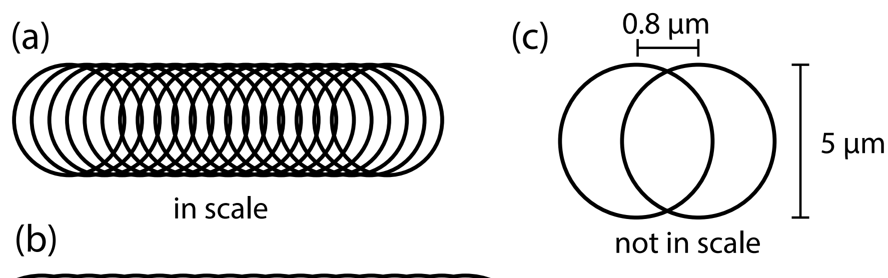

FIGURE 3-20: (a) The shape of the ablated groove as defined by the successive laser pulses, **(b)** the tracing line of the groove and, **(c)** the geometry of two successive craters (not to scale).

3.7 Ablated polymer structures - smoothing by solvent vapor treatment

The QD/polymer waveguide presented in Figure 3-19 suffers from high surface roughness, debris re-deposited on the structure and incomplete ablation of the underlying clad layer. To account for all these issues a solvent vapor treatment was developed. As shown illustratively in Figure 3-21, the ablated structure was placed inside a small purpose built chamber of volume of about 80 cm^3 made of two petri dishes, along with 150 μl of chloroform drop. The chamber was then heated at 55°C by use of a hot plate, at a temperature close to the boiling point of the chloroform (61.2°C) for complete evaporation of the solvent. The chloroform vapor concentration inside the chamber is then about 1.58×10^{-2} mol/l. SEM micrographs of the same structure shown in Figure 3-22 after the exposure to chloroform vapor to validate the success of the smoothing treatment. A set of treatments at different amounts of chloroform is shown in Figure 3-23.

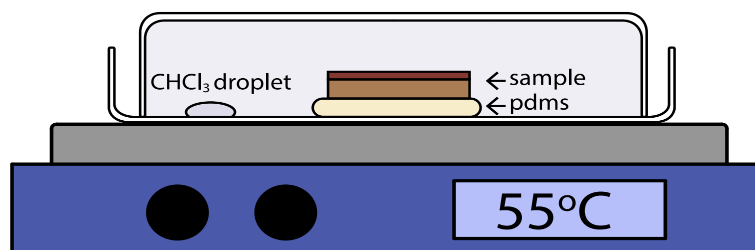

FIGURE 3-21: Illustration of the chloroform vapor procedure for smoothing the polymeric ablated structures.

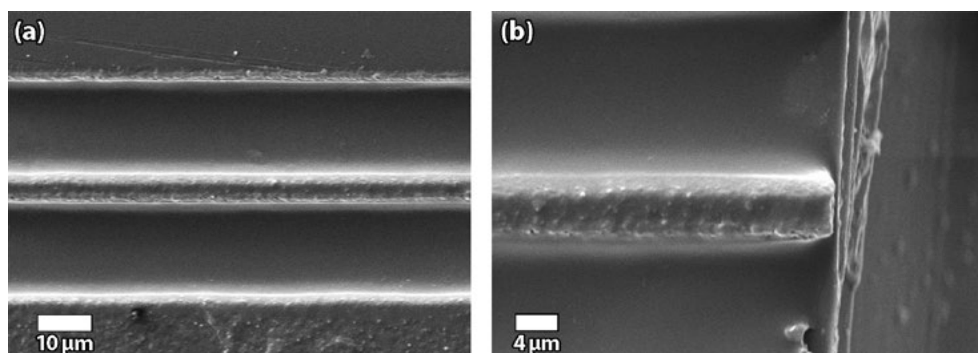

FIGURE 3-22: (a) SEM micrograph of the QD-doped PMMA/P3FEMA waveguide on silicon fabricated after the solvent vapor smoothing treatment, **(b)** the edge of the waveguide.

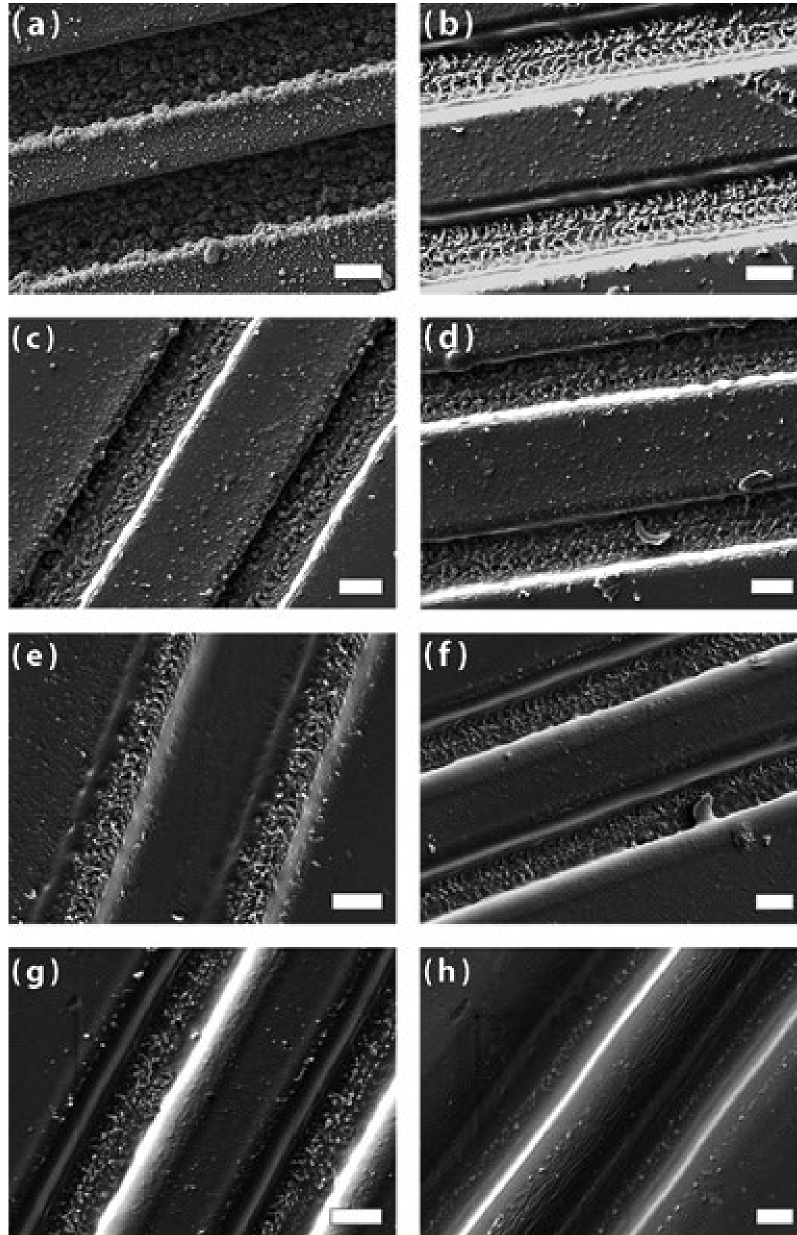

FIGURE 3-23: Processing of laser ablated polymeric waveguides with chloroform vapors for smoothing: **(a)** unprocessed waveguide, **(b)** processed at 2.1×10^{-3} mol/l of chloroform vapor concentration, **(c)** 4.2×10^{-3} mol/l, (d) 6.3×10^{-3} mol/l, **(e)** 8.4×10^{-3} mol/l, **(f)** 1.05×10^{-2} mol/l, **(g)** 1.58×10^{-2} mol/l and, **(h)** 2.11×10^{-2} mol/l. In all instances the scale bar corresponds to 10 μm.

3.8 Excimer laser microfabrication of micro-ring resonators

Polymer micro-ring resonators have been designed and fabricated on fused silica substrates. The low refractive index of fused silica (n_{FS}=1.456)[88] makes it ideal for using in waveguiding applications while its high ablating threshold, more than 10 times higher than that of polymers allows for the fabrication of such structures using the direct laser ablation method.

As shown in the simulation of Figure 3-24, waveguiding is feasible for ridge waveguide of dimension of 3×2 μm. Polystyrene has been chosen as the micro-ring waveguide material due to the higher than the acrylic polymers refractive index. The design of micro-ring resonators are determined by a) the coupling coefficient, b) the high free spectral range (FSR) and, c) the radius. FSR, defined as the spectral distance of successive resonance peaks, is given by the formula:[145–147]

$$FSR = \frac{\lambda^2}{n_{eff} L} = \frac{\lambda^2}{n_{eff} 2\pi R} \qquad (3.4)$$

λ being the working wavelength, n_{eff} the effective index of the structures, L the circumference and R the micro-ring radius. It is apparent from this formula that large FSRs are achieved for devices of lower refractive index, where the optical field is confined less tightly, and also for structures of small radius. This requirement however of small R opposes the requirement to keep the bending (or radiation) losses as low as possible since the exponential attenuation coefficient α has a strong dependence on the bending radius R of the resonator:[148]

$$\alpha = C_1 \exp(-C_2 R) \qquad (3.5)$$

In this formula C_1 and C_2 are constants that depend on the dimensions of the waveguide

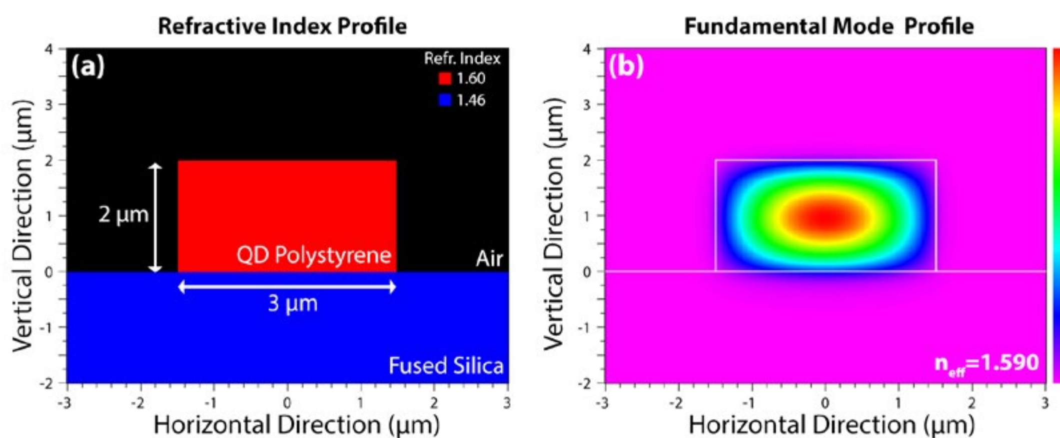

FIGURE 3-24: Theoretical modeling of a QD/polystyrene ridge waveguide on fused silica substrate: (a) Transverse profile of the refractive index, and (b) the computed profile of the fundamental mode using the BPM.

and the shape of the optical mode. BPM simulations provide the design guidelines for the fabrication of polymer micro-ring resonators in terms of the FSR and the existence or no of a viable waveguiding mode inside the resonator for a given geometry as shown in Figure 3-25.

For the fabrication of polymer micro-rings, the fabrication protocol described in paragraph 3.4 has been exploited using ArF excimer laser radiation at λ=193 nm. Polystyrene toluene solution containing 0.15 g/ml of polymer, also incorporating 2.5 μM of CdSe/ZnS QDs, was spin-coated on cleaned fused silica substrates of dimensions 1.5×1.5 cm and baked in an over at 100°C for 10 minutes. The 2 μm (approx.) thick polymer film was stripped from the edge of the substrate using a sharp razor to expose the substrate an area about 2 mm from the edge and allow for the simple fabrication of isolated micro-rings. The structures are fabricated near the strip line using the camera of the microfabrication station for alignment.

The single pulse fluence delivered on the polymer film is of the order of 100 mJ/cm^2 and 20 pulses impinge in each firing point for an accumulative fluence of 2 J/cm^2 enabling the complete stripping of the 2 μm thick polystyrene film without damaging the substrate. Single pulse produce a circular trace on the polystyrene film of radius of about 4 μm and an overlap of about 5 % between successive firing points was used for

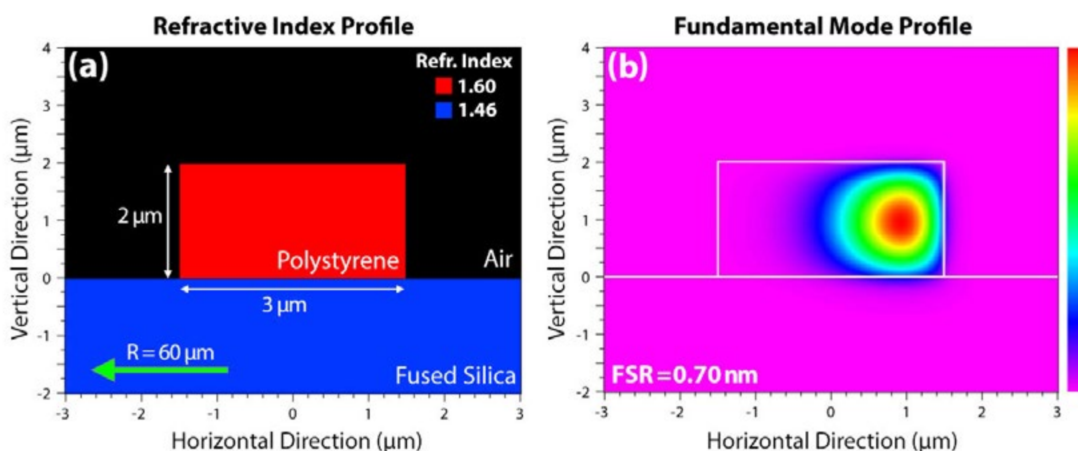

FIGURE 3-25: Theoretical modeling of a polystyrene micro-ring resonator of radius R=60 μm on a fused silica substrate : **(a)** Transverse profile of the refractive index, **(b)** the computed profile of the fundamental mode using the PBM. The green arrow depicts the center of the curvature of the structure.

minimum corrugation of the ablated trace. Concentric circular structures were ablated in the inner and outer area of the micro-ring using the corresponding feature of the excimer laser micromachining station suite to expose the micro-ring structure. To further isolate the structure from the remaining film, a large area around the ring was stripped by laser. The pinhole was removed from the microfabrication station configuration and was replaced by a custom made slit aperture of about 200 μm width. This aperture was then used to mask the laser beam and was projected on to the film. A repetition rate of 200 pps for a total power of 22 mW was used to rapidly strip the film under an air flow to drive the ablated photofragments away from the micro-ring structure and prevent their re-deposition of the structure. Microscope images of the micro-ring before and after their isolation are shown in Figure 3-26, Figure 3-27 and Figure 3-28.

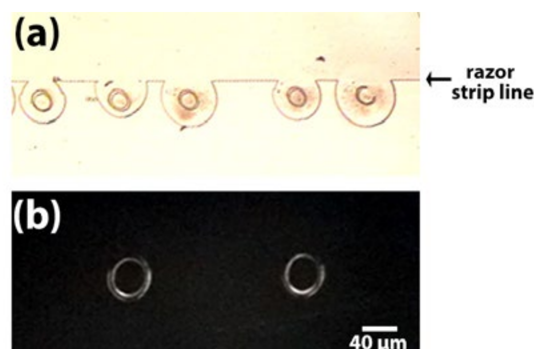

FIGURE 3-26: Microscope images of laser ablated micro-rings: **(a)** bright field images of micro-rings of R=20 μm prior to stripping and, **(b)** dark field image of micro-rings after their complete isolation.

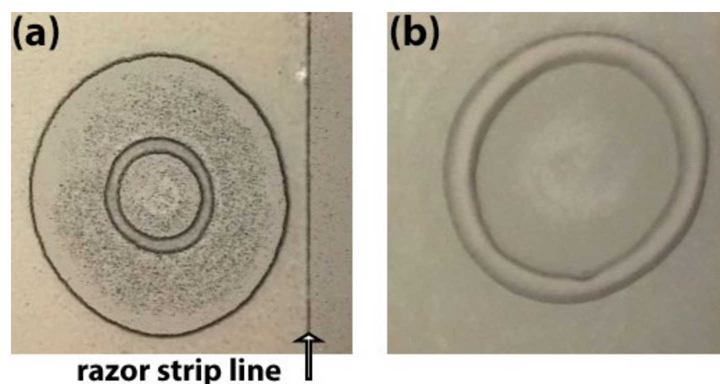

FIGURE 3-27: Microscope close up images of laser ablated polystyrene micro-rings: **(a)** prior to isolation and **(b)** after striping the area around the structure.

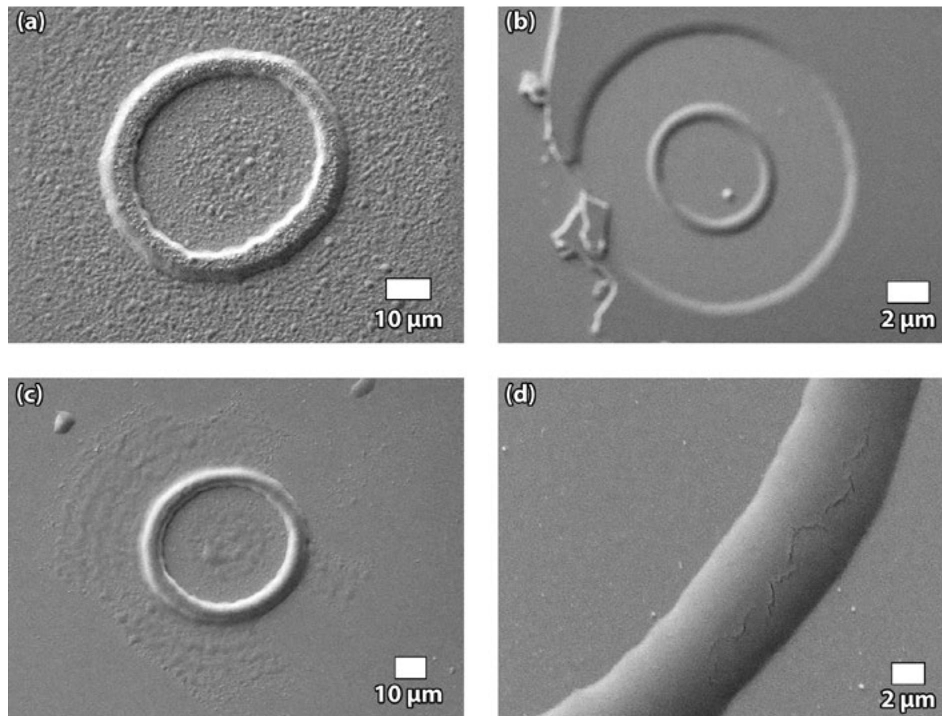

FIGURE 3-28: SEM micrographs of laser ablated micro-rings fabricated on QD/polystyrene films: **(a)** a micro-ring prior to solvent vapor smoothing, **(b, c)** micro-ring structures after smoothing and, **(d)** detail of a micro-ring structure (the observed cracks were induced by the electron beam of the SEM).

The SEM micrograph of Figure 3-29 summarizes all fabrication consideration of polymer micro-ring structures using excimer laser microfabrication. The lack of an air stream and the use of high power pulses instead of a burst of multiple pulses of lower energy may lead to debris distribution on the structure which could not be removed by air blowing cleaning after fabrication of by solvent vapor smoothing. Furthermore, high energy pulses may exhibit a peak above the ablating threshold of the substrate and lead to substrate damage. Such sub-micron ablated holes on the fused silica substrate are also demonstrated in Figure 3-29. Finally, large distance between laser shoot points may lead to corrugation of the side walls of the structure. In is proposed here that this feature could be exploited for the fabrication of complex photonic structures in the concept of combination of micro-ring and lateral DFB resonators for the fabrication of coupled resonator device. This formulates the scope of future work.

The laser microfabricated micro-ring resonators can be coupled to an external waveguide such as a tapered optical fiber by use of a micropositioning system.[149]

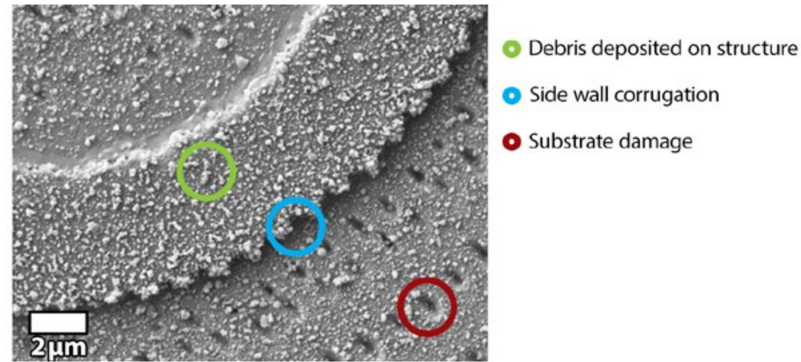

FIGURE 3-29: SEM micrograph of an ablated polymer micro-ring resonator outlining the main fabrication issues: **(a)** deposition of ablated fragments back on to the structure, **(b)** corrugation of the side walls of the structure due to an insufficiently small step and **(c)** substrate damage due to high laser pulse energy.

Plastic optical fibers (POF) have been tapered by immersion in chloroform after etching the cladding layer using acetone, while common glass fibers have been etched using hydrofluoric acid. Examples of both structures are shown in Figure 3-30. Although both tapers led to sufficient shrinkage of the diameter of the tip of the waveguide, the bad quality and the non-adiabatic character of the tapering region induce severe loses and low performance of the waveguides.[150]

High quality CO_2 laser tapered glass fibers have been provided by Prof. Michalis Zervas, ORC-University of Southampton, UK. The minimum diameter of these tapers is 6 μm and 8 μm, close to the width of the fabricated QD/polystyrene micro-rings. Proximity of the tip of the fiber was achieved under a stereo microscope by fixing the fiber into an appropriate mount on a micropositioning system. A 50 mW laser emitting at λ_{exc}=405 nm was focused on the structure for an intensity of about 2.5 W/cm^2 while a LPF filter was used to isolate the luminescence of the QD from the excitation irradiation.

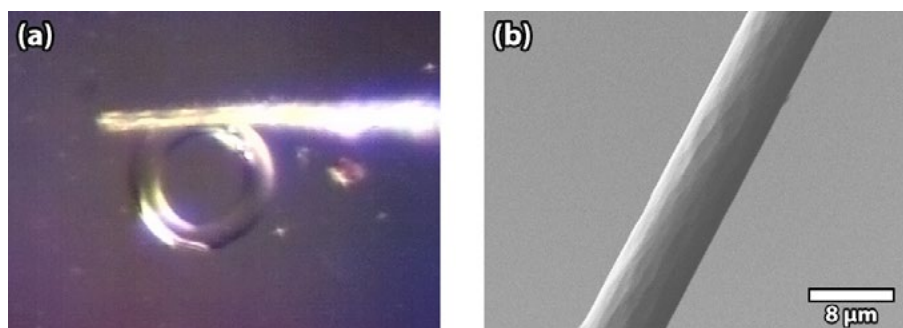

FIGURE 3-30: (a) A solvent tapered POF in proximity with a QD/polystyrene micro-ring and, **(b)** SEM micrograph of a glass optical fiber etched with hydrofluoric acid.

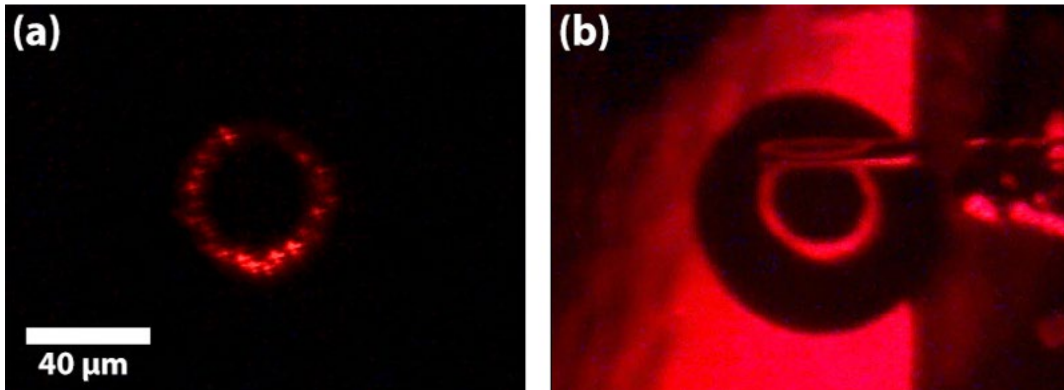

FIGURE 3-31: (a) Microscope image of a micro-ring structure of R=20 μm upon excitation at 405 nm and, **(b)** a micro-ring in proximity with a tapered glass fiber.

3.9 Waveguide fabrication using the soft lithography method and materials of the ORMOCER family

OrmoClad and OrmoCore materials are designed for the fast, simple and low cost replication of photonic structures using the soft lithography technique. Soft lithography, in contrast to the tradition photolithographic techniques, does not utilize mask or direct laser writing to expose a photosensitive resist exposed to UV radiation but rather prepatterned elastomeric stamps and molds for replication of the micro or nanostructure.[151–159] The term "*soft*" is attributed to the typical use of elastomeric materials for the fabrication of the stamp, most notably polydimethylsiloxane (PDMS). Soft lithographic techniques employing PDMS stamps have been used for the replication of various patterns in the micro and nanometer scales while the lowest resolution to be reported is as small as 15 nm,[160] smaller than that of traditional photolithographic techniques. Besides its low cost and high throughput, soft lithography methods can be applied for a wide range of materials including biomaterials, plastic electronics and other sensitive materials including sensing materials. Other advantages of soft lithography include the suitability for patterning non-planar surfaces and the ability for combination with other pattern-transferring methods (e.g. microcontact printing -μCP[155,161,162]).

The fabrication of hybrid polymer waveguides using soft lithography route starts with a silicon stamp patterned with channels that will subsequently define the waveguides.¶¶ The stamp is fabricated using the standard electron beam lithography technique. The silicon substrate is first covered with an appropriate electron-sensitive resin by spin-coating. The structure is then defined by an electron beam altering the solubility of the resin layer followed by immersion in a developer to remove the areas that were exposed to the e-beam (or the areas that were not exposure in the case of negative tone resin). The remaining pattern on the resin serves as an etching mask for the subsequent reactive ion etching (RIE) step that defines grooves on the silicon substrate on the not covered by the resin areas. Finally the remaining resin is removed from the substrate.

For the silicon or other material patterned substrate to be used as a stamp with a soft lithography or nanoimprint lithography (NIL) technique, it is crucial that the stamp can be detached from the layer to be patterned safely (peel off) without damaging the defined structure. For this purpose a treatment of the stamp surface is used to provide antisticking properties. The chemical compound (tridecafluoro -1, 1, 2, 2-tetrahydroctyl) trichlorosilane (F_{13}-TCS), a chlorosilane with a long partially fluorinated alkyl chain shown schematically in Figure 3-32 is used to functionalize the surface of the silicon. A simple interpretation of the functionalization mechanism is that the chlorosilane groups react spontaneously

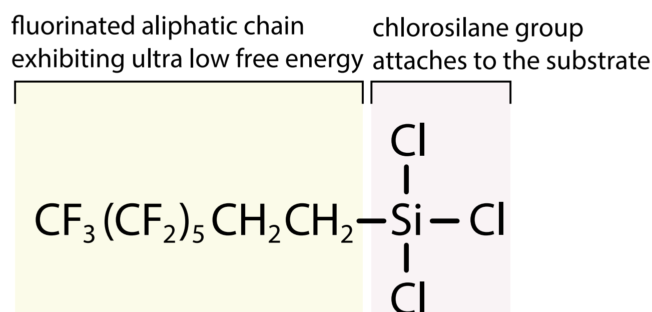

FIGURE 3-32: The (tridecafluoro -1, 1, 2, 2-tetrahydroctyl) trichlorosilane molecule structural form (abbreviation F_{13}-TCS).

¶¶ Dr Nikos Kehagias from ICN, Barcelona, Spain is acknowledged for providing the silicon stamps.

with hydroxylated silicon or silicon dioxide surfaces and bond covalently leaving the CF_3 groups at the interface exposed, which have among the lowest free energy of the order of 6 dyn/cm.[163–166] The process is similar to the solvent smoothing technique previously discussed and is demonstrated in Figure 3-21. The silicon stamp is placed in a small chamber made of two petri dishes along with a small drop of chlorosilane (20 μl). The chamber is heated at 250°C, well beyond the chlorosilane boiling point of 192°C. The chlorosilane vapors allows molecules to bond to the silicon substrate to form a monolayer and render it highly hydrophobic.

The silicon pattern is transferred to a soft stamp (hence the name of soft lithography) made of polydimethylsiloxane (PDMS). The most common form of PDMS, Dow Corning™ Sylgard® 184, optimized for the soft lithography technique is used here. The material is delivered in a highly viscosity form which solidifies upon mixing with a curing agent. Cured PDMS is an elastomeric, hydrophobic material of high stability. Although it is relatively soft (shear elastic modulus[167] $G \approx 250$ kPa), it tends to maintain any structure pattern on its surface even when deformed. Apart from its excellent mechanical properties, PDMS exhibits high transmittance in the UV region above 340 nm, thus it is used in combination with UV curable resins for micro and nano-fabrication. The common proportion of PDMS/curing agent is a 10:1 weight ratio mixing followed by intense stirring. The mixture is placed in vacuum for several minutes to remove any bubbles formed during stirring (debubbling), then poured on the patterned silicon substrate and left for a few minutes to settle and effectively fill the grooves. After a 25 minute curing steps at 125°C in an oven, the stamp is left to cool at room temperature and can then be easily detached from the silicon substrate (peel off) with tweezers. It is also possible to cut the stamp to any size with a razor. An illustration of the silicon master used for the production of waveguides and the PDMS stamp is shown in Figure 3-33.

The OrmoClad/OrmoCore hybrid materials are delivered in liquid form of high viscosity and solidify upon curing with UV radiation. All these materials are

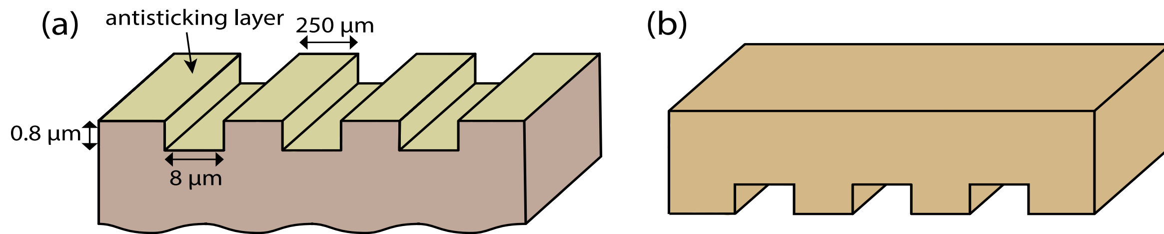

FIGURE 3-33: (a) Depiction of the silicon stamp containing grooves that define the waveguide to be made. The stamp is covered with an antisticking layer. **(b)** PDMS stamp after molding and detaching from the silicon substrate is a negative replica of the initial structure. The figure is not in scale.

sensitive to broadband UV radiation and exhibit their maximum sensitivity near the i-line (365 nm) emission of the mercury vapor lamp. Processing prior to curing such as spin-coating is performed in a light-tight fume hood. High intensity commercially available red LEDs serve as a safety light to allow vision without affecting the materials. For temperature processing outside the fume hood such as oven baking and vacuum evaporation the samples are placed in an opaque container.

An in-house, custom-made configuration has been constructed for UV curing of the OrmoCore/OrmoClad hybrid polymers. This set-up comprises an Osram Supratec HTC 400-241 mercury vapors lamp that delivers 82W in the UVA window (315-400 nm) and 12W in the UVB window (280-315 nm) after 30 minutes warming. The distance from the lamp to the position of the sample is about 10 cm thus the UV radiation on the sample is calculated to be about 75 mW/cm^2 without accounting for the losses of the quartz window used to seal the small chamber. Both UV lamp setup and quartz sealed chamber are shown in Figure 3-34(a) and (b) respectively. The UV lamp set-up also includes an exhaust fan to cool the lamp (not shown in for simplicity).

The curing process of the OrmoClad/OrmoCore/OrmoStamp materials requires an oxygen-free atmosphere to prevent partial oxygen quenching of the polymerization process. This leads to the formation of a viscous liquid layer (inhibition layer), on top of the cured film that consists of soft, non-curable material. Although

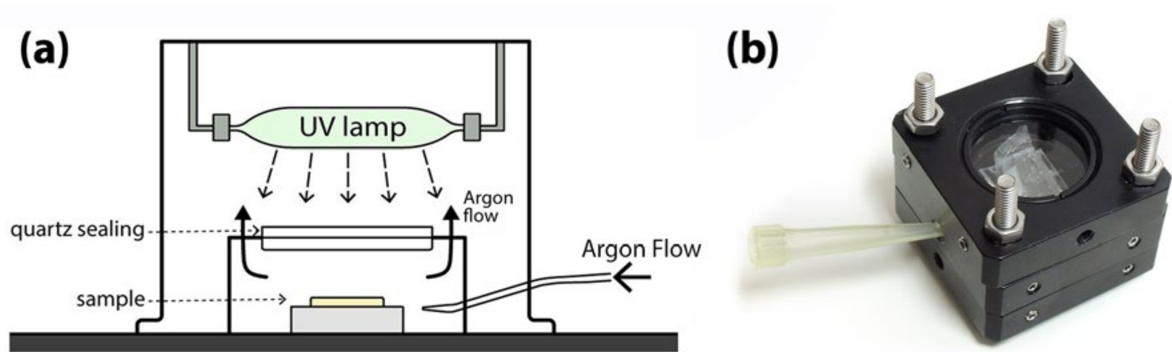

FIGURE 3-34: (a) Schematic of the UV curing setup, **(b)** the quartz sealed chamber used for the establishment of oxygen free atmosphere during curing under an argon flow.

it is possible to remove it using a solvent that does not affect the underlying cured material (developer), this inhibition layer needs to be prevented to fully control the fabrication process. For this reason the sample were placed in a small chamber shown Figure 3-34(b) which is sealed except for an input inlet that allows argon flow and a 1” diameter quartz flat that fits loosely on the top of the chamber. The argon flow from the inlet to the optical window edges is depicted in Figure 3-34 (a). The quartz flat exhibits high transmission beyond 315 nm of the lamp UV radiation while partially blocking the IR radiation. The latter characteristic is beneficial to the curing process as it reduces the heat delivered to the sample under processing that could lead to delamination effects.

For the transfer of the PDMS stamp pattern to OrmoClad, silicon wafers of about 2×2 cm were thoroughly cleaned with acetone and isopropanol and processed with acetic acid for at least 3 hours. Acetic acid acts as a gentle etching factor and enhances the adhesion of OrmoClad to silicon.[168] The substrates were then cleaned with piranha solution (3:1 sulfuric acid and oxygen peroxided), cleaned with purified water and dried at 200°C for 2 hours. Substrate preparation were completed by spin-coating Ti-Prime adhesion promoter at 3000 rpms for 20 s followed by a 10 minute bake at 130°C. A drop of OrmoClad was placed on each silicon substrate followed by the placement of the PDMS, taking care to avoid formation of air bubbles. A 10 minutes pre-exposure heat treatment at 80°C, although optional

for these solvent-free materials, enhance the homogeneity of the simple and the adhesion to the substrate.[168] The samples were UV-cured under an argon flow for 60 s to solidify OrmoClad followed by a 10 minutes post exposure bake at 130°C to further enhance the adhesion to the substrate. The PDMS stamp were then removed and the OrmoClad layers were dipped into a 50-50 solution of PGMEA and isopropanol to remove any traces of uncured material and dried by a nitrogen flow. Finally, a hardbake step at 130°C for 3 hours was used in order to improve the thermal and environmental stability of the material. The fabrication up to this point resulted in a thick (<5 μm) layer of OrmoClad with patterned surface shown in the SEM micrographs of Figure 3-35 and Figure 3-36.

A main fabrication challenge faced while processing such hybrid materials was dewetting effects during casting of additional layers due to their highly hydrophobic nature. Oxygen plasma treatment is proposed by the supplier to process the surface of

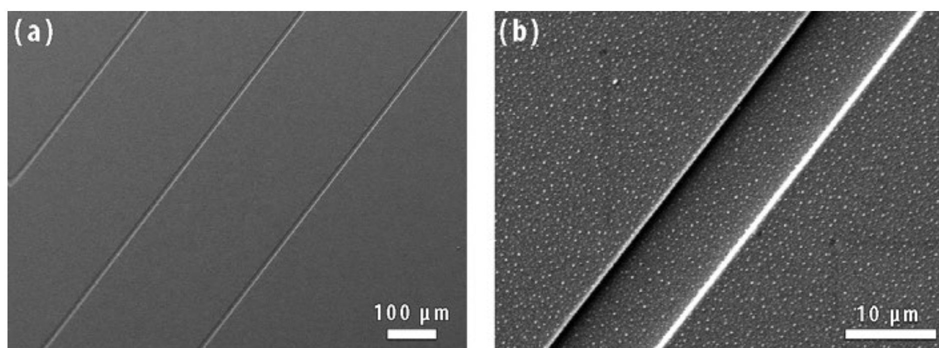

FIGURE 3-35: (a) SEM micrograph of the waveguide grooves on OrmoClad, **(b)** close up of the structure.

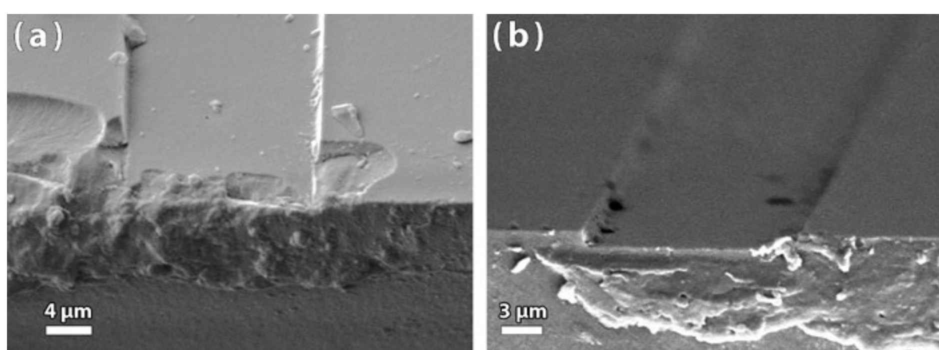

FIGURE 3-36: (a-b) SEM micrograph of a cross section of an OrmoClad groove prior to filling with OrmoCore.

these materials and render them less hydrophobic. Here an alternative wet chemistry route was followed by processing the OrmoClad cast substrates with piranha solution for 30 minutes. The samples were then thoroughly cleaned with DI water and dried in oven at 100°C for 15 minutes. The change of the wetting angle of the OrmoClad surface prior and after piranha treatment is demonstrated in Figure 3-37. Both oxygen plasma and piranha treatments result in the removal of the exposed hydrophobic alkyl groups from the surface of the material and their replacement by hydrophilic silanols (Si-OH) groups.[169]

Following the fabrication of the cladding layer, the top layers of the waveguides were cast on top of the thick patterned OrmoClad. Spin-coating of less than 5 μm thick OrmoCore films is feasible by reducing the viscosity of the initial material. PGMEA is the solvent used in a 1:1 weight ratio for the production of about 1.7 μm thick films. In order to completely remove the solvent from the film prior to exposure, the samples are placed in vacuum for at least 2 hours. This process has been found to yield films of better quality than the thermal evaporation of the solvent on a hot plate or inside an oven at 80°C proposed by the supplier as it prevents dewetting. A summary of all processing steps for the implementation of ORMOCER waveguides is shown in Table 3-2. Figure 3-38 shows a cleaved cross-section of the reverse rib waveguide while in Figure 3-39 the profiles of an OrmoClad groove and that of the final structure are demonstrated. The very small valley of the waveguide over the OrmoClad channel confirms the thorough fill of the groove by OrmoCore.

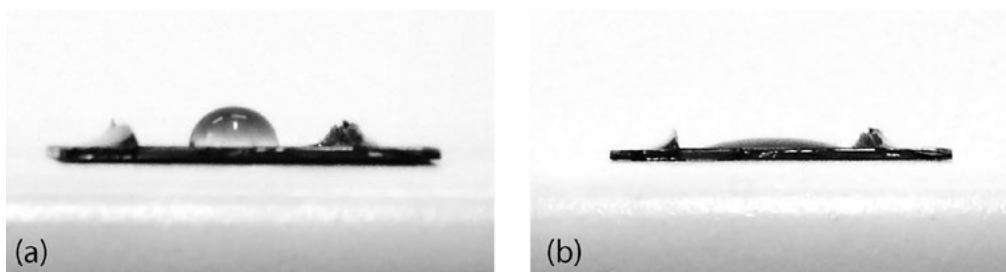

Figure 3-37: (a) A water droplet on the cured OrmoClad surface after curing, inhibition layer removal and hard baking, **(b)** a water droplet on the same surface after treatment with piranha solution for 20 min and drying.

Figure 3-40 illustrates waveguiding at λ=633nm from a reverse rib structure and the waveguiding modes as recorded using a camera. Finally Figure 3-41 shows the computed fundamental transverse mode profile.

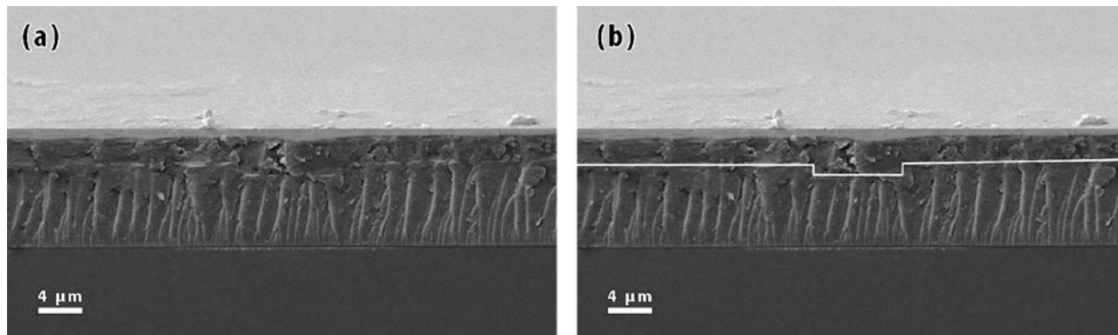

FIGURE 3-38: (a) SEM micrograph of a cross section of a reverse ridge waveguide of OrmoCore/ OrmoClad materials, **(b)** the same micrograph with white lines outlining the edges of the waveguide structure.

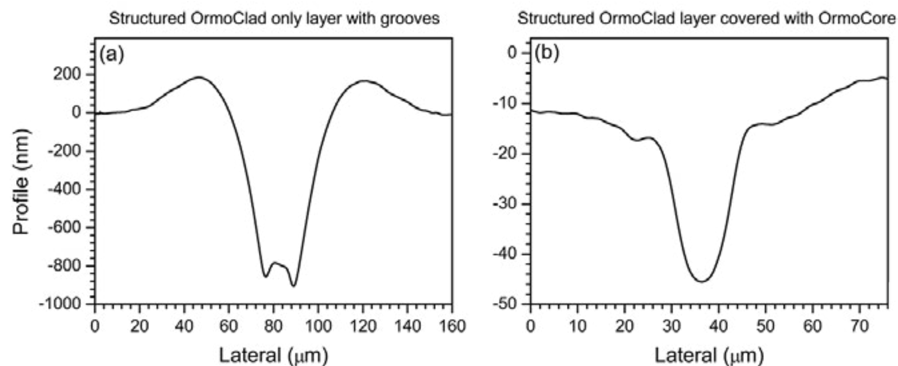

FIGURE 3-39: (a) The profile of an OrmoClad groove (KLA-Tencor Alpha Step), **(b)** the profile of a fully fabricated waveguide with an OrmoCore layer on top of the initial OrmoClad groove (Bruker DektakXT).

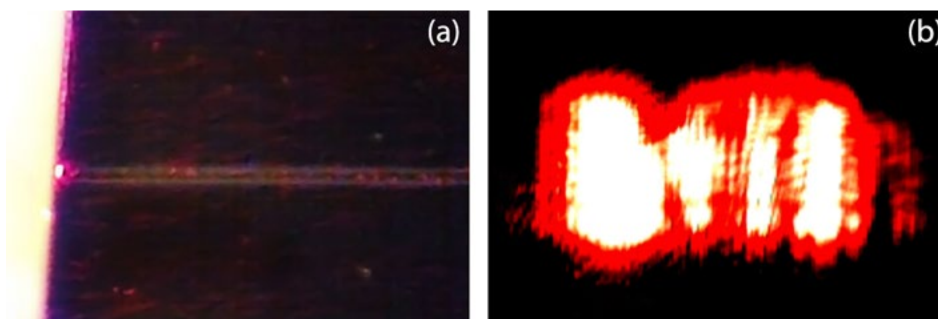

FIGURE 3-40: (a) top view of the waveguiding edge, **(b)** the waveguide modes as projected with a 4X microscope objective.

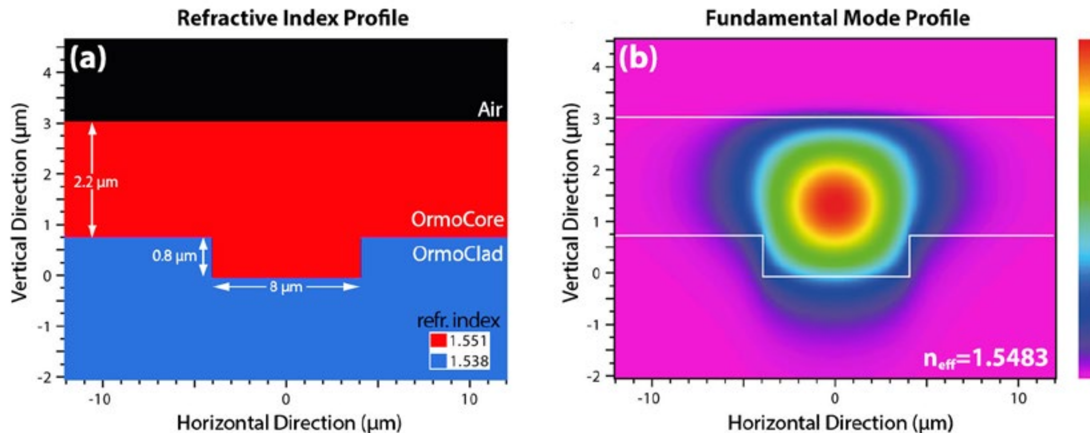

FIGURE 3-41: **(a)** The transverse refractive index profile of the OrmoCore/OrmoClad reverse rib waveguide, **(b)** the fundamental mode of the waveguide as computed using the BPM method. The white lines outline the waveguide edges.

3.10 Laser cleaving of OrmoCore/OrmoClad reverse rib waveguides

The quality of the end facet of a waveguide defines the coupling loses and is a key parameter in the fabrication procedure. As demonstrated earlier, the choice of silicon as the substrate enables the easy and effective cleaving of polymer waveguides (Figure 3-19 and Figure 3-22). Application of such a process in the case of soft lithographed OrmoClad based structures suffers from poor repeatability due to the large thickness of the hybrid materials layers which varies between 5 and 30 µm. Moreover, hybrid materials exhibits a partially elastomeric character due to their dense, entangled organic-inorganic network. In combination to the non-ideal adhesion on the silicon substrate, cleaving of hybrid materials waveguides is challenging process as shown in Figure 2-42.

To accommodate for such issues, an excimer laser cleaving procedure has been employed using the ArF laser excimer microfabrication station. A custom made slit with an opening of 200 µm was used to shape the beam instead of the small ablated pinhole. This slit opening was projected on the sample perpendicular to the waveguide for the ablation of a large orthogonal area of about 15×200 µm at a pulse energy of about 500 µJ. By moving the sample along the waveguide axis, successful cleaving was performed, demonstrated in Figure 3-43(a and b). A severe debris problem shown in in Figure 3-43(c).

TABLE 3-2: Summary of the successive process steps for the OrmoClad/OrmoCore waveguide fabrication.

Si substrate preparation		
Cutting of Si substrate		
Acetic acid surface treatment	50% with DI	3 h
Spin-coating with acetone and isopropanol	6000 rpm	20 sec each
Oven dry	200°C	overnight
OrmoClad layer fabrication		
Drop cast on substrate		
Stamp positioning & mild pressure to remove air bubbles		
Pre exposure baking / stamp relaxation	80°C	10 min
Exposure	3 J/cm^2	60 sec
Post exposure baking	130°C	10 min
Stamp removal		
Development and N_2 dry		30 sec
Hardbake	130°C	3 h
Piranha treatment	(3:1)@RT	30 min
Thorough cleaning (DI water, acetone, isopropanol)		
OrmoCore layer fabrication		
Spin-coating	3000 rpm	30 sec
Vacuum dry		2 h
Exposure	1 J/cm^2	20 sec
Post exposure bake	100°C	10 min
Development and N_2 dry		30 sec
Hardbake	110°C	3 h

Debris from the hybrid material tend to adhere to the ablated edge in a latch geometry at low pulse energy, a problem also demonstrated in Figure 3-43(c). Such debris cannot be removed using a solvent vapors smoothing procedure since due to their dense organic-inorganic network, cured hybrid material are stable to common solvents.

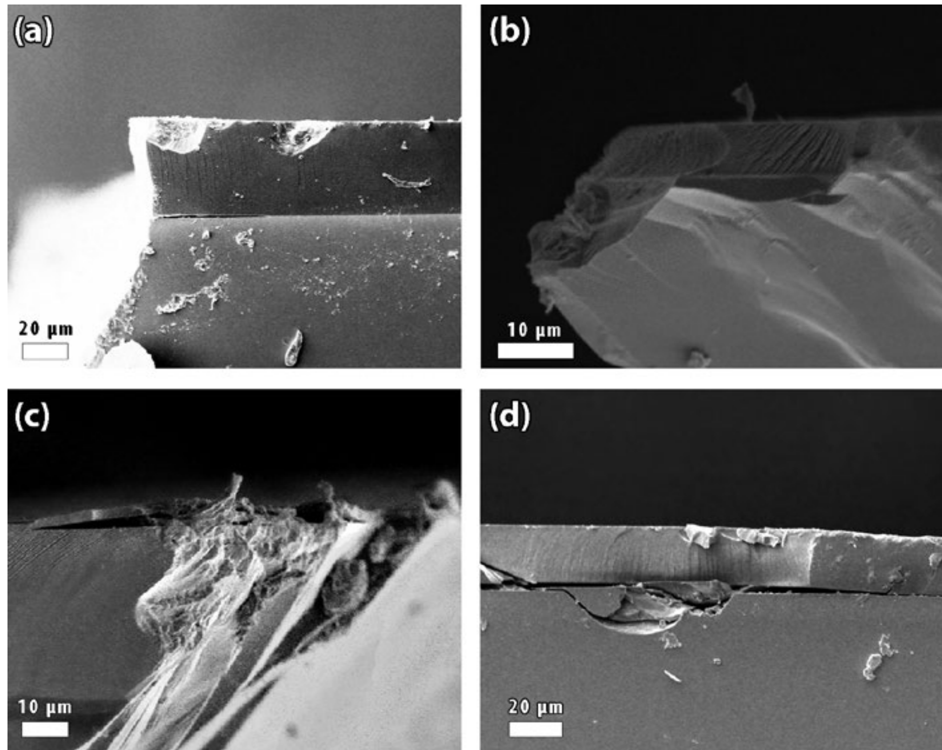

FIGURE 3-42: SEM micrographs of common cleaving problems of waveguides fabricated on silicon substrates: **(a-b)** the deposited film is cleaved at an angle relative to the cleaving facet, **(c)** delamination at the edge region, and **(d)** substrate damage due to the cleaving process.

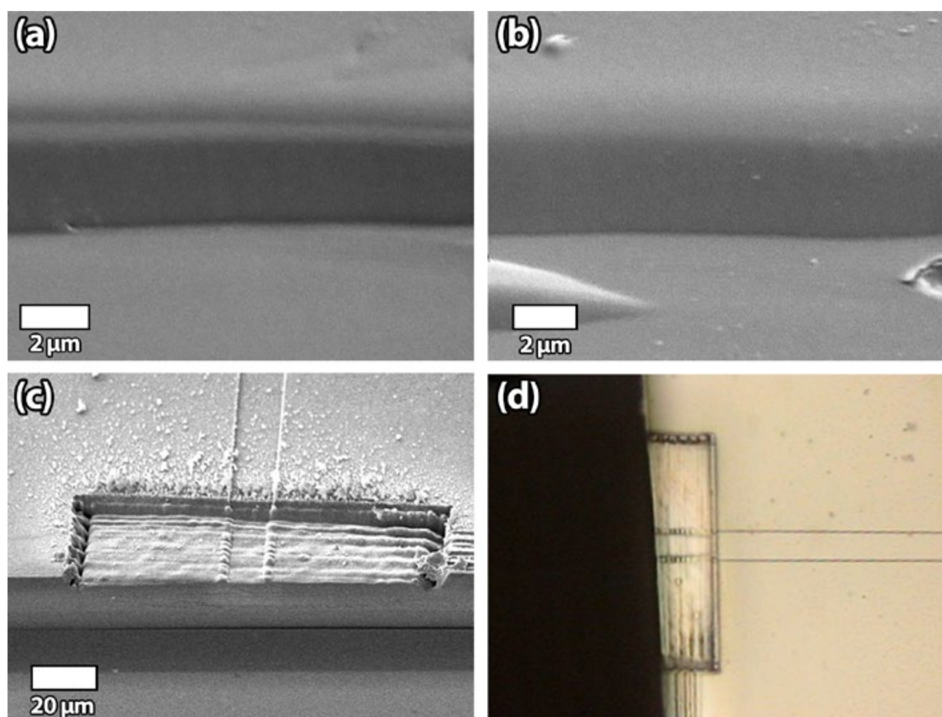

FIGURE 3-43: (a-c) SEM micrographs and, **(d)** microscope image of OrmoCore/OrmoClad reverse rib waveguides laser cleaving.

Laser ablation cleaving also provides a route for the correction of the structure misalignment during the soft lithography procedure as shown in Figure 3-43. In this microscope image a waveguide fabricated with a small angle in respect to the silicon cut edges is shown. The misalignment was corrected by laser cleaving for a sharp edge perpendicular to the waveguide.

Interesting results were observed during laser cleaving of thick OrmoClad layers are shown in the SEM micrographs in Figure 3-44. Upon irradiation with ArF excimer laser, microcones of various diameters are formed with angle of about 60°. Ablated diffraction patterns with a period resembling that of the ArF excimer laser (λ=193nm) observed in the base of some cones shown in Figure 3-44(c) indicate the diffraction of the laser beam from centers on the top of the cones. Indeed, a close examination of the microcones reveals crystals-like particulates on the vertex of every each cone, highlighted by red circles in Figure 3-44(d). Such formulations have

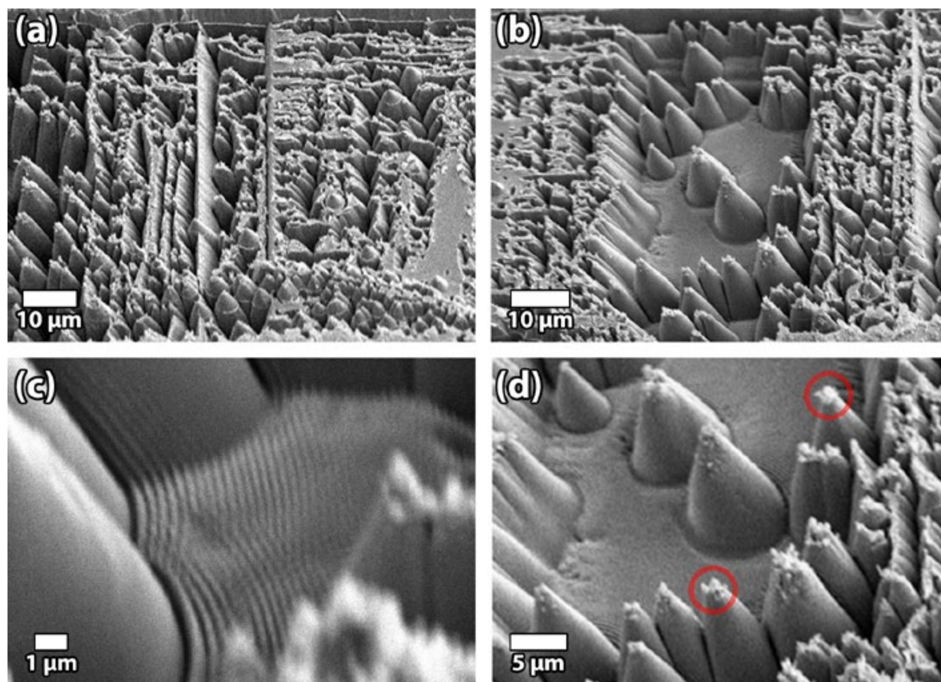

FIGURE 3-44: SEM micrographs of patterned surface of OrmoClad by 193 nm ArF excimer laser radiation: **(a,b)** cone formation, **(c)** ablated fringes due to diffraction of the laser radiation by the cones and, **(d)** crystal-like structures on the top of every each cone (red circles) suggest the formation of inorganic particulates that diffract the laser radiation.

been reported in the literature during the ablation of polyvinyl chloride films and their formation has been attributed to the presence of impurities inside the polymer.[170] It is suggested here that due to the hybrid nature of OrmoClad, the inorganic part of the material responds differently to the excimer laser radiation than the organic part. In a specific fluence range of about 5 mJ/cm^2 the organic part is photo-decomposed while the inorganic part formulates the observed particulates which diffract the laser beam and lead to the formation of the microcones. Further studies using EDX mapping is expected to elucidate the exact nature of this observation

3.11 Implementation of QD/polymer reverse rib waveguides

The high refractive index of polystyrene (n_{PS}=1.6), further increased by the presence of QDs, allows the implementation of reverse rib waveguides on OrmoClad ($n_{OrmoClad}$=1.538), as predicted by BPM simulations shown in Figure 3-45. Indeed such structures have been fabricated and are demonstrated in Figure 3-46.

This implementation however suffers from the poor planarization of the QD/polystyrene film which tend to follow the groove geometry as shown in Figure 3-46d(b). This microscopy image of such a waveguide upon excitation (λ_{exc}=405 nm) exhibits clear waveguiding from the slab structure but not optical confinement the reverse rib waveguide as predicted in Figure 3-45. A close examination of the geometry of the films reveals the non-planar upper surface of the structure. Random structures however are found to yield the desired geometry and rib waveguiding such as the waveguide shown in Figure 3-45(a) and (c).

3.12 Soft lithographic replication of complex photonic structures of QD/polymer nanocomposites

The soft lithographic technique has been employed for the fabrication of polymer and QD-doped polymer photonic structures. The use of soft PDMS stamps for the replication of non-curable materials, either by UV radiation or thermal treatment, is

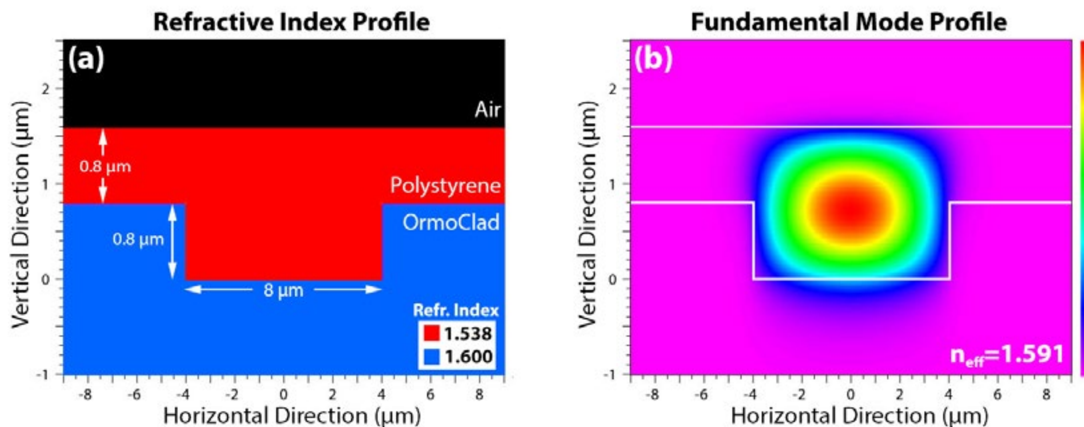

FIGURE 3-45: (a) The transverse refractive index profile of the QD-Polystyrene/OrmoClad reverse rib waveguide, **(b)** the fundamental mode of the waveguide as computed using the BPM method.

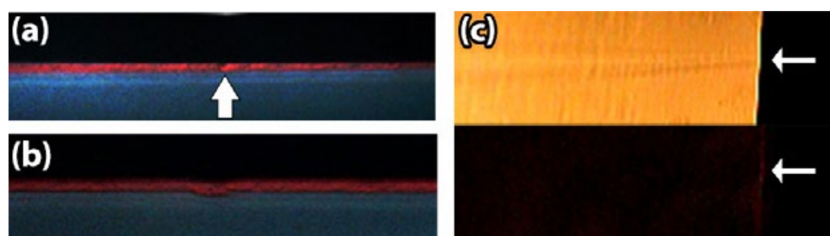

FIGURE 3-46: (a) Microscope image of the edge of a 2 μM QD-doped polystyrene reverse rib waveguide on OrmoClad where waveguiding can be observed (excitation at 405 nm), **(b)** a waveguide where the geometry does not favor waveguiding and **(c)** top view of the waveguiding structure. An LPF has been used to isolate the QD luminescence from the excitation radiation.

not trivial since it requires the deformation of the polymer film followed by the peel off of the stamp without damaging the patterned surface. A simple yet effective protocol using a modification of the Solvent-Assisted Micromolding (SAMIM)[155,159,161,171] soft lithography technique is demonstrated here. In the SAMIM method the stamp is applied under pressure on a spin-coated film which has been softened by wetting it with a suitable solvent. The softening process and the pressure forces the stamp to penetrate the film and pattern it while the solvent evaporated through the PDMS stamp, a procedure feasible due to the solvent and gas permeability properties of PDMS[159,172–174] (PDMS has a gas permeability coefficient higher than other polymers and the highest recorded for N_2 and O_2[159]). After some time the films re-harden and the stamp can be removed and reused. Due its inherent hydrophobic properties, an antisticking agent treatment is not required for PDMS stamps. A schematic

illustration of the method is shown in Figure 3-47(a). An inherent disadvantage of many fabrication methods of the NIL/soft lithography family, the formation of an inhibition layer, is also shown in Figure 3-47(b). This layer, usually of some tens of nanometers can be easily removed with oxygen plasma cleaning if required.

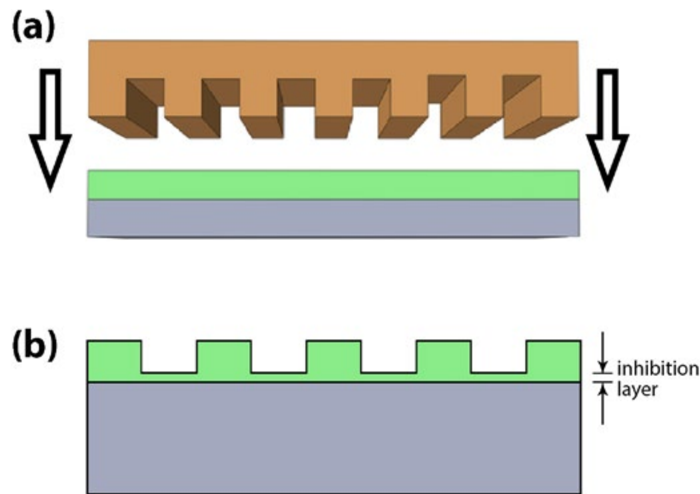

Figure 3-47: (a) Schematic illustration of the solvent-assisted micro molding (SAMIM) method and **(b)** schematic of the diffraction grating cross section depicting the inhibition layer.

The CGH mask design of the “PhASMa” logo discussed in paragraph 3.5 is used her for the demonstration of the modified SAMIM method. The CGH design was transformed into a file format suitable for the electron beam lithography systems (gds file) using the klayout software*** published under GNU public license. We chose a 1×1 μm square pixel and a 20×20 replication array of the unit structure for a square structure of total area of 1 cm^2. The master stamp was fabricated by our colleagues in ICN Barcelona, Spain, using a standard EBL/RIE procedure with an engraving depth of 200 nm and processed with the F13-TCS antisticking agent. The pattern from the silicon master was transferred into a PDMS stamp using the standard 10:1 mixing ratio for the curing agent. SEM micrographs of the PDMS stamp are shown in Figure 3-48.

The challenging procedure of transferring the PDMS pattern on a QD-doped polymer film spin-coated on a silicon substrate necessitated the development of

*** www.klayout.de

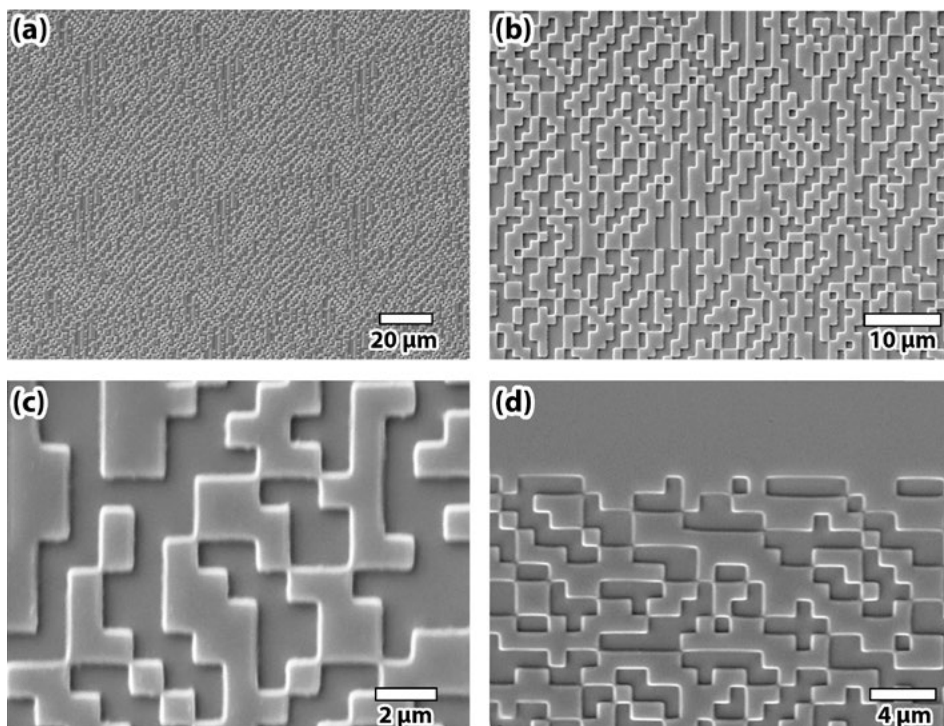

FIGURE 3-48: (a-c) SEM micrographs of the CGH PDMS stamp at different magnifications levels, **(d)** SEM micrograph of the edge of the CGH PDMS stamp.

a modification of the SAMIM fabrication protocol in our lab. This method is based on application of uniform pressure of the PDMS stamp which has been immersed in toluene against the polymer film and is depicted illustratively in Figure 3-49(a). A small, portable, custom made apparatus comprising several optomechanical parts (60 mm cage system from ThorLabs™) shown in Figure 3-49(b) was used for this purpose. The polymer coated substrate and the solvent absorbed PDMS stamp on top of it were placed in the bottom part of the apparatus while an optical flat distributed the pressure evenly. The middle part of the apparatus was used to constrain the movement of the flat into a strict vertical direction and eliminate any circular movement of the flat or the stamp. Finally the upper part was tied on to the cage and a treaded retaining ring was screwed to provide the required pressure.

The geometry of the fabrication procedure indicates the need of a stamp with completely parallel faces. Although the side in contact with the silicon master follows the geometry of the flat silicon substrate, a meniscus is often formed on the

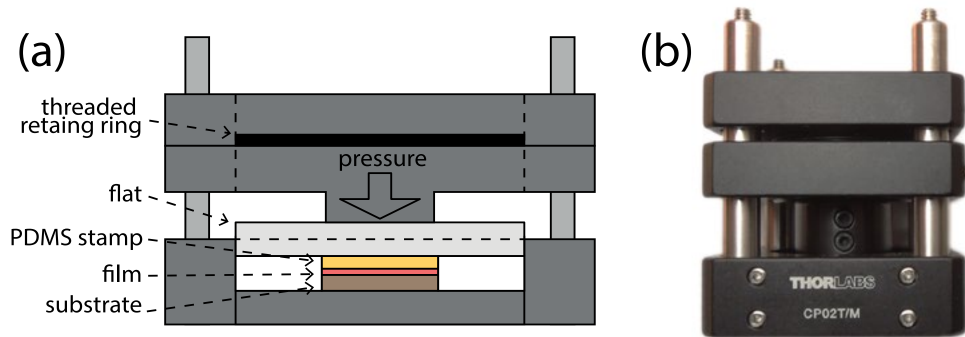

FIGURE 3-49: (a) Sketch of the soft lithography apparatus for the transfer of a PDMS stamp design to a thin film deposited on a hard substrate. **(b)** Photograph of the portable custom made apparatus which can be placed on a hot plate, inside an oven or a vacuum chamber.

top surface. To accommodate this flaw, pouring of the liquid PDMS on the silicon master prior to curing was performed in larger than the silicon master container made from aluminum foil which was totally filled with PDMS. The upper surface then planarized due to gravity upon allowing the mixture to settle. Menisci formed at the walls of the container were cut with a scalpel after peel off.

A crucial factor for the success of the fabrication protocol is the use of a tiny amount of solvent to facilitate the pattern transferring. Instead of softening the film by wetting it with a solvent, toluene was absorbed by the PDMS stamp by immersion. The solvent has no effect on the properties or geometry of the stamp except from a small swelling which barely affects the final structure as shown in the following SEM micrographs. After about 5 minutes the stamp was removed from the solvent and the excess of the solvent was removed with a lint free cleaning tissue. Finally the spin-coated film on silicon substrate and the stamp were placed in the apparatus and pressure was applied (the pressure applied is estimated to be around 100 Pa). The fasten apparatus was now placed in a vacuum chamber for 2 hours for the thoroughly evaporation of the solvent through the PDMS stamp prior to peel off. SEM micrographs of a QD/polystyrene CGH are shown in Figure 3-50. An increase of the dimensions of less than 5 % is attributed to the PDMS swelling due to the immersion to the solvent. Finally, the successful reconstruction of the CGH upon illumination with a small portable green laser is shown in Figure 3-51.

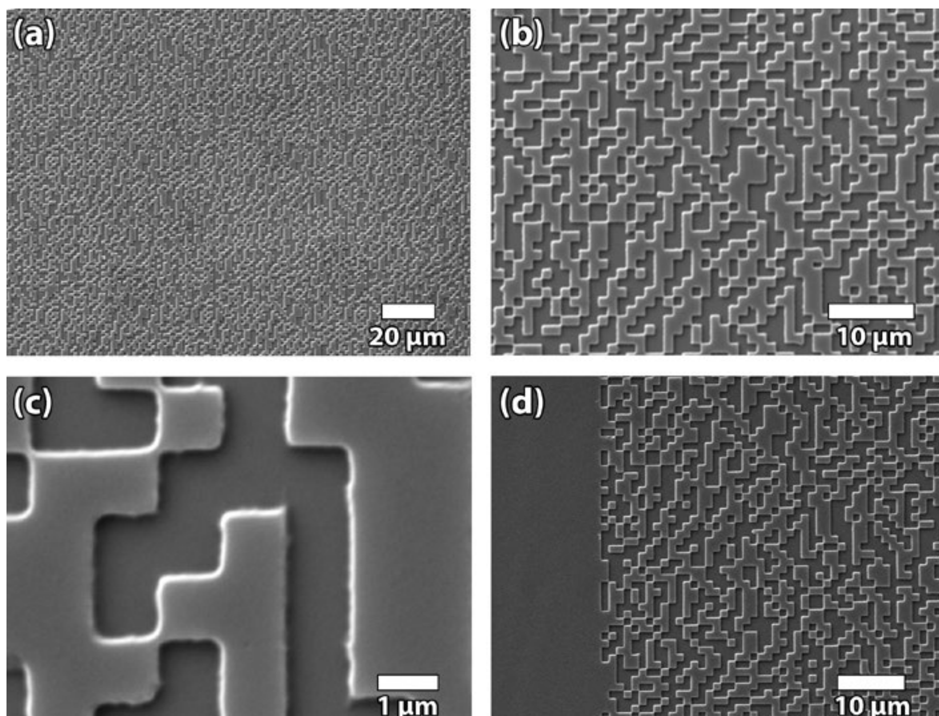

FIGURE 3-50: (a-c) SEM micrographs of the QD-doped polystyrene CGH fabricated using the soft lithography method, **(d)** detail of the edge of the CGH.

FIGURE 3-51: Reconstruction of the QD-doped polystyrene CGH using a 532 nm laser source. The distance between the CGH and the screen is about 10 cm.

Although this fabrication procedure shows good repeatability, detachment of the polymer film is observed if solvent traces remain on the stamp prior to applying the PDMS stamp on the film (except from the solvent absorbed by the stamp), or if the vacuum drying stage is stopped prior to the complete dry of the solvent. Figure 3-52 demonstrates such local (Figure 3-52(a)) and extensive, (Figure 3-52(b)) detachment. It is noted here that the folded film in Figure 3-52 is fully patterned and

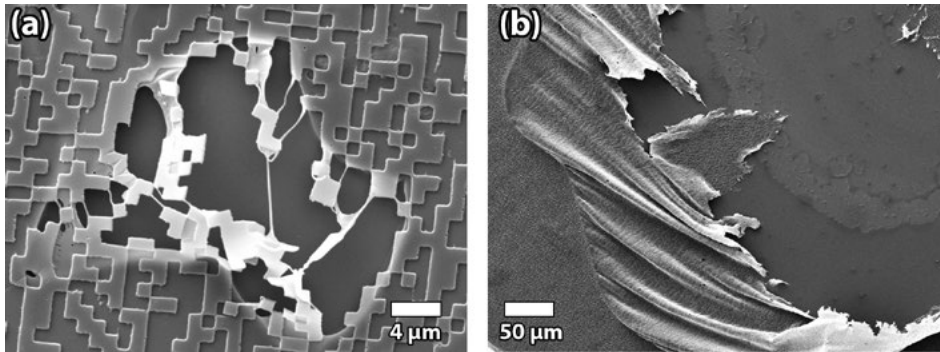

FIGURE 3-52: SEM micrographs of some common problems faced due to the poor adhesion of the polymeric film on the substrate: **(a)** local defect of the film, **(b)** extensive detachment of the patterned film during stamp separation.

the fabricated features remain even on this non-planar topology. Detachment of the polymer film can also be prevented by use of an adhesion promoter.

3.13 Towards the fabrication of low cost QD/polymer and QD/sol-gel Distributed Feedback structures

Low cost fabrication routes of distributed feedback (DFB) photonic structures of QD embedded matrices are explored here towards the implementation of active resonance devices. An illustration of the structure design under consideration is depicted in Figure 3-53. A thick OrmoClad layer deposited on silicon substrate was soft lithographically patterned as discussed in paragraph 3.9 for the implementation of 8×0.8 μm channels. The patterned cladding was then spin-coated with a polymer or QD/polymer nanocomposite for the fabrication of reverse rib active polymer waveguides. Polystyrene was used since it exhibits high refractive index, thus allowing the use of OrmoClad as the cladding layer. A diffraction grating periodic pattern is then transferred to the film using the modified SAMIM method described in paragraph 3.12.

Two periodic structures of period 1 μm and 200 nm has been used for demonstration of the above photonic structure, both exhibiting a duty cycle of 0.5. The diffraction gratings were designed by us and fabricated on silicon substrates by our patterns using the same procedure described in paragraph 3.9. The engraving depth of both structures is 200 nm yielding an aspect ratio (minimum feature over

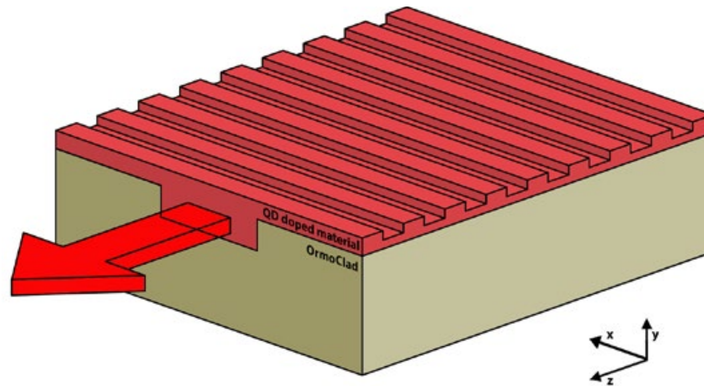

FIGURE 3-53: Conceptual illustration of the DFB structure under consideration.

engraving depth) of 0.4 for the 1 μm structure featuring lines of 500 nm, and 2 for the 200 nm structure featuring 100 nm line. The total dimensions of both diffraction gratings are large enough (3×4 cm and 1.5×1 cm respectively) to cover a big portion of the reverse rib waveguides structures area.

As previously discussed, polystyrene spin-coated films on OrmoClad channels tend to lack planar top surface and follow the geometry of the grooves. The soft lithography step however can accommodate for this issue by distributing the softened (due to the presence of the solvent) polymer film when a high enough pressure is applied. Again the complete remove of any residue solvent from the PDMS stamp prior to the soft lithography step was found to be a crucial factor for the fabrication procedure. Indeed the excess of solvent cause the drastic softening of the polymer and leads to extended distribution of the material as shown in Figure 3-54 also showing the severe deformation of the structure geometry due to PDMS swelling. SEM micrographs of Figure 3-55 demonstrate the successful fabrication of such photonic structures when the solvent absorbed for the stamp is minimum. In most cases the planarization of the surface is so effective that the reverse rib structure (outlining by the white lines in the figure) can be barely observed with the electron microscope. Various aspects of the fabricated structures are demonstrated in Figure 3-56 including positions where the polymer films has been intentionally been striped to reveal the underlying channels.

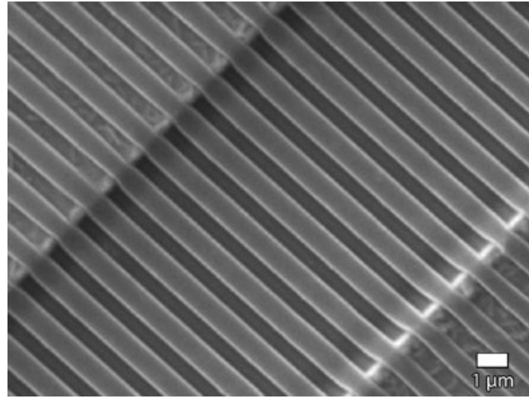

FIGURE 3-54: SEM micrograph of a soft lithographed QD-doped polystyrene DFB structure with a 1µm where the excess of solvent was not completely removed from the PDMS stamp.

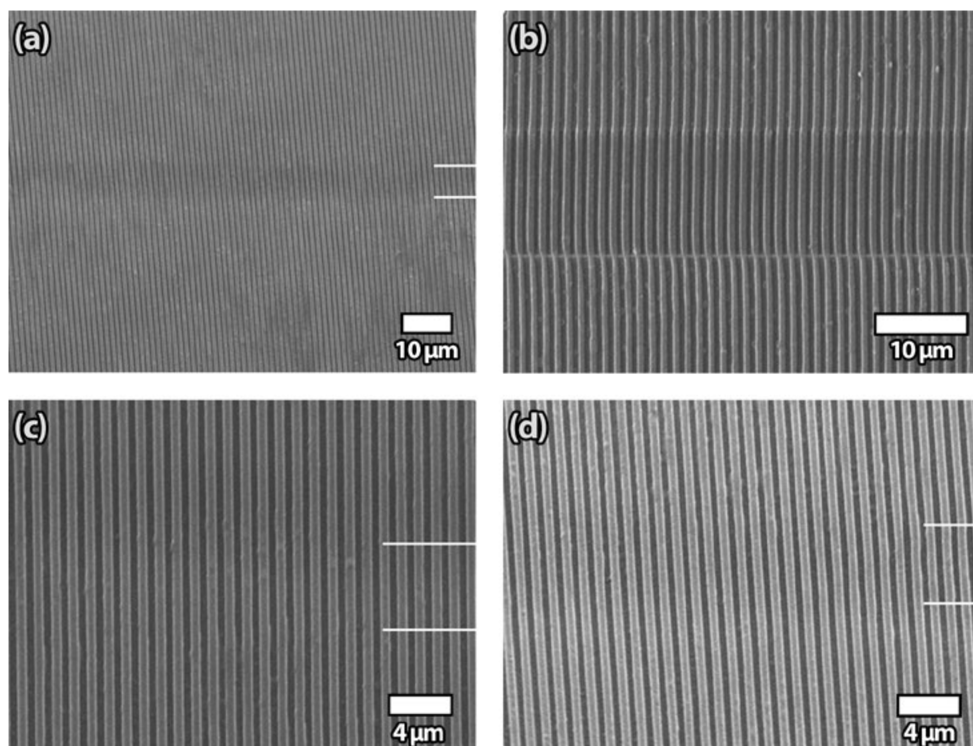

FIGURE 3-55: SEM micrograph of the soft lithographed QD-doped polystyrene DFB structure with a 1µm grating. The white lines depict the position of the buried rib waveguide.

The resonance wavelength of a DFB structure are predicted by the coupled mode equations and is given by the formula:[175]

$$\lambda = \frac{2n_{eff}\Lambda}{p} \quad (3.6)$$

n_{eff} being the effective refractive index, Λ being the period of the grating and p the grating order. BPM simulation presented in Figure 3-45 (page 100) reveals an effective index of n_{eff}=1.59 for QD/polystyrene reverse rib waveguide on OrmoClad,

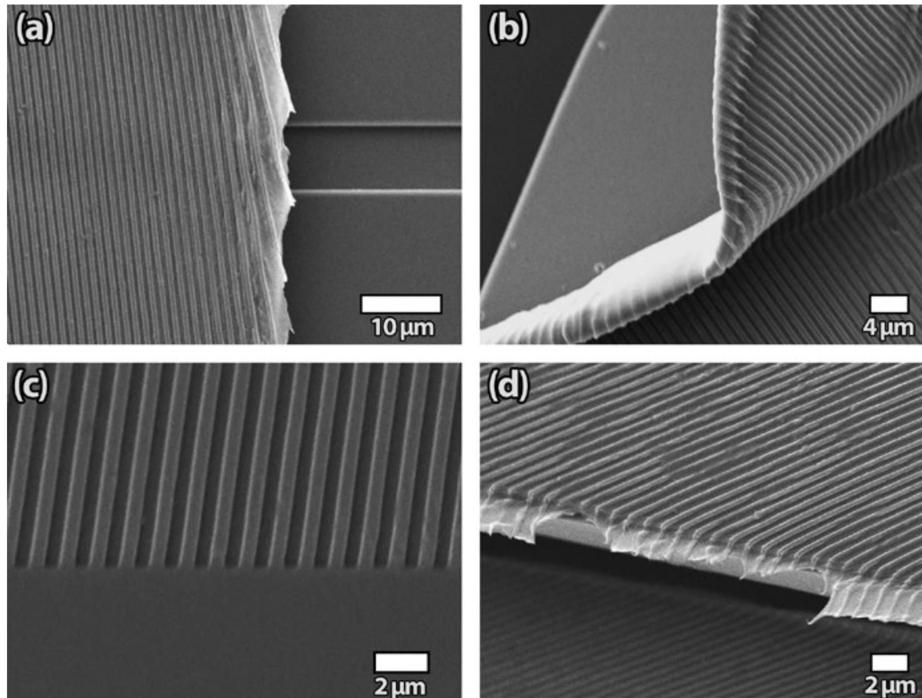

FIGURE 3-56: SEM micrographs of various aspects of the soft lithographed QD-doped polystyrene DFB structure with a 1 µm grating: **(a)** the polymeric film has been intentionally peeled off to reveal the underlying groove on OrmoClad, **(b)** detached and folded polymeric film retaining the micro patterning, **(c)** the edge of the micro pattern polymeric film and, **(d)** cross section of the film at a damaged position of the structure.

thus a 1 µm grating is calculated to operate as a 5th order DFB. Such a high order operation is expected to deteriotate the filtering performance of the structures, thus a grating of lower period is beneficial. Indeed a grating of 200 nm period leads to the desired 1st order DFB. The aspect ratio of 2 of this structure however makes the soft lithography fabrication of this structure difficult and special care is needed to avoid deformation of the PDMS stamp. In such fine structures the PDMS replication of the silicon master, shown in Figure 3-57(a), is often incorrect due to line collapse in the PDMS replica[161] as shown in Figure 3-57(b). To improve the quality of the PDMS stamp a 5:1 ratio of the curing agent and longer curing times of 24 hours at low temperature of 40°C yield the desired results with minimum line collapse as shown in Figure 3-57(c) and (d). The transfer of the fine pattern of the QD/polystyrene film casted on OrmoClad channels is shown in Figure 3-58.

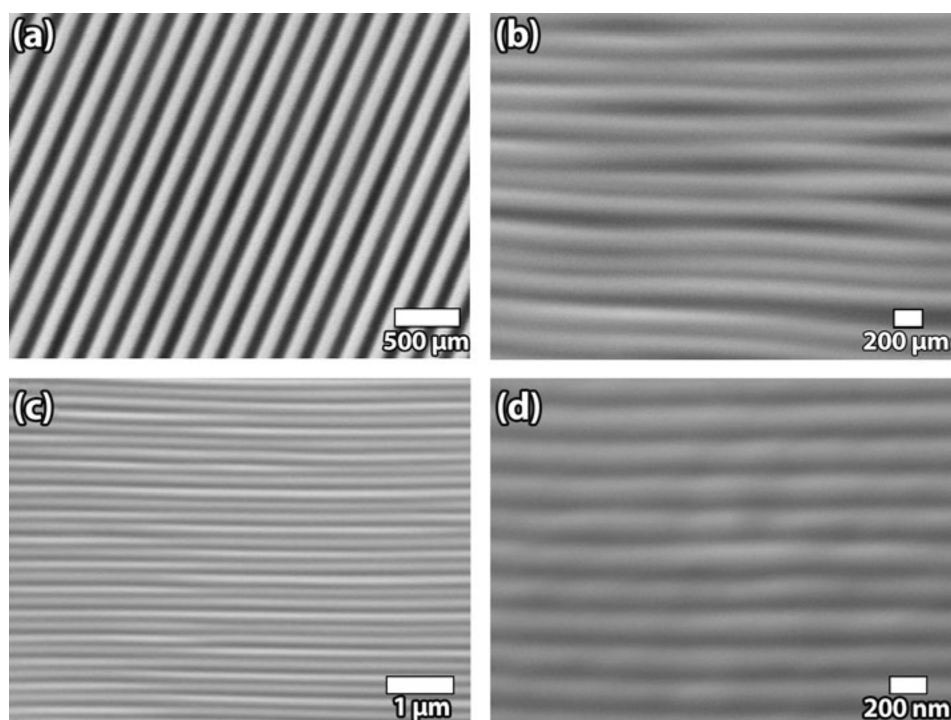

Figure 3-57: SEM micrographs of the 200 nm grating: **(a)** the silicon master, **(b)** 10:1 PDMS stamps exhibiting line collapse, **(c)** 5:1 PDMS stamp with some line collapse and, **(d)** 5:1 PDMS stamp with no line collapse.

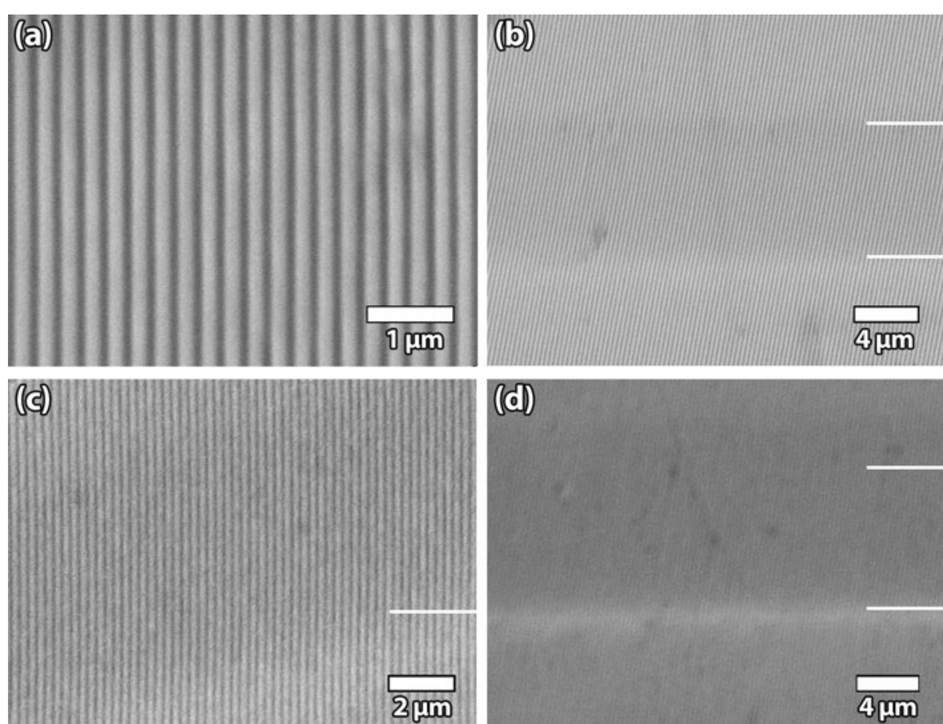

Figure 3-58: SEM micrographs of the QD/polymer soft lithographed fine pattern of the 200 nm grating on top of reverse rib waveguides.

The soft lithography procedure can been easily used in the case of sol-gel derived material. The acetylacetone stabilized titania precursor discussed in paragraph 2.7 incorporating QD was spin-coated at 3000 rpm for 30 s on the OrmoClad channels and hydrolyzed in the presence of the patterning stamp. After casting, the apparatus was placed inside an oven at 150°C for 1 hour. Again the high permeability of PDMS allows for the evaporation of the hydrolysis produced alcohols and water for the controlled hydrolysis and condensation steps. Furthermore, the high refractive index of titania of $n_{titania}$=2.60 (without accounting for the embedded QDs) and the high contrast to the refractive index of OrmoClad give rise to strong confinement of the propagating field as shown in the BPM simulation demonstrated in Figure 3-59.

SEM micrographs of the 1 μm grating structure shown in Figure 3-60 demonstrate structures of good quality with a minimum residual layer. Moreover, the produced structures are crack free in the entire area covered by the PDMS stamp. Interestingly, as shown in Figure 3-60(d) the titania film outside this area is full of crack suggesting that the presence of the stamp allows for the better control of the sol-gel hydrolysis and thus for the production of patterned films of good quality.

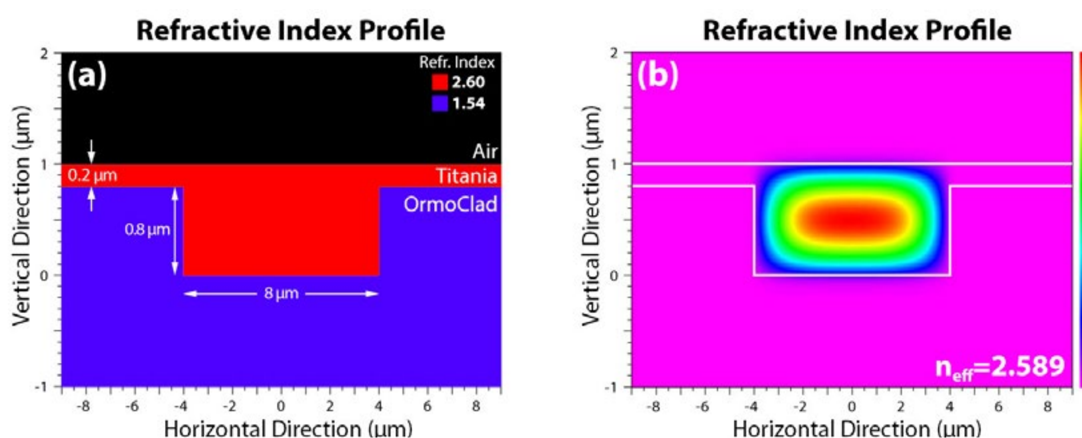

FIGURE 3-59: **(a)** The transverse refractive index profile of the QD-TiO_2/OrmoClad reverse rib waveguide, **(b)** the fundamental mode of the waveguide as computed using the BPM method.

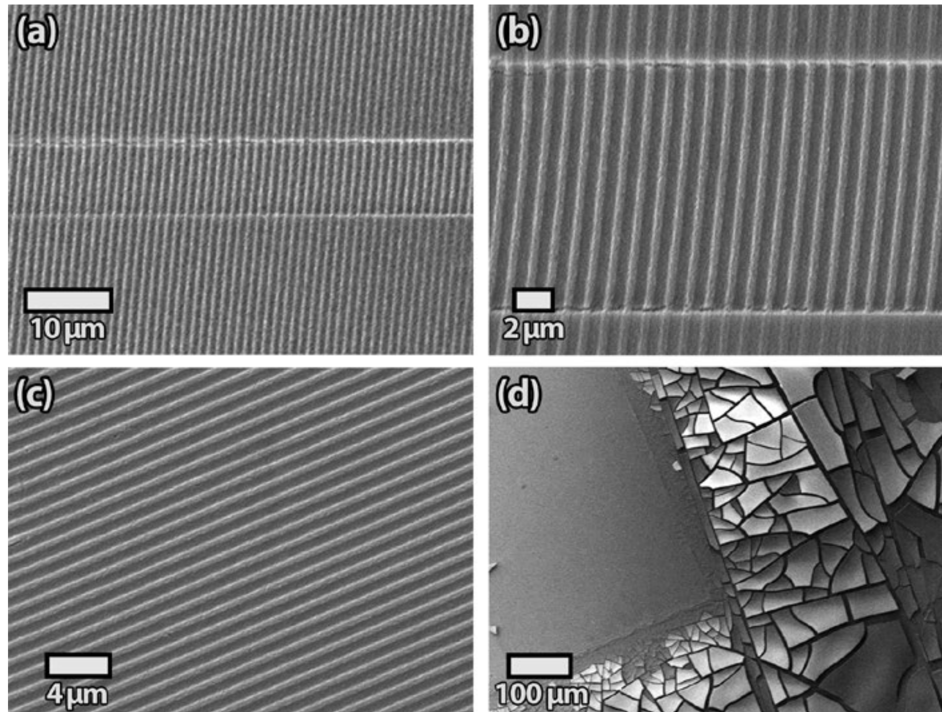

FIGURE 3-60: SEM micrographs of the QD-doped TiO_2 DFB structure on OrmoClad grooves: **(a, b)** the top view of the structure, **(c)** the grating structure at a plain area and, **(d)** the QD-TiO_2 film at the patterned by the PDMS stamp edge. The presence of the stamp causes the effective crack-free hydrolysis of the sol-gel material.

3.14 Conclusions

Two fabrication methods for complex photonic structures were studied in this chapter: the DLAM method and soft lithography. An ArF excimer laser station emitting at λ=193 nm was established in the Dept. of Materials Science (PhASMa lab) for precise microfabrication. The station was fully automated and apart from the excimer laser, other components such as a laser beam attenuator and a power/energy detector were computer controlled through a DAQ card and custom-made electronics. Moreover, a nanopositioner platform of an 80 nm step enabled the automated fabrication of complex photonic structures. A laser microfabrication suite was developed under the LabView™ platform. The laser beam was delivered on to the workpiece through a custom-made pinhole for spatially filtering and a 15X fused silica objective for the ablation of 1 µm features structures, while a suitable protocol was developed for the

accurate determination of the laser pulse energy. To demonstrate the effectiveness of the DLAM method a CGH was successfully fabricated.

QD/polymer photonic structures were designed using the BPM and fabricated using the DLAM. Thermally oxidized silicon wafer were used for the ease cleaving along the crystallographic axis of silicon as substrates. Simulations however indicated the need for an additional cladding layer. In this context, a low refractive index fluorinated acrylic polymer was cast on the substrate prior to the deposition of the QD/polymer nanocomposite. DLAM fabricated waveguides and micro-ring structures were fabricated and their structural quality was evaluated using SEM measurements. To significantly enhance the polymer structures quality a solvent vapor smoothing protocol was applied after laser fabrication.

In addition to DLAM, soft lithography was evaluated as an effective fabrication route for the rapid, low cost fabrication of photonic structures. Commercially available hybrid organic/inorganic UV curable material (OrmoCore and OrmoClad), designed for soft lithography processes were used for the fabrication of waveguides. To account for cleaving issues of such structures, a laser ablation cleaving method was established. Furthermore, a custom-made set-up was developed for the micro and nanopatterning of QD/polymer films using a modified version of the solvent-assisted micromolding (SAMIM) method. Rapid, low cost fabrication of DFB structures was demonstrated by combining the SAMIM method for QD doped polymers and QD doped sol-gel derived matrices and soft lithography channels patterning of OrmoClad.

3.15 Ongoing and future work

Micro-ring resonators commonly fabricated using the expensive and complex electron beam lithography methods are usually integrated along with a bus waveguide laterally coupled to the resonator. Implementation of such a geometry via laser micromachining is very challenging due to the narrow feature of about

100-200 nm required between the micro-ring and the bus. Vertical coupling is an alternative approach where the bus is positioned over of bellow the micro-ring. Implementation of this geometry by means of the laser microfabrication procedure discussed in this chapter requires the fabrication of a bus waveguide from a "*hard*" material exhibiting a high ablation threshold, much higher than that of the material under processing. Such a structure would allow the processing of the polymer film without affecting the underlying bus structure if the laser ablation pulse energy is tuned accordingly.

Fabrication of soda lime waveguides embedded in fused silica substrate is an ongoing research activity demonstrated here. Soda lime glass exhibits a refractive index of about $n_{soda\lim e} \approx 1.5$ rendering this material suitable for fabrication of waveguides coupled to PMMA micro-ring incorporating nanoparticles. Fabrication begun by engraving channels in fused silica substrate as shown in Figure 3-61(a) using the excimer laser microfabrication station. Laser radiation at a repetition rate of 200 pps of 300 μW average power was delivered to the substrate while moving at the speed of 64 μm/s for the implementation of 4 mm long parallel grooves at a distance of 350 μm between each other. The pulsed laser deposition technique (PLD) is then used to fill the channels with soda lime glass. Briefly, the patterned substrate and the target material are placed inside an ultra-high vacuum chamber (vacuum pressure about 2×10^{-6} mbar). The excimer laser beam of 200 mW average power at 200 pps enters the chamber through a fused silica window and is focused on the soda lime target material by means of a planar convex lens with focal length of 50 mm. The target material is ablated and transferred in the ultra-high vacuum in the form of plasma plume shown in Figure 3-62 and is deposited on the substrate. Rotation of the target and swinging of the laser beam was applied for the enhancement of the deposited film homogeneity. The PLD set-up established in the PhASMa lab is shown schematically in Figure 3-63. Due to the big difference between the melting point of soda lime glass and fused silica it was possible to heat the structure to a high temperature

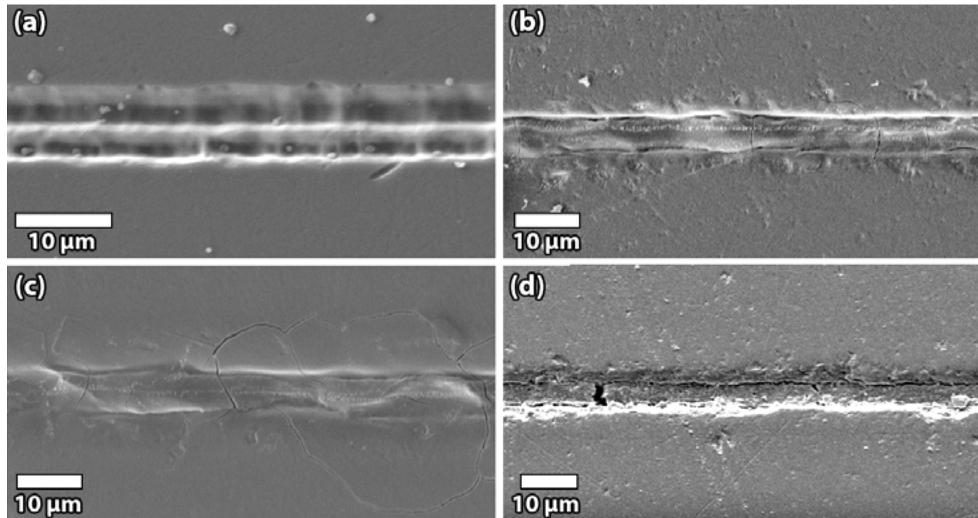

FIGURE 3-61: SEM micrographs of the fabricated soda lime wave guides on fused silica substrates: **(a)** the ablated grooves on fused silica, **(b)** the soda lime waveguide after polishing, **(c)** cracking of the waveguide formed during polishing and, **(d)** defect (unfilled area) on the waveguide.

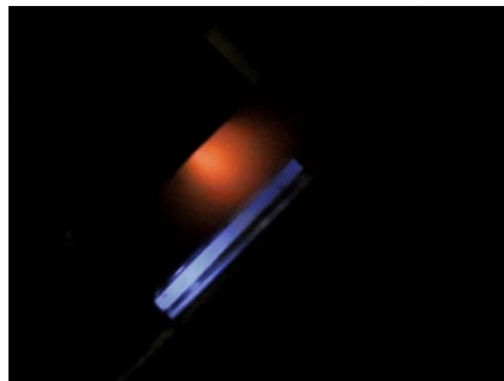

FIGURE 3-62: Photograph of the PLD process where the plume is clearly observed.

of 1000°C for the soda lime to reflow without affecting the substrate. This high temperature treatment allows the evenly fill of the channels and also the enhancement of the adhesion to the substrate. In the last step the structure is polished (Struers™ TegraForce-1) using polishing solutions (Struers DiaPro 3 μm water-based diamond suspension and Struers OP-U colloidal silica suspension). Examples of structures fabricated using the aforementioned protocol are shown in Figure 3-61(c-e). The main challenges of such a procedure is the precise polishing of the waveguides without inducing cracking and other flaws. Moreover, annealing times and temperature of the waveguides is very important to avoid stresses that damage the structure. Elaboration of the several

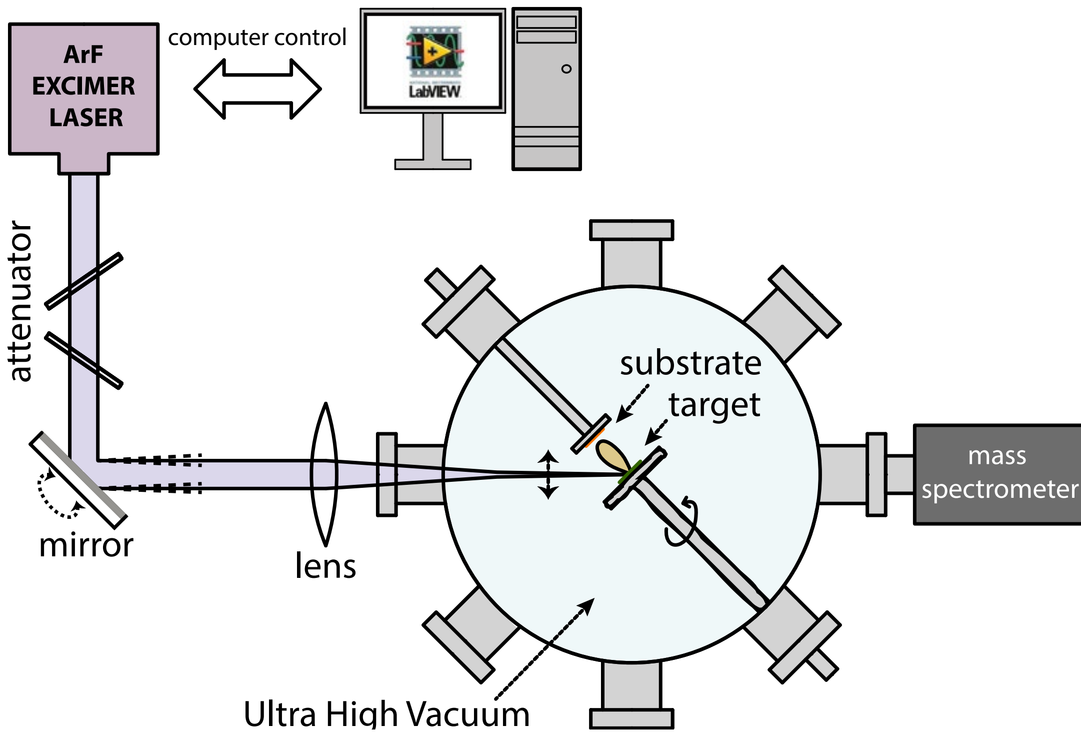

FIGURE 3-63: Schematic of the Pulsed Laser Deposition (PLD) set-up used for the fabrication of soda lime waveguides on fused silica substrates.

parameters of the protocol is expected to yield soda lime glass waveguides that could be covered with polymer film which will be lase patterned without affecting the glass waveguide.

Although fused silica is an excellent material for use as the substrate of photonic integrated circuits (PICs), it is an expensive and not easily processed material while silicon apart from the moderate cost has the limitation of high refractive index necessitating the use of an addition cladding layer. All-polymer PICs on the other hand are favored not only due to the low cost of polymer materials, but also the facile processing and the ability to fabricate flexible non-planar topologies. PDMS exhibiting a low refractive index of n_{PDMS}=1.42 can be exploited as a substrate material. The main challenge for such implementations is the poor adhesion of most polymer film on the PDMS surface which can be accommodated using typical oxygen plasma or laser processing.

Excimer laser microfabrication is proposed here for the implementation of low cost all-polymer micro-ring resonators. Polymer film, e.g. PMMA or polystyrene, can be spin-coated on thick self-standing PDMS substrates and patterned using excimer laser radiation. Due to the elastomeric nature of PDMS, substrate damaging is inevitable in such a procedure and the subsequent increase of the optical losses due to scattering. By embedding however the whole structure in PDMS of the same consistency, reduction of the optical quality of the structure can be avoided. Moreover, integration of the taped fiber or other waveguide into the PDMS host can immobilize and passivate the extremely sensitive due to its narrow size tapered fiber. BPM calculations of polystyrene micro-ring resonators (R=30 μm and 50 μm) embedded in PDMS are shown in Figure 3-64.

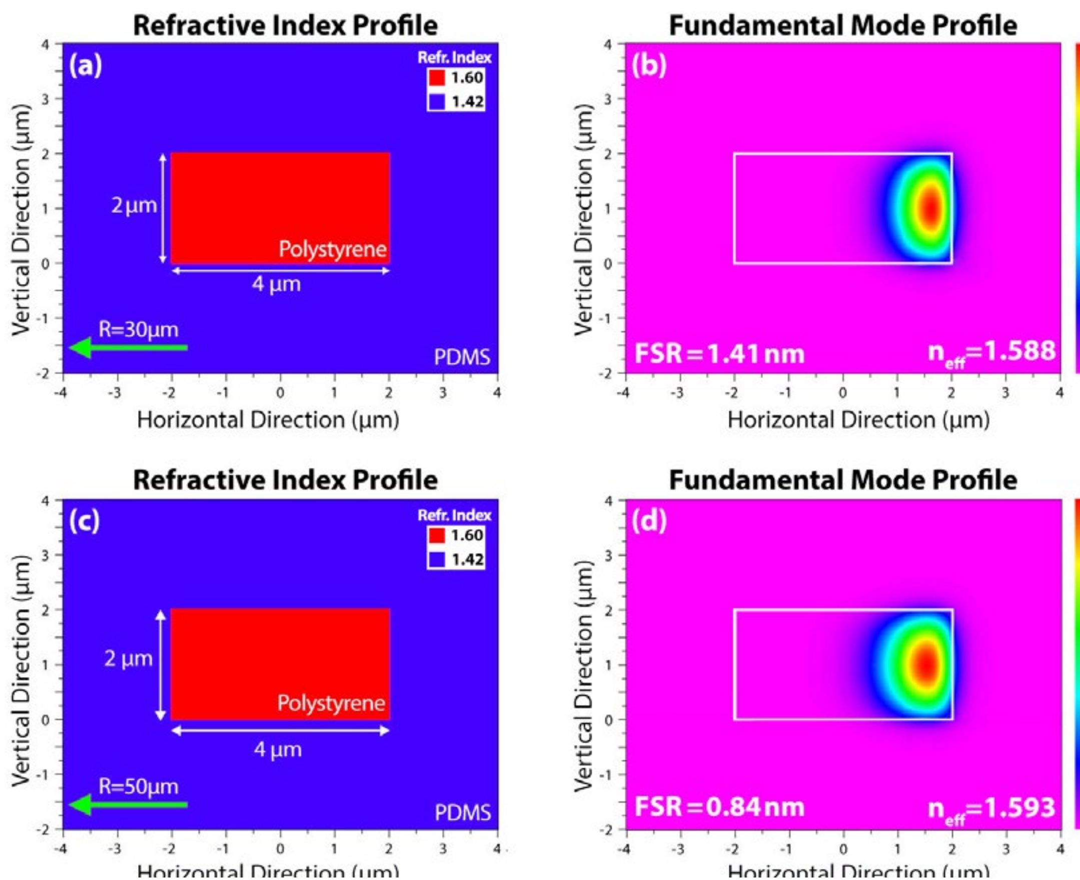

FIGURE 3-64: Theoretical modeling of a polystyrene micro-ring resonator of radius: **(a, b)** R=30 μm and **(c, d)** R=50 μm embedded on PDMS. The transverse profiles of the refractive indices are shown in (a) and (c) while the profiles of the fundamental mode calculated using the BPM are shown in (b) and (d). The green arrow depicts the center of the curvature of the structures.

The high transmittance of PDMS in the UV region can also be exploited for the implementation of optically active structures. Indeed, QD or dye doped photonic structures can be optical excited through the PDMS host. Finally, the high permeability of PDMS can be used for the implementation of gas or solvent sensor in such configuration.

Chapter 4
Sensing the Environment with Nano-entity Photonic Sensors

4.1 Introduction to photonic sensors

The ever-increasing need for sensing the chemical and physical parameters[176–187] has resulted in a vast number of their applications, ranging from large scale monitoring in industrial production to domestic safety and from life-critical technologies in the medical sector to gadget devices for the entertainment industry. The endless list of such applications also includes sensor automations, for agricultural, building and construction monitoring, telecommunications and electronic systems scientific research, space and defense and security applications, to name just a few. Moreover, environmental protection and public safety become crucial factors that lead to an increased demand for accurate, intelligent, and low cost sensing devices. The recent advances in sensor research and technology have labeled the first decade of the 21st century as the "*sensor decade*".[176]

Currently available technologies for chemical sensing are based mainly on electrochemical approaches[176,180–183,188–191] where an electronic circuit monitors the change of the electronic properties (e.g. resistivity, conductivity etc.) of a suitable sensitive material, upon exposure to the agent under measurement. In this context

a wide range of materials has been developed, ranging from insulating oxides[192–200] to conductive polymers.[201–207] Operation at elevated temperatures, poor selectivity, high power consumption and vulnerability to electromagnetic interference are some of the drawbacks of this technology although recent advantages of nanotechnology now provides advanced materials which enable moderation of such impediments.[157,180,208–211]

Among the various sensing schemes, optics offer alternative sensing schemes having striking advantages as compared to conventional electronic chemical sensors.[184–187,212] Assisted by the advances in the field of photonics and optoelectronics technologies made in the last decades, new approaches have emerged. The market for photonic sensors grows more than 50 % per year resulting in multi-billion dollar figures in 2009 according to the Optoelectronics Industry Development Association -OIDA, USA.[185] The availability of low cost optical components and the growth of the telecommunication industry allows the deployment of photonic devices, the integration with electronic circuits and the blooming of the field of photonic sensors. This upsurge in interest is also reflected on the increasing number of scientific publications in the field and the publication of new dedicated journals and magazines as well as special journal issues and dissemination events. In comparison to conventional electronic and mechanical counterparts, optical sensing schemes usually increased sensitivity attributed to the strong dependence of the optical properties to the environment. Depending on the operating configuration high dynamic sensing range and low noise are possible. Further to the interaction of light to its environment with the maximum speed possible, namely the speed of light, significant advantages relate to the inherent ability for remote, non-contact, non-destructive probing of the and the inherent immunity to electromagnetic noise and ability to multiplexing. Such schemes are, in addition, capable for low cost system deployment and operation.

Optical sensing schemes is based on various fluorimetric/colorimetric[213–217] and surface plasmon effects,[187,218–220] while their implementation involves fiber optics/waveguides,[221–226] optical resonators,[227–229] photonic crystals,[230–233] spectroscopic techniques,[234–236] interferometric platforms,[237–239] integrated path operations,[240] and other configurations[184–187] or their combination.

Whatever the sensing method is, the key targets for sensing relate to: (i) high sensitivity, (ii) increased selectivity, (iii) reversibility of state, (iv) long-term reliability, (v) low cost, and (vi) capacity for system miniaturization. Depending on the sensing application sought, the above targets are prioritized to conform to respective requirements.

4.2 The Remote Point Sensing scheme

The Remote Point-Sensing scheme (RPS) is a new proposed photonic concept allowing low cost, versatile, reliable all-optical detection based on remote interrogation of a distantly placed sensor head by use of light beams. It is an alternative to other optical sensing methods such as fiber optic and waveguiding sensors. It features a spatially-localized sensing and remote character for the measurement process. It comprises a simple passive sensor head placed in the environment to be monitored which can be interrogated from a far distance (up to few kilometers) using a laser source. Upon interaction with the physical or chemical agent the sensor head material changes its properties and the laser beam “reads out” the changes which is using a photodetector. An outline of the basic operation principle of the RPS scheme is presented in Figure 4-1. This spatially local RPS sensing is to be contrasted to the well-known integrated-path operations, such as the light detection and raging technology (LIDAR).[240] In this latter case measurement and detection is performed over an integrated optical path. LIDAR is extensively used for atmospheric research and meteorology. It is based on atmospheric transmission of one of more laser beams, detection and analysis of the back-scattered light.

The different operating configurations of the RPS scheme are envisaged. The transmission mode presented in Figure 4-1(a) where the laser beam is recorded after passing through the head, while reflectance mode shown in Figure 4-1(b-c) where the laser beam is reflected and directed for recording at a position adjacent to the laser source. In the latter case the sensor head can inherently be reflective (e.g. the sensing material is either reflective or casted on top of a mirror) or retroreflective, when used to redirect the laser beam back to the position of the laser source. It is stressed here that the retroreflecting configuration greatly facilitates the alignment of the sensing setup and thus benefits from a lower installation and operating cost. As shown in Figure 4-1(c), a parallel shift of the optical path induced by the retroreflector is required to allow placement of the photodiode close to the laser source. Since an ideal retroreflector would guide the beam at the exact position of the laser, the use of a cube-corner reflector or prism (e.g. double Porro prism) could provide the require geometry.

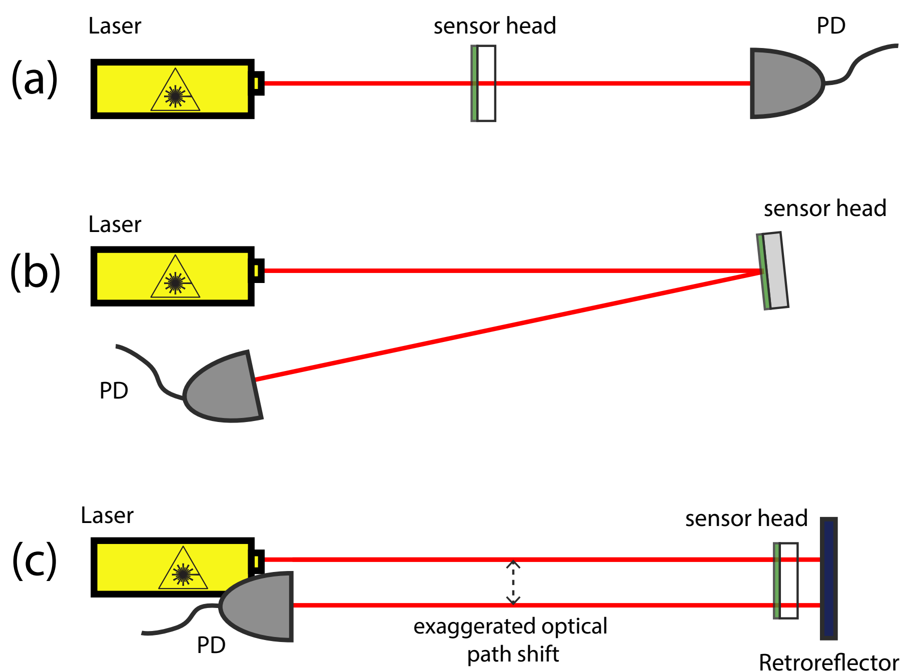

FIGURE 4-1: The Remote Point Sensing scheme in **(a)** transmission operation mode, **(b)** reflection mode using a reflective substrate, and **(c)** reflection mode using a retroreflector (cube-corner reflector or prism) to guide the monitor beam.

Since each sensor head comprises a specific sensing material designed to respond to a certain (class of) chemical or physical agent, multiple sensors can be utilized for the simultaneous multiple-agent monitoring. The sensing diversity is both determined and limited by the design of the sensing materials used. Monitoring multiple agents can also be beneficial for sensing using materials exhibiting of relatively low sensing selectivity since the signals from different sensor heads can be de-correlated using appropriate algorithms. As it is described in the final paragraph of this chapter, multiple agent monitoring from a single sensor head can be accomplished by use of advanced photonic structures. Moreover multiple sensor heads can be placed at different positions to monitor a desired area, with the only limitation being the need for line-of-sight contact between the laser source/photodetectors and the sensor heads.

In a practical sensing application the RPS can be configured in either giving emphasis on fast real time monitoring of multiple heads or on low cost operation. In the former case multiple laser sources/photodetectors are continuously interrogating multiple sensor heads targeting either multiple agents sensing and/or covering spatially a large area. The response of the measuring system is practically defined by the response time of the sensing material, time taken to interact with the agent, milliseconds to seconds for the sensors developed in this thesis. A single laser source and a photodetector operating with an automation system (e.g. a motorized mirror) can remotely interrogate all “*sensor heads*” consecutively. This configuration can drastically limit the cost of the sensing setup while constrain the speed of the sensing procedure.

The main advantages of the RPS are summarized below:

- **Remote point sensing** that allows spatially localized detection from a long distance away. The sensor heads are positioned in the area to be monitored and are remotely interrogated without the need for any physical interconnect such as data transmission wire, fiber optics or connections to the power grid that increase the installation cost. Moreover the lack of batteries or

other power sources enables seamless operation eliminating the necessity for regular maintenance and power charge. This facilitates sensing in areas difficult to reach (e.g. agricultural fields, large industrial complexes etc.).

- **Low cost** sensor fabrication, installation and operation. The sensor fabrication cost is mainly defined by the sensing material used and the thin film nanopatterning procedure used as described in this work. Low cost materials can be used such as the silica sol-gel matrix with $NiCl_2$ nano-entities studied here. Most materials compatible with the RPS scheme can be cast on simple substrates (e.g. microscope glass or polymeric sheets) of negligible cost using a lost cost method such as the roll casting, suitable for large scale production or spin-coating. For the microfabrication of photonic structure an ultra-low cost soft-lithographic method as well as a more versatile direct laser etching method are proposed here. The installation cost of the sensing system is minimum since only the passive sensor heads comprising the sensing thin films preassembled, with the retroreflector needs to be positioned at the desired area at a long distance. Moreover, the use of a retroreflector facilitates beam alignment and contributes to the low installation cost. The cost of the system can be drastically reduced further if a single light source/detector system is used for multiple sensor interrogation.
- **Small size and lightweight sensor heads** allows fast and easy installation in large scales thus contributing to the low installation cost.
- **Accuracy and reliability** mainly defined by the properties of the sensing material. The RPS benefits from the recent advantages in the field of nanotechnology and the synthesis of innovative nanocomposite materials exhibiting enhanced sensing properties.
- **Completely passive operation** of the sensor head not only offers immunity to electromagnetic interference but also eliminates the prerequisite to use

of the wireless transmission. The absence of batteries or other power supply systems (e.g. solar cells) increases the reliability of the system.

- **Operation in free space and in a hostile environment**. As a consequence to the all-optical, passive nature of the sensor head, the RPS can be exploited in hazardous environments where the danger of a possible explosion due a spark (e.g. in refinery chimneys) places restriction on the use of electrical and electronic systems. Moreover the lack of in-situ electronic circuits enables the use of the RPS in environments of radiation hazard (e.g. nuclear plants).
- **Room temperature operation.** Combined with suitable sensing materials the sensor head operates under ambient conditions without the need for heating or cooling the device.
- **Ability for multiplexing** as multiple sensor head can be closely pack for the simultaneously monitoring of various physical and/or chemical agents.

The main disadvantage of the RPS scheme is the requirement for permanent optical contact (line-of-sight) between the sensor head and the interrogating system. This places constraints on the installation of the system and limits the area that can be monitored. Moreover the occurrence of any obstacles can disable the operation of the RPS scheme system, however this also be prove beneficial if exploited properly, e.g. if the disruption of the sensor signal is used to trigger an alarm to indicate unexpected obstacles in the area or the presence of smoke, or fire, disrupting the signal.

A crucial factor that affects the performance of the RPS scheme is the effect of the possibly unstable media in which the laser beam propagates (usually the atmosphere) between the interrogating system and the sensor head. Since the RPS scheme is based on dynamically monitoring the optical properties of the sensor heads, the presence of dust, fog or smoke that can alter the characteristics of the laser beam and may interfere to the sensor operation. Moreover, turbulence of the atmosphere caused by meteorological phenomena (e.g. wind combined with humidity) can give rise to corresponding perturbations of the propagating beam

by optical turbulence.[241–243] Accommodation of all these perturbations can easily accomplished by means of a reference beam drawn from the same source, co-propagating in parallel and close to the signal beam and being reflected back to the interrogating system without interacting with the sensor head allowing calibration and effective elimination of any parasitic data in the acquisition system. Furthermore, it is relatively simple to generate two parallel beams (signal and reference beam) of equal intensity by splitting the laser beam emitted by a low cost non-stabilized laser source and account for all fluctuations. In our group we have studied photonic interrogation schemes under conditions of heavy optical turbulence. Operation under the RPS scheme is feasible by exploiting a set of several beams interacting with the sensor head instead of a single beam. This set of beams may be generated using a Computer Generated Hologram (CGH) fan-out element, while the perturbation due to the optical turbulence can be compensated by using relatively simple algorithms. A detailed discussion on such a system is beyond of the scope of this thesis.

4.3 Operating principle of the Remote Point Sensing scheme

The operation principle of a RPS system is depicted in Figure 4-2 for the transmittance mode while the same principles apply equally well for reflectance mode operation. The sensor head is exposed to the environment to be monitored and it is interrogated by a laser beam from a distance. It comprises a thin film of a sensing material designed to respond to the physical/chemical agent to be measured. The film is cast on a low cost transparent substrate (e.g. microscope glass) using a low cost method (e.g. roll casting or spin-coating). Upon exposure to the agent to be measured the sensing material film exhibits alteration of its optical, interferometrical or diffractive properties that consequently leads to a spatial modulation of the optical path of the laser beam inside the film and thus to a modulation of the interrogating laser beam. The modulated beam if finally recorded by a photodetector (commonly a photodiode) and the presence of the agent is identified by the data acquisition system. The change of the optical path

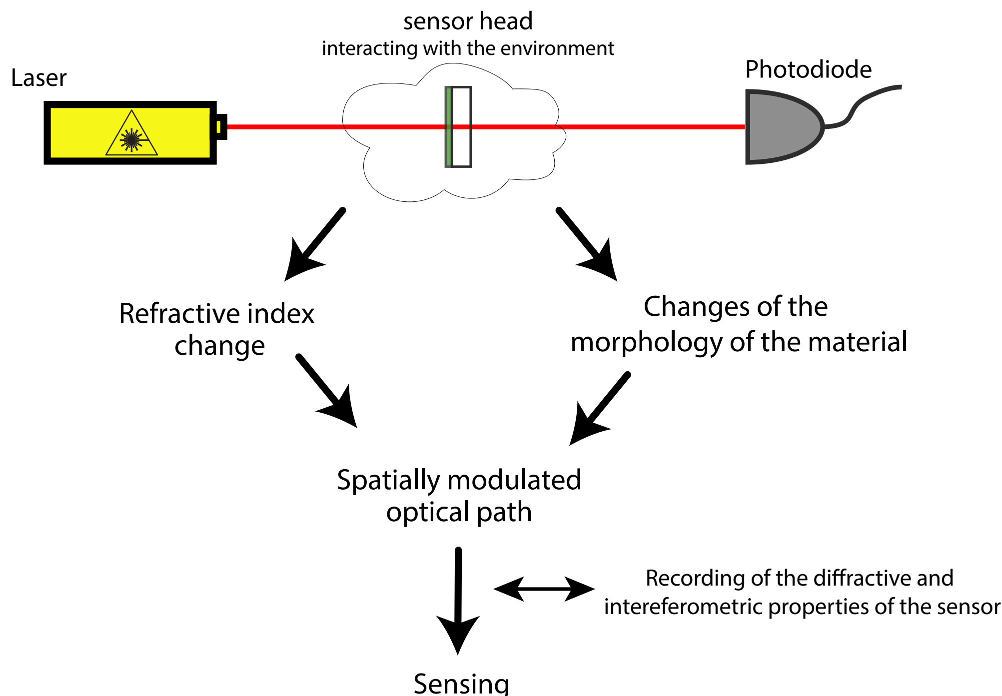

FIGURE 4-2: Principle of operation of the Remote Point Sensing Scheme

inside the sensing film can result from an alteration of the refractive index of the material due to the interaction to the agent, from a change of the morphology of the film material (e.g. swelling or shrinkage) or a combination of both.

Upon exposure to the agent, the sensing material exhibits a variation of its optical and geometrical (morphological) properties. These effects lead to a spatio-temporal modulation of the optical path, which reflects on the interferometric and or diffractive properties of the structure as a whole, the latter detected by the interrogating laser beam. The output signal beam is detected by a photodetector (usually a photodiode) and the measure of the agent is recorded by the data acquisition system.

It is worth underlying here that the change of the optical path caused by refractive and morphological alterations (e.g. swelling, shrinkage, or other spatial modulation) in the sensing medium is of our main interest here. Absorptive variations of the material, though of interest in some other sensing schemes, is not favored in our case due to the optical power loss which is to the detriment of the whole operation. In addition reversibility of operation is a key issue here. In this context irreversible colour changes of the material caused by chemical interactions (dye effects) are not of our interest.

4.4 Different configurations of the RPS scheme

To fulfill the requirement for high sensitivity and high signal-to-noise ratio, the use of a sensing material that produces a substantial response to the presence of the agent in terms of reversible refractive index alteration is of crucial importance. Such changes of the optical path within the sensing material need to be transferred efficiently to the interrogating beam. Therefore, in addition to the sensing material design, another route for responsivity enhancement is the exploitation of functional optical structures exhibiting properties strongly dependent on the refractive index of the sensing material.

In the simplest case of an unpatterned sensing film the modulation of the interrogating beam is caused by the alternation of its interferometric properties originating from the multiple reflection between the film-air and film-substrate surfaces. This change is seen in the transmittance and reflectance properties of the sensor head and thus on the intensity of the transmitted and reflected components of the laser beam. Calculating the Fresnel coefficients for a laser beam incident on the sensing material film and accounting for the successively reflected and transmitted beams we find that the reflectance R and transmittance T are given by the following formulas:[244]

$$R = \frac{(n_0^2+n_1^2)(n_1^2+n_2^2) - 4n_0n_1^2n_2 + (n_0^2-n_1^2)(n_1^2-n_2^2)\cos(\frac{4\pi}{\lambda}n_1\ \mathrm{d}\cos\varphi)}{(n_0^2+n_1^2)(n_1^2+n_2^2) + 4n_0n_1^2n_2 + (n_0^2-n_1^2)(n_1^2-n_2^2)\cos(\frac{4\pi}{\lambda}n_1\ \mathrm{d}\cos\varphi)} \quad (4.7)$$

$$T = \frac{8n_0n_1^2n_2}{(n_0^2+n_1^2)(n_1^2+n_2^2) + 4n_0n_1^2n_2 + (n_0^2-n_1^2)(n_1^2-n_2^2)\cos(\frac{4\pi}{\lambda}n_1\ \mathrm{d}\cos\varphi)} \quad (4.8)$$

where λ is the free space wavelength of the laser beam, d is the thickness of the sensing film, ϕ is the angle of incidence and n_0, n_1 and n_2 are the refractive indices of air (closely equal to 1), the sensing material and substrate respectively.

In Figure 4-3 we calculate the transmittance spectrum of a hypothetical 1 μm thick thin film deposited on a microscope glass substrate (soda lime glass with a

base refractive index in the visible n_{sub}~1.52) is drawn with a black line. We assume that the film material initial exhibits a refractive index of n_{film}=1.55 assuming no dispersion and with the imaginary part of the refractive index set to zero. We also assume that upon exposure to an environmental agent the film material undergoes a small refractive index alteration at n_{film}=1.551. We observe a new trasmittance spectrum shown by the red line and denote that by monitoring the film trasmittance at the wavelength region near the transmittance minima, a maximum transmission change with the refractive index change may be recorded as a modulation of the intensity of the interrogating beam.

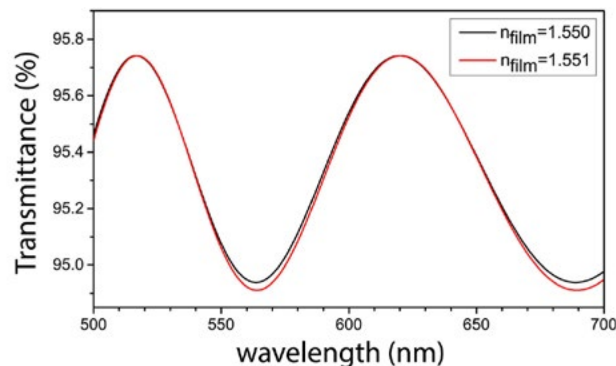

FIGURE 4-3: Transmittance spectrum of a 1 μm thin film on a soda lime glass substrate (n_{sub}=1.52) as calculated using equation for two different values of the refractive index of the film material: n_{film}=1.55 (black line) and n_{film}=1.55 (red line).

The main drawback of the aforementioned sensing configuration is the low sensitivity of the film reflectance and transmittance to both changes of film thickness d and film refractive index n_1. To drastically enhance the efficiency of the sensor, we tailor the optical interfaces by means of microsturing Diffraction Optical Elements (DOE) on the sensor film. The key motivation for such micropatterning is the large dependency of the diffractive property of DOE on the optical path of the film. In this concept Surface Relief Gratings (SRG) has been etched by direct laser processing using ArF excimer laser radiation, without altering the materials sensing properties of the film due to the selective microablation of the film and the minimal thermal effects involved at the 193 nm deep ultraviolet radiation. This micropatterning

method was found to yield superior results in terms of diffraction and sensitivity than simpler patterning methods, such as casting of the sensing material on pre-patterned diffraction gratings made by conventional photolithography. The latter photonic structures suffer from the low refractive index contrast between the substrate and the sensing material. The fabrication protocol of the SRG on sensing films is presented in section 4.4.

The principle of operation of a diffractive optic sensor operating under the RPS scheme is depicted in Figure 4-4. A relatively large period of the grating (of the order of 100μm) may be desirable in some cases, as it yields small angle between the diffraction orders (~0.5^{o}) to facilitate the laboratory configuration. Although more photodetectors are required for the sensor evaluation only one diffraction order (the one exhibiting the larger Signal-to-Noise Ratio -SNR), thus one photodetector, is required to be monitored in real life applications, while further orders may be monitored for referencing and optimization.

Performance prediction of the diffractive optic photonic sensors operating under the RPS scheme is studied in section 4.7 calculated using the well-established Rigorous Coupled-Wave Analysis (RCWA) method. In the same paragraph fabrication guidelines are provided for designing sensors of maximum sensitivity.

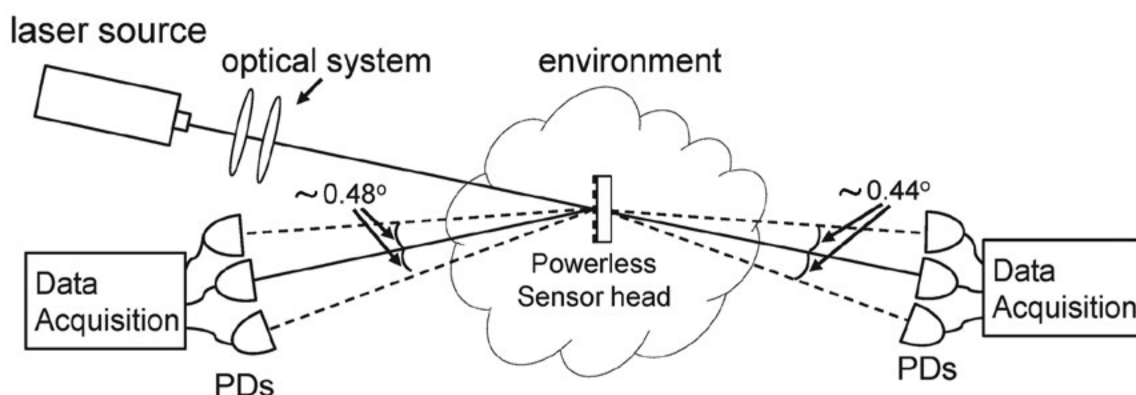

FIGURE 4-4: Principle of the Remote Point Sensing scheme using a diffractive optic sensor head in transmission and reflection mode.

4.5 Nano-entities for ammonia sensing

A sol-gel silica nanocomposite incorporating $NiCl_2$ cluster nano-entities has been synthesized and used for the demonstration of a low cost, high performance diffractive photonic ammonia sensor operating under the RPS scheme. This material was chosen as a best-case result of our studies involving a range of nanocomposite materials of the kind. The importance of ammonia detection in the industrial, the agricultural and the urban environment, the superior performance as a sensing application the low cost synthesis further corroborated this choice.

Ammonia is widely used by the chemical industry as it is an intermediate for many plastics (e.g. nylon), for the production of fertilizers, explosives and pharmaceutics, in medical analysis, for treatment in the metal and the automobile industry, to name just a few of its many fields of application.[245] It is found in various household and industrial detergents, while due to its vaporization properties it is used as a refrigerant instead of Freon, usually in industrial scale refrigerators.[246] Moreover, ammonia is generated by decomposition of organics, in combustion processes and engines, and natural decomposition of wood, agro and chemical materials. Despite its abundance, ammonia is considered to be extremely hazardous for human health and the environment. The European Union has classified ammonia to be an irritant at low concentrations (5-10% w/w), corrosive at moderate concentrations (10-25% w/w) and both corrosive and a dangerous for the environment at higher concentrations (>25% w/w).[247] Exposure at even low ammonia levels (50 ppm) can cause irritation in the upper respiratory tract and chronic coughing while prolonged exposure at lower concentrations (25 ppm) may cause eye burning, tearing, corneal abrasion, blurred vision or blindness.[248–252] A short acceptable period of 15 minutes exposure limit for humans at a concentration of 35 ppm by volume in air and a longer exposure limit during a daily working period of 8 hours at the lower concentration of 25 ppm have been set by the U.S. Occupational Safety and Health Administration (OSHA) and the

American Conference of Industrial Hygienists.[249] The widespread use of ammonia in industry combined with the strict exposure limits and the vaporization properties of ammonia water solutions (pure ammonia has a boiling point of -33°C and a vapor pressure of 8573 hPa), suggests the importance of ammonia concentration monitoring in areas such as industries and warehouses.

4.6 Microstructuring of diffractive optical elements in thin film sensing materials using ArF direct etching method at 193 nm

Microstructuring of environmentally sensitive thin films is a challenging task. The sensing functionality of the material is based on surface interactions and, thus, any reactive effect may be deleterious to the sensing property itself. Tailoring the surface morphology is not, therefore, a trivial issue and any microstructure fabrication method must ensure the preservation of the sensor's physical and chemical functionality. In this respect, conventional lithographic processing[253–256] is not suitable, since casting of the nanoporous silica sol-gel with a photoresist would destroy the porous network near the surface, while rinsing the film in solvents and reactive agents during the development and etching steps would permanently affect the structure of the nanocomposite and its properties, as liquids tend to penetrate the porous matrix. On the other hand, casting the sensing material on diffractive optical elements fabricated, for example, in photoresist yield poor diffraction efficiency results due to the low refractive index contrast attended between the photoresist and the silica nanocomposite.[257] For the fabrication of high performance SRG sensors, a direct etching technique is required for optimum results. Direct laser microetching techniques used here, have been proved to offer some unique and versatile microfabrication tools. Alternatively, state-of-the-art micro and nanopatterning methods which are able to preserve the materials properties, such as soft lithography, nanoimprint lithography, or scanning probe lithography, could also be exploited in this context and are also discussed in this thesis.[155]

High quality ablative processes at 60 µJ/cm^2 pulse energy density results in diffraction gratings with spatial period in the range of Λ=5-100 µm fabricated on the sensitive surface. A scanning electron micrograph (SEM, model JEOL 6300) and a surface profile (Tencor Alpha-Step 500IQ with a stylus of radius of 6.5 µm) of a typical structure are shown in Figure 4-5. This structure features a film h=thickness of 1.65 ± 0.05 µm, a period of Λ = 80 µm at duty cycle of ~0.39. The good quality nearly square profile produces clear multi–ordered diffraction patterns upon laser illumination, of which the zero– and higher–order diffracted beams may be used for sensor interrogation. Close-up SEM micrographs shown in Figure 4-6 indicates the suitability of the direct laser etching method since the material near the etching edge close to the ablated region is not affected by the fabrication process. It is evident that the profile shown in Figure 4-5 deviates from the ideal rectangular shapes. This is attributed to both fabrication limitations and film thickness variation due to non-ideal spin-coating. Profilometry also imposes measurement limitations due to the geometry of the stylus. Real deviations will have some minor effect on the quality of the diffraction pattern and will also introduce some mismatch between theoretical and experimental results as it will be discussed later.

4.7 Protocols for photonic sensor testing and analysis under the RPS scheme

Diffractive sensor structures of silica sol-gel/$NiCl_2$ have been experimentally tested to mimic remote photonic sensing operation under the RPS scheme in the transmission mode. The micropatterned sensor head was placed inside a testing chamber of known volume equipped with optical windows where the desired analyte environment can be established. The chamber which is actually a hermitically sealed vacuum chamber is also equipped with electrical feedthroughs allowing the connection of heating elements and various testing probes a required. A vacuum pump connected to the chamber isolated through a solenoid valve was used to

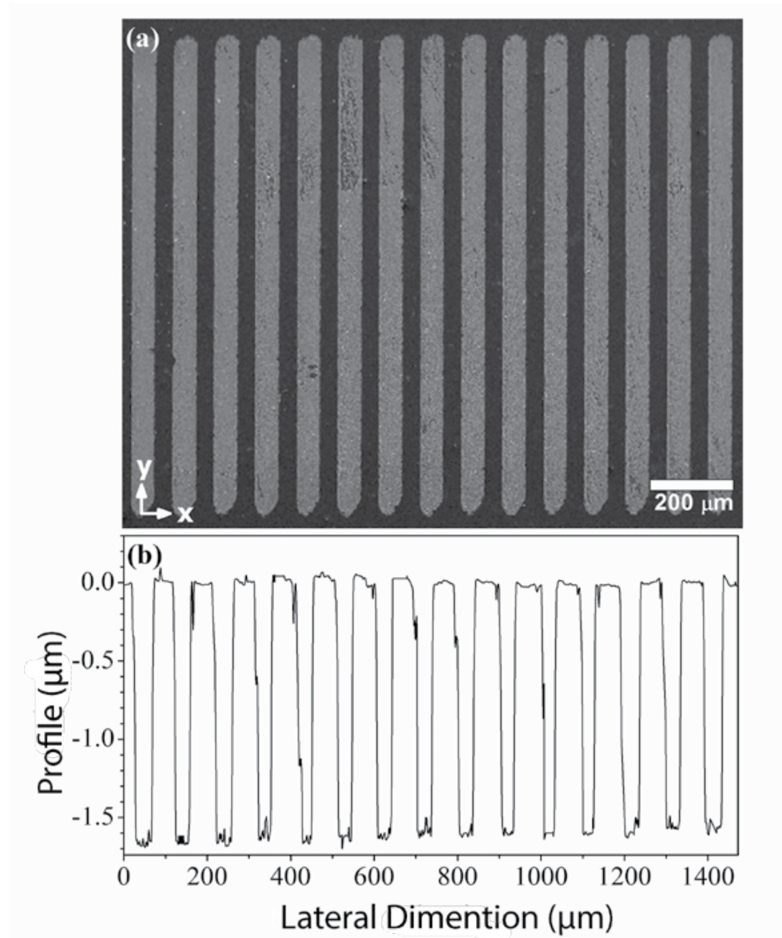

FIGURE 4-5: (a) SEM micrograph of the sol-gel/$NiCl_2$ diffraction grating photonic sensor, **(b)** the profile of the surface relief structure measured using a KLA-Tensor Alpha Step profilometer.

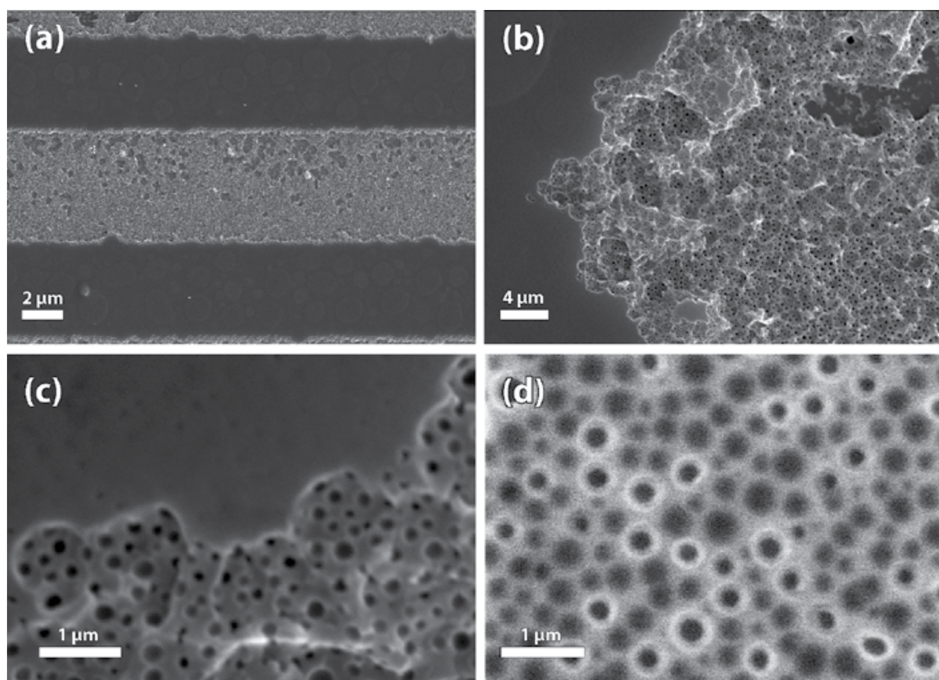

FIGURE 4-6: SEM micrographs of: **(a-c)** the edges of the ablated regions of the sol-gel/$NiCl_2$ diffractive structure, **(d)** the untreated surface of the film.

rapidly restore ambient conditions after each measurement with atmospheric air flow by pumping the chamber with its lid open.

For analytes in liquid form or solutions of known concentrations, a known volume in the form of micro-droplets (~ μl) was introduced into the chamber as measured with a precision pipette (Eppendorf) through a small lid open on top of the chamber. The chamber was sealed immediately after the introduction. The analyte was fully evaporated by use of Peltier device heated at moderate temperatures in the range of 30-40°C at max for the case of ammonia solutions. The analyte concentration in gas form is calculated for known volume of the chamber (2.7 l). A photograph of the actual experimental testing station is shown in Figure 4-7(a) together with an integrated version of the sensor system using retroreflective optics as depicted in Figure 4-7(b).

As schematic illustration of the experimental setup used for testing and evaluation of photonic sensors is depicted in Figure 4-8. The sensor head was remotely interrogated using a signal beam emitted by a HeNe laser source (total power 5 mW) at λ = 632.8 nm. The signal is directed and transmitted through the thin film sensor head structure and the various diffracted orders are simultaneously monitored. A reference beam was also provided to balance out any laser power fluctuations. It was generated by a 50-50 beam splitter while a mirror was used to guide it in parallel very close to the signal beam. This reference beam also passed through the

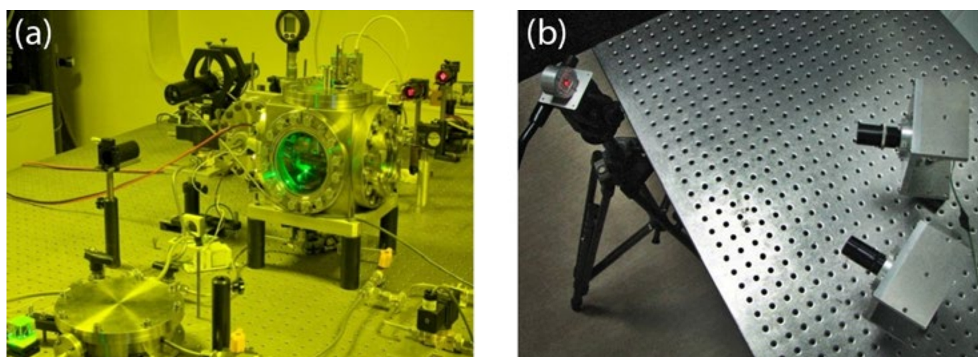

FIGURE 4-7: (a) Photograph of the vacuum chamber used to evaluate the photonic sensors operating under the RPS scheme, **(b)** a testing setup comprising a laser source, a photodiode receiver and a mobile sensing film fixed on top of a retroreflector.

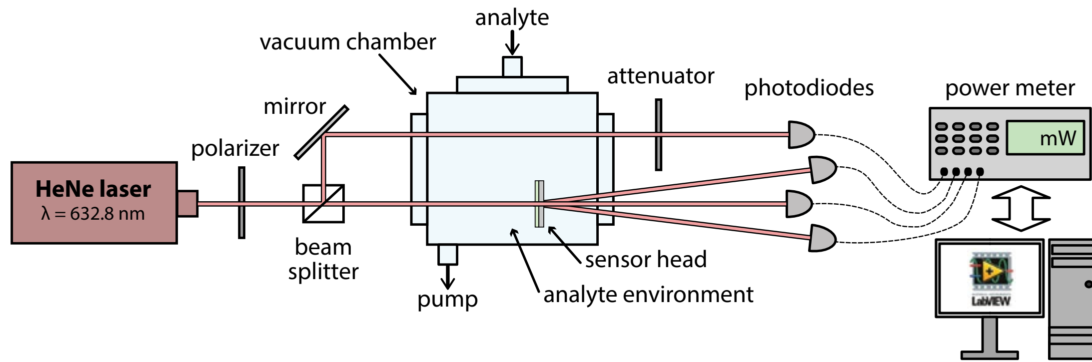

FIGURE 4-8: Schematic illustration of the experimental setup used for the evaluation of the nano-entity diffractive optic photonic sensors.

testing chamber without however interacting with the sensor head. An attenuator is used to closely balance the two beams so they exhibits the same power when a sensor head is not present leading to a power of about 2 mW for both beams. With this method, the response of the sensor can be easily calculated by division of the measured signal by the measured reference beam. It is important to underline here that this is a direct (raw) measurement process and does not involve any lock-in detection or other mathematical estimation. The sensor signal and the reference are finally recorded using two identical dual-channel power meters (Newport model 2832-C) to simultaneous record up to four channels controlled by a data acquisition system operating in LabView™ environment developed in this work and used for data logging and real time display.

For the simple thin film sensor, the sensor responsivity, R, is defined as the normalized variation of optical transmission of the film:

$$R = \frac{\Delta T}{T_0} = \frac{\Delta I}{I_0} \tag{4.9}$$

where T_0 and T'_0 is respectively the transmissivity of the sensor head before and after the introduction of the gas to be detected, $\Delta T = T'_0 - T_0$ is the change of the transmissivity upon exposure to the analyte while $\Delta I = I'_0 - I_0$ is the change of the signal beam (the one that interacts with the sensor) and I_0 is the laser beam intensity that impinges on the sensing film. As already explained, I_0 can be set for convenience to equal the reference beam: $I_0 = I_{reference}$ for fast and simple signal processing by the data

acquisition system. The sensor sensitivity magnitude is defined as the sensitivity per analyte concentration change δC (usually expressed in ppm):

$$S = \frac{R}{\delta C} = \frac{\Delta \mathrm{I}}{\mathrm{I}_0\, \delta C} \quad (4.10)$$

Alternatively, for microstructured sensors, the light intensity of various diffraction orders is monitored and diffraction efficiency is defined by the ratio of the diffraction order intensity I_m to the total intensity of the beam impinging the sensor head I_0:

$$\eta_m = \frac{I_m}{I_0} \quad (4.11)$$

The responsivity function for the mth order may then be defined as the normalized mth–order diffraction efficiency variation:

$$R = \frac{\Delta \eta_m}{\eta_{m,0}} = \frac{\Delta I_m}{I_0} \quad (4.12)$$

where $\Delta\eta_m = \eta_m - \eta_{m,0}$ is the variation of diffraction efficiency of the specific diffraction order while the sensor sensitivity in this case is may be given by:

$$S = \frac{R}{\delta C} = \frac{\Delta \mathrm{I}_m}{\mathrm{I}_0\, \delta C} \quad (4.13)$$

We may note that the definition of responsivity and sensitivity may be defined using the zero-order undiffracted beam in a diffractive system as above. In that case the overall diffraction from the structure is taken into account.

4.8 Evaluation of ammonia sensors

Although the silica/$NiCl_2$ nanocomposite material exhibits a good selectivity to ammonia, it shows a small but detectable response to water vapor as will be presented later. To account for this cross sensing and since the analyte is introduced in water solutions, a well-designed protocol is required. To allow for maximum reliability and repeatability of the measurements, ammonia-water solutions at various concentrations are prepared for identical humidity concentration changes inside the chamber for each cycle. The quantity of water introduced into the chamber is always the same,

of the order of 1% RH (relative humidity) as measured by a commercial humidity probe (model USB humidi probe) while the ammonia environment is established by varying the ammonia concentration of the solution. The same probe configuration has been also used to verify that the temperature change inside the chamber during the analyte heating and pumping steps are kept low (in the order of 1°C).

Typical time traces of real time monitoring of a sensor responsivity at various ammonia concentrations is shown in Figure 4-9 for the case of a simple planar thin film sensor of about 1.5 μm thickness at high ammonia content exposure levels. In Figure 4-10 the 1st diffraction order of a typical microstructured sensor exposed to moderate ammonia levels (2100-3500 ppm) is recorded. In both cases the dotted lines indicate the instants of the ammonia insertion and that of the chamber evacuation by pumping and refilling with fresh atmospheric air for the re-establishment of ambient conditions. A responsivity plateau is reached at a timescale ranging from a few tens of seconds (10-30 sec), at low ammonia content, to a few hundred of seconds for full interaction of the sensing material for exposure to high ammonia levels. In all cases the rise time to the plateau is similar to the fall time from plateau to the ambient levels. Notably the sensing material exhibits a fully reversible behavior as the signal level is restored even when the sensor is exposed to a high ammonia concentration of up to 5000 ppm. Response time also accounts for the time required for the evaporation of the ammonia solution and vapor diffusion into the chamber, as well as the time needed for return to the ambient environment by evacuation. Both times are estimated to be $\sim$3 sec.

Figure 4-11(a) depicts the responsivity curve of a thin film ammonia sensor for a wide range of ammonia concentrations. The sensor shows a clear saturation trend at very high ammonia content in the 4000-5000 ppm region. However the sensor performance evaluation is focused on the lower ammonia concentrations (bellow 1000 ppm) presented in Figure 4-11(b).

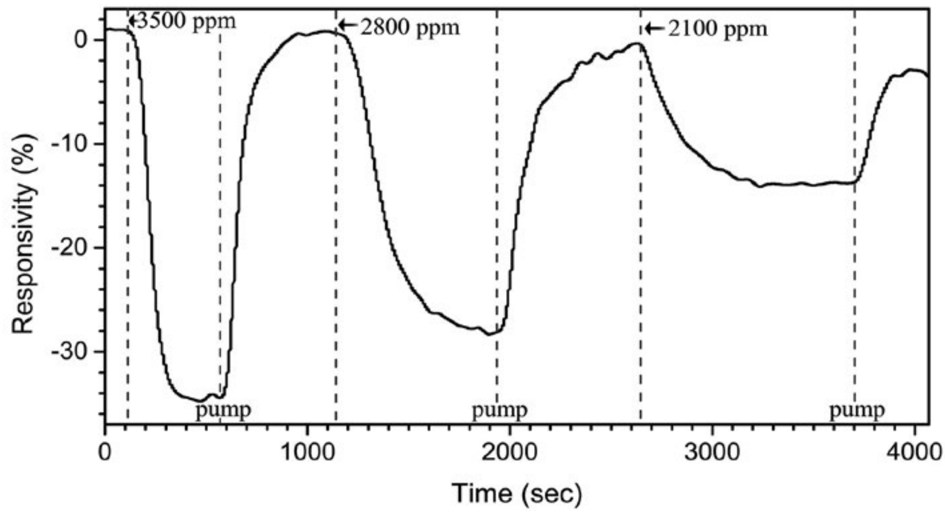

FIGURE 4-9: Temporal evolution of the real time responsivity of a thin film sensor exhibiting exposure at different concentrations of ammonia vapors. The dotted lines indicate the instant of ammonia insertion at known values into the chamber and consecutive evacuation by air flow to restore ambient, ammonia-free environment.

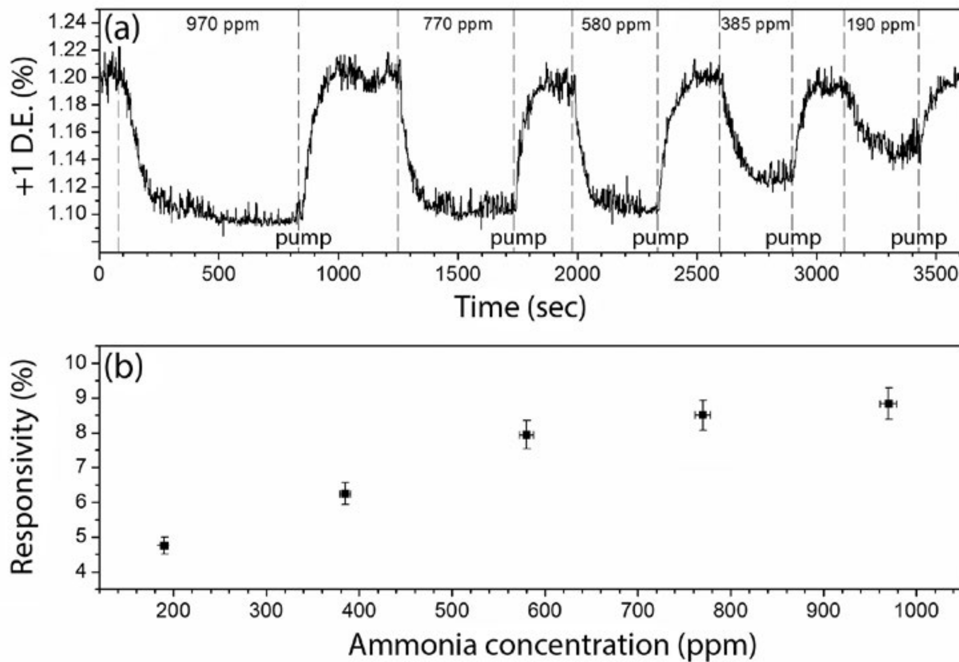

FIGURE 4-10: (a) Temporal response of the first diffraction order diffraction efficiency of consecutive cycles at various ammonia levels followed by evacuation down to the ambient environments and **(b)** the corresponding responsivity, R(%).

To highlight the sensor performance enhancement by incorporating of diffraction optics, particularly at concentration levels lower than 100 ppm, a diffraction grating (Λ = 60 μm, duty cycle 0.5) has been etched on the same sensor film covering an area of about 2×2mm to allow full coverage of the laser beam.

The use of the same thin film allows a direct performance comparison not affected by possible variation in the material and coating preparation. The responsivity of the 1st diffraction order is shown in Figure 4-11(a) revealing a clear responsivity enhancement over the simple thin film sensor.

A more systematic analysis of a sol-gel $SiO_2/NiCl_2$ diffractive optic ammonia sensor was performed by the simultaneous monitoring of several diffraction orders in transmission mode at relatively low ammonia levels. A diffraction grating with period Λ = 80 μm was etched on a 1.65 μm thin film with a duty cycle of 0.39. The -1, 0, and +1 diffraction orders, as well as the reference beam, were monitored. The photonic sensor head is positioned for interrogation at $\sim 22^o$ angle of incidence to attain the experimentally determined maximum responsivity. This geometry, which corresponds to the maximum slope of the diffraction efficiency curve, has been verified by a series of real time recordings at varying incidence. The diffraction

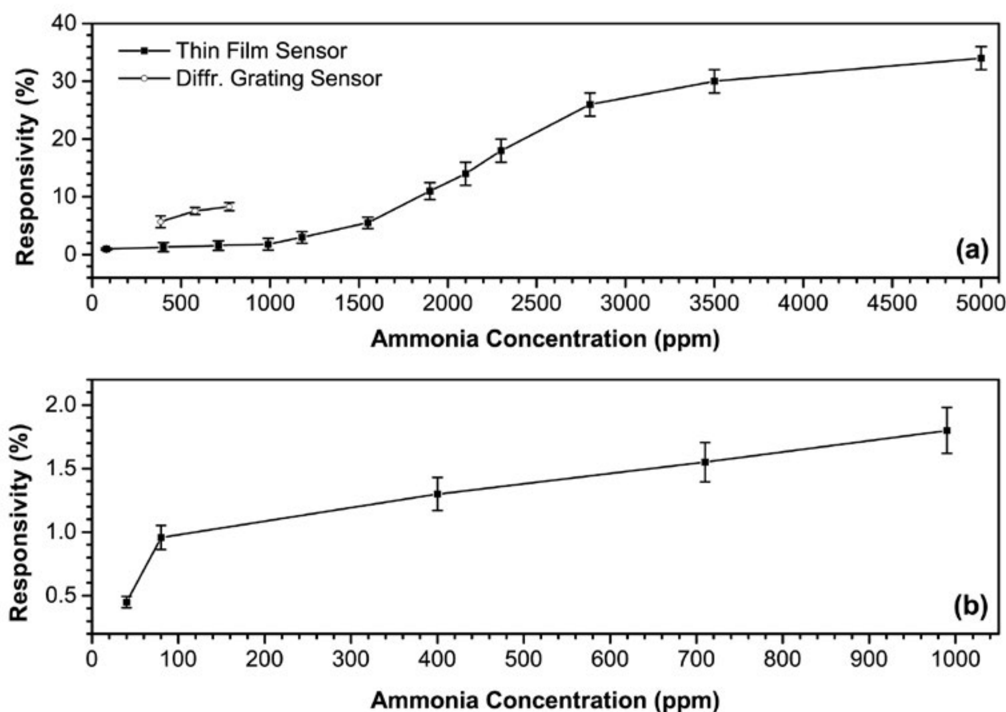

FIGURE 4-11: Responsivity curve of a sol-gel $SiO_2/NiCl_2$ planar thin film photonic ammonia sensor: **(a)** over a wide ammonia levels range up to sensor saturation region, and **(b)** a blow up at low ammonia concentrations. The response of the 1st order of a diffractive structure fabricated on the same film is also shown in **(a)** for comparison.

angle of the ±1 orders, measured with respect to the zero order, is found at 0.45°, while diffracted beams up to the 10th order were observable. Typical real-time recordings of the transmitted signals are shown in Figure 4-12. In these recordings a 150 ppm ammonia environment is established and is consequently followed by the pure atmospheric ambient. The small apparent bias is vanishing slowly with the out diffusion of ammonia at a longer time scale, of the order of 15-20 minutes.

In Figure 4-13 the responsivity of the sensor for various ammonia concentrations for all recorded diffractions orders is presented. The responsivity of the unprocessed planar thin film sensor was recorded from the laser beam being incident on the same sample at an area adjacent to the diffraction grating at the same angle of incidence. The measured zero–order sensitivity values $S_0 \sim 8.8 \times 10^{-5}$ ppm^{-1} was found similar to those of the unprocessed planar interface, $S_T \sim 1.3 \times 10^{-4}$. It is noted here that the expected value due to the reflection variation of

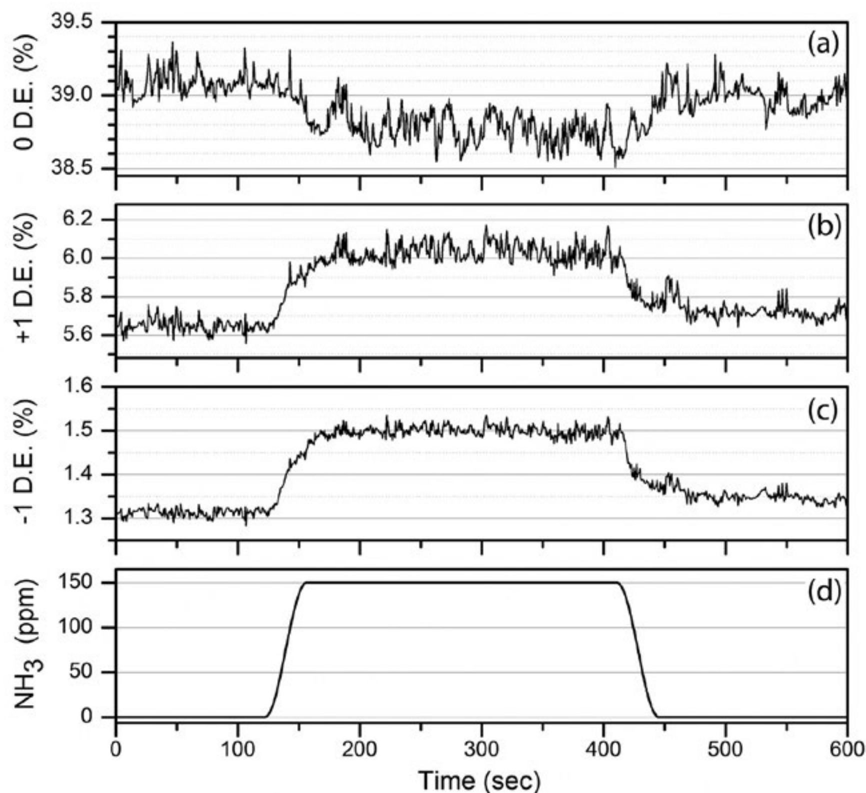

FIGURE 4-12: Temporal responsivity of **(a)** zero order, **(b)**, **(c)** ± 1 order to 150 ppm of ammonia and **(d)** the temporal concentration of ammonia.

the unpatterned thin film is $\sim 10^{-6}$ ppm^{-1} supporting the argument that the observed value was a result of the interferometric behavior of the thin film.

A six fold sensitivity increase for the ±1–order beams was, however found for $R_{-1} \sim 8.2\times10^{-4}$ ppm^{-1} and $R_{+1} \sim 3.2\times10^{-4}$ ppm^{-1}. The difference between the +1–order and -1–order sensitivity is attributed to the geometry of the diffraction grating combined with the asymmetric readout. In the same figure the small but traceable response to humidity is indicated for a 0 ppm ammonia responsivity. This measurement explained by inserting an equivalent quantity of water identical to the water content of the ammonia water solutions of all measuring steps. The ±1–order responsivity also exhibited a higher signal-to-noise ratio (SNR), defined as the ratio

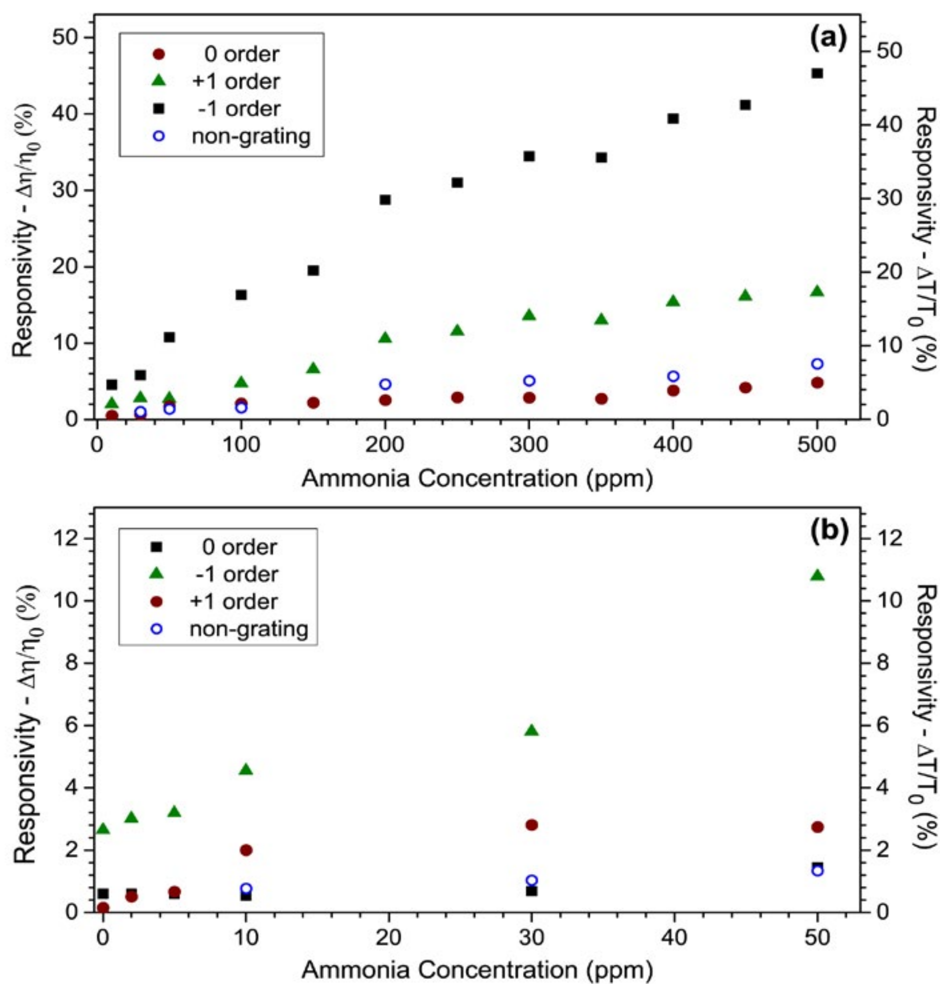

FIGURE 4-13: Responsivity of the diffraction grating sensor to various ammonia concentrations of zero order and ± 1 order. The response of the unprocessed planar sensor thin film sensor is shown in the same figure for comparison. **(a)** Overall responsivity and **(b)** low ammonia level responsivity.

of the diffraction efficiency change over the standard deviation of the signal. SNR for the +1–order is 18.6, as contrasted to the 3.5 found for the zero order. Moreover in Figure 4-13 where the low concentration section is presented a lowest detectable value at 2 ppm is feasible for the -1–order.

The repeatability of the diffractive optic sensor is illustrated in Figure 4-14 with a series of measurements at moderate ammonia level concentrations. The alteration of the responsivity of the first diffraction order of an ammonia sensor is measured for various ammonia volumes followed by re-establishment of the ambient environment. The nano-entity sensing material shows no memory and a fully reversible behavior at the time range of about 10 minutes between different exposures has been observed.

4.9 Ultra-low cost fabrication method of diffractive optic sensors micropatterning by soft lithography

Since the Remote Point Sensing scheme aims at low cost monitoring of large areas for physical and chemical agents, alternative fabrication methods for the production of cheap diffractive optic sensors have been explored in this work. As already demonstrated, the direct laser etching microfabrication allows for fabrication of high quality photonic structures without alterig the non-processed material properties. While the scheme may be ideal for scientific research, it is time consuming and cannot provide a high production throughput suitable for large scale industrial production. On the other hand, conventional photolithographic methods widely

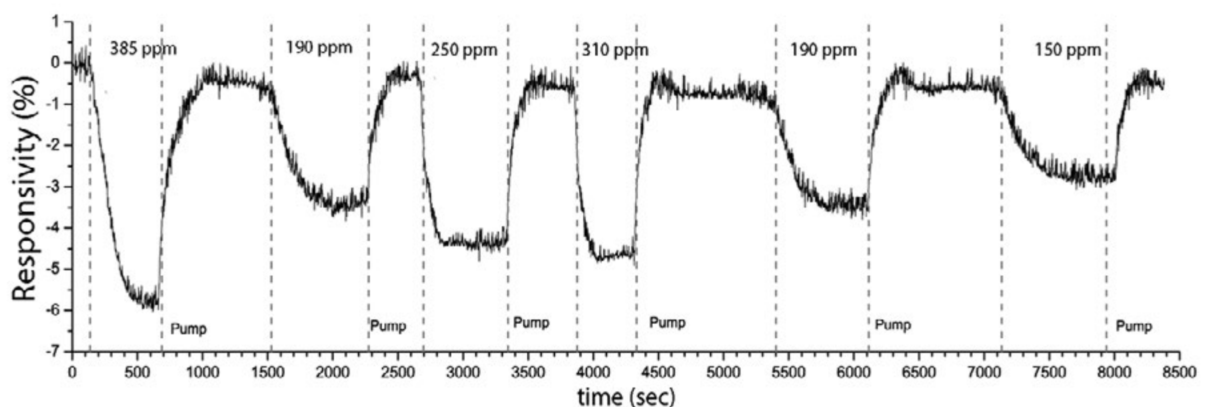

FIGURE 4-14: Repeatability recordings of diffractive optic sensor tested.

used for mass production cannot be applied as they produce irreversible damage to the sensing material. Alternative lithographic methods, however, developed for low replication cost and versatility such as soft lithography have been explored here to fabricate $SiO_2/NiCl_2$ diffractive optic sensors.

For soft lithographic replication, an initial master stamp is fabricated. This task can be accomplished by means of standard photolithographic techniques, e-beam lithography or any other micro/nanofabrication method. The master stamp is then transferred to a re-usable PDMS stamp. In our studies, the ArF excimer laser microfabrication technique was applied for the fabrication of the master. Polystyrene (M_w = 3500 purchased from Aldrich) solution in toluene at 0.1 gr/ml concentration is prepared and spin coated on a clean precut microscope glass substrate at 2000 rpm for 60 seconds, to form a 1.5 μm thick thin film as measured with a KLA Tencor Alpha Step profilometer. The film is baked at 120°C for 15 minutes to completely remove the remaining solvent prior to micropatterning. A 3×3 mm diffraction grating is then patterned on the polystyrene film with a period of Λ = 100 μm and duty cycle of 0.29. The stamp is prepared by mixing the PDMS precursor (Dow Corning Sylgard 184) with its curing agent at the standard 10:1 mass ratio and left in vacuum for 30 minutes to remove any trapped air inside the viscous liquid (debubbling). The uncured PDMS is then slowly poured onto the master placed inside a simple container to prevent formation of air bubbles and heated at 125°C for 30 minutes for curing. Finally, the already hardened stamp is released from the master and cut to size with a scalpel. Since an antisticking agent has not been used, parts of the initial polystyrene master might detach from the glass substrate and migrate to the PDMS stamp. To account for this, the PDMS is rinsed in a toluene bath for one hour to dissolve the polystyrene remains. The solvent does not affect the PDMS material and only induces swelling. The stamp was subsequently heated in the oven at 125°C for 30 more minutes and placed in vacuum for a couple of hours to dry it in order to enable its use in the next step.

The soft lithography technique is usually exploited with UV curable materials in combination with the high transmissivity of the PDMS in the UV spectral window (even the 340 nm range), with thermo-curable materials, or with ink transfer usually for low viscosity materials. The $SiO_2/NiCl_2$ nanocomposite exhibits none of the aforementioned properties, thus two alternatives of the standard soft lithography methods have been used, namely the solvent-assisted micro molding (SAMIM)[155,159,161,171] and the molding in capillaries (MIMIC).[155,159,161,258–260]

The use of SAMIM method has been previously discussed in paragraph 3.12. The stamp is applied under pressure on a film softened previously by wetting in a solvent. The solvent evaporates through the PDMS mask and the pattern is cured. The silica sol-gel material cannot, however, be softened after hydrolysis and polymerization and thus a simplified technique has been applied, originally designed for further reducing the fabrication time. A droplet of the $TMOS/NiCl_2$ solution (in liquid form) prepared as described in paragraph 2.9 is deposited on a glass substrate on top of which the PDMS stamp is applied. The alcohol and water in the mixture, as well as those produced by the hydrolysis, evaporate through the stamp while the sensing material is slowly hardened over a time scale of 3 hours. Finally, the stamp is removed gently from the newly formed micropattern as it is allowed by the inherently poor adhesion of the sol-gel on to the PDMS stamp for fast and accurate replication of the diffractive structure.

The main disadvantage of the SAMIM method is the presence of a thin inhibition layer that remains on the grooves of the diffraction grating shown in Figure 3-47(b), a deviation from the ideal SRG.

As alternative, the MIMIC method does not suffers from any inhibition layer, as the stamp is first firmly applied on the glass substrate prior to the addition of $TMOS/NiCl_2$ solution. The liquid to be cast is then applied as a droplet on one side of the open edges of the stamp as shown in Figure 4-15(a). Capillary ensures the filling of the grooves with sensing material, which then exhibits full hydrolysis and

polymerization (in about 3 hours). The excess of the material is removed with a razor after the removal of the stamp. Although there is no inhibition layer remains as shown in Figure 4-15(b), the main drawback of the MIMIC method is the limited uneven filling of the grooves and the large processing time. None of these issues imposes a considerable problem since a 2×2 mm diffraction grating is easily fabricated. An active area large comparable to the laser beam spot size is thus adequate for using the diffractive optic sensors under the RPS scheme.

A microscope image of the diffraction grating structures fabricated using the simplified MIMIC method is shown in Figure 4-16(a). The uneven filing of the channels is shown in Figure 4-16(b). Profilometry measurements of both the PDMS stamp and a diffractive optic sensor presented in Figure 4-17(a) and (b) respectively reveal a difference in the heights due to the shrinkage of the material during evaporation of the solvent. It is apparent from these figures that the diffractive structure profoundly deviates from the ideal SRG. It is noted, however, that this low quality, ultra-low cost sensing diffraction gratings exhibit clear diffraction orders and good responsivity to ammonia. The well-defined diffraction pattern of the structures illuminated by a HeNe laser beam at 632.8 nm is shown in Figure 4-18(a) while the power distribution among the diffraction orders in terms of diffraction efficiency, η, is shown in Figure 4-18(b).

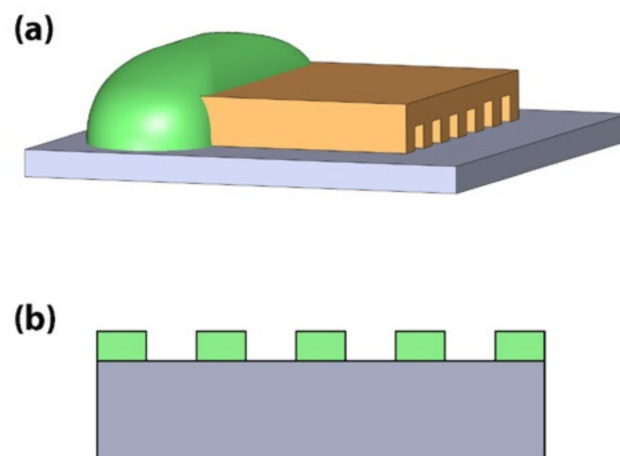

FIGURE 4-15: (a) Schematic illustration of the molding in capillaries (MIMIC) fabrication method, **(b)** schematic of the inhibition layer free cross section of the diffraction grating.

Sensing performance for ammonia detection is shown in Figure 4-19 for three different materials by monitoring the +1st diffraction order. The silica sol-gel/$NiCl_2$ responsivity is shown in Figure 4-19(a) for moderate ammonia levels while in Figure 4-19(b) another silica sol-gel nanocomposite has been studied where the $NiCl_2$ nano-entities have been replaced by $CuCl_2$ in a synthetic route similar to the one presented in paragraph 2.9. This nanocomposite exhibits inferior ammonia sensing performance to its $NiCl_2$ counterpart. Finally, in order to investigate the applicability of the MIMIC fabrication method to another family of materials, the performance of a novel block copolymer (polystyrene sulfonate-b-tert-butylstyrene – SPS-b-PtBS, initially dissolved in methanol) as an ammonia sensor has been studied and shown in Figure 4-19(c). The performance of this advanced block copolymer overcomes the inorganic nanocomposites with the limitation of reduced selectivity. Its responsivity however can be adjusted at a predefined level for each agent by choosing the ratio of the hydrophobic and hydrophilic blocks during synthesis. More details on the synthesis and characterization of the SPS-b-PtBS block copolymer can be found in ref. [261]

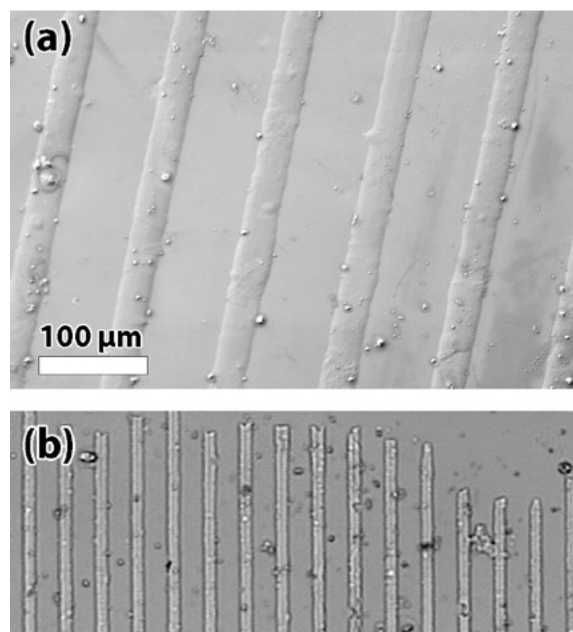

Figure 4-16: Microscopy images of diffraction grating using the MIMIC procedure. **(a)** A close up of the diffractive pattern, **(b)** unevenly filled channels at the edges of the diffraction grating

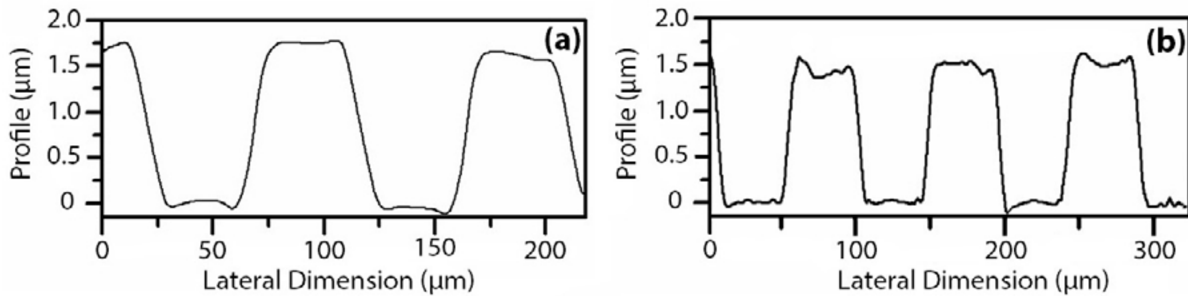

FIGURE 4-17. Profilometry measurements of **(a)** the PDMS stamp and **(b)** a diffractive optic sensor fabricated using the MIMIC method.

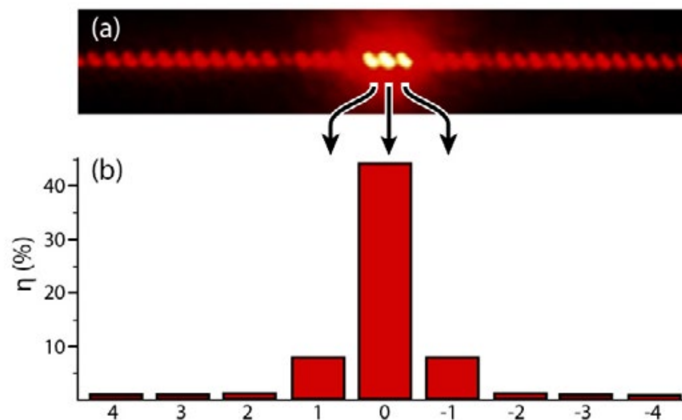

FIGURE 4-18: (a) Photograph of the diffraction pattern of the structure shown in Figure 4-16 illuminated with a HeNe laser at 632.8 nm and **(b)** the power distribution for orders from +4 to the -4 diffraction orders expressed in diffraction efficiency η.

Compared to the diffractive optic sensors fabricated using the direct laser etching method of the same sensing material (silica sol-gel/$NiCl_2$), soft lithographically produced structures lack the high quality of the DLAM structures as observed under an optical microscope or SEM and in terms of generation of clear, well-defined diffraction orders. The sensing performance however is almost comparable with that of the directly etched sensors exhibiting a maximum sensitivity of $S_{-1} \sim 4.2\times10^{-4}$ ppm^{-1} for the 1st diffraction order, value of the order of $S_{-1} \sim 8.2\times10^{-4}$ ppm^{-1} and $S_{+1} \sim 3.2\times10^{-4}$ ppm^{-1} of the higher quality direct laser etched sensor.

In conclusion soft lithography techniques provide an alternative fast and reliable microstructuring route for the fabrication of ultra-low cost diffractive optic sensors of adequate quality operating under the RPS scheme, suitable for large volume, high throughput production.

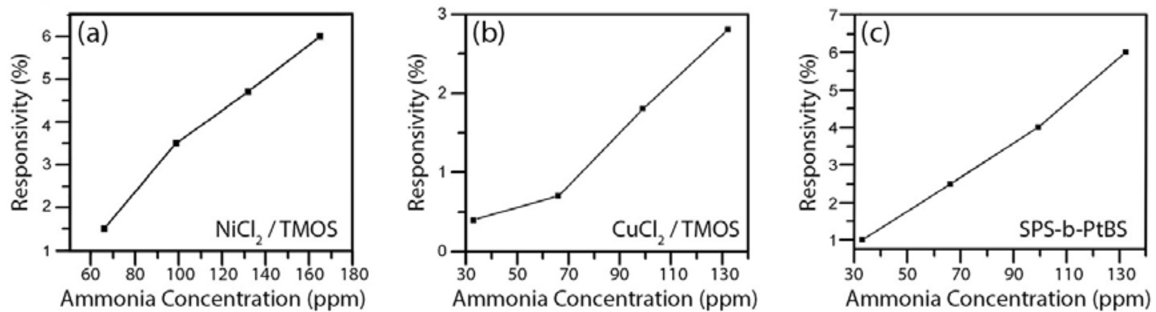

FIGURE 4-19: The +1st diffraction order responsivity of three different diffraction grating ammonia sensors fabricated using the MIMIC method with different sensing materials: **(a)** $CuCl_2$ nanoclusters in silica matrix sol-gel (TMOS) matrix, **(b)** (a) $NiCl_2$ nanoclusters in silica matrix sol-gel (TMOS) matrix, and **(c)** block copolymer SPS-b-PtBS.

4.10 Theoretical study for optimum design of the diffraction sensors

To fulfill the requirement of high sensitivity and high signal-to-noise ratio, the diffractive optic sensor needs to be built with a sensing material that produces a substantial response to the presence of the agent to be detected in terms of reversible refractive index alteration. Such changes of the optical path in the sensing material need to be transferred efficiently to the interrogating beam. Therefore, in addition to the sensing material design, another route for responsivity enhancement is the exploitation of functional optical structures having properties strongly dependent on the refractive index of the sensing material.

Diffractive optical elements (DOEs), as well as more complex diffractive structures such as photonic crystals, offer a unique potential for detecting effective changes of the materials. In the case of DOEs, the intensity and/or the position of the diffraction fringes strongly depend on the refractive index of the patterned material. Diffraction gratings in the form of SRG are a most cost effective solution, due to their simplicity and convenient fabrication compared to other DOEs and photonic crystals.

To enable an optimum sensing operation in terms of high sensitivity, design guidelines are provided by means of simulation and theoretical study of the diffractive optic sensor. It is intuitive that a small change δC of the concentration of the agent to be detected corresponds to a fixed refractive index variation. The aim of the theoretical study is thus to identify which combination of sensor geometrical characteristics for a given sensing material delivers the maximum diffraction efficiency alteration for a small change of the refractive index of the material, ensuring the maximum slope of the $\eta_m(n)$ function, i.e. $\max\{\partial\eta_m/\partial n\}$. To this end, it is convenient to modify for simplicity the definition of the sensor sensitivity as the normalized derivative of the mth order diffraction efficiency over the refractive index:

$$S_m = \frac{|d\eta_m / dn|}{n_{m,0}} \tag{4.14}$$

This allows us isolation of the sensitivity enhancement due to diffraction of the structure as a response of the sensing material as a function of the refractive index.

In this context the Rigorous Coupled Wave Analysis (RCWA) has been exploited.[262–264] RCWA is a well-established method for the modeling of SRG and is described in Appendix C. Figure 4-20 depicts the typical geometry of an SRG. Three regions are identified: region I the surrounding medium (usually air in the case of operation under the RPS scheme), region II the corrugated grating and region III the substrate. In Figure 4-20 the SRG geometrical characteristics of interests are also depicted: the diffraction grating h (the film thickness), the grating period a and the line width w. Moreover the duty cycle is defined as the ratio of the line w over the grating period:

$$duty\,cycle = \frac{w}{\mathrm{a}} \tag{4.15}$$

To analyze the SRG in the context of RCWA, the rigorous wave equation is solved in the three regions without any assumptions, as commonly applied in regular coupled mode theory and the solutions for the electric and magnetic fields are matched at the boundaries. RCWA is practically an efficient algorithm to solve

coupled-wave amplitudes by diagonalizing the coefficient matrix defined by the rigorous (assumptions-free) coupled-wave equations. This is facilitated by means of state-variable representation of the coupled amplitudes. RCWA encompasses the accuracy of full modal approaches and the computational efficiency of approximation bounded common coupled-wave theories.

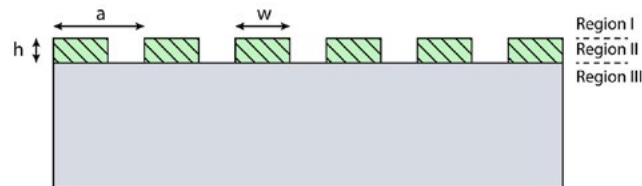

FIGURE 4-20: The SRG geometry used for theory and design.

For the optimization process the goal is to identify sensor configurations that exhibit maximum slope, $|d\eta_m / dn|$ since that is translated into maximum sensitivity as expressed by equation . On the contrary, configurations showing a maximum or minimum value of η_m versus n, correspond to zero slope and thus exhibit minimum sensitivity. The study is limited to the first and second–order terms, as these terms are more sensitive to changes of the refractive index. This fact has been confirmed experimentally. Moreover, the responsivity to the first– and second–order terms, show a higher signal-to-noise ratio as compared to the zero–order (DC term). The higher–order terms usually exhibit a low intensity therefore they are more difficult to measure. The optimization study, also aims at forcing power out of the zero order, and channel it to the more sensitive higher orders, preferably to the first order. As it will be shown, the responsivity of the sensor spans from 0 to 300 for different configurations, thus a proper choice of geometrical characteristics is crucial for maximum responsivity to be achieved.

Figure 4-21(a) shows the change of the first–order diffraction efficiency of for a normal incidence as a function of grating depth (h). It is evident that a small change in grating depth of the order of 0.1 μm for a given value of n translates into a drastic change

of the diffraction efficiency. This is crucial for establishing the appropriate fabrication protocol. The alteration of the diffraction efficiency versus refractive index is shown in Figure 4-21(b). However, for the graph of interest in the RPS scheme, the optical path inside the sensing material mainly changes due to alternation of n. The effect of refractive index, n, is less acute for the range of refractive index under consideration. It acts as a scaling factor for some configurations as shown in the figure. A proper choice of the film depth leads to a higher sensor sensitivity for the first order as indicated by the larger slope for h = 1.0 μm and h = 1.2 μm compared to h = 1.4 μm. On the contrary, the second–order diffraction shown in Figure 4-21(c) and (d) behaves differently since the slope for h = 1.4 μm in Figure 4-21(d) is large while the expected responsivity for h = 1.2 μm is smaller. It is also noted here that these trends are in agreement with previous studies on holographic concentrators.[265] In these studies, valid for small refractive index variations, a $\sim \sin^2(h)$ dependence of the diffraction efficiency is shown.

The dependence of the first–order diffraction efficiency on the grating period (a) for various refractive indices of the sensing material is shown in Figure 4-22(a) and that on the refractive index for various grating periods is shown in Figure 4-22(b). Correspondingly, the same dependence of the second–order is shown in Figure 4-22 (c) and (d). The diffraction efficiency of the SRG has a quasi-periodic dependence on grating period similar to the thickness dependence, but is more complex. These results also agree with the analytical studies[265] for the low refractive index cases. An oscillatory behavior is shown in Figure 4-22 with decreasing strength as the period increases since longer periods generate higher orders that draw optical power with the consequent reduction of the diffraction efficiency of the first and second orders. In Figure 4-22(b), a set of different grating periods from 40 to 100 μm is examined. It is evident that for the said refractive index range a period of a=40 μm exhibits a maximum diffraction efficiency for the first–order while for the same diffraction order the curves for a=60 μm and, a=80 μm, and a=100 μm exhibit a negative slope,

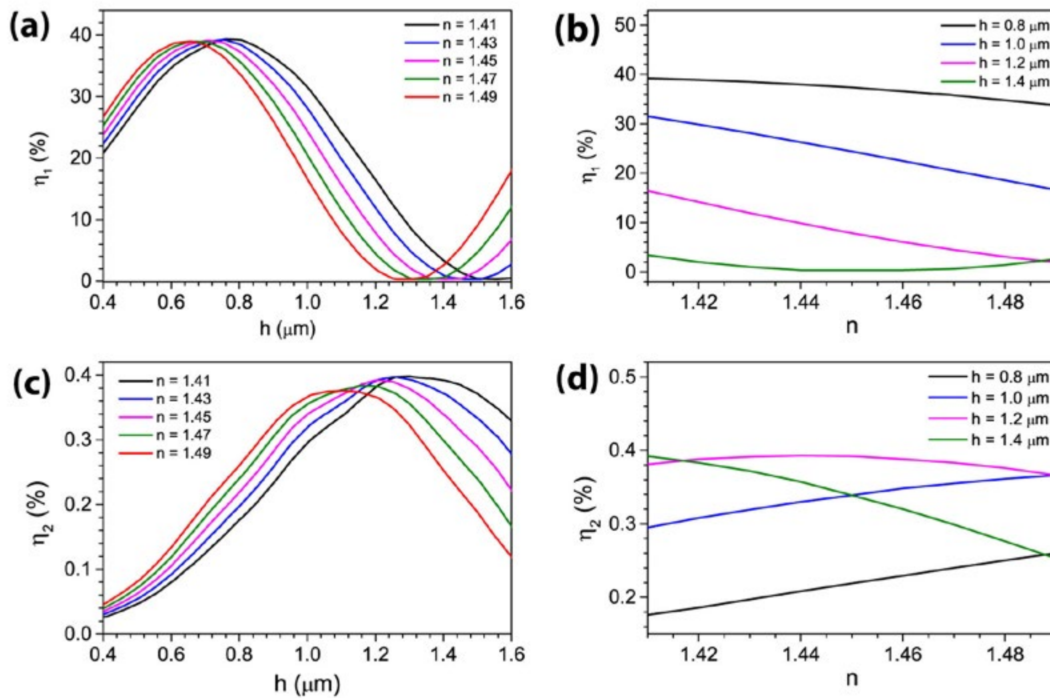

FIGURE 4-21: Variation in the diffraction efficiency as a function of grating depth, h, for various refractive indices and corresponding change with refractive index, n, for various grating depths of: **(a-b)** the first diffraction order and **(c-d)** the second diffraction order. The other characteristics of the diffraction grating are: period a = 100 μm and duty cycle = 0.5.

a positive slope and a minimum value, respectively, indicating the a=60 μm and a=80 μm value as the proper grating period, ensuring maximum sensitivity, under these circumstances. This behavior of the second–order again differs as shown in Figure 4-22(c). Its exhibits a maximum close to the values of the period where the first–order exhibits a minimum. Moreover, the positive slope dη/dn for a=60 μm in Figure 4-22(d), opposite to that of the first order, indicates a power transfer from the first to the second and higher orders for a small refractive index change.

The study of the influence of the last geometrical parameter of a SRG, the duty cycle, is shown in Figure 4-23 for the first–order diffraction efficiency versus duty cycle for various refractive indices in Figure 4-23(a) and versus refractive index for various duty cycles in Figure 4-23(b) while the same dependences of the second–order are shown in Figure 4-23(c) and Figure 4-23(d) respectively. The power dependence of the first diffractive order is almost symmetric with a maximum at around 0.5. The behavior is similar for the second–order although its strength issignificantly smaller in most duty

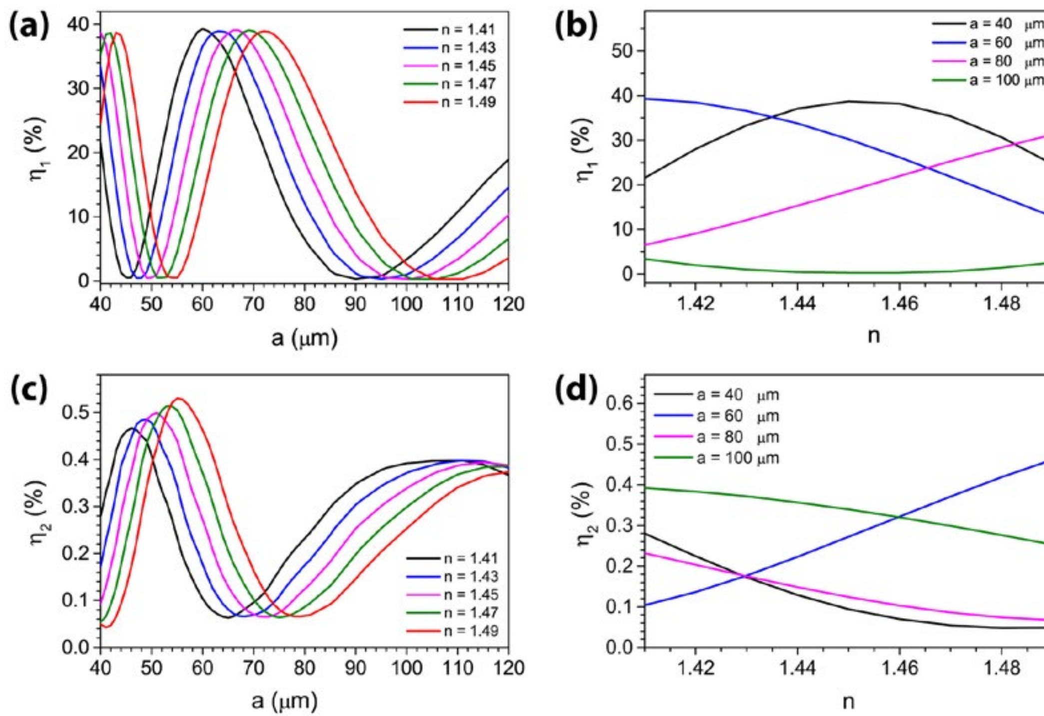

FIGURE 4-22: Change in the diffraction efficiency as a function of grating period, a, for various refractive indices and corresponding change with refractive index, n, for various grating periods of **(a-b)** the first diffraction order and **(c-d)** the second diffraction order. The other characteristics of the diffraction grating are: grating depth h = 1.4 μm and duty cycle = 0.5.

cycles. The curves versus the refractive index show the existence of sensor configurations exhibiting minimum sensitivity (zero slope). It is clear that such configurations should be avoided. It is also noted that minima of the first and second orders are obtained for different values of n while the diffraction efficiency curves resemble a parabolic shape.

A convenient way to experimentally increase diffraction efficiency and sensor responsivity is by varying the angle of incidence, θ, of the interrogating beam. This additional degree of freedom is inherent to the RPS scheme operating here. Figure 4-24 shows the variation of diffraction efficiency as a function of angle of incidence for various refractive indices and as a function of the refractive index for various angles of incidence. Depending on the refractive index of the grating, the diffraction efficiency can be monotonically increased or it can have a minimum value (close to zero) at a certain angle. As depicted in Figure 4-24, at certain angles the second–order diffraction efficiency becomes higher that the first–order. Proper choice of angle of

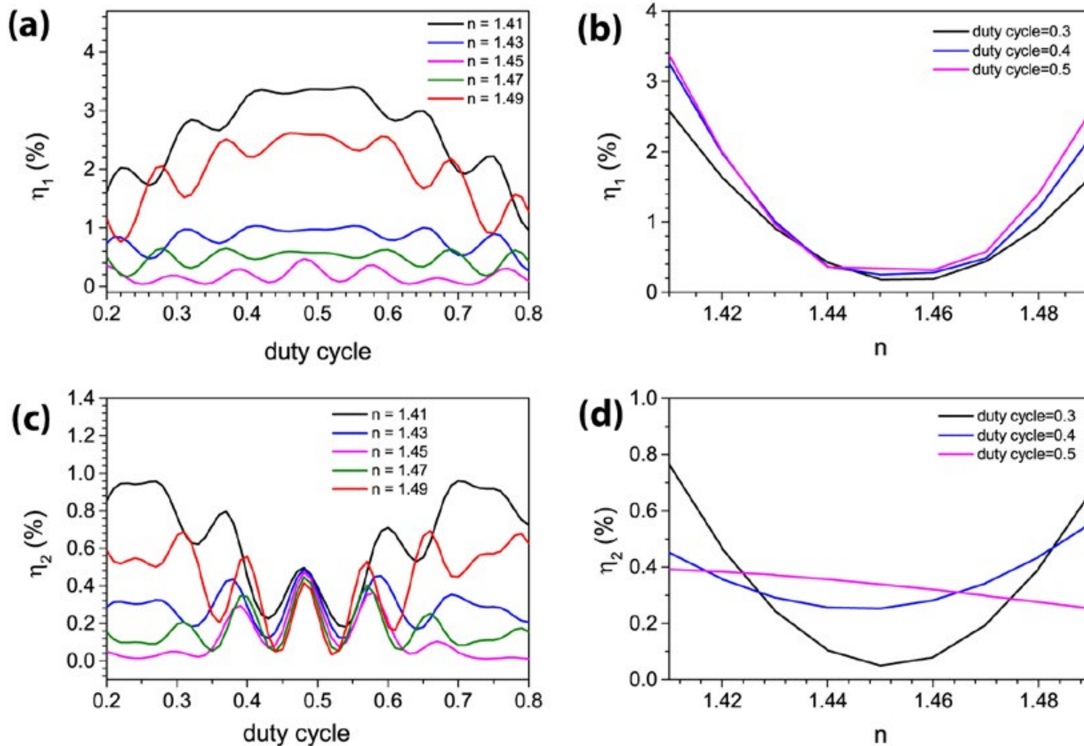

FIGURE 4-23: Change in the diffraction efficiency as a function of grating duty cycle for various refractive indices and corresponding change with refractive index, n for various duty cycles of **(a-b)** the 1st diffraction order and **(c-d)** the 2nd diffraction order. The other characteristics of the diffraction grating are: grating depth h = 1.4 μm and period = 100 μm.

interrogation is therefore critical in order to optimize the responsivity. From the above discussion it becomes clear that for a sensor configuration maximum responsivities cannot be obtained for both orders. This has been verified experimentally for a sensor with h = 1.39 μm, a = 100 μm and duty cycle 0.39. For this configuration the sensor exhibits a response R_0= 5.73±0.45 % at θ=0° and R_{20}=4.95±0.43% at θ=20° for the first diffraction order when exposed to 150 ppm of ammonia, while the second–order shows a response of 0.78±0.50% for θ=0° and 1.83±0.50% for θ=20°.

Figure 4-21 to Figure 4-24 demonstrate the behavior of the 1st and 2nd orders, which attain maxima in an alternating manner. The predicted trends of Figure 4-24 have been confirmed experimentally and are shown in Figure 4-25 which present the diffraction efficiency of the 1st and 2nd order of sol–gel $SiO_2/NiCl_2$ SRGs (again h=1.39 μm, a=100 μm and duty cycle = 0.39). By varying the incidence angle, the behavior of both 1st and 2nd orders confirms the theoretical predictions.

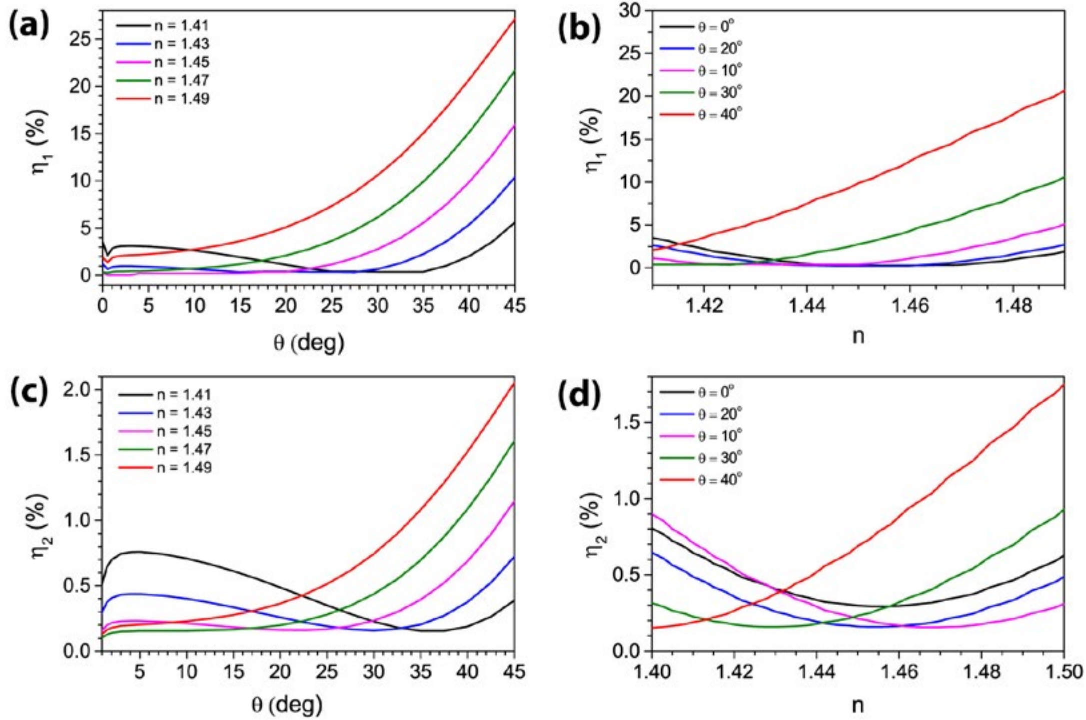

FIGURE 4-24: Variation in the diffraction efficiency with the angle of the incident beam –θ for various refractive indices and corresponding change with refractive index, n, for various angles of **(a-b)** the 1st diffraction order and **(c-d)** the 2nd diffraction order. The other characteristics of the diffraction grating are: grating depth h = 1.4 μm, grating period a = 100 μm and duty cycle = 0.39.

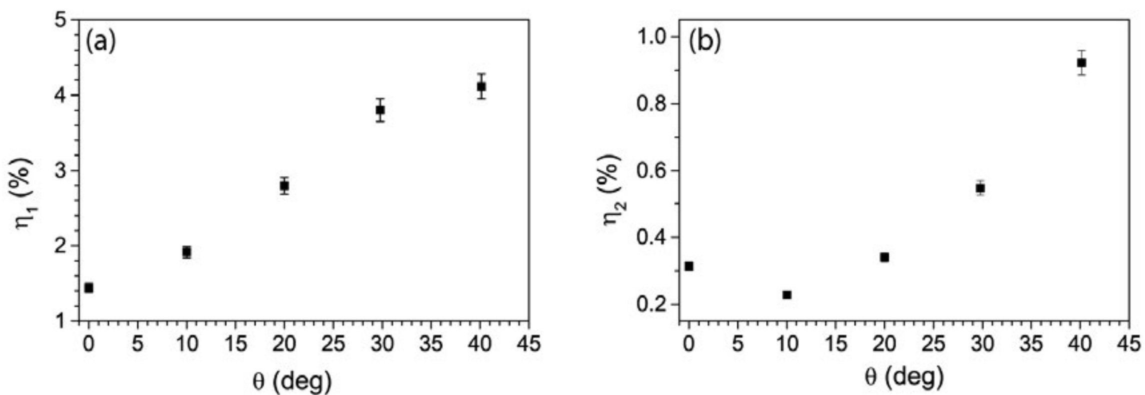

FIGURE 4-25: Experimentally measured diffraction efficiency of the **(a)** first and **(b)** second diffraction orders of a SGR with a = 100 μm, h = 1.39 μm, and duty cycle = 0.39.

We may note at this point, that a full matching of the experimental measurements and the theoretical predictions is not possible. This is mainly attributed to the real parameter values which are very difficult to be accounted in the theoretical models. They relate to geometrical differences due to fabrication factors, material imperfections and scattering losses. A comparison of Figure 4-21 to Figure 4-24 implies that the

diffraction efficiency of the SRG becomes quite dependent on geometrical irregularities of the produced diffractive structure. The limited accuracy of the fabrication method, the fluctuations of the thin film thickness and deviation from the ideal square profile are important issues. Nevertheless, the present study serves quite well to identify the optimal design aspects and the trends for maximum sensor responsivity.

4.11 Conclusions

In conclusion, diffractive optic sensors operating under the RPS scheme meet the requirements for effective sensing, including an improved sensitivity and reliability. Combined with high performance sensing materials such as the silica sol-gel/$NiCl_2$ studied here exhibiting excellent ammonia sensing with good selectivity, RPS can be exploited for monitoring of a large area benefiting from the low cost of the RPS method. This cost effectiveness stems from the low device fabrication and operation cost of the RPS scheme. The usage of low cost sensing materials and casting methods provides a cheap and simple fabrication method for the diffractive structure, namely the direct laser etching method and soft lithography. In addition, soft lithography merits from its inherent suitability for high throughput production. Diffractive optic sensor fabricated using direct Deep UV laser microfabrication techniques were tested at the laboratory environment and were found to yield sensitivity value of 8.4×10^{-4} ppm^{-1} for the detection of ammonia at a lowest possible level of 1 ppm. Soft lithographically produced yield a sensitivity of 4.2×10^{-4} ppm^{-1}. Experimental measurements also confirm the superior performance of diffractive optic sensors in comparison to the planar, unprocessed thin films. Moreover an elaborate theoretical study of SRGs for the enhancement of the operational characteristics of optical sensors, provides useful design guidelines for achieving maximum sensor performance.

4.12 Future work

Although the present work focuses on ammonia sensors operating under the RPS scheme which has been synthesized with the sol-gel route, a wide range of materials can be used as well for sensing of a large variety of gases. Moreover the RPS has been successfully demonstrated for temperature sensing using oxide multilayer structures. This work is discussed briefly in Appendix B. The actually limitation on the choice of materials is the requirement for not only effective sensing in terms of sensitivity and selectivity but also the ability of the sensing material to be compatible with a casting technique yielding thin films of good optical quality. The method thereby can be combined with materials with entirely different properties such as polymers (already discussed briefly), metal oxides, semiconductors etc. Almost no limitation on the fabrication of DOEs applies since the Deep UV direct laser microetching techniques exploited here is highly versatile and can be used to pattern almost any film of any material. The ultra-low cost soft lithography technique however is less versatile and the compatibility with each material needs to be explored. Alternative fabrication techniques such as the nanoimprinting lithography (NIL)[151–156,159,266–273] can also be explored aiming at the low cost replication of the DOEs. Probably the most desired method for the large scale production of ultra-low cost sensor heads operating under the RPS scheme is the roll to roll method[151,268,273–277] for the simultaneous casting and micropatterning of the sensing material on flexible low cost substrates (e.g. polyethylene terephthalate –PET, a common polymer material with excellent optical material and durability). Such a fabrication system would be expected to allow for fabrication cost reduction by more than one order of magnitude. Thus the plethora of sensing materials and fabrication techniques that can be exploited in the context of the RPS scheme provides opportunities for further studies of this effective sensing scheme.

In addition to the fabrication procedure enhancements, routes for the performance enhancement of the RPS sensors can be provided by use of photonic

structures exhibiting larger sensitivity to refractive index alteration than the diffraction gratings used here. Such structures may include computer generated holograms (CGHs) and photonic crystals. It should be noted that although providing designing guideline for such structures is challenging due to the advanced theoretical models that needs to be develop, the fabrication methods, thus the fabrication cost of the sensor head will not be altered significantly.

Simultaneous multiple sensing from a single sensor head can also be demonstrated by use of cross grating structures and other type of moiré patterns. These multi-levels structures generate complex diffraction patterns at different orientations. Fabrication of each level with a different sensing material can provide sensing abilities for different agents at each diffraction pattern orientation. Structuring of the upper levels without damaging the lower patterns however poses a serious challenge for the fabrication of such devices. In this context, micro contact printing (μCP) and direct inkjet printing[278–281] are methods that can be exploited effectively.

Lastly, diffractive optic sensors operating under the RPS are to be tested under real life applications for long distance monitoring. The reliability of the optical systems required for long paths transmittance (> 1 km) of the beams through the atmosphere needs to be evaluated and designs to account for compensating transmission disruption (e.g. optical turbulence) need to be tested in-situ.

CHAPTER 5
QUANTUM DOTS IN HIGHLY RESONANT SEMICONDUCTOR STRUCTURES

5.1 Introduction

High speed internet and device connectivity have played a huge role in modern society advancement, allowing for changes that have re-shaped the way the global economy, marketplaces and societies function and operate. These revolutionary technological advancements have been mainly based on three inventions of the second half of the 20th century: a) the development of integrated electronics and computers, b) the development of optoelectronics and c) the invention of low attenuation fiber optics, along with the development of information theory by Shannon in 1948.[282]

Massive data transfers along the globe would have probably never become possible only with the use of copper wires and satellite communications, due to their limited bandwidth. On contrary, fiber optics networks allow for low-cost, long-distance, high-volume, high-speed data transfer and have played a crucial role in the advent of the information age. Long-distance fiber optics communication systems usually operate in the O-band (around 1330 nm) and C-band wavelength (around 1550 nm) and are based on fast modulation and light transfer. The requirements

of high performance optical communication systems for long distance data transfer such as fiber optics, apart from the need of low loss waveguides, include transmitters and modulators capable for ultra-fast, error-free generation and modulation.

Semiconductor heterojuction lasers were the first high performance optoelectronical light sources available. Their performance was significantly enhanced in the 1970s by exploiting the effect of quantum confinement in low dimensional semiconductor structures. In quantum well (QW) optoelectronic components quantum confinement occurs in one dimension and such devices are still today the most commonly available semiconducting lasers. Briefly, low dimensional semiconductor devices benefit from the alteration of the density of states (DOS) and the reduction of the degrees of freedom in the carriers movement, and therefore the increase of the density of available carriers in the band edges. QW lasers typical exhibit lower threshold currents and higher gain compared to bulk heterojunctions. An illustration of the DOS of lower dimensional semiconductors is given in Figure 5-1.[283,284]

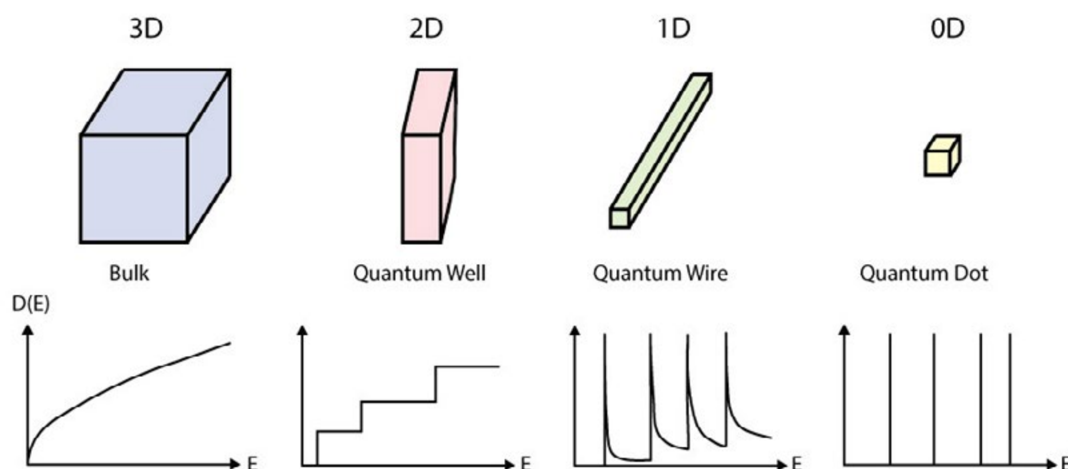

FIGURE 5-1: Density of state function of energy for bulk semiconductor materials and successively reduced dimension semiconductor structures: quantum wells (2D quantum confinement), quantum wires (1D quantum confinement), and quantum dots (0D quantum confinement).

In quantum dots the carriers are confined in all three dimensions and the DOS has a fully discrete, δ-function form (neglecting homogeneous broadening) forcing the carrier to concentrate at narrow energy levels. Their special properties give rise to a number of advantages over QW active devices such as semiconductor lasers including:[285]

- lower threshold current
- higher gain and differential gain
- better temperature stability
- possible higher modulation speed
- lower linewidth enhancement factor
- narrower lasing linewidth
- low damage threshold of the facets due to suppression of facet heating, attributed to the tight carrier confinement

Due to the discrete nature of the DOS, QDs exhibit properties not found in other semiconductor gain material such as QWs. The purpose of this chapter is to explore the possibilities of exploiting these properties in highly resonance structures such as vertical cavity semiconductor optical amplifier (VCSOAs) and micro-ring amplifiers by use of a theoretical model developed for the performance prediction of such devices. Moreover, fabrication guidelines are provided for the design of device exhibiting special properties.

5.2 Epitaxially grown quantum dots

QDs emitting at the common optical communications bands can be growth on semiconductor substrates using the molecular beam epitaxy (MBE) and metal-organic chemical vapor phase epitaxy (MOPVE) using the Stranski-Krastanov (S-K) method.[284–290] Briefly, a thin film is epitaxially grown on a higher gap semiconductor surface of different lattice constants (typically more than 1% and up to 7%). A thin, highly strained, layer (the wetting layer –WL) is initially formed. After a critical thickness is reached, islands of the deposited material are formed spontaneously for

the strain to be relax. These islands, which usually resemble the shape of pyramids, although are not entirely surrounded by a higher gap semiconductor (since there are positioned on top of a wetting layer), they exhibit a 3D confinement of the carriers wavefunctions, thus QDs properties. In this configuration the thin wetting layer is actually a QW that plays the role of a carrier reservoir for the carrier pumping of the QDs.

The main challenges for the growth of high performance QDs using the S-K method is the precise control of the process for the growth of high density and uniformity QDs. Due to random fluctuations and the stochastic nature of the process, the size and shape of the nanoentities fluctuates, giving rise to a broadening of the luminescence spectrum. Typical values of this inhomogeneous broadening are in the 20-50 meV range for InGaAs/GaAs QDs.[291,292] Moreover, the QD density defines the material gain, thus efforts have been made for the growth of as dense QD layers as possible. To further increase the material gain available, successive multiple QD layers can be growth by epitaxial growth of intermediate layers of the substrate materials.

5.3 Vertical cavities photonic structures

Vertical cavity photonic structures such as vertical cavities surface emitting layers (VCSEL)[293–296] and vertical cavity semiconductor optical amplifiers (VCSOAs)[297–300] are active optoelectronic device with light emission perpendicular to the top surface of the structure. The cavity axis of such devices coincides the growth axis for structures grown using the MBE and MOVPE methods. These devices comprise high reflectivity distributed Bragg reflectors made of alternating semiconductor layers of high refractive index contrast (e.g. AlAs/GaAs). In summary, the benefits of vertical cavity geometry for the implementation of active semiconductor devices include:

- The inherent polarization insensivity
- High-fiber coupling efficiency
- On-wafer testing

- Wavelength tenability
- Low noise figure
- Integration in two-dimensional arrays
- Enhancement of non-linear optical properties

An illustration of a VCSEL is shown in Figure 5-2.

Incorporating QDs in vertical cavities as the gain material instead of the commonly used QWs have been extensively studied in the case of QD-VCSELs and have been reported to yield high performance QD-VCSELs[293,301–307] operating mainly in the O-band (QDs operating in the C-band have also been reported). The use of QDs however in highly resonance SOAs has not drawn attention mainly due to the inherent deficiency of VCSOAs, the requirement for bellow threshold operation. The novel combination of QDs and VCSOAs, or in general highly resonant structures for use in amplifiers, is shown here to offer the newly reported possibility of threshold-less design for QD-VCSOAs. This property is inherent to QDs and not possible for QWs. It enables high currents injection while ensuring no lasing operation and, the most importance, the fully exploitation of the fast dynamics of QDS for high-bit-rate signal processing.

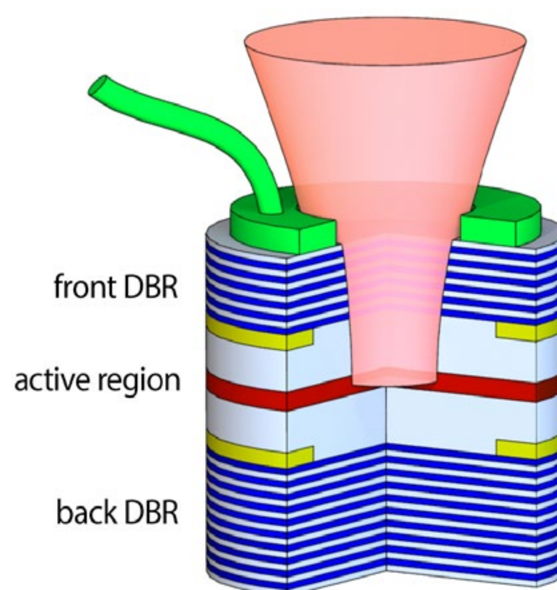

FIGURE 5-2: Section schematic of a Vertical Cavity Surface Emitting Laser (VCSEL).

The benefits of vertical a cavity configuration have be exploited not only in lasers but also in semiconductor optical amplifiers (SOAs). Such structures geometry resembles that of a VCSEL apart from the use of front of rear DBR of smaller reflectivity to allow small amount of the input light to penetrate the mirror and enter the cavity to be amplified. A VCSOA can operate in both reflection or transmission configuration as illustrated in Figure 5-3, while Figure 5-4 shows the refractive index profile of such a structure. For a VCSOA device to operate as an amplifier instead of a laser, it is crucial to be driven with a below threshold current.[308,309]

Meanwhile, the performance of QDs as the gain material in travelling-wave SOAs has been appreciated for high-bit-rate signal processing (>160 Gb/s)[292,310] stemming from the fast carrier dynamic of the QDs. The combination however of QDs with VCSOAs structures is a new research field.

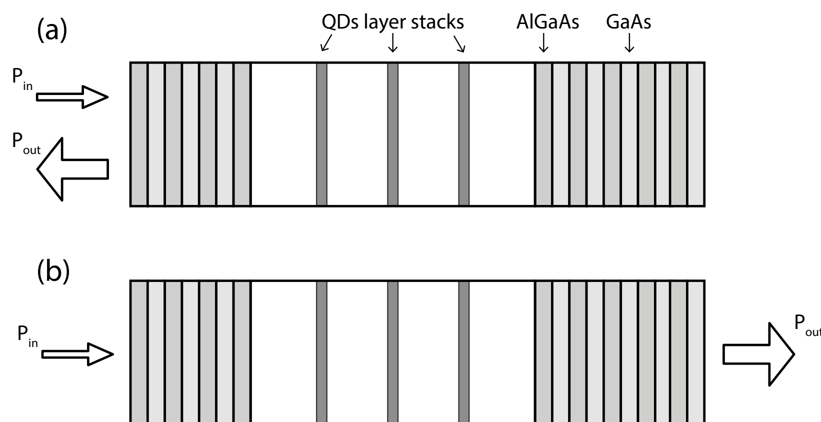

FIGURE 5-3: Illustration of the two operating mode of a VCSOA structure: **(a)** reflection mode and **(b)** transmission mode.

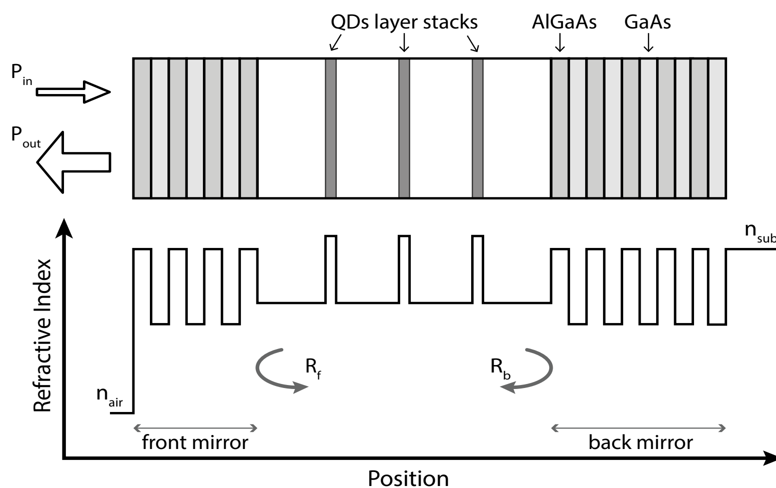

FIGURE 5-4: Schematic of a QD-VCSOA and the refractive index profile.

5.4 QD-Vertical Cavity Semiconductor Optical Amplifier modelling

A theoretical model for the performance prediction of QD-VCSOA has been developed and presented. This model is based on the cavity characteristics discussed here, coupled to the performance of the QD gain material described in the next section.

Assuming a given single-pass gain G_s, Fabry-Pérot amplifier in reflection mode G_R and in transmission mode G_T is given by:[297,299,308]

$$G_R = \frac{(\sqrt{R_f} - \sqrt{R_b} G_s)^2 + 4\sqrt{R_b R_f} G_s \sin^2 \Phi}{(1 - \sqrt{R_b R_f} G_s)^2 + 4\sqrt{R_b R_f} G_s \sin^2 \Phi} \tag{5.1}$$

$$G_T = \frac{(1 - R_f) \cdot (1 - R_b) G_s}{(1 - \sqrt{R_b R_f} G_s)^2 + 4\sqrt{R_b R_f} G_s \sin^2 \Phi} \tag{5.2}$$

In this approach the cavity is assumed to be comprised of hard mirrors of reflectivities R_f (front mirror) and R_b (back mirror) separated by an effective cavity length L_c which defines the detuning of the signal wavelength λ from the cavity resonance λ_c is given by the phase Φ: [297,311]

$$\Phi = 2\pi n_c L_c \left(\frac{1}{\lambda} - \frac{1}{\lambda_c} \right) + \frac{2\pi L_c}{hc} E_m \Delta n \tag{5.3}$$

The second term on the right-hand side accounts for any phase shift due to nonlinear phase change, E_m being the photon energy of the single optical mode supported by the cavity. The presence of carriers near the band edges, or in the case of QDs at the GS, give rise to refractive index alteration, hence shifts the cavity resonance. The term Δn is given by:

$$\Delta n = \left(\mathrm{N} - \mathrm{N}_1 \right) \frac{dn}{dN} \tag{5.4}$$

where N_1 is the carrier density where no light is entering the cavity (no input), while dn/dN is the differential refractive index.[312]

As mentioned previously, operation of a VCSOA as an amplifier instead of a laser is feasible by use of a bellow threshold current. For $\Phi = 0$ where the maximum

gain is achieved, threshold is reached when the denominator of equation, or equivalently of equation, equals zero. Therefore, bellow threshold operation is ensured when the following inequality holds:[297]

$$G_s^2 R_f R_b < 1 \tag{5.5}$$

This formula is used to calculate the threshold current and also provides the DBR reflectivity design. Morevoer, the single-pass gain G_s of the VCSOA is needed to exceed the losses of the back mirror (in reflection mode) for the device to provide above unity amplification: [297]

$$G_s^2 > R_b^{-1} \tag{5.6}$$

The DBRs reflectivities of m periods (2m layers) are given by:[313]

$$_{DBR} \quad \left(\frac{qp^{2\quad 1}}{qp^{2\quad 1}} \right) \tag{5.7}$$

p being the low-to-high refractive index rations of the two DBR layers while q and α are the first and last DBR interfaces respectively. Given those reflectivities, modelling of a vertical cavity device can be significantly simplified by replacing the DBRs in the model with two "*hard*" mirrors. In this case however, the penetration of light inside the DBRs needs to be considered for the precise calculation of the Fabry-Pérot cavity length. The penetration length L_m is given by:[297,311]

$$_{f\ p} = \frac{}{4n} \cdot \frac{q}{1-p} \cdot \frac{(1-\ {}^{2}p^{2m\ \ 1})(1-p^{2m})}{1-q^{2}\ {}^{2}p^{4\ \ 2}} \tag{5.8}$$

for a total cavity length of:

$$L_c = L_f + L_m + L_b \tag{5.9}$$

λ_c being the cavity resonance, n_c the cavity refractive index and L_m the distance between the DBR mirrors. An illustration of the Fabry-Pérot geometry for a cavity length of $L_c=3\lambda_s/2$, λ_s being the wavelength of the signal under amplification, is depicted in Figure 5-5.

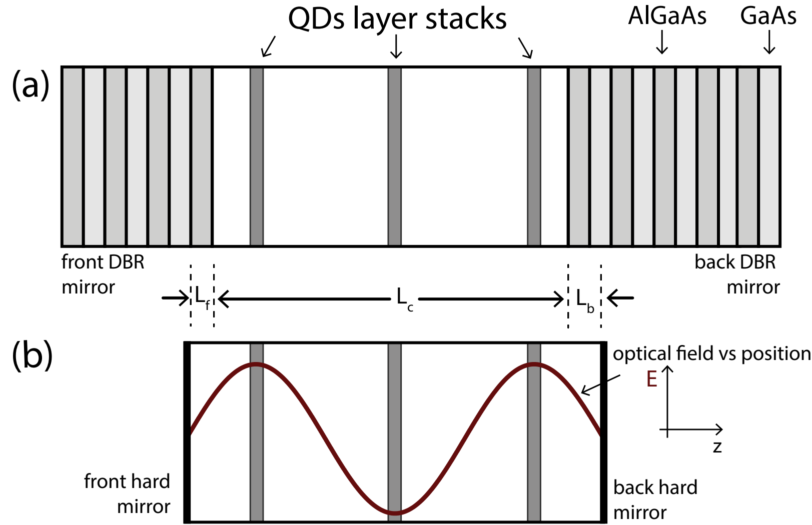

FIGURE 5-5: (a) Schematic of a VCSOA structure with the precise placement of the QD layer stacks. **(b)** The 3λ/2 length VCSOA cavity has been replaced by a FP cavity with hard mirrors using the penetration depths. The red line indicates the antinodes of the oscillating optical field inside the cavity where the QD layer stacks has been placed. The distortion of the optical field inside the DBR mirror is not shown for simplicity.

The modal gain of a vertical cavity structure can also be enhanced by a tricky placement of the active regions at the peaks of the standing optical wave for maximum interaction with the field, also shown in Figure 5-5. Here three QD stacks each one comprising of 5 QD layers are used for a total o3 3×5=15 QD layers inside the cavity. Then, a gain enhancement factor ξ:[314,315]

$$\xi = 1 + \frac{\sin\left(2\pi n_c L_{QD} / \lambda_c\right)}{2\pi n_c L_{QD} / \lambda_c} \tag{5.10}$$

is introduced into the modal gain formula:

$$g = \xi \Gamma g_m - a_{cav} \tag{5.11}$$

L_{QD} being the thickness of each QD stack (including the QD layers thickness d and the spacing between d_s), g_m the material gain provided by the QDs discussed later, a_{cav} the cavity loss and finally Γ is the longitudinal confinement factor given by the ratio of the total active region length L_a over the cavity length L_c:

$$\Gamma = \frac{L_a}{L_c}, \quad L_a = L_{QD} \times (total\ number\ of\ QDs\ layers) \tag{5.12}$$

The single-pass gain can now be calculated by the modal gain expression as:

$$G_s = \exp\left[gL_c\right] = \exp\left[\xi g_m L_a - a_{cav} L_c\right] \tag{5.13}$$

5.5 Modelling of the QDs inside a vertical cavity

We have developed a rate-equations model for predicting the performance of a QD-VCSOA.[292,310,316–319] As discussed previously, each QD layer live on top of a wetting layer, common for all QDs, which is in fact a narrow QW of thickness L_W. QDs exhibit two energy levels: an excited state (ES) and a ground state (GS). Carriers are assumed to be injected directly to the WL which has the role of a carrier reservoir for the ES and GS. An illustration of the energy diagram of a QD is shown in Figure 5-6, where the characteristic times for the carrier dynamics are also demonstrated. The carrier dynamics are assumed to be limited by electrons due to their lower relaxation times attributed to their smaller effective mass and resulting level spacing relatively to holes.[317]

Such a RE model is necessary to account for both homogeneous and inhomogeneous broadening of the QD transition energy distribution. The intraband, scattering-induced homogeneous broadening results into a broadening of the

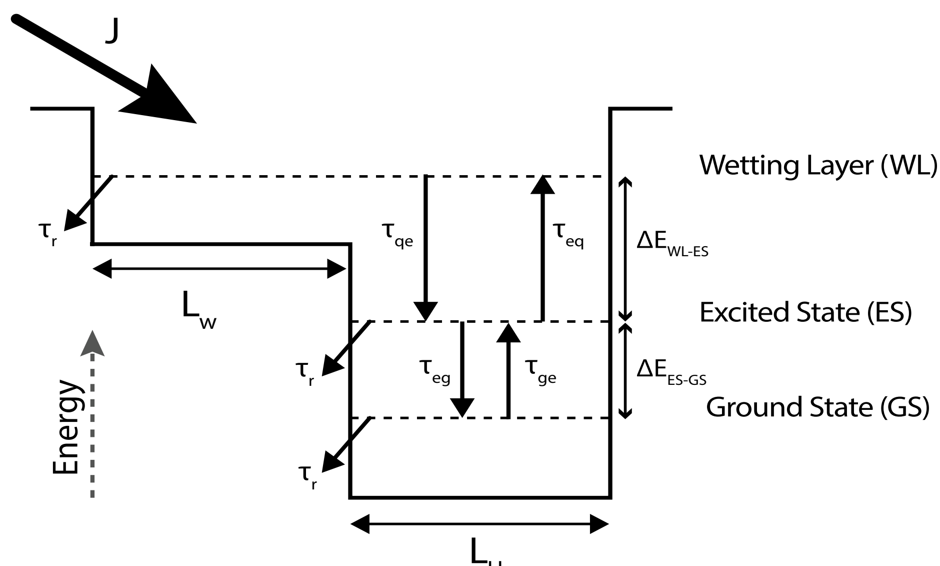

FIGURE 5-6: Schematic of the energy states diagram of a quantum dot also depicting the characteristic times of the carrier dynamics.

energy levels, thus of the carrier transition energy, and can be given by a Lorentzian line shape function:[292]

$$L(E-E_{cv})=\frac{\hbar\Gamma_{cv}/\pi}{\left(\mathrm{E}-\mathrm{E}_{cv}\right)^2+\left(\hbar\Gamma_{cv}\right)^2} \quad (5.14)$$

where $2\hbar\Gamma_{cv}$ is the FWHM of the homogeneous broadening, being the dephasing rate. On the other hand, inhomogeneous broadening of the QDs transition energies due to size, shape, and composition fluctuations during the growth process is described by a Gaussian function:[292]

$$G_{inh}\left(E_j-E_{cv}\right)=\frac{1}{\sqrt{2}\sigma_0}\exp\left(-\frac{\left(E_j-E_{cv}\right)^2}{2\sigma_0^2}\right) \quad (5.15)$$

which is distributed around a center energy E_{cv} with a FWHM of $\Gamma_{inh}=2.35\sigma_0$. To account for such a broadening, the QD distribution is divided into energy groups of energy width ΔE, as shown illustratively in Figure 5-7. QDs in each groups are assumed to exhibit the same energy while the percentage of QD of each group is:

$$G^j=G_{inh}\left(E_j-E_{cv}\right)\Delta E \quad (5.16)$$

E_j being the center energy of each group. Accounting for an energy span of 3 σ_0 includes 99.7% of all QDs and was found to be sufficient for calculations.

For equal filling of the QDs, an assumption valid for high currents,[320] the rate-equations take the following form:

Wetting layer:
$$\frac{dN_{WL}}{dt}=\frac{J}{eL_w}-\frac{N_{WL}}{\tau_{qr}}-\frac{N_{WL}}{\overline{\tau}_{qe}^j}+\frac{\sum_j N_{ES}^j}{\tau_{eq}} \quad (5.17)$$

Excited states:
$$\frac{dN_{ES}^j}{dt}=\frac{G^jN_{WL}}{\tau_{qe}^j}+\frac{N_{ES}^j}{\tau_{ge}^j}-\frac{N_{ES}^j}{\tau_{eg}^j}-\frac{N_{ES}^j}{\tau_{eq}}-\frac{N_{ES}^j}{\tau_r} \quad (5.18)$$

Ground states:
$$\frac{dN_{GS}^j}{dt}=\frac{N_{ES}^j}{\tau_{eg}^j}-\frac{N_{GS}^j}{\tau_r}-\frac{N_{GS}^j}{\tau_{ge}^j}-\Gamma S\ g(E^m,E_j) \quad (5.19)$$

Photons density:
$$\frac{dS}{dt}=(\Gamma g-a_i-\tilde{a}_m)\upsilon_g S+\frac{P_i}{h\nu V_p}+\Gamma\beta_{sp}\frac{\sum_i N_{gs}^i}{\tau_r} \quad (5.20)$$

where N_{WL} is the WL carrier density N_{ES}^j, N_{GS}^j the ES and GS carrier densities of the jth QDs, E_m and E_j are the mode and dot resonance energy, J the injection current density,

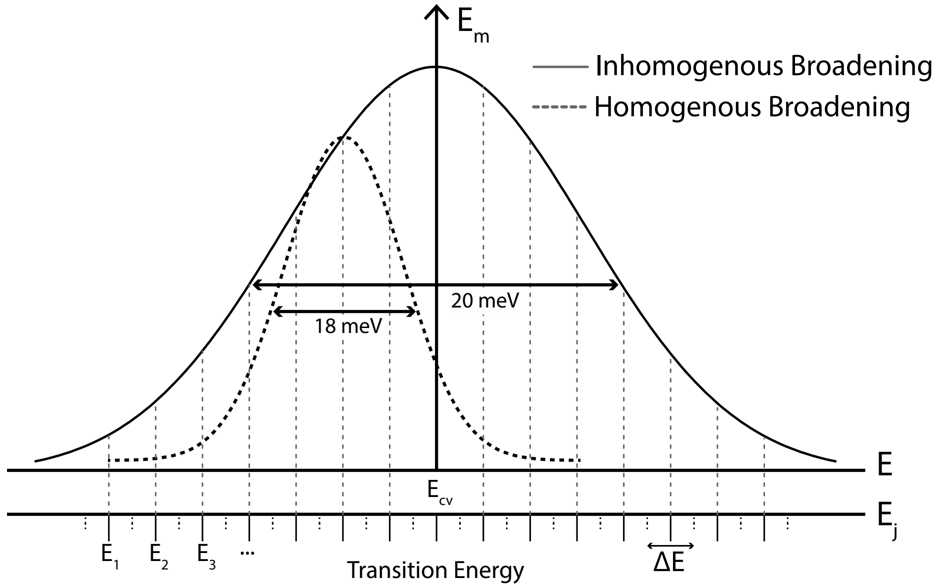

FIGURE 5-7: Illustration of the homogeneous and inhomogeneous broadening of quantum dots and the energy discretization for the numerical solution of the equations. The figure is not to scale.

$\tilde{a}_m$ is the modified mirror loss discussed in the next paragraph, $\upsilon_g = c / n_g$ is the light speed inside the cavity, P_i is the input optical signal power and β_{sp} is the spontaneous emission factor. Finally, $\tau_{xx'}$ are the characteristics transition time depicted in Figure 5-6 and discussed later.

The linear material gain is given by:[292]

$$g_m\left(E^m, E_j\right) = \frac{2\pi e^2 \hbar \mathrm{N}_D^{3D}}{c n_g \varepsilon_0 m_0^2} \frac{|P_{cv}|^2}{E_{cv}} \left(2P_{GS}^j - 1\right) G^j L(E^m - E_j) \qquad (5.21)$$

where $|P_{cv}|^2$ is the transition dipole moment and N_D^{3D} is the volume density of QDs. The carriers occupation probability in the GS P_{GS}^j of the jth QD group is given by:

$$P_{GS}^j = \frac{N_{GS}^j}{2\rho_{GS} N_D^{3D} G^j} \qquad (5.22)$$

ρ_{GS} being the degeneracy of the GS while the factor 2 accounts for the spin.

The characteristic lifetimes are calculated as follows:

→ The <u>carrier lifetime in the WL</u> is:[318]

$$\tau_{qr} = \frac{1}{A_W + B_W N_{WL} + C_W N_{WL}^2} \qquad (5.23)$$

A_W, B_W, C_W being the defect and surface recombination, the spontaneous recombination and the Auger recombination in the WL respectively.

→ The carrier capture times from the WL to the ES for the case of zero carrier occupation in the ES τ_{qe0} and for non-empty states τ_{qe} are:

$$\tau_{qe0} = \frac{1}{A_C + C_C N_{WL}}, \qquad \tau_{qe}^{-1} = \left(1 - P_{ES}^{j}\right)\tau_{qe0}^{-1} \tag{5.24}$$

A_c and C_c being the multiphonon and the Auger processes for capture to ES respectively while P_{ES}^{j} is the occupation probability in the ES:

$$P_{ES}^{j} = \frac{N_{ES}^{j}}{2\rho_{ES} N_{D}^{3D} G^{j}} \tag{5.25}$$

ρ_{GS} being the degeneracy of the ES.

→ The carrier relaxation times from the ES to the GS τ_{eg0} and for non-empty states τ_{eg} are:

$$\tau_{eg0} = \frac{1}{A_0 + C_0 N_{ES}}, \qquad (\tau_{eg}^{j})^{-1} = \left(1 - P_{ES}^{j}\right)\tau_{eg0} \tag{5.26}$$

A_0 and C_0 being the multiphonon and the Auger relaxation time for capture to ES respectively.

→ The carrier escape rates from the ES to the WL, τ_{eq}, and from GS to WS, τ_{eg}, are related to the capture times:

$$\tau_{eq}^{-1} = \left(1 - P_{WL}\right)\tau_{eq0}^{-1}, \qquad where:\ \tau_{eq0} = \frac{2N_D \rho_{ES}}{D_W}\tau_{qe0}\, \mathrm{e}^{\frac{\Delta E_{WL-ES}}{k_B T}} \tag{5.27}$$

$$\tau_{ge}^{-1} = \left(1 - P_{ES}\right)\tau_{ge0}^{-1} \qquad where:\ \tau_{ge0} = \frac{\rho_{GS}}{\rho_{ES}}\tau_{eg0}\, \mathrm{e}^{\frac{\Delta E_{ES-GS}}{k_B T}} \tag{5.28}$$

where τ_{eq0}, τ_{eg0} are the respective times for empty states. Also $\Delta E_{WL\text{-}ES}$ and $\Delta E_{ES\text{-}GS}$ are the resonance energy separation between WL and ES, and ES and GS respectively, while P_{WL} and D_W are the occupation probability in the WL and the DOS of the WL, given by:

$$P_{WL} = \frac{N_{WL}}{2D_W} \tag{5.29}$$

$$D_W = \frac{m^* k_B T}{2\pi\hbar^2 L_W} \tag{5.30}$$

Finally, m* is the electron effective mass in the WL, ħ is the reduced Planck constant and kBT is the thermal energy. Apart from Figure 5-6, a summary of all symbols use along with their values found in literature for InGaAs/GaAs QDs is given in Table 5-1.

TABLE 5-1: List of parameters of the QD-VCSOA used in calculations.

Quantity		Value
Group refractive index	n_g	4
Cavity refractive index	n_c	3.32
Active layer width (single layer)	d	5 nm
QD layer spacer	d_s	10 nm
Spontaneous emission factor	β_{sp}	1×10^{-4}
Resonant energy of QD GS	E_{cv}	0.954 eV (=1.3 μm)
Degeneracy of excited state (ES) without spin	ρ_{ES}	6
Degeneracy of ground state (GS) without spin	ρ_{GS}	1
Transition dipole moment	$\|P_{cv}\|^2$	2.94×10^{-30} eV kg
Effective cavity length	L_c	3.1×10^{-6} m
Active Area	A	400 μm^2
Losses in the cavity	α_{cav}	5×10^2 m^{-1}
Quantum dot radius	L_R	10 nm
Quantum dot height	L_H	5 nm
Thickness of the WL	L_W	5 nm
Inhomogeneous broadening (FWHM)	Γ_{inh}	20 meV
Homogeneous broadening (FWHM)	$2\hbar\Gamma_{cv}$	18 meV
Temperature	T	300 K
Resonant energy separation between WL & ES	$\Delta E_{WL-ES}^{center}$	100 meV
Resonant energy separation between ES & GS	$\Delta E_{ES-GS}^{center}$	70 meV
Multiphonon processes (capture to ES)	A_C	1×10^{12} s^{-1}
Auger processes (capture to ES)	C_C	1×10^{-14} m^{3}s^{-1}
Multiphonon processes (relaxation to ES)	A_0	5×10^{11} s^{-1}
Auger processes (relaxation to ES)	C_0	3.5×10^{-13} m^{6}s^{-1}
Defect and surface recombination in the WL	A_W	1×10^8 s^{-1}
Spontaneous recombination in the WL	B_W	7×10^{-16} m^{3}s^{-1}
Auger recombination in the WL	C_W	1×10^{-41} m^{6}s^{-1}

5.6 Calculation of the mirror losses

The mirror loss $\tilde{a}_m$ found in equation accounts for the photon transmission through the mirrors and is usually calculated by:[297]

$$a_m = \frac{1}{L_c}\ln\left[\frac{1}{\sqrt{R_f R_b}}\right] \tag{5.31}$$

However, as has been demonstrated by P. Royo et al.[321] this formula is invalid in the case of bellow lasing threshold operation, such in a case of as a VCSOA, since it does not satisfy the energy conversion. Therefore, a modified mirror loss formula is used

for the calculation of $\tilde{a}_m$, given by the following set of formulas: [321]

$$\tilde{a}_m = \left(\Gamma g - a_c\right)\frac{G_{signal}P_I}{\left(G_{signal}-1\right)P_I} \tag{5.32}$$

where G_{signal} is the total gain of the amplifier:

$$G_{signal} = G_T + G_R = \frac{\left(1-R_f\right)\left(1+R_bG_s\right)\left(G_s-1\right)}{\left(1-\sqrt{R_fR_b}G_s\right)^2 + 4\sqrt{R_fR_b}G_s\sin^2\Phi} \tag{5.33}$$

5.7 Results of a QD-VCSOA modelling

The device under consideration here is a QD-VCSOA consisting of 3 QD layers stacks placed at the optical field antinodes for a gain enhancement factor of ξ=1.643, each consisting of 5 QD layers for a total of 3×5 = 15 QD layers. The InGaAs/GaAs QDs have an average volume of about 3140 nm^3 and dimensions (assuming cylindrical shape[292]) of L_H=5 nm height and L_R=10 nm radius. The QD surface densities range between 1-10×10^{10} cm^{-2} and is connected to the 3D density by $N_D^{3D}=N_D/L_H$. Typical values found in the literature have been used for the homogeneous[292,322] ($2\hbar\Gamma_{cv}$=18 meV) and inhomogeneous broadening[323–327] (G_{inh}=20 meV). The cavity has a total length of $3\lambda_c/2$, λ_c being the cavity resonance wavelength, while the cavity loss are set to a_c=5 cm^{-1} and the device operates at $\lambda_m=\lambda_c$=1300 nm. The DBRs are made of 26 and 15 successive layers of AlAs/GaAs for total reflectivities of R_f=98.55% and R_b=99.95%.

The most interesting result from the study of the operational characteristics of a QD-VCSOA, is the dependence of the lasing threshold on the QD surface density, shown in Figure 5-8(a). As expected, at higher QD densities N_D the device exhibit a lower threshold due to the more material gain provided by the QDs. In the N_D= 6.2 to 6.3 ×10^{10} cm^{-2} range however the threshold increases abruptly at decreasing N_D while bellow a key parameter of about N_D= 6.21 ×10^{10} cm^{-2}, the QD-VCSOA exhibit no threshold. Such a properties not present in QW devices actually allows for d of threshold-less devices that can be pumped at high currents. Figure 5-8(b)

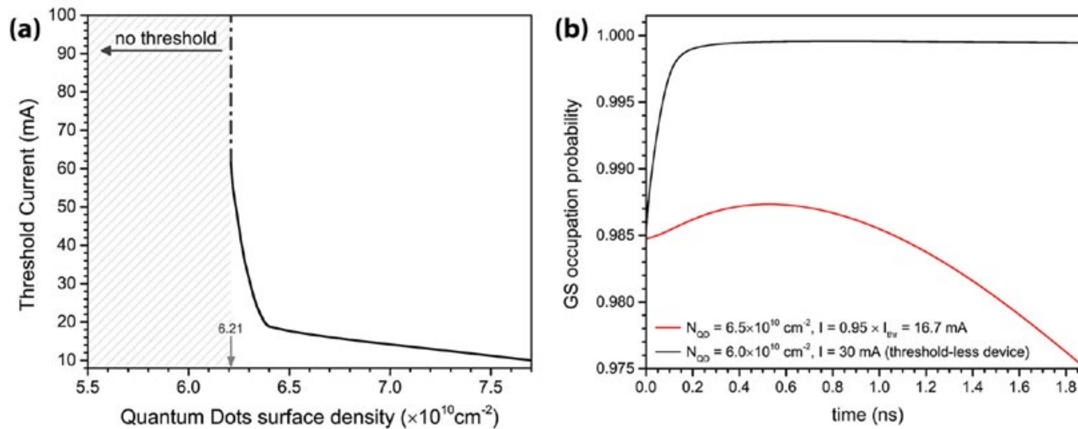

FIGURE 5-8: (a) The threshold current versus surface QD density of a 3×5 layers QD-VCSOA, and **(b)** the time evolution of the GS occupation probability of two QD-VCSOA, one exhibiting a threshold current operating at $I=0.95\times I_{thr}$ and one threshold-less device driven at 40 mA.

provides an interpretation of this effect: in a QD-VCSOA with a low N_D value of $N_D= 6.0 \times 10^{10}$ cm^{-2} (black line) the GS saturate with carrier (the GS occupation probability equals unity) placing an absolute limit to the maximum gain the device can provide. In the case however of a device of $N_D= 6.5 \times 10^{10}$ cm^{-2} which exhibits a threshold current of about I_{thr}=15 mA, an above threshold pumping ot I=30 mA cause lasing and carriers depletion from the GS as illustrated by the red line of Figure 5-8(b).

Gain curves shown in Figure 5-9(a) shows the gain versus input power for various injection currents of a threshold-less QD-VCSOA ($N_D=5.5\times10^{10}$ cm^{-2}). The gain curve exhibits two regions: a linear gain region where the device gain in independent from the input signal power, and a non-linear gain region where the gain decreases upon increase of the input signal power due to the carrier depletion of the carriers in the GS. The key parameter here is the input saturation power P_{sat} defined as the input signal power where the device gain drops to half the gain in the linear region, or a 3dB gain reduction in the cases of logarithmic plots such as those demonstrated here. The dependence of the QD-VCSOA gain input saturation power P_{sat} on the pumping current is shown Figure 5-9(b). Such devices can exhibit a surprisingly wide linear region of even above 15 dBm of input power if high currents are used. It is noted here however that thermal effects are not included in the model, hence heat damage or other physical limitations on the maximum device currents are not studied.

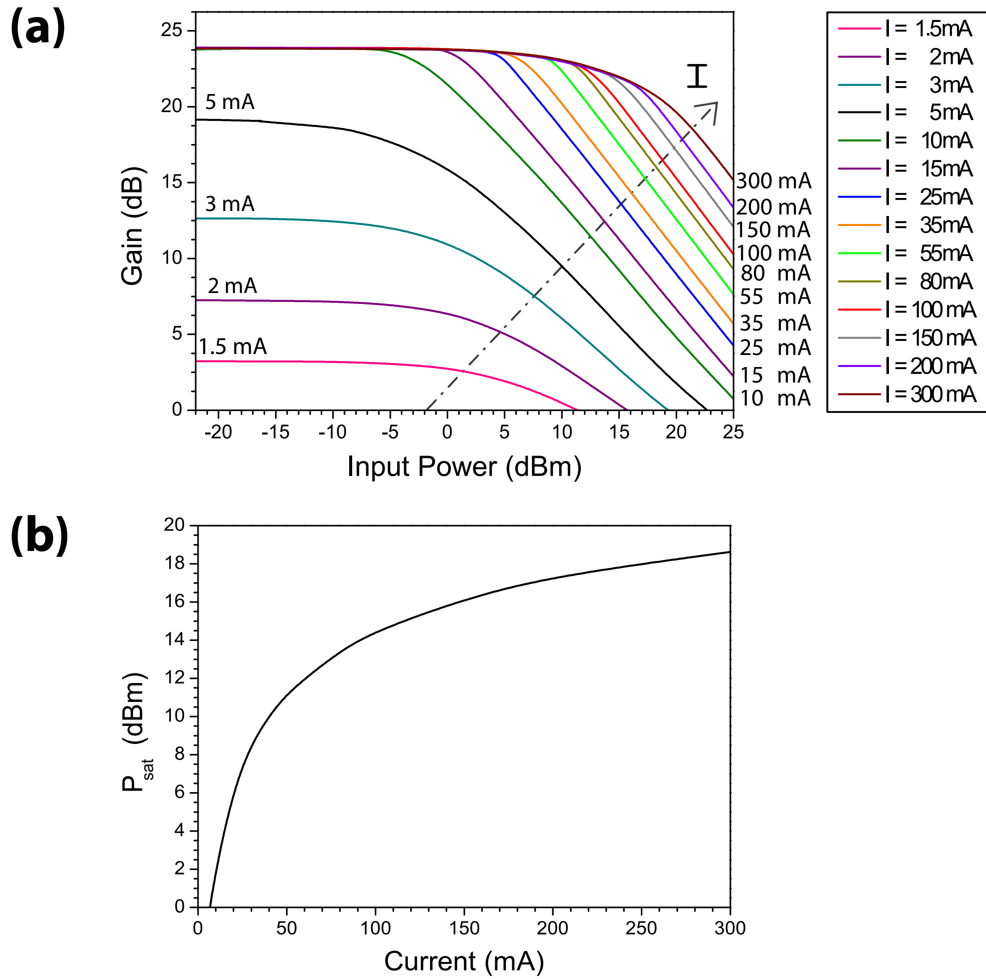

FIGURE 5-9: (a) Gain curves of a threshold-less 3×5 QD-VCSOA in reflection mode of QD density N_D=5.5×10^{10} cm^{-2} driven at various currents in a wide range of 1.5 mA to 300 mA. The arrow indicates the trend for increasing current. **(b)** The saturation gain as a function of the current for the same device.

Gain curves for a set of 3×5 QD-VCSOAs of various threshold-less QD surface densities in the range (N_D=3.5-6 ×10^{10} cm^{-2}) are show in Figure 5-10. Higher N_D structures exhibit higher linear gain but also lower input saturation powers (P_{sat}) due to ease depletion of the GS. The dependences of both the maximum linear gain and the input saturation power (P_{sat}) on N_D are shown in Figure 5-11.

As expected, QD-VCSOA being a microcavity exhibits a very narrow gain spectrum shown in Figure 5-12. In the absence of any phase shift when the differential refractive index is zero (dn/dN=0), the gain spectrum peak coincides that of the cavity resonance, as demonstrated in Figure 5-12(a). If however the differential refractive index has a different value, the gain spectrum shifts as shown in Figure 5-12(b) for

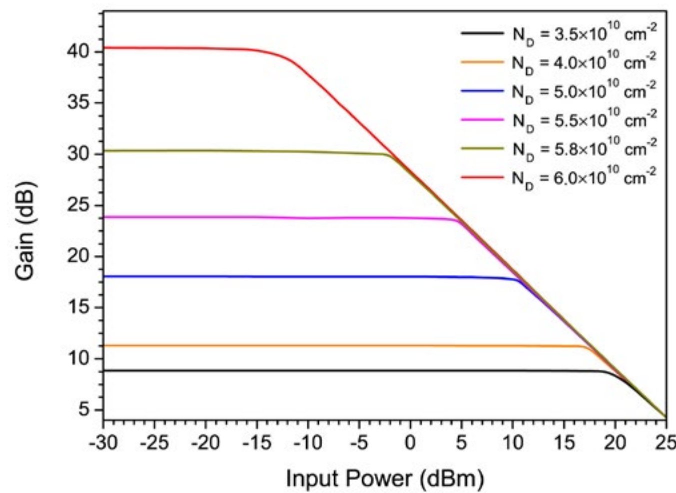

FIGURE 5-10: Gain curves of a 3x5 QD-VCSOA driver at I=25 mA for various surface QD densities.

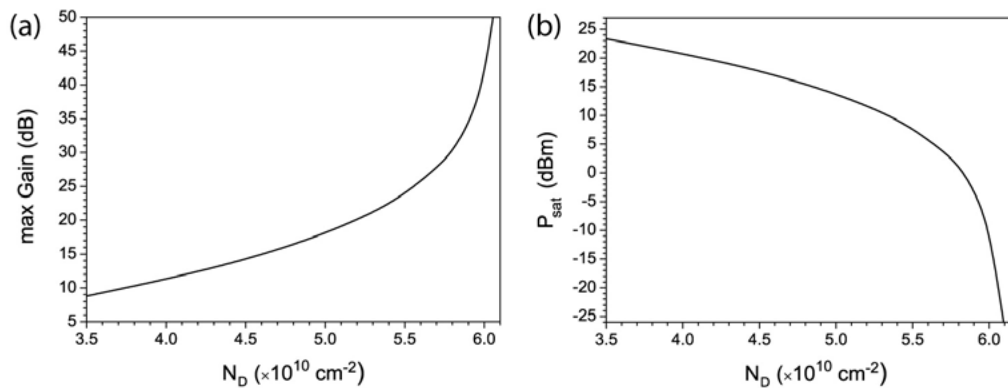

FIGURE 5-11: (a) The maximum achievable gain of a 3×5 QD-VCSOA driven at I=25 mA as a function of the surface QD density, and **(b)** the dependence of the saturation input power of the same device on the surface QD density.

a value of ($dn/dN=-2.8\times 10^{-26}$ m^{-3}). The detuning from initial cavity resonance of the 3×5 QD-VCSOA ($N_D=5.5\times10^{10}$ cm^{-2}, I = 25 mA) gain spectrum maximum from the cavity resonance wavelength is shown in Figure 5-13.

5.8 Comparison of the dynamic response between a QD-VCSOA and a QW-VCSOA

The main benefits of combining QDs in highly resonance structures for the implementation of threshold-less amplifiers is demonstrated here based on the requisite of pattern-free amplification of high-bit-rate signals. QD travelling wave SOA have been demonstrated to

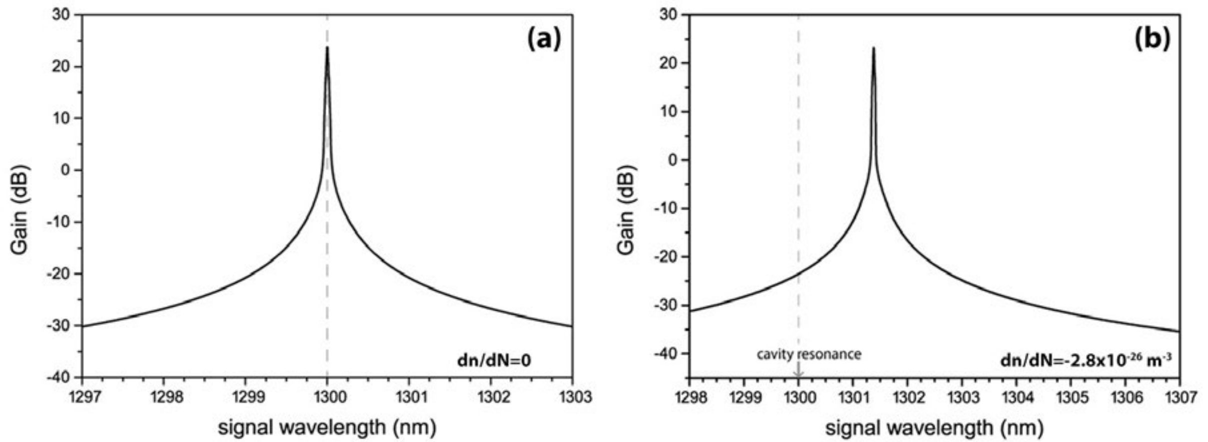

FIGURE 5-12: The amplification spectrum of a 3×5 QD-VCSOA of QD density N_D=5.5×10^{10} cm^{-2} driven at I = 25 mA for two carrier induced refractive index change values: **(a)** dn/dN=0, **(b)** dn/dN=-2.8×10^{-26} m^{-3}.

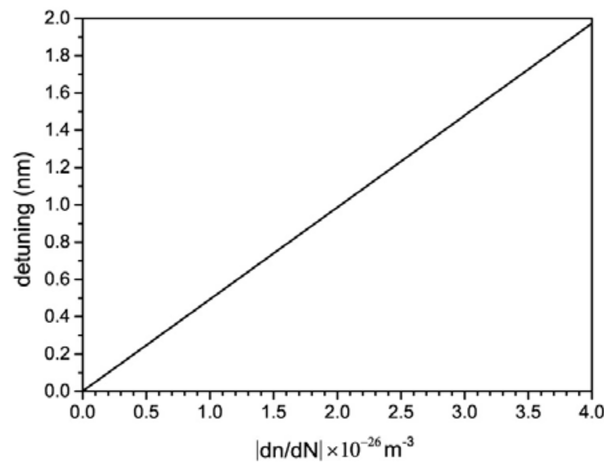

FIGURE 5-13: Detuning of the 3×5 QD-VCSOA (N_D=5.5×10^{10} cm^{-2}, I = 25 mA) gain spectrum maximum from the cavity resonance wavelength (λ_{cavity}=1300 nm) as a function of the carrier induced refractive index change value dn/dN.

allow amplification of signals[292] of up to 160 Gb/s due to the fast carrier dynamics of QDs rendering QDs an effective material for high-speed signal amplification. On the other hand, QD based amplifiers need to operate at high currents to ensure such pattern-free amplification,[292,310] prerequisite in contrast to the bellow threshold operation of VCSOA. The special nature of QDs however allows not only for the exploitation of fast carrier dynamics of such a gain material, but also for the implementation of threshold-less QD-VCSOA devices with no limitation on the current.

In order to demonstrate the superiority of QDs over QWs as the gain material in VCSOAs for the pattern-free amplification of high-bit-rate signals, a QW-VCSOA

RE model[328–331] has been developed allowing for performance comparison between the two devices. For the effective comparison the two devices are assumed to be of identical cavity geometry, each consisting of 3 stacks of 5 QD or QW layer each. High performance GaInNAs-based QW emitting at 1300 nm are used in the calculations.

The RE of the QW-VCSOA take the following form:

Carrier density
$$\frac{dN}{dt} = \frac{J\eta_i}{eL_w} - R_{tot} - \xi \cdot S \cdot \frac{c}{n_g} \cdot gain(E) \tag{5.34}$$

Photon density
$$\frac{dS}{dt} = (\Gamma g - a_i - \tilde{a}_m)\upsilon_g S + \frac{P_i}{h\nu V_p} + \Gamma \beta_{sp} B N^2 \tag{5.35}$$

where the materials gain is given by:

$$gain = \alpha_0(\mathrm{N} - \mathrm{N}_0) - \alpha_1(\lambda_s - \lambda_N)^2 \tag{5.36}$$

$$\lambda_\mathrm{N} = \lambda_0 - a_2(N - N_0) \tag{5.37}$$

α_0, α_1, α_2, λ_0 and λ_N are fitting parameters for the material gain calculation while the recombination rate R_{tot} is given by:

$$R_{tot} = A\,N + B\,N^2 + C\,N^3 \tag{5.38}$$

Values of these parameters for GaInNAs-based QWs were found in literature[330] are summarized in Table 5-2.

Table 5-2: List of the fitting parameters for the QW-VCSOA modelling.

Quantity		**Value**
Cavity refractive index	n_c	3.32
Active layer width (single layer)	d	7 nm
Spontaneous emission factor	β_{sp}	1×10^{-4}
Effective cavity length	L_c	3.1×10^{-6} m
Losses in the cavity	α_{cav}	5×10^{2} m^{-1}
Temperature	T	300 K
Peak wavelength at transparency	λ_0	1310 nm
Differential modal gain	α_0	5.5×10^{-21} m^2
Modal gain parameter	α_1	1.5×10^{18} m^{-3}
Modal gain parameter	α_2	5×10^{-33} m^4
Monomolecular recombination coefficient	A	2×10^{8} s^{-1}
Spontaneous emission recombination coeff.	B	3×10^{-17} m^3 s^{-1}
Auger recombination coefficient	C	4×10^{-41} m^6 s^{-1}

The threshold current of this device was calculated to be I_{thr}=8.9 mA. Gain curves demonstrated in Figure 5-14 for various currents show the limited linear amplification region of this structure.

In order to evaluate the dynamical performance of the VCSOA structures, a high-bit-rate optical signal of an random pulse return to zero pulse-train at 100 Gb/s has been applied as the input of the structures after reaching equilibrium. The extinction ration of the signal was is 23 dB (P^0=-20 dBm, P^1=3 dBm) while the bellow threshold currents were used for amplifiers exhibiting a threshold.

Figure 5-15 shows the decrease of the gain due to the presence of the input signal as well as the input and output signal pulse trains and the corresponding eye-diagrams of the QW-VCSOA exhibiting a threshold of I_{thr}=8.9 mA driven at different currents: I=0.90×I_{thr}, and I=0.95×I_{thr}. It is apparent from this results that pattern-free amplification is not feasible for this device for the signal under consideration. In particular, gain decrease due to carrier depletion near the band edges is not allowed to recover between successive pulses. The eye-diagrams are wider open in the case of low current, however the gain provided by the device in much lower (initially above 16 dB vs about 23 dB).

Similar results are obtained in the case of QD-VCSOA exhibiting threshold of I_{thr}=16.9 mA shown in Figure 5-16. This 3×5 QD-VCSOA of N_D=6.5×10^{10} cm^{-2} is

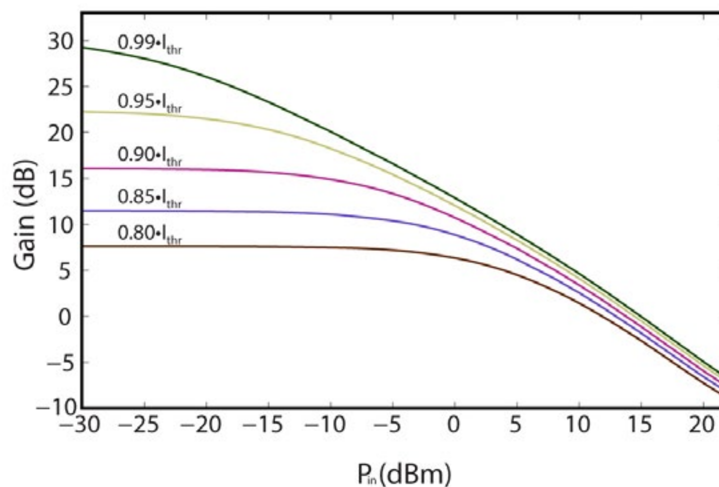

FIGURE 5-14: Gain curves of a QW VCSOA amplifier pumped at various currents. The threshold current of the device is I_{thr}=8.9 mA.

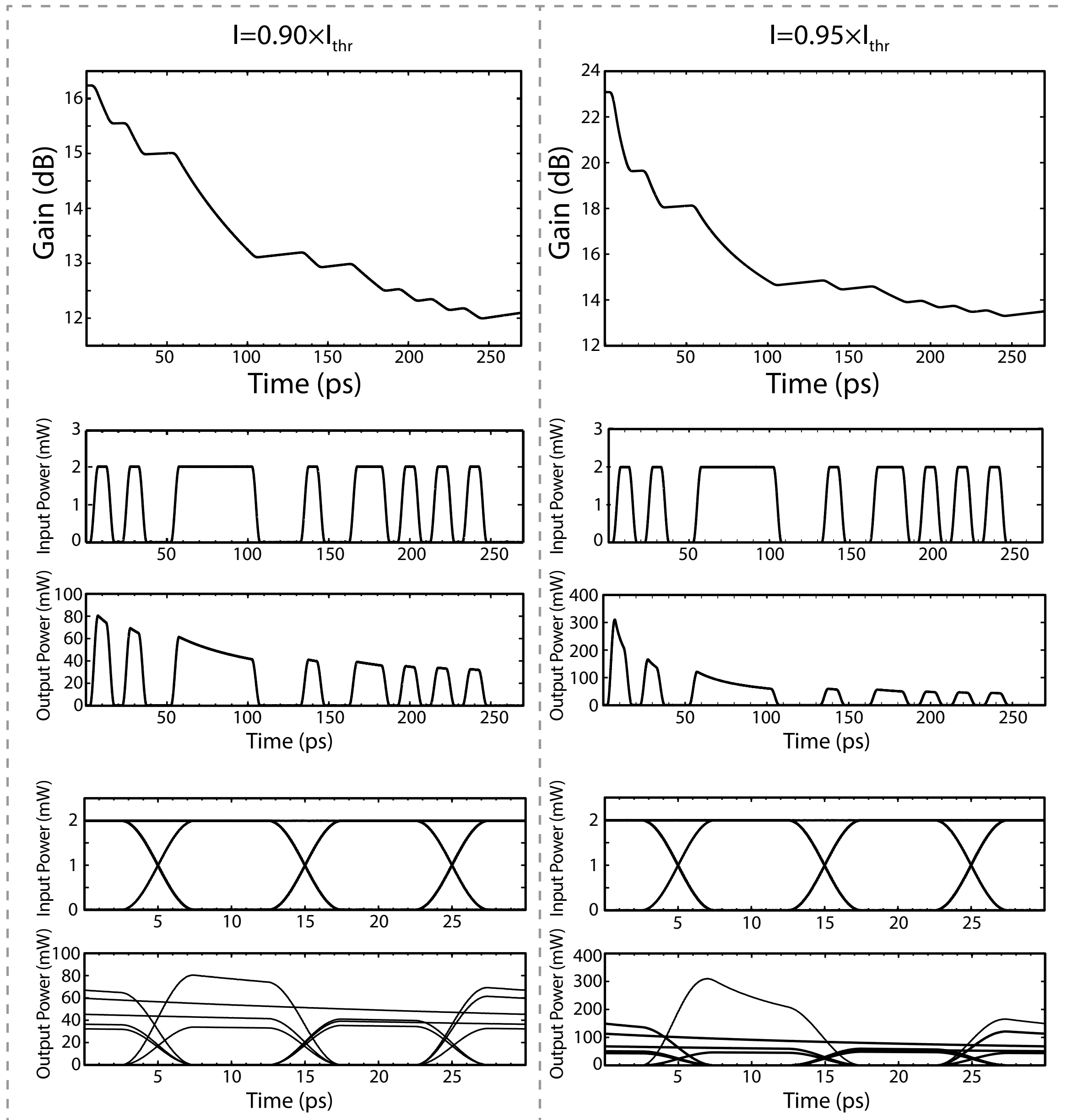

FIGURE 5-15: Dynamical response of a 3×5 QW-VCSOA exhibiting a threshold of I_{thr}=8.9 mA driven at **(a-c)** I=0.90×I_{thr}, and (d-f) I=0.95×I_{thr}: **(a & d)** gain change due to carrier depletion, **(b & e)** input and output signal waveforms at 100 Gb/s and, **(c & f)** eye diagrams of the input and output waveforms.

driven at I=0.90·I_{thr} and gain patterning effects are obvious. In the case however of a QD-VCSOA of N_D=5.5×10^{10} cm^{-2}, the absent of a threshold allows us to drive the device at high current to prompt the high-speed dynamic nature of QDs. Indeed, the performance of such a structure demonstrated in Figure 5-17 shows negligible gain alteration and pattern-free amplification of the high-bit-rate signal at I=30 mA.

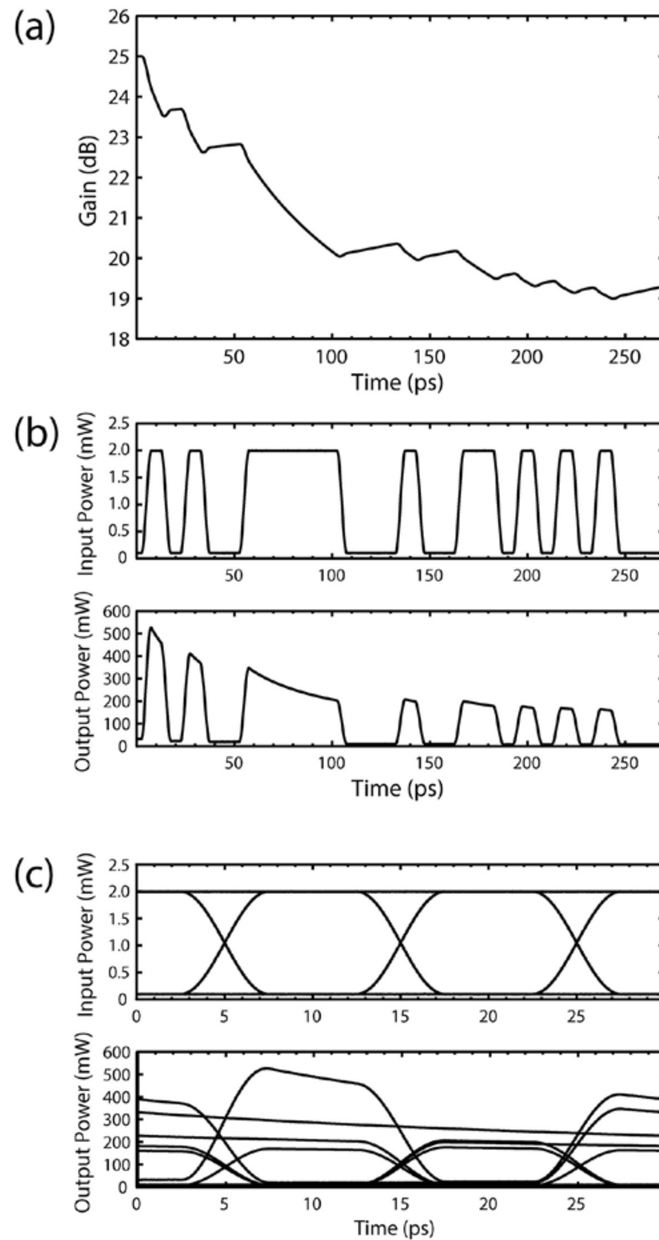

FIGURE 5-16: Dynamical response of a 3×5 QD-VCSOA of N_D=6.5×10^{10} cm^{-2} exhibiting a threshold of I_{thr}=16.9 mA driven at I=0.90·I_{thr}: **(a)** gain change due to carrier depletion, **(b)** input and output signal waveforms at 100 Gb/s and, **(c)** eye diagrams of the input and output waveforms.

5.9 QD micro-ring amplifiers

The merits or combining QD in high-Q resonance structures for high-bit-rate signal amplification are not limited to the case of QD-VCSOA but also accounts in any highly resonance structure. The case of QD-micro-ring amplifiers is briefly discussed here and steady state performance is evaluated.

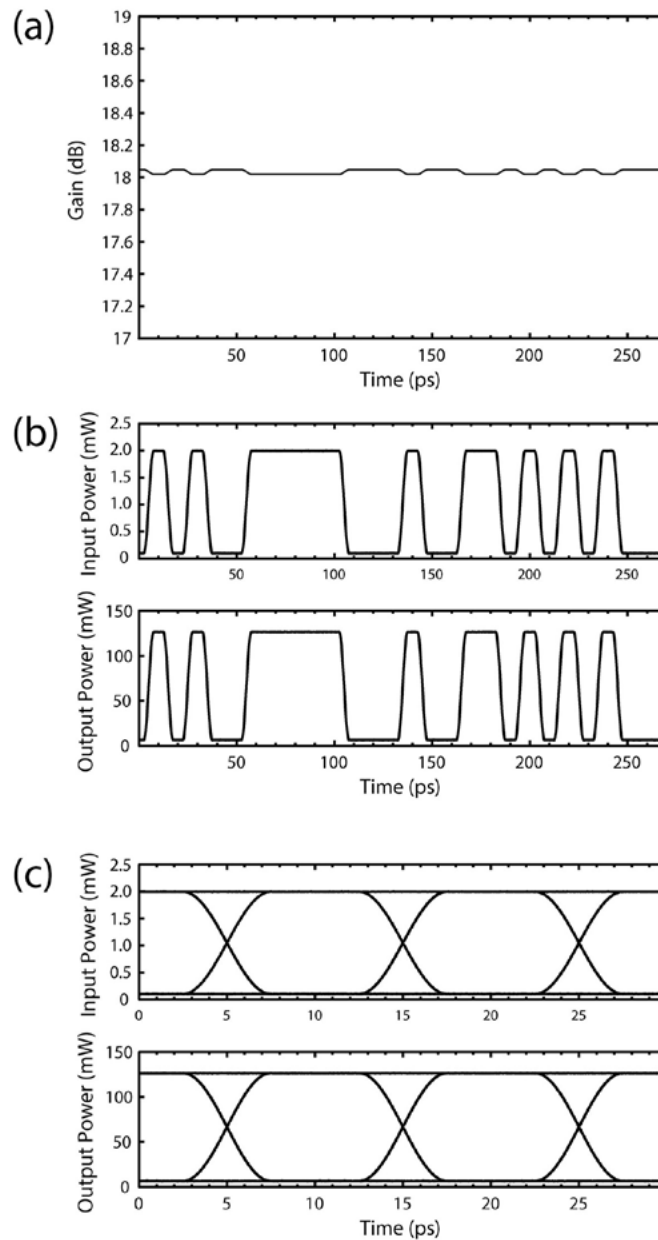

FIGURE 5-17: Dynamical response of a 3×5 threshold-less QD-VCSOA of N_D=5.5×10^{10} cm^{-2} driven at I=30 mA: **(a)** gain change due to carrier depletion, **(b)** input and output signal waveforms at 100 Gb/s and, **(c)** eye diagrams of the input and output waveforms.

Micro-ring structures are of particular importance for the implementation of semiconductor PICs being ideal components for photonics VLSI. Indeed, semiconductor micro-ring resonators are a multifunctional platform for a large range of functionalities, e.g. lasers, amplifiers, filters, all optical logic etc. The key advantage of using micro-rings in PICs is the lack of mirrors or gratings and the entirely planar geometry, enabling the implementation of complex photonic structures

in a single wafer without the need of wafer cleaving, edge polishing, labored device alignment and wafer bonding. Various aspects of a semiconductor active micro-ring geometry are illustrated in Figure 5-18. The striking difference in modelling a QD-micro-ring as opposed to a QD-VCSOA is the placement of the active material along the axis of the propagation of light, similar to the case of a travelling wave SOA.

QD-micro-ring amplifier is modelled here using a modification of the standard RE model demonstrated for the case of QD-VCSOA. The longitudinal travelling wave formalism developed (LATWA) proposed by M. Adams[331–333] has been employed. According to the this model, the propagating field F(z,E) is given by:

$$\frac{dF(z,E)}{dz} = \pm\frac{g(z,E)F(z,E)}{2} \mp ikF(z,\mathrm{E}) \tag{5.39}$$

g(z,E) being the modal gain, E the energy, and k the wavenumber. By averaging the optical field travelling along the cavity, the photon density can be found and used instead of the photon density RE. The average signal intensity $S_{m,average}$ in the micro-ring cavity in the all pass configuration shown in Figure 5-18(a), is then given by:[334]

$$S_{m,average} = \frac{\left(e^{gL}-1\right)}{gL}\frac{\kappa^2\left|\mathrm{E}_{in}\right|^2}{\left(1-\tau e^{gL/2}\right)^2+4e^{gL/2}\tau\sin\left(\varphi^j/2\right)} \tag{5.40}$$

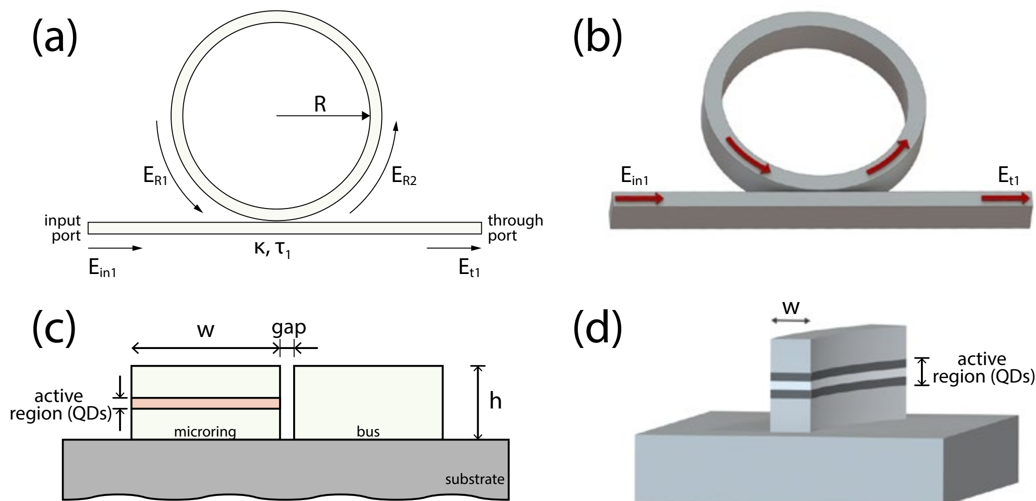

FIGURE 5-18: (a) 2D and, **(b)** perspective schematic illustrations of a QD micro-ring resonator in the all pass configuration, **(b) 2D** and, **(d)** perspective schematics of a cross section.

where g is the modal gain, L is the circumstance of the micro-ring (L=2πR, being the micro-ring radius), E_{in} is the input signal field intensity. Finally, τ and κ are the coupling constants and the transmittance, related to κ by $\tau=(1-\kappa^2)^{1/2}$. The gain of the micro-ring amplifier is given by: [334]

$$G=\frac{\left(\tau_1-e^{gL/2}\right)^2+4e^{gL/2}\tau_1\sin^2\left(\varphi/2\right)}{\left(1-\tau_1 e^{gL/2}\right)^2+4e^{gL/2}\tau_1\sin^2\left(\varphi/2\right)} \tag{5.41}$$

Apart from the two aforementioned formulas for $S_{m,average}$ and G, all other formulas of the VCSOA model also account here.

The key demonstration of QD-VCSOA performance, the existence of threshold-less configurations is shown in Figure 5-19. Indeed, the dependence of micro-ring threshold current on the QD surface density N_D for an amplifier of characteristics summarized in Table 5-3 is shown in Figure 5-19. Structures of N_D < 7.3×10^{10} cm^{-2} indeed lack a threshold and can be driven at high currents for pattern-free high-bit-rate amplification. Gain curves for various currents are shown in Figure 5-19. Moreover, the influence of the coupling constant κ and the QD surface density are demonstrated in Figure 5-21 and Figure 5-22 respectively.

An interesting aspect of active micro-ring amplifiers is illustrated in Figure 5-23 where the gain spectrum of a QD-micro-ring amplifier of a standard differential refractive index value of dn/dN=-2.8×10^{-26}m^{-3} is plotted for various coupling constants κ. Due to the large interaction volume of the active material with the optical field, nonlinearities emerging from both the active materials and the high-Q nature of the microcavity are intensified, inducing not only a swift of the gain maximum as in the case of QD-VCSOA, bur also deformation of the gain spectrum. Such a deformation strongly depends on the coupling constant as demonstrated. Moreover, Figure 5-24 shows a gain spectrum of a QD-micro-ring amplifier exhibiting a hysteresis loop. Indeed by shifting the input signal from lower to higher wavelengths, a leap is observed due to optical bistability of the structure. A subsequent scan of input signal

TABLE 5-3: List of parameters of the QD-micro-ring used in calculations

Quantity		Value
Group refractive index	n_g	4
Cavity refractive index	n_c	3.32
AlGaAs refractive index	n_{AlGaAs}	3.285
GaAs refractive index	n_{GaAs}	3.45
Active layer width (single layer)	d	5×10^{-9} m
Resonant energy of QD GS	E_{cv}	0.954 eV (=1.3 μm)
Losses in the cavity	α_{cav}	40×10^{2} m^{-1}
Quantum dot radius	L_R	10 nm
Quantum dot height	L_H	5 nm
Thickness of the WL	L_W	5 nm
Inhomogeneous broadening (FWHM)	Γ_{inh}	20 meV
Homogeneous broadening (FWHM)	$2\hbar\Gamma_{cv}$	18 meV
Micro-ring height	h	2 μm
Micro-ring width	w	2 μm
Numbers of QD layers	N_{lay}	5
Coupling constant	K	0.20
Micro-ring radius	R	20 μm

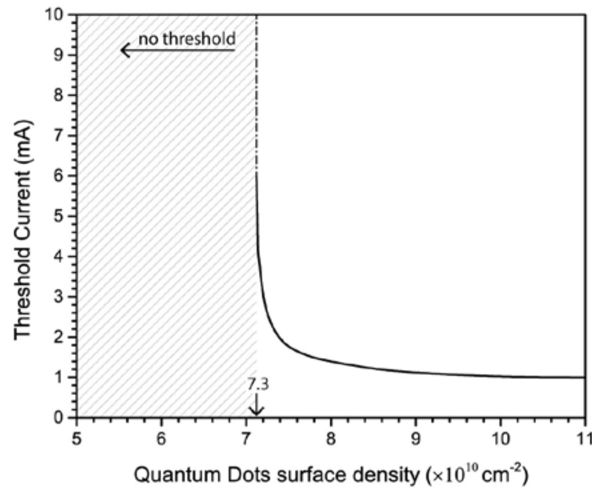

FIGURE 5-19: The dependence of the threshold current of a QD micro-ring amplifier of on the QDs surface density.

of the opposite direction, from higher to lower wavelengths, yields a gain leap at a different position resulting the formation of the hysteresis loop. Such a performance has been previously predicted theoretically for QW-micro-ring structures[334] and has been proposed for implementation of optical memories and optical logic gates.

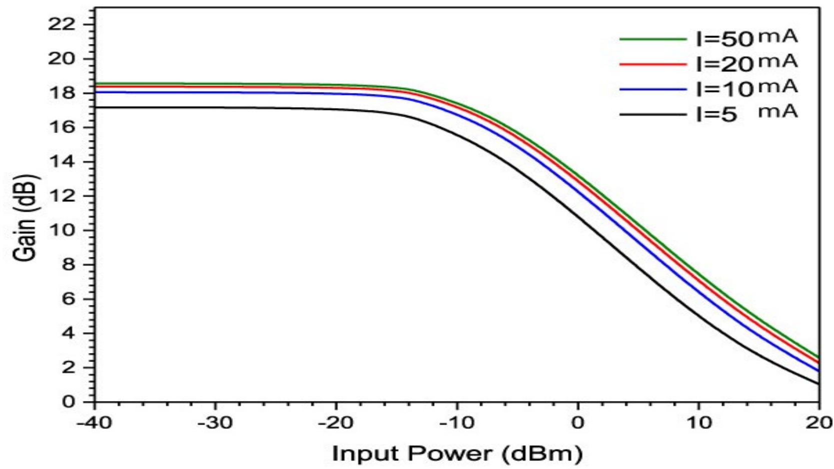

FIGURE 5-20: Gain curves of a threshold-less QD micro-ring amplifier pumping at different currents.

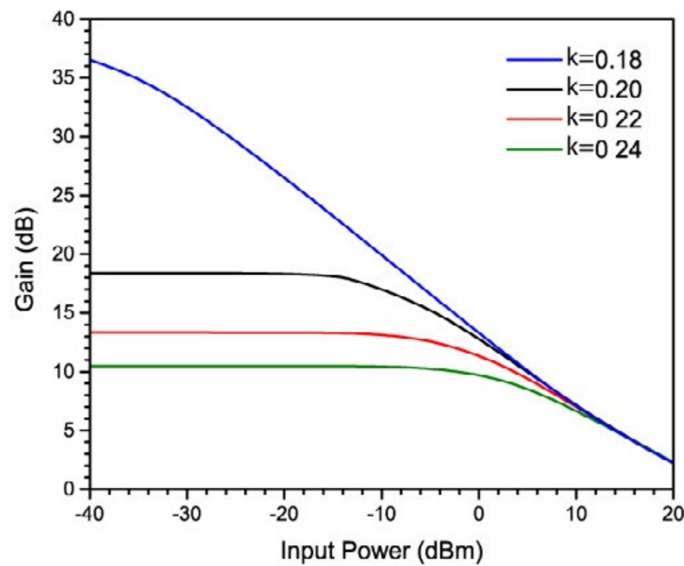

FIGURE 5-21: Gain curves of a QD micro-ring amplifier for various coupling constants κ.

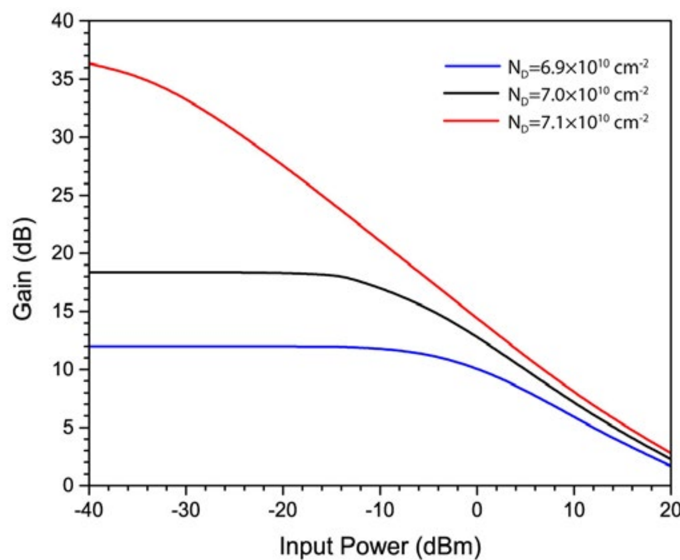

FIGURE 5-22: Gain curves of QD micro-ring amplifier for various QD surface densities N_D.

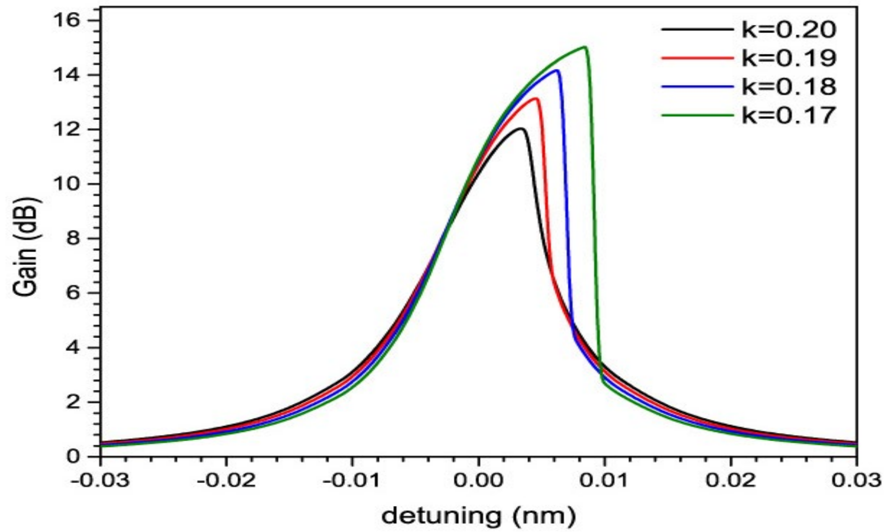

FIGURE 5-23: Gain spectrums of QD micro-ring amplifier exhibiting a differential refractive index of $dn/dN=-2.8\times 10^{-26}$ m^{-3} for various coupling constants κ.

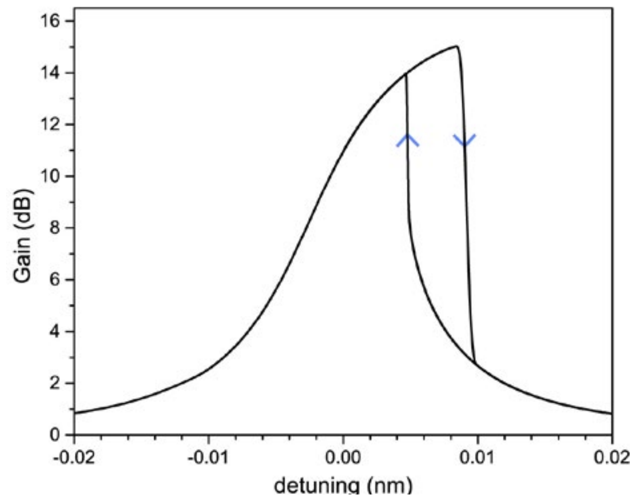

FIGURE 5-24: Gain spectrum of a QD micro-ring amplifier for various coupling exhibiting a hysteresis loop.

5.10 Conclusions

The merits of combining QD in highly resonance structures for the design of high performance optical amplifiers has been clearly demonstrated here by use of a theoretical model for the case of QD-VCSOA and QD-micro-ring amplifiers. The special nature of the DOS of QD allows for the design of threshold-less amplifiers by exploiting the upper limit of the current density in the GS. By-passing the limitation

of below threshold currents, the fast carrier response of InGaAs/GaAs QD found in travelling wave SOAs can also be enhanced in highly resonance structures. The developed model can also provide the design guidelines for the fabrication of such QD-VCSOAs and QD-micro-ring amplifiers that do not exhibit a threshold current.

5.11 Future work

The potential of combining QD in highly resonance structures in not limited in vertical cavities or micro-ring structures, nor in the case of amplification of high-bit-rate signals. Indeed, the key findings of the work presented here could be applied in other resonance structures, e.g. QD-DFB-SOAs. A suitable RE model for each structure could provide not only the performance predictions of such devices, but also the design guidelines for threshold-less operation. The expansion of the proposed model in QD-DFB-SOA is thus subject to future work. Moreover, the possibility of driving high-Q active amplifiers at high currents offers a new approach in studying optical bistability is such structures for application in optical memories and optical logic circuits. Such effects, only briefly discussed here, can be systematically studied with the models developed and presented here, and newly proposed designs of PICs with novel or enhanced functionalities can be provided by further studies.

Chapter 6
Conclusions

The research activities in the scope of this thesis were focused on the study of novel photonic structures incorporating quantum dots and other nanoentities functionalized composites. In this context, the work presented here included the demonstration of various photonic materials, routes for the fabrication of complex photonic structures and design of photonic devices.

Chemically-synthesized QDs, a beneficial active photonic material over other candidates, e.g. dyes, can be incorporated in easily processable matrices. The case of polymers was studied by synthesizing and testing tailored-made polymers for QD hosts while the fabrication of waveguides of such materials by direct laser ablative microfabrication was demonstrated. Measurement of the refractive index of these nanocomposites is needed prior to any design of photonic structure. Reflectrometry was the method used here for the low-cost measurement of the actual refractive index of polymer films in a non-destructive way. Moreover, inorganic matrices synthesized via the sol-gel route was also used for the incorporation of QDs and other nanoentities using custom-made recipes and recipes found in the literature, in order to explore their potential in complex photonic structure using novel fabrication methods. Sol-gel matrices incorporating salt nanocrystals were also studied for the demonstration of advance photonic sensors. Finally, commercially available hybrid organic/inorganic materials of the ORMOCER family were

studied under the perspective of utilizing them as a platform of the subsequent fabrication of photonic structures of different materials. Such materials can be easily microstructured using the low-cost soft lithography methods. In this context, prepatterned silicon masters provided by our collaborators were replicated using PDMS for the rapid low-cost fabrication of waveguides and CGHs.

Fabrication routes for advanced photonic structures incorporating the photonic materials under study were also provided and the cases of DLAM and soft lithography were explored. An ArF excimer laser microfabrication station was developed and its operation was fully automated for the implementation of elaborated fabrication protocols. The precise control of the pulse energy by the station and beam shaping from a custom-made spatial filter enabled us to fabricate a wide range of photonic structures of small features in the 1 μm range. In this context, CGH featuring an about 3 μm radius pixel was demonstrated. Moreover, polymer and sol-gel thin films were patterned at various geometries for the demonstration of QD/polymer waveguides and micro-rings following their design using the BPM. The quality of all ablated structures was determined using a set of SEM measurements. Further enhancement of the quality of the fabricated structures made by use of a vapor solvent smoothing protocol. The DLAM method was also found to be a versatile tool for the effective cleaving of hybrid material waveguides.

In parallel to the excimer laser microfabrication, soft lithography techniques were studied for the fabrication of newly proposed complex photonic structures. To overcome the restriction of using curing materials in combination to soft lithography, a custom made apparatus was created for the solvent-assisted soft lithographically micropatterning. The feasibility of the method was initially demonstrated for CGHs. Novel combination of this fabrication method to prepatterned channels on hybrid materials was demonstrated towards the fabrication of low-cost, active DFB structures of polymer and sol-gel nanocomposites incorporating QDs. The suitability of the material combination was confirmed by use of BPM simulations.

A novel sensing scheme enabling for the localized remote sensing (RPS) was established and demonstrated for the case study of silica matrix incorporating $NiCl_2$ nanoentities synthesized via the sol-gel method for ammonia sensing. The RPS scheme is based on the change of a laser beam signal interacting with the sensor head upon exposure to an analyte. Sensors microstructuring by engraving SRG on the sensing materials thin films was found to yield superior performance over bulk, unpatterned sensors. Indeed, a six fold performance increase was demonstrated by monitoring the ammonia response of the 1st diffraction order upon illumination with a laser beam at λ=632.8 nm, compared to the unpatterned sensor, while a lowest detection limit of 1 ppm ammonia concentration was shown. Theoretical studies using the RCWA methods establish the necessary fabrication guidelines for the design of SRG diffractive sensors of maximum performance.

Another novel combination of advanced photonic structures and advanced photonic materials explored here theoretically is that of epitaxially grown QDs in highly resonance amplifiers for telecommunication applications. The special, fully discrete nature of the DOS of QDs stemming for the 3D quantum confinement of the exciton wavefunction, sets a limit to the carrier density of the excited states and hence to the maximum gain provided by the device. This property can be exploited in designing threshold-less, high-resonant SOAs that enable the use of high injection currents that accelerate the carrier dynamics and enable the pattern-free amplification of high-bit-rate signals. The cases of QD-VCSOAs and QD-micro-ring amplifiers were studied theoretically using a novel RE model accounting for both the QDs and the cavity characteristics. Indeed, pattern-free amplification of 100 Gb/s signals results were theoretically demonstrated and design guidelines for the fabrication of threshold-less devices were provided. Comparison to the performance of QW-VCSOA using a model found in literature supports the superiority of QD-VCSOAs. Finally, interesting results stemming from nonlinear effects of QDs and enhanced by the micro-ring resonator have been demonstrated to induce

bi-stable operation and a potential for use in optical logic circuits and optical memories.

In conclusion, a set of novel combinations of photonic materials and photonic structures has been investigated, giving emphasis to the design, synthesis and fabrication protocols. Such protocols can contribute to the extension of the photonics horizons for improved and new applications in the ever-growing field of photonics, with a scope to offering new tools for emerging nanophotonics, nanoplasmonics, all-optical signal processing and sensing technologies.

Appendix A
Automation of the Excimer Laser Microfabrication Facility

The various features of the laser microfabrication station suite, programmed under the LabView™ interface are briefly presented here by demonstration of the program screenshots. The devices controlled by the suite are:

- The excimer laser, via a National Instruments PCI DAQ cards with analog and inputs outputs communicating with the laser through a custom made intermediate electronic interface.
- The nanopositioners controller which in respect controls the nanopositionig system also exhibiting an optical feedback motion control system.
- The rotation of the attenuator/compensator pair which is mounted on a gear coupled stepper motor of a 0.9^o step via a custom made controller connected digitally to the DAQ card.
- The energy/power detector.

Moreover, a USB camera used for monitoring of the microfabrication procedure is controlled independently by available software.

Figure A-1 shows the main control widows for the independent control of the laser shoot or the nanopositioners movement. Apart from setting the laser force (a term

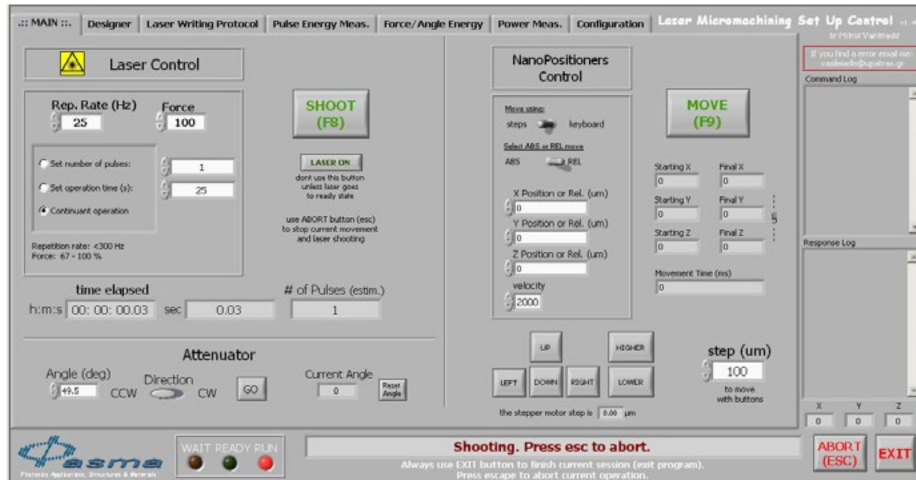

FIGURE A-1: The main control window for operating the laser, the picomotors movement and the attenuator angle separately.

used to determine the output power relatively to the maximum power of the laser) and repetition rate, the user can choose either a continuum firing until the stop button is pressed, a finite number of pulses per shoot or shoot for a finite time. The translation stages move can be set either in absolute positioning values or relative moving steps.

In the external writing section, the precise geometry of the structure under fabrication can be set as an external text file of the matrix containing all the firing points (Figure A-2) and the laser pulses per stop characteristics (number of pulses per stop, laser force, attenuator position and repetition frequency). Alternatively, the firing points map can be entered in the form of a bitmap file containing back and white pixels (Figure A-3)

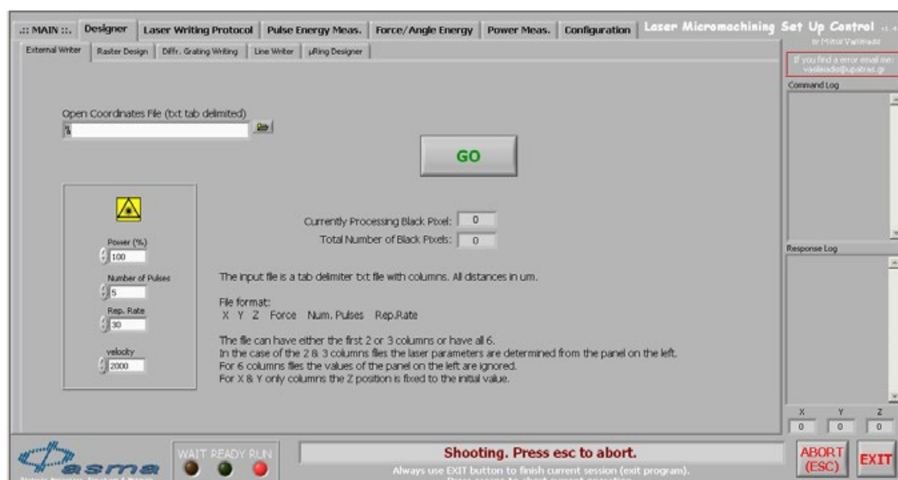

FIGURE A-2: The external writer window for inserting a txt file containing the writing instruction that has been calculated externally.

FIGURE A-3: The "Raster Design" window for inserting a jpg image file containing black and white pixels. The black pixels indicate the spots to be laser etched. The number pitch distances between pixels to be written and the force/number of pulses at each pixel are defined.

where white pixels are interpreted as firing points. The complementary data required by the user are the pitch between pixels and the lasers pulses characteristics per stop.

For the completely automated fabrication of common structures, appropriate algorithms can conveniently calculate the exact geometry for the implementation of diffraction gratings (Figure A-4), sets of lines and spots also allowing for repetitive step sequences (Figure A-5), circles and micro rings (Figure A-6), and arrays of spots of different laser pulse characteristics or focusing distance (z axis) for the

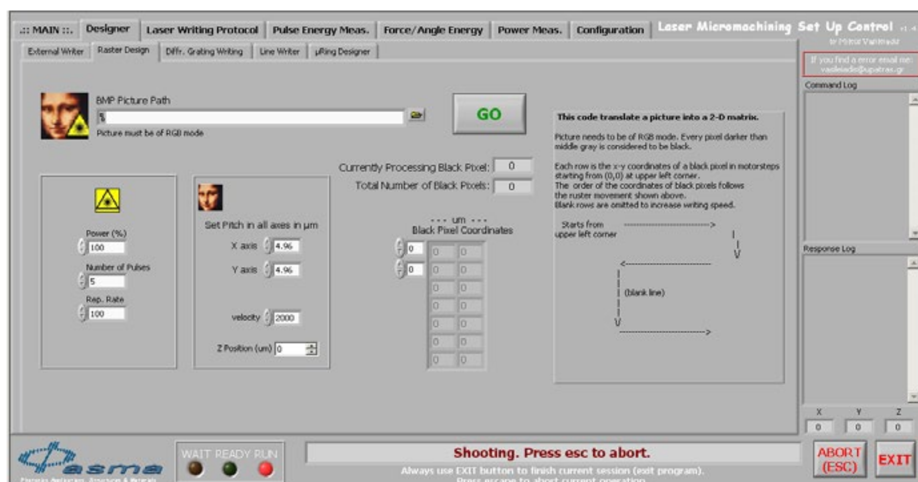

FIGURE A-4: The "Diff. Grating Writing" window for the fabrication of diffraction grating either using the fast writing method of the more precise stop-and-shoot method.

FIGURE A-5: The "Line Writer" window where individual steps and their repeats can be programmed.

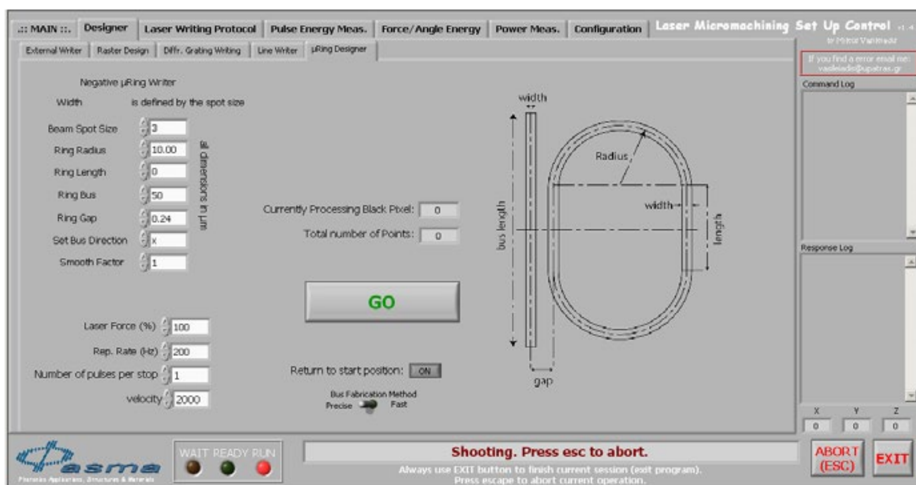

FIGURE A-6: The "μRing Designer" window for the fabrication of micro-ring resonators.

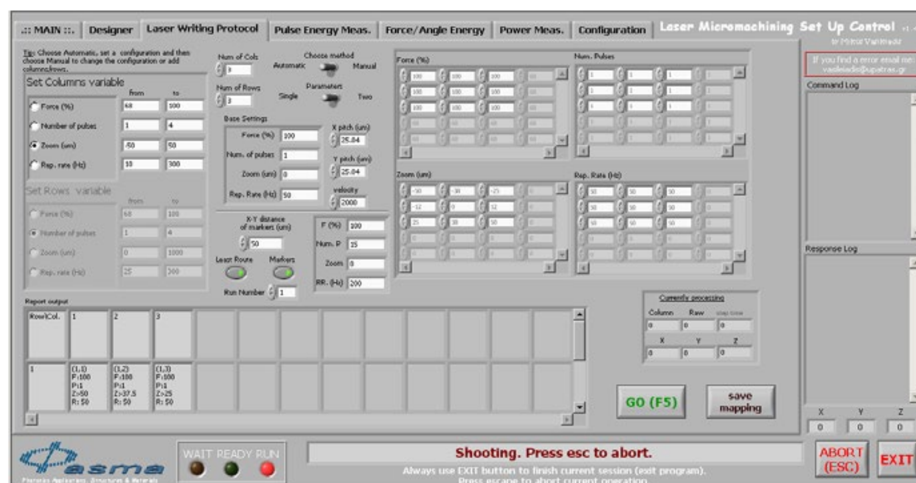

FIGURE A-7: The "Laser Writing Protocol" window for the evaluation of the material ablation procedure at different conditions (pulse energy, number of pulses, repetition rate and z position-focus).

implementation of laser writing protocols (Figure A-7). In these windows the user can choose either the accurate stop and shoot protocol or the much faster laser firing while the sample is moving method.

The laser pulse energy or the laser power can be monitored by automated features of the laser microfabrication station suite (Figures A-8, A-9), also allowing for monitoring of the laser stability (Figure A-10). Finally, the dependence of the pulse energy delivered on the sample on the laser force, and the angle of the attenuator angle is automatically recorded (Figure A-11). In all cases a number of pulses per measurement is set for calculation of average values and standard errors.

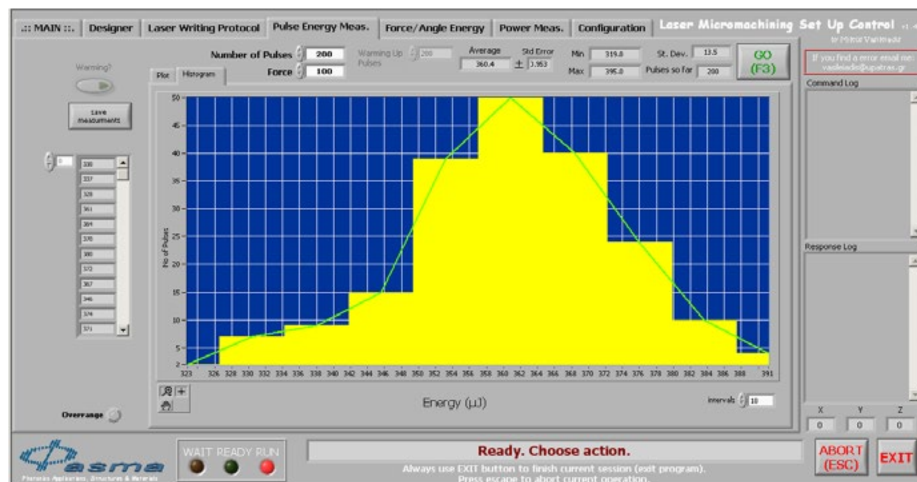

FIGURE A-8: The "Pulse Energy Meas." window in histogram mode for the measurement of the pulse energy distribution and calculation of the mean value and standard error.

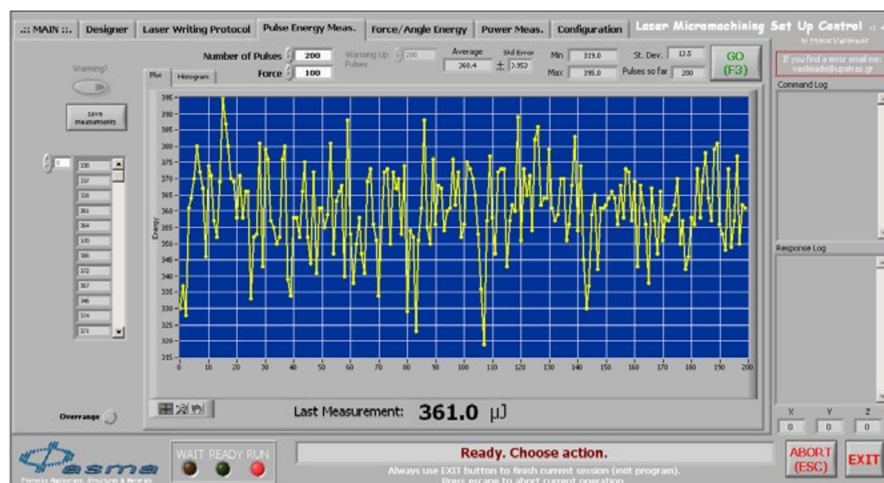

FIGURE A-9: The "Power Meas." window for measuring the power of the laser pulse train at a given repetition rate and angle of attenuator.

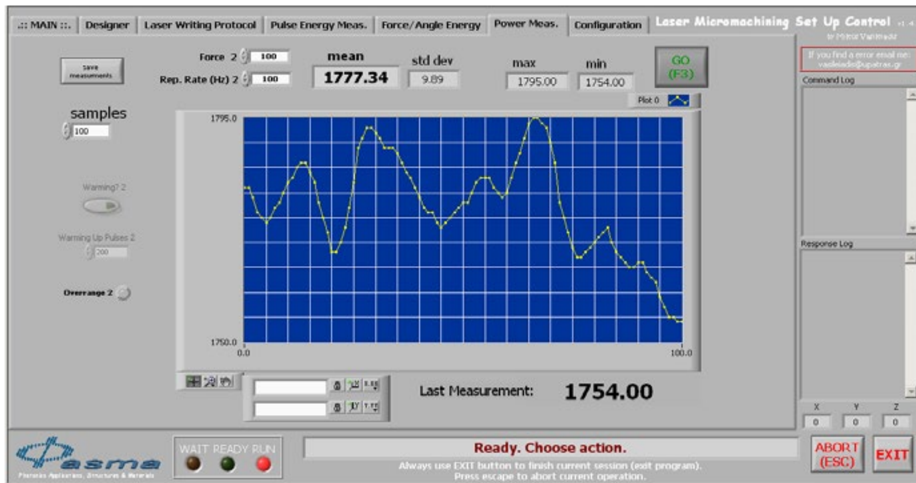

FIGURE A-10: The “Pulse Energy Meas.” window in time trace mode for monitoring the laser stability.

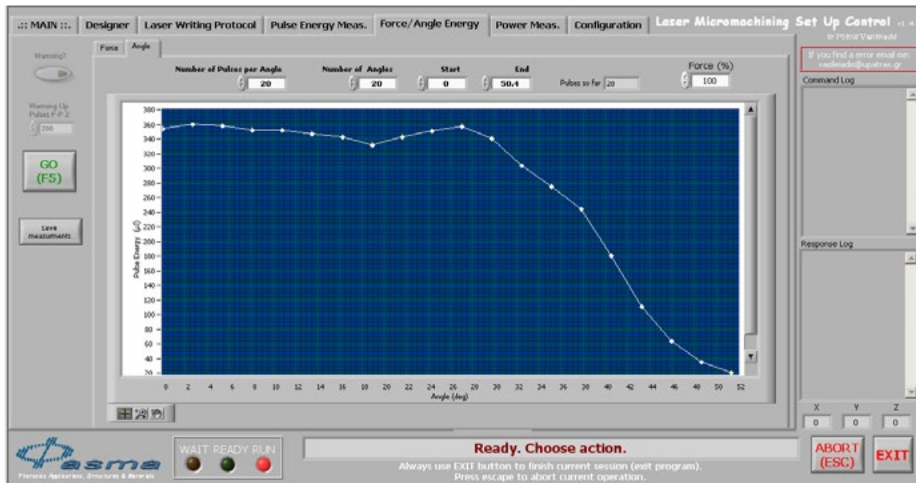

FIGURE A-11: The “Force/Angle Energy” window for measuring the pulse energy on different angles of the attenuator.

Appendix B
Temperature Sensor Operating under The RPS Scheme

A temperature photonic sensor operating under the RPS scheme has been fabricated and tested. The sensor comprises alternating metal/metal-oxide layer of Pt and SnO_x of SiO_2/Pt/SnO_x/Pt/SnO_x/Pt:SiO_2/100/170/5/170/5 (all values in nm) grown on glass by DC sputtering and O_2/Ar plasma. Common photolithography techniques followed by inert Ar^+ ion etching have been used for structuring of surface relief diffractive gratings of a 4 μm period of the multilayer composite.

The temperature of the sensor varied by use of a Peltier device while a 5 mW HeNe laser at λ=632.8 nm at an incidence angle of 19.4^o was used to remotely interrogate the structure. The mth order diffraction efficiencies in reflection mode (R_m) and transmittance mode (T_m, where m=0, ±1, ±2) were recorded using photodiodes connected to a PC control as shown in Figure B-1. Reversible refractive index changes due by the temperature alteration induce changes to the diffraction efficiency of the photonic structure, thus to the signals recorded by the photodiodes. A measurements set in a temperature range of 20-60°C is shown in Figure B-2. The temperature sensitivity of the structure is of order of ~10% per ^{o}C.

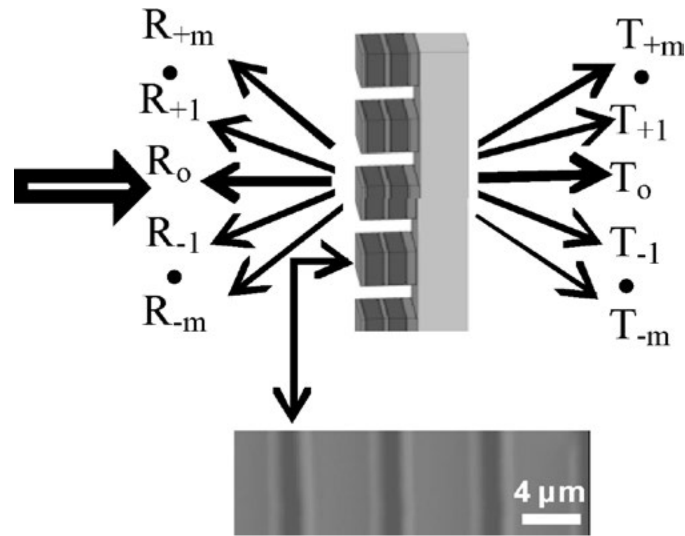

FIGURE B-1: Schematic illustration of the structure design and SEM micrograph (bottom).

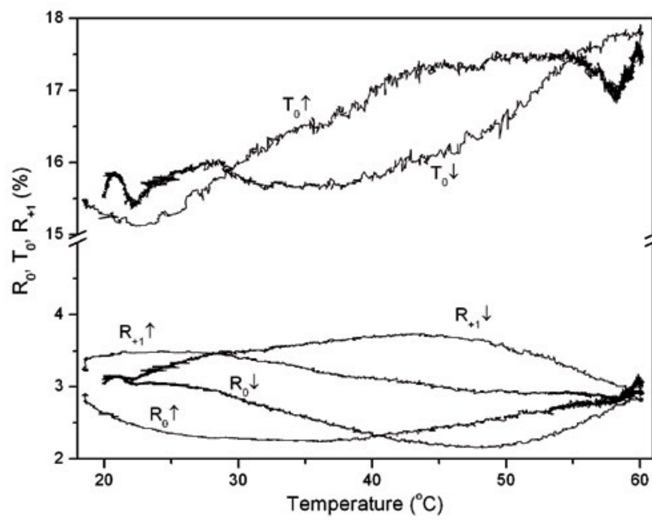

FIGURE B-2: Measurements of R_0, T_0 and R_{+1} for ascending (↑) and descending (↓) temperatures.

Appendix C
Rigorous Coupled-Wave Analysis (RCWA)

The rigorous coupled-wave analysis (RCWA) is a semi-analytical algorithm for modeling scattering from periodic dielectric structures with low to moderate index contrast.[262–264] The method is based on the Floquet's theorem that simplifies the solution of periodic differential equations. The term rigorous implies that the method is full vector and it includes no approximations to Maxwell's equations while it can easily incorporates any material dispersion parameters. RCWA is a frequency-domain method where the wave equation is treated analytically with no restriction in the direction of propagation while a numerical treatment is used in the transverse direction with the assumption of structure of width on the order of a wavelength in this direction.

In the context of RCWA, periodic structures are divided into equal, homogeneous layers in the longitudinal direction. In the case of curved geometry a stair-case a staircase approximation is used. In the transvers direction the problem is solved in reciprocal space by substituting the field with a sum of spatial harmonics by applying a Fourier expansion. The optical field is then calculated in each layer by enforcing matching boundaries conditions at the interfaces of neighboring layers to form a matrix. The layer by layer calculation finally allows for the propagation of the optical field through the layers.

References

1. Photonics21 - Photonics Industry Report 2013, available online at: http://www.photonics21.org/download/UT_Photonik_Handout_English.pdf
2. R. L. Verma, "Al-Hazen: father of modern optics," 1969.
3. F. J. Goes, The Eye in History. Jaypee Brothers Medical Pub, 2013.
4. G. N. Lewis, "The Conservation of Photons," Nature, vol. 118, no. 2981, pp. 874–875, Dec. 1926.
5. European Technology Platform for Photonics (Photonics21), available online: ftp://ftp.cordis.europa.eu/pub/etp/docs/photonics_en.pdf
6. D. Hondros and P. Debye, "Elektromagnetische Wellen an dielektrischen Drähten," Ann. Phys., vol. 337, no. 8, pp. 465–476, 1910.
7. United Nations, General Assembly 68th session agenta, available online: http://www.un.org/en/ga/68/agenda/
8. R. Rossetti, S. Nakahara, and L. E. Brus, "Quantum size effects in the redox potentials, resonance Raman spectra, and electronic spectra of CdS crystallites in aqueous solution," J. Chem. Phys., vol. 79, no. 2, pp. 1086–1088, 1983.
9. A. P. Alivisatos, "Perspectives on the Physical Chemistry of Semiconductor Nanocrystals," J. Phys. Chem., vol. 100, no. 31, pp. 13226–13239, Jan. 1996.
10. J. Y. Kim, O. Voznyy, D. Zhitomirsky, and E. H. Sargent, "25th anniversary article: Colloidal quantum dot materials and devices: a quarter-century of advances.," Adv. Mater., vol. 25, no. 36, pp. 4986–5010, Sep. 2013.
11. A. Ekimov and A. Onushchenko, "Quantum size effect in three-dimensional microscopic semiconductor crystals," J. Exp. Theor. Phys. Lett., vol. 34, no. 6, pp. 363–366, 1981.
12. G. C. Papavassiliou, "Luminescence Particles Spectra and Raman Excitation Profiles in Small CdS," J. solid state chem., vol. 40, pp. 330–335, 1981.
13. G. Papavassiliou - Personal communication (2013).

14. A. I. Ekimov, A. L. Efros, and A. A. Onushchenko, "Quantum Size Effects in Semiconductor Microcrystals," Solid State Commun., vol. 56, no. 11, pp. 921–924, 1985.

15. M. A. Reed, R. T. Bate, K. Bradshaw, W. M. Duncan, W. R. Frensley, J. W. Lee, and H. D. Shih, "Spatial quantization in GaAs–AlGaAs multiple quantum dots," J. Vac. Sci. Technol. B Microelectron. Nanom. Struct., vol. 4, no. 1, p. 358, Jan. 1986.

16. V. I. Klimov, "Nanocrystal Quantum Dots," no. 28, pp. 214–220, 2003.

17. U. Woggon, Optical Properties of Semiconductor Quantum Dots. Springer, 1997.

18. S. Gaponenko, Optical Properties of Semiconductor Nanocrystals. Cambridge University Press, 2005.

19. M. Nirmal and L. Brus, "Luminescence Photophysics in Semiconductor Nanocrystals," Acc. Chem. Res., vol. 32, no. 5, pp. 407–414, May 1999.

20. C. L. Choi and P. Alivisatos, "From artificial atoms to nanocrystal molecules: preparation and properties of more complex nanostructures.," Annu. Rev. Phys. Chem., vol. 61, pp. 369–89, Jan. 2010.

21. L. Brus, "Electronic wave functions in semiconductor clusters: experiment and theory," J. Phys. Chem., vol. 90, no. 12, pp. 2555–2560, Jun. 1986.

22. B. O. Dabbousi, F. V Mikulec, J. R. Heine, H. Mattoussi, R. Ober, K. F. Jensen, and M. G. Bawendi, "(CdSe) ZnS Core-Shell Quantum Dots: Synthesis and Characterization of a Size Series of Highly Luminescent Nanocrystallites," J. Phys. Chem. B, vol. 101, no. 46, pp. 9463–9475, 1997.

23. M. A. Hines and P. Guyot-Sionnest, "Synthesis and Characterization of Strongly Luminescing ZnS-Capped CdSe Nanocrystals," J. Phys. Chem., vol. 100, no. 2, pp. 468–471, 1996.

24. X. Peng, M. C. Schlamp, A. V. Kadavanich, and A. P. Alivisatos, "Epitaxial Growth of Highly Luminescent CdSe/CdS Core/Shell Nanocrystals with Photostability and Electronic Accessibility," J. Am. Chem. Soc., vol. 119, no. 30, pp. 7019–7029, Jul. 1997.

25. C. Bullen and P. Mulvaney, "The effects of chemisorption on the luminescence of CdSe quantum dots.," Langmuir, vol. 22, no. 7, pp. 3007–13, Mar. 2006.

26. J. J. Li, Y. A. Wang, W. Guo, J. C. Keay, T. D. Mishima, M. B. Johnson, and X. Peng, "Large-scale synthesis of nearly monodisperse CdSe/CdS core/shell nanocrystals using air-stable reagents via successive ion layer adsorption and reaction.," J. Am. Chem. Soc., vol. 125, no. 41, pp. 12567–75, Oct. 2003.

27. J. Jasieniak and P. Mulvaney, "From Cd-rich to Se-rich -the manipulation of CdSe nanocrystal surface stoichiometry.," J. Am. Chem. Soc., vol. 129, no. 10, pp. 2841–8, Mar. 2007.

28. O. Masala and R. Seshadri, "Synthesis Routes for Large Volumes of Nanoparticles," Annu. Rev. Mater. Res., vol. 34, no. 1, pp. 41–81, Aug. 2004.

29. C. B. Murray, D. J. Norris, and M. G. Bawendi, "Synthesis and characterization of nearly monodisperse CdE (E = sulfur, selenium, tellurium) semiconductor nanocrystallites," J. Am. Chem. Soc., vol. 115, no. 19, pp. 8706–8715, Sep. 1993.

30. R. Xie, U. Kolb, J. Li, T. Basché, and A. Mews, "Synthesis and characterization of highly luminescent CdSe-core CdS/$Zn_{0.5}Cd_{0.5}S$/ZnS multishell nanocrystals.," J. Am. Chem. Soc., vol. 127, no. 20, pp. 7480–8, May 2005.
31. J. van Embden and P. Mulvaney, "Nucleation and growth of CdSe nanocrystals in a binary ligand system.," Langmuir, vol. 21, no. 22, pp. 10226–33, Oct. 2005.
32. H. Rong, Y. Xiaogang, T. Hongye, G. Feng, C. Daxiang, and G. Hongchen, "Synthesis and characterization of monodisperse CdSe quantum dots in different organic solvents," Front. Chem. China, vol. 4, pp. 378–383, 2006.
33. V. K. LaMer and R. H. Dinegar, "Theory, Production and Mechanism of Formation of Monodispersed Hydrosols," J. Am. Chem. Soc., vol. 72, no. 11, pp. 4847–4854, Nov. 1950.
34. P. Prabhakaran, W. J. Kim, K. Lee, and P. N. Prasad, "Quantum dots (QDs) for photonic applications," Opt. Mater. Express, vol. 2, no. 5, pp. 1844–1849, 2012.
35. S. Coe, W.-K. Woo, M. Bawendi, and V. Bulović, "Electroluminescence from single monolayers of nanocrystals in molecular organic devices.," Nature, vol. 420, no. 6917, pp. 800–3.
36. N. Tessler, V. Medvedev, M. Kazes, S. Kan, and U. Banin, "Efficient near-infrared polymer nanocrystal light-emitting diodes.," Science, vol. 295, no. 5559, pp. 1506–8, Feb. 2002.
37. S. Coe-Sullivan, W.-K. Woo, J. S. Steckel, M. Bawendi, and V. Bulović, "Tuning the performance of hybrid organic/inorganic quantum dot light-emitting devices," Org. Electron., vol. 4, no. 2–3, pp. 123–130, Sep. 2003.
38. Q. Sun, Y. A. Wang, L. S. Li, D. Wang, T. Zhu, J. Xu, C. Yang, and Y. Li, "Bright, multicoloured light-emitting diodes based on quantum dots," Nat. Photonics, vol. 1, no. 12, pp. 717–722, Nov. 2007.
39. V. I. Klimov, A. A. Mikhailovsky, S. Xu, A. Malko, J. A. Hollingsworth, C. Leatherdale, H.-J. Eisler, and M. G. Bawendi, "Optical Gain and Stimulated Emission in Nanocrystal Quantum Dots," Science, vol. 290, no. 5490, pp. 314–317, Oct. 2000.
40. A. V. Malko, a. a. Mikhailovsky, M. a. Petruska, J. a. Hollingsworth, H. Htoon, M. G. Bawendi, and V. I. Klimov, "From amplified spontaneous emission to microring lasing using nanocrystal quantum dot solids," Appl. Phys. Lett., vol. 81, no. 7, p. 1303, 2002.
41. V. C. Sundar, H.-J. H. Eisler, T. Deng, Y. Chan, E. L. Thomas, M. G. Bawendi, and B. V. C. Sundar, "Soft-Lithographically Embossed, Multilayered Distributed-Feedback Nanocrystal Lasers," Adv. Mater., vol. 16, no. 23–24, pp. 2137–2141, Dec. 2004.
42. Y. Chan, P. T. Snee, J. Caruge, B. K. Yen, G. P. Nair, D. G. Nocera, and M. G. Bawendi, "A Solvent-Stable Nanocrystal-Silica Composite Laser," pp. 3146–3147, 2006.
43. H.-J. Eisler, V. C. Sundar, M. G. Bawendi, M. Walsh, H. I. Smith, and V. Klimov, "Color-selective semiconductor nanocrystal laser," Appl. Phys. Lett., vol. 80, no. 24, p. 4614, 2002.

44. F. Todescato, I. Fortunati, S. Gardin, E. Garbin, E. Collini, R. Bozio, J. J. Jasieniak, G. Della Giustina, G. Brusatin, S. Toffanin, and R. Signorini, “Soft-Lithographed Up-Converted Distributed Feedback Visible Lasers Based on CdSe – CdZnS – ZnS Quantum Dots,” Adv. Mater., vol. 22, pp. 337–344, 2012.

45. I. Gur, N. a Fromer, M. L. Geier, and a P. Alivisatos, “Air-stable all-inorganic nanocrystal solar cells processed from solution.,” Science, vol. 310, no. 5747, pp. 462–5, Oct. 2005.

46. W. U. Huynh, J. J. Dittmer, and A. P. Alivisatos, “Hybrid Nanorod-Polymer Solar Cells,” Science, vol. 2425, no. 2002, pp. 2425–2427, 2010.

47. J. Jasieniak, B. I. MacDonald, S. E. Watkins, and P. Mulvaney, “Solution-processed sintered nanocrystal solar cells via layer-by-layer assembly.,” Nano Lett., vol. 11, no. 7, pp. 2856–64, Jul. 2011.

48. A. J. Moulé, L. Chang, C. Thambidurai, R. Vidu, and P. Stroeve, “Hybrid solar cells: basic principles and the role of ligands,” J. Mater. Chem., vol. 22, no. 6, p. 2351, 2012.

49. J. Seo, M. J. Cho, D. Lee, A. N. Cartwright, and P. N. Prasad, “Efficient heterojunction photovoltaic cell utilizing nanocomposites of lead sulfide nanocrystals and a low-bandgap polymer.,” Adv. Mater., vol. 23, no. 34, pp. 3984–8, Sep. 2011.

50. S. A. McDonald, G. Konstantatos, S. Zhang, P. W. Cyr, E. J. D. Klem, L. Levina, and E. H. Sargent, “Solution-processed PbS quantum dot infrared photodetectors and photovoltaics.,” Nat. Mater., vol. 4, no. 2, pp. 138–42, Feb. 2005.

51. K. Roy Choudhury, W. J. Kim, Y. Sahoo, K.-S. Lee, and P. N. Prasad, “Solution-processed pentacene quantum-dot polymeric nanocomposite for infrared photodetection,” Appl. Phys. Lett., vol. 89, no. 5, p. 051109, 2006.

52. D. Qi, M. Fischbein, M. Drndić, and S. Šelmić, “Efficient polymer-nanocrystal quantum-dot photodetectors,” Appl. Phys. Lett., vol. 86, no. 9, p. 093103, 2005.

53. P. E. Burrows, G. Gu, V. Bulovic, Z. Shen, S. R. Forrest, and M. E. Thompson, “Achieving full-color organic light-emitting devices for lightweight, flat-panel displays,” IEEE Trans. Electron Devices, vol. 44, no. 8, pp. 1188–1203, 1997.

54. L. Kim, P. O. Anikeeva, S. A. Coe-Sullivan, J. S. Steckel, M. G. Bawendi, and V. Bulović, “Contact printing of quantum dot light-emitting devices.,” Nano Lett., vol. 8, no. 12, pp. 4513–7, Dec. 2008.

55. Z. Yue, F. Lisdat, W. J. Parak, S. G. Hickey, L. Tu, N. Sabir, D. Dorfs, and N. C. Bigall, “Quantum-dot-based photoelectrochemical sensors for chemical and biological detection.,” ACS Appl. Mater. Interfaces, vol. 5, no. 8, pp. 2800–14, Apr. 2013.

56. M. F. Frasco and N. Chaniotakis, “Semiconductor quantum dots in chemical sensors and biosensors.,” Sensors (Basel)., vol. 9, no. 9, pp. 7266–86, Jan. 2009.

57. P. Jorge, M. A. Martins, T. Trindade, J. L. Santos, and F. Farahi, “Optical Fiber Sensing Using Quantum Dots,” Sensors, vol. 7, no. 12, pp. 3489–3534, Dec. 2007.

58. J. Callan and F. Raymo, Quantum Dot Sensors: Technology and Commercial Applications. Pan Stanford Publications, 2013.

59. S. Nie, Y. Xing, G. J. Kim, and J. W. Simons, “Nanotechnology Applications in Cancer,” Annu. Rev. Biomed. Eng., vol. 9, pp. 257–288, 2007.

60. X. Michalet, F. F. Pinaud, L. a Bentolila, J. M. Tsay, S. Doose, J. J. Li, G. Sundaresan, a M. Wu, S. S. Gambhir, and S. Weiss, “Quantum dots for live cells, in vivo imaging, and diagnostics.,” Science, vol. 307, no. 5709, pp. 538–44, Jan. 2005.

61. A. P. Alivisatos, W. Gu, and C. Larabell, “Quantum dots as cellular probes.,” Annu. Rev. Biomed. Eng., vol. 7, pp. 55–76, Jan. 2005.

62. X. Li, Y. Wu, D. Steel, D. Gammon, T. H. Stievater, D. S. Katzer, D. Park, C. Piermarocchi, and L. J. Sham, “An all-optical quantum gate in a semiconductor quantum dot.,” Science, vol. 301, no. 5634, pp. 809–11, Aug. 2003.

63. K. Ludge, Ed., Nonlinear Laser Dynamics: From Quantum Dots to Cryptography. Wiley-VCH, 2011.

64. P. Michler, Ed., Single Semiconductor Quantum Dots. Springer, 2009.

65. W. W. Yu, L. Qu, W. Guo, and X. Peng, “Experimental Determination of the Extinction Coefficient of CdTe, CdSe, and CdS Nanocrystals,” Chem. Mater., vol. 125, no. 17, pp. 2854–2860, 2003.

66. H. C. v. c. Hulst, light scattering by small particles, 2nd ed. Dover, 1981.

67. N. Tomczak, D. Jańczewski, M. Han, and G. J. Vancso, “Designer polymer–quantum dot architectures,” Prog. Polym. Sci., vol. 34, no. 5, pp. 393–430, May 2009.

68. M. Tamborra, M. Striccoli, M. L. Curri, and A. Agostiano, “Hybrid Nanocomposites Based on Luminescent Colloidal Nanocrystals in Poly (methyl methacrylate): Spectroscopical and Morphological Studies,” 2008.

69. M. Peres, L. C. Costa, A. Neves, M. J. Soares, T. Monteiro, A. C. Esteves, T. Trindade, A. Kholkin, and E. Alves, “A green-emitting CdSe/poly (butyl acrylate) nanocomposite,” Nanotechnology, vol. 16, pp. 1969–1973, 2005.

70. M. Tamborra, M. Striccoli, R. Comparelli, M. L. Curri, a Petrella, and a Agostiano, “Optical properties of hybrid composites based on highly luminescent CdS nanocrystals in polymer,” Nanotechnology, vol. 15, no. 4, pp. S240–S244, Apr. 2004.

71. H. Gordillo, I. Suárez, R. Abargues, P. Rodríguez-Cantó, S. Albert, and J. P. Martínez-Pastor, “Polymer/QDs Nanocomposites for Waveguiding Applications,” J. Nanomater., vol. 2012, pp. 1–9, 2012.

72. J. Lee, C. Sundar, J. R. Heine, M. G. Bawendi, and K. Jensen, “Full Color Emission from II-VI Semiconductor,” Adv. Mater., vol. 12, no. 15, pp. 1102–1105, 2000.

73. S. Kim and M. G. Bawendi, “Oligomeric Ligands for Luminescent and Stable Nanocrystal Quantum Dots,” J. Am. Chem. Soc., vol. 125, pp. 14652–14653, 2003.

74. H. Uyeda and I. Medintz, “Synthesis of compact multidentate ligands to prepare stable hydrophilic quantum dot fluorophores,” J. Am. Chem. Soc., vol. 127, pp. 3870–3878, 2005.

75. H. Song and S. Lee, “Photoluminescent (CdSe)ZnS quantum dot–polymethylmethacrylate polymer composite thin films in the visible spectral range,” Nanotechnology, vol. 18, no. 5, pp. 055402, Feb. 2007.

76. L. Pang, Y. Shen, K. Tetz, and Y. Fainman, “PMMA quantum dots composites fabricated via use of pre-polymerization,” Opt. Express, vol. 13, no. 1, pp. 44–49, 2004.

77. D. Jańczewski, N. Tomczak, M.-Y. Han, and G. J. Vancso, “Synthesis of functionalized amphiphilic polymers for coating quantum dots.,” Nat. Protoc., vol. 6, no. 10, pp. 1546–53, Oct. 2011.

78. M. Wang, M. Zhang, J. Li, S. Kumar, G. C. Walker, G. D. Scholes, and M. A. Winnik, “Self-assembly of colloidal quantum dots on the scaffold of triblock copolymer micelles.,” ACS Appl. Mater. Interfaces, vol. 2, no. 11, pp. 3160–9, Nov. 2010.

79. M. P. Schaub, The design of plastic optical systems. Spie Press Book, 2009.

80. V. Kovalevskij and V. Gulbinas, “Photomodification of CdSe nanocrystals incorporated in a poly (butylmethacrylate) polymer film,” J. Appl. Phys., vol. 99, no. 014305, pp. 1–6, 2006.

81. M. Tamborra, M. Striccoli, R. Comparelli, M. L. Curri, a Petrella, a Agostiano, “Optical properties of hybrid composites based on highly luminescent CdS nanocrystals in polymer,” Nanotechnology, vol. 15, no. 4, pp. S240–S244, Apr. 2004.

82. Y. K. Olsson, G. Chen, R. Rapaport, D. T. Fuchs, and V. C. Sundar, “Fabrication and optical properties of polymeric waveguides containing nanocrystalline quantum dots,” vol. 85, no. 19, pp. 4469–4471, 2004.

83. J. E. MArk, Ed., Physical Properties of Polymers Handbook, 2nd ed. springer, 2007.

84. J. M. G. Cowie and V. Arrighi, Polymers: Chemistry and Physics of Modern Materials, 3rd ed. CRC Press, 2007.

85. D. L. Lee, Electromagnetic Principles of Integrated Optics. John Wiley & Sons, 1986.

86. M. Bass, C. DeCusatis, J. Enoch, V. Lakshminarayanan, G. Li, C. McDonald, V. Mahajan, and E. Van Stryland, Handbook of Optics, 3rd ed. McGraw-Hill, 2009.

87. M. Quinten, A Practical Guide to Optical Metrology for Thin Films. Wiley-VCH, 2013.

88. E. D. Palik, Handbook of Optical Constants of Solids. Academic Press, 1997.

89. I. Filiński, “The effects of sample imperfections on optical spectra,” Phys. Status Solidi, vol. 49, no. 2, pp. 577–588, Feb. 1972.

90. J. Szczyrbowski and A. Czapla, “Optical absorption in dc sputtered InAs films,” Thin Solid Films, vol. 46, pp. 127–137, 1977.

91. C. C. Katsidis and D. I. Siapkas, “General transfer-matrix method for optical multilayer systems with coherent, partially coherent, and incoherent interference,” Appl. Opt., vol. 41, no. 19, pp. 3978–3987, 2002.

92. J. Nelder and R. Mead, “A simplex method for function minimization,” Comput. J., vol. 7,

pp. 308–313, 1965.

93. W. H. Press, S. A. Teukolsky, W. T. Vetterling, and B. P. Flannery, Numerical Recipes: The Art of Scientific Computing, 3rd ed. Cambridge University, 2007.

94. J. C. M. Garnett, "Colours in Metal Glasses and in Metallic Films," Philos. Trans. R. Soc. A Math. Phys. Eng. Sci., vol. 203, no. 359–371, pp. 385–420, Jan. 1904.

95. D. A. G. Bruggeman, "Berechnung verschiedener physikalischer Konstanten von heterogenen Substanzen. I. Dielektrizitätskonstanten und Leitfähigkeiten der Mischkörper aus isotropen Substanzen," Ann. Phys., vol. 5, no. 24, pp. 636–679, 1935.

96. H. Gordillo, R. Abargues, S. Albert, and J. Martinzez-Pastor, "Photoluminescence waveguiding in CdSe and CdTe QDs – PMMA nanocomposite films," Nanotechnology, vol. 22, no. 435202, pp. 1–8, 2011.

97. L. L. Hench and J. K. West, "The sol-gel process," Chem. Rev., vol. 90, no. 1, pp. 33–72, Jan. 1990.

98. C. J. Brinker and G. W. Scherer, Sol-Gel Science: The Physics and Chemistry of Sol-Gel Processing. Academic Press, 1990.

99. L. C. Klein, Ed., Sol-Gel Optics, Processing and Applications. Springer, 1994.

100. P. K. Biswas, "Sol–gel thin films for optics and photonics," J. Sol-Gel Sci. Technol., vol. 59, no. 3, pp. 456–474, Dec. 2010.

101. G. C. Righini and A. Chiappini, "Glass optical waveguides: a review of fabrication techniques," Opt. Eng., vol. 53, no. 7, p. 071819, Mar. 2014.

102. G. Philipp and H. Schmidt, "New materials for contact lenses prepared from Si- and Ti-alkoxides by the sol-gel process," J. Non. Cryst. Solids, vol. 63, no. 1–2, pp. 283–292, Feb. 1984.

103. A. Lukowiak and W. Strek, "Sensing abilities of materials prepared by sol-gel technology," J. Sol-Gel Sci. Technol., vol. 50, no. 2, pp. 201–215, Mar. 2009.

104. M. a. Petruska, A. V. A. V Malko, P. M. P. M. Voyles, V. I. V. I. Klimov, Q. Dot, and B. M. A. Petruska, "High-Performance, Quantum Dot Nanocomposites for Nonlinear Optical and Optical Gain Applications," Adv. Mater., vol. 15, no. 78, pp. 610–613, Apr. 2003.

105. V. Sundar, H. Eisler, and M. Bawendi, "Room-Temperature, Tunable Gain Media from Novel II–VI Nanocrystal–Titania Composite Matrices," Adv. Mater., vol. 14, no. 10, pp. 739–743, 2002.

106. M. a. Petruska, a. V. Malko, P. M. Voyles, and V. I. Klimov, "High-Performance, Quantum Dot Nanocomposites for Nonlinear Optical and Optical Gain Applications," Adv. Mater., vol. 15, no. 78, pp. 610–613, Apr. 2003.

107. M. Bockmeyer and P. Löbmann, "Crack formation in TiO_2 films prepared by sol–gel processing: Quantification and characterization," Thin Solid Films, vol. 515, no. 13, pp. 5212–5219, May 2007.

108. C. Urlacher, C. M. De Lucas, and J. Mugnier, "Chemical and physical aspects of sol—gel

process for planar waveguides elaboration: application to zirconia waveguides," Synth. Met., vol. 90, no. 3, pp. 199–204, Nov. 1997.

109. D. Bradley, R. C. Mehrotra, I. Rotwell, and A. Singh, Alkoxo and Aryloxo Derivatives of Metals. Academic Press, 2001.

110. B. J. Jasieniak, J. Pacifico, R. Signorini, A. Chiasera, M. Ferrari, A. Martucci, and P. Mulvaney, "Luminescence and Amplified Stimulated Emission in CdSe – ZnS-Nanocrystal-Doped TiO_2 and ZrO_2 Waveguides," Adv. Funct. Mater., vol. 17, pp. 1654–1662, 2007.

111. K.-H. Haas and H. Wolter, "Synthesis, properties and applications of inorganic–organic copolymers (ORMOCER®s)," Curr. Opin. Solid State Mater. Sci., vol. 4, no. 6, pp. 571–580, Dec. 1999.

112. G. Schottner, "Hybrid Sol−Gel-Derived Polymers: Applications of Multifunctional Materials," Chem. Mater., vol. 13, no. 10, pp. 3422–3435, Oct. 2001.

113. R. Houbertz, G. Domann, C. Cronauer, a. Schmitt, H. Martin, J.-U. Park, L. Fröhlich, R. Buestrich, M. Popall, U. Streppel, P. Dannberg, C. Wächter, and a. Bräuer, "Inorganic–organic hybrid materials for application in optical devices," Thin Solid Films, vol. 442, no. 1–2, pp. 194–200, Oct. 2003.

114. R. Buestrich, F. Kahlenberg, M. Popall, P. Dannberg, R. Müller-Fiebler, and O. Rösch, "ORMOCERs s for Optical Interconnection Technology," J. Sol-Gel Sci. Technol., vol. 20, pp. 181–186, 2001.

115. M. a. Fardad, O. V. Mishechkin, and M. Fallahi, "Hybrid sol-gel materials for integration of optoelectronic components," J. Light. Technol., vol. 19, no. 1, pp. 84–91, 2001.

116. R. Houbertz, L. Fröhlich, M. Popall, U. Streppel, P. Dannberg, a. Bräuer, J. Serbin, and B. N. Chichkov, "Inorganic–Organic Hybrid Polymers for Information Technology: from Planar Technology to 3D Nanostructures," Adv. Eng. Mater., vol. 5, no. 8, pp. 551–555, Aug. 2003.

117. C. Sanchez, F. Ribot, and B. Lebeau, "Molecular design of hybrid organic–inorganic nanocomposites synthesized," J. Mater. Chem., vol. 9, pp. 35–44, 1999.

118. G. S. Sur and J. E. Mark, "Elastomeric networks cross-linked by silica or titania fillers," Eur. Polym. J., vol. 21, no. 12, pp. 1051–1052, Jan. 1985.

119. Fraunhofer ISC, Manufacturing processes of ORMOCERs(R), available online: http://www.ormocere.de/Manufacturing-processes.herstellungsverfahren.0.html

120. M. Robertsson, J. Haglund, C. Johansson, P. Gibaud, D. Lambert, M. Popall, A. Tolvgård, A. Alping, L. Linden, J. Rodekirch, M. I. Zemel, and C. C. Nunes, "Large area patterning of high density interconnects by novel UV-excimer lithography and photo patternable ORMOCER TM -dielectrica," in IMAPS Conference, May 30 - June 1, 2001.

121. U. Streppel, P. Dannberg, C. Waechter, A. Braeuer, P. Nicole, L. Froehlich, R. Houbertz, and

M. Popall, “Development of a new fabrication method for stacked optical waveguides using inorganic-organic copolymers,” in First International IEEE Conference on Polymers and Adhesives in Microelectronics and Photonics. Incorporating POLY, PEP & Adhesives in Electronics. Proceedings (Cat. No.01TH8592), 2001, pp. 329–335.

122. “Processing Guidelines – OrmoCore and OrmoClad.” micro resist technology GmbH, Berlin, Germany, pp. 1–9.

123. A. Neumeister, C. Materlik, T. Temme, A. Osterdorf, and R. Himmelhuber, “Process accuracy during laser based stero lithograpy and production of Ormocer micro systems with related mechanical properties,” in Virtual and Rapid Manufacturing: Advanced Research in Virtual and Rapid Prototyping, P. J. da S. Bartolo, M. A. Jorge, F. da C. Batista, H. A. Almeida, J. M. Matias, J. C. Vasco, J. B. Gaspar, M. A. Correia, N. C. Andre, N. F. Alves, P. P. Novo, P. G. Martinho, and R. A. Carvalho, Eds. Balkema, 2007, pp. 501–508.

124. A. Yusop, A. Kassir, A. A. Ehsan, and S. Shaari, “Determination of Thermo-Optic Coefficient of a UV Curable Polymer using Prism Coupling Technique,” in ICSE2004 Proc 2004, Kuala Lumpur, Malaysia, 2004, vol. 00, no. c, pp. 482–485.

125. U. Streppel, P. Dannberg, C. A. Waechter, A. H. Braeuer, P. Nicole, L. Froehlich, R. Houbertz, and M. Popall, “Multilayer optical fan-out device composed of stacked monomode waveguides,” in Materials and Devices for Photonic Circuits II, SPIE Proceedings, vol. 4453, 2001, pp. 61–68.

126. C. Bullen, P. Mulvaney, C. Sada, M. Ferrari, A. Chiasera, and A. Martucci, “Incorporation of a highly luminescent semiconductor quantum dot in ZrO_2-SiO_2 hybrid sol-gel glass film,” J. Mater. Chem., vol. 14, no. 7, p. 1112, 2004.

127. F. Del Monte, Y. Xu, and J. Mackenzie, “Preparation and characterization of PbS quantum dots doped Ormocers,” J. sol-gel Sci., vol. 17, pp. 37–45, 2000.

128. N. K. Chaudhury, R. Gupta, and S. Gulia, “Sol-gel Technology for Sensor Applications,” Def. Sci. J., vol. 57, no. 3, pp. 241–253, 2007.

129. J. Wang, “Sol–gel materials for electrochemical biosensors,” Anal. Chim. Acta, vol. 399, no. April, pp. 21–27, 1999.

130. J. Lin and C. Brown, “Sol-gel glass as a matrix for chemical and biochemical sensing,” TrAC Trends Anal. Chem., vol. 16, no. 4, pp. 200–211, 1997.

131. C. Garzella, E. Comini, and E. Tempesti, “TiO_2 thin films by a novel sol–gel processing for gas sensor applications,” Sensors Actuators B, vol. 68, pp. 189–196, 2000.

132. C. McDonagh, B. D. Maccraith, and a K. McEvoy, “Tailoring of sol-gel films for optical sensing of oxygen in gas and aqueous phase.,” Anal. Chem., vol. 70, no. 1, pp. 45–50, Jan. 1998.

133. C. Cantalini, M. Post, D. Buso, M. Guglielmi, and a. Martucci, “Gas sensing properties of nanocrystalline NiO and Co3O4 in porous silica sol–gel films,” Sensors Actuators B Chem., vol. 108, no. 1–2, pp. 184–192, Jul. 2005.

134. M. G. Manera, J. Spadavecchia, D. Buso, C. de Julián Fernández, G. Mattei, a. Martucci,

P. Mulvaney, J. Pérez-Juste, R. Rella, L. Vasanelli, and P. Mazzoldi, “Optical gas sensing of TiO_2 and TiO_2/Au nanocomposite thin films,” Sensors Actuators B Chem., vol. 132, no. 1, pp. 107–115, May 2008.

135. G. Wirnsberger, P. Yang, B. J. Scott, B. F. Chmelka, and G. D. Stucky, “Mesostructured materials for optical applications: from low-k dielectrics to sensors and lasers,” Spectrochim. Acta. A. Mol. Biomol. Spectrosc., vol. 57, no. 10, pp. 2049–60, Sep. 2001.
136. G. Manasis, A. Tsigara, A. Giannoudakos, G. Anyfantis, K. Gatsouli, G. Mousdis, S. Pispas, and N. Madamopoulos, N.; Vainos, “Cobalt chloride based nanocomposite humidity sensors,” Glas. Technol. - Eur. J. Glas. Sci. Technol. Part A, vol. 46, no. 2, pp. 171–174, 2005.
137. N. A. Vainos, Ed., Laser growth adn processing of photonic devices. Woodhead Publishing, 2012.
138. H. Misawa and S. Juodkazis, Eds., 3D Laser Microfabrication. Wiley-VCH, 2006.
139. R. Srinivasan, “Ablation of polymers and biological tissue by ultraviolet lasers,” Science, vol. 234, no. 4776, pp. 559–565, Oct. 1986.
140. D. Basting and G. Marowsky, Eds., Excimer Laser Technology. 2005.
141. J. Fischer and M. Wegener, “Three-dimensional optical laser lithography beyond the diffraction limit,” Laser Photon. Rev., vol. 7, no. 1, pp. 22–44, Jan. 2013.
142. T. Lippert, “Laser Application of Polymers,” in Polymers and Light, T. K. Lippert, Ed. Springer-Verlag, 2004, pp. 51–246.
143. B. E. A. Saleh and M. C. Teich, Fundamentals of Photonics, 2nd ed. Wiley, 2006.
144. M. D. Shirk and P. A. Molian, “A review of ultrashort pulsed laser ablation of materials,” J. Laser Appl., vol. 10, no. 1, p. 18, 1998.
145. D. G. Rabus, Integrated Ring Resonators. Springer, 2007.
146. J. E. Heebner, R. Grover, and T. A. Ibrahim, Optical Microresonators. Springer, 2008.
147. I. Chremmos, O. Schwelb, and N. Uzunoglu, Eds., Photonic Microresonators, Research and Applications. Springer, 2010.
148. R. G. Hunsperger, Integrated Optics Theory and Technology, 6th ed. New York, NY: Springer, 2009, pp. 53–84.
149. T. J. Kippenberg, S. M. Spillane, D. K. Armani, B. Min, and K. K. Vahala, “Fabrication, coupling and nonlinear optics of ultra-high-Q micro-sphere and chip-based toroid microcavities,” in Optical Microcavities, K. Vahala, Ed. World Scientific, 2004, pp. 177–238.
150. S. Xue, M. A. Eijkelenborg, G. Barton, and P. Hambley, “Theoretical, Numerical, and Experimental Analysis of Optical Fiber Tapering,” J. Light. Technol., vol. 25, no. 5, pp. 1169–1176, 2007.
151. C. M. Sotomayor Torres, Ed., Alternative Lithography: Unleashing the Potentials of Nanotechnology. Springer, 2003.
152. M. J. Madou, Fundamentals of Microfabrication and Nanotechnology, 3rd ed. CRC Press, 2011.

153. S. Cabrini and S. Kawata, Eds., Nanofabrication Handbook. CRC Press, 2012.

154. Y. Xia, J. a. Rogers, K. E. Paul, and G. M. Whitesides, “Unconventional Methods for Fabricating and Patterning Nanostructures.,” Chem. Rev., vol. 99, no. 7, pp. 1823–1848, Jul. 1999.

155. B. D. Gates, Q. Xu, M. Stewart, D. Ryan, C. G. Willson, and G. M. Whitesides, “New approaches to nanofabrication: molding, printing, and other techniques.,” Chem. Rev., vol. 105, no. 4, pp. 1171–96, Apr. 2005.

156. S. R. Quake and A. Scherer, “From Micro- to Nanofabrication with Soft Materials,” Science, vol. 290, no. 5496, pp. 1536–1540, Nov. 2000.

157. R. Shenhar, T. B. Norsten, and V. M. Rotello, “Polymer-Mediated Nanoparticle Assembly: Structural Control and Applications,” Adv. Mater., vol. 17, no. 6, pp. 657–669, Mar. 2005.

158. J. A. Rogers and R. G. Nuzzo, “Recent progress in soft lithography,” materials today, pp. 50–56, 2005.

159. Z. Cui, Nanofabrication: Principles. Capabilities and Limits. Springer, 2008.

160. Z. Li, Y. Gu, L. Wang, H. Ge, W. Wu, Q. Xia, C. Yuan, Y. Chen, B. Cui, and R. S. Williams, “Hybrid nanoimprint-soft lithography with sub-15 nm resolution.,” Nano Lett., vol. 9, no. 6, pp. 2306–10, Jun. 2009.

161. Y. Xia and G. M. Whitesides, “Soft Lithography,” Angew. Chemie Int. Ed., vol. 37, no. 5, pp. 550–575, Mar. 1998.

162. Y. Xia, J. Tien, D. Qin, and G. M. Whitesides, “Non-Photolithographic Methods for Fabrication of Elastomeric Stamps for Use in Microcontact Printing,” Langmuir, vol. 12, no. 16, pp. 4033–4038, 1996.

163. W. A. Z. Elaine G. Shafrin, “Constitutive relations in the wetting of low energy surfaces and the theory of the retraction method of preparing monolayers,” J. Phys. Chem., vol. 64, pp. 519–524, 1960.

164. T. Nishino, M. Meguro, K. Nakamae, M. Matsushita, and Y. Ueda, “The Lowest Surface Free Energy Based on −CF 3 Alignment,” Langmuir, vol. 15, no. 13, pp. 4321–4323, Jun. 1999.

165. F.-C. Chen, Jem-Kun and Ko, Fu-Hsiang and Hsieh, Kuen-Fong and Chou, Cheng-Tung and Chang, “Effect of fluoroalkyl substituents on the reactions of alkylchlorosilanes with mold surfaces for nanoimprint lithography,” J. Vac. Sci. Technol. B, vol. 22, pp. 3233–3241, 2004.

166. H. Schift, S. Saxer, S. Park, C. Padeste, U. Pieles, and J. Gobrecht, “Controlled co-evaporation of silanes for nanoimprint stamps,” Nanotechnology, vol. 16, no. 5, pp. S171–S175, May 2005.

167. J. Lötters, W. Olthuis, P. H. Veltink, and P. Bergveld, “The mechanical properties of the rubber elastic polymer polydimethylsiloxane for sensor applications,” J. Micromechanics Microengineering, vol. 7, pp. 145–147, 1997.

168. micro-resist technogy, “Processing Guidelines – OrmoCore and OrmoClad OrmoCore and

OrmoClad Processing Guidelines".

169. B. Bhushan, "Self-Assembled Monolayers for Nanotribology and Surface Protection," in Springer Handbook of Nanotechnology, 3rd ed., B. Bhushan, Ed. Springer, 2010, pp. 1309–1346.

170. D. W. Thomas, C. Foulkes-Williams, P. T. Rumsby, and M. C. Gower, "Laser Ablation of Electronic Materials: Basic Mechanisms and Applications," in Laser Ablation of Electronic Materials: Basic Mechanisms and Applications, S. Lazare, Ed. Elsevier, 1992.

171. B. E. Kim, Y. Xia, X. Zhao, and G. M. Whitesides, "Solvent-Assisted Microcontact Molding: A Convenient Method for Fabricating Three-Dimensional Structures on Surfaces of Polymers," Adv. Mater., vol. 9, no. 8, pp. 651–654, 1997.

172. M. Leemann, G. Eigenberger, and H. Strathmann, "Vapour permeation for the recovery of organic solvents from waste air streams: separation capacities and process optimization," J. Memb. Sci., vol. 113, no. 2, pp. 313–322, May 1996.

173. Y. Hu, X. Chen, G. M. Whitesides, J. J. Vlassak, and Z. Suo, "Indentation of polydimethylsiloxane submerged in organic solvents," J. Mater. Res., vol. 26, no. 06, pp. 785–795, Jan. 2011.

174. M. a Eddings and B. K. Gale, "A PDMS-based gas permeation pump for on-chip fluid handling in microfluidic devices," J. Micromechanics Microengineering, vol. 16, no. 11, pp. 2396–2402, Nov. 2006.

175. S. L. Cuang, Physics of Photonic Devices. Wiley, 2009.

176. J. S. Wilson, Ed., Sensor Technology Handbook. Elsevier, 2005.

177. J. Fraden, Handbook of Modern Sensors: Physics, Designs, and Applications, 4th ed. Springer, 2010.

178. M. J. Usher and D. A. Keating, Sensors and Transducers: Characteristics, Applications, Instrumentation, Interfacing, 2nd ed. Palgrave Macmillan, 1996.

179. H. Gopel, Sensors: A Comprehensive Survey. Wiley VCH, 2001.

180. K. Kalantar-zadeh and B. Fry, Eds., Nanotechnology-Enabled Sensors. Springer, 2008.

181. F.-G. Banica, Chemical Sensors and Biosensors: Fundamentals and Applications. Wiley, 2012.

182. B. R. Eggins, Chemical Sensors and Biosensors (Analytical Techniques in the Sciences. Wiley, 2002.

183. J. Janata, Principles of Chemical Sensors, 2nd ed. Springer, 2009.

184. J. Hauss, Optical Sensors: Basics and Applications. Wiley-VCH, 2010.

185. G. C. Righini, A. Tajani, and A. Cutolo, An Introduction to Optoelectronic Sensors. World Scientific, 2009.

186. F. Baldini, A. N. Chester, J. Homola, and S. Martellucci, Eds., Optical Chemical Sensors. Springer, 2006.

187. P. V Lambeck, "Integrated optical sensors for the chemical domain," Meas. Sci. Technol.,

vol. 17, no. 8, pp. R93–R116, Aug. 2006.

188. G. Korotcenkov, Handbook of Gas Sensor Materials: Properties, Advantages and Shortcomings for Applications Volume 1: Conventional Approaches. Springer, 2013.

189. R. Knake, P. Jacquinot, A. W. E. Hodgson, and P. C. Hauser, “Amperometric sensing in the gas-phase,” Anal. Chim. Acta, vol. 549, no. 1–2, pp. 1–9, Sep. 2005.

190. A. Hodgson and P. Jacquinot, “Amperometric gas sensors with detection limits in the low ppb range,” Anal. Chim. Acta, vol. 393, no. 1–3, pp. 43–48, 1999.

191. I.-D. Kim, A. Rothschild, and H. L. Tuller, “Advances and new directions in gas-sensing devices,” Acta Mater., vol. 61, no. 3, pp. 974–1000, Feb. 2013.

192. C. Wang, L. Yin, L. Zhang, D. Xiang, and R. Gao, “Metal oxide gas sensors: sensitivity and influencing factors.,” Sensors, vol. 10, no. 3, pp. 2088–106, Jan. 2010.

193. P. K. Basu, S. K. Jana, H. Saha, and S. Basu, “Low temperature methane sensing by electrochemically grown and surface modified ZnO thin films,” Sensors Actuators B Chem., vol. 135, no. 1, pp. 81–88, Dec. 2008.

194. P. K. Basu, P. Bhattacharyya, N. Saha, H. Saha, and S. Basu, “The superior performance of the electrochemically grown ZnO thin films as methane sensor,” Sensors Actuators B Chem., vol. 133, no. 2, pp. 357–363, Aug. 2008.

195. V. Srivastava and K. Jain, “Highly sensitive NH3 sensor using Pt catalyzed silica coating over WO3 thick films,” Sensors Actuators B Chem., vol. 133, no. 1, pp. 46–52, Jul. 2008.

196. Y. Zhang, N. Raman, J. K. Bailey, C. J. Brinker, and R. M. C. Tt, “A New Sol-Gel Route for the Preparatlon of Nanometer-Scale Semiconductor Particles That Exhibit Quantum Optical Behavior,” J. Phys. Chem., vol. 96, pp. 9098–9100, 1992.

197. C. S. Rout, M. Hegde, a Govindaraj, and C. N. R. Rao, “Ammonia sensors based on metal oxide nanostructures,” Nanotechnology, vol. 18, no. 20, p. 205504, May 2007.

198. N. I. Hammer, T. Emrick, and M. D. Barnes, “Quantum dots coordinated with conjugated organic ligands : new nanomaterials with novel photophysics,” Nanoscale Res. Lett., vol. 2, pp. 282–290, 2007.

199. M. A. Carpenter, S. Mathur, and A. Kolmakov, Eds., Metal Oxide Nanomaterials for Chemical Sensors. Springer, 2012.

200. K. Zakrzewska, “Mixed oxides as gas sensors,” Thin Solid Films, vol. 391, no. 2, pp. 229–238, Jul. 2001.

201. H. Bai and G. Shi, “Gas Sensors Based on Conducting Polymers,” Sensors, vol. 7, no. 3, pp. 267–307, Mar. 2007.

202. J. Janata and M. Josowicz, “Conducting polymers in electronic chemical sensors.,” Nat. Mater., vol. 2, no. 1, pp. 19–24, Jan. 2003.

203. C. M. Hangarter, N. Chartuprayoon, S. C. Hernández, Y. Choa, and N. V. Myung,

"Hybridized conducting polymer chemiresistive nano-sensors," Nano Today, vol. 8, no. 1, pp. 39–55, Feb. 2013.

204. M. Ates, "A review study of (bio)sensor systems based on conducting polymers," Mater. Sci. Eng. C. Mater. Biol. Appl., vol. 33, no. 4, pp. 1853–9, May 2013.

205. B. Adhikari and S. Majumdar, "Polymers in sensor applications," Prog. Polym. Sci., vol. 29, no. 7, pp. 699–766, Jul. 2004.

206. U. Lange, N. V Roznyatovskaya, and V. M. Mirsky, "Conducting polymers in chemical sensors and arrays.," Anal. Chim. Acta, vol. 614, no. 1, pp. 1–26, Apr. 2008.

207. a. L. Kukla, Y. M. Shirshov, and S. a. Piletsky, "Ammonia sensors based on sensitive polyaniline films," Sensors Actuators B Chem., vol. 37, no. 3, pp. 135–140, Dec. 1996.

208. X.-J. Huang and Y.-K. Choi, "Chemical sensors based on nanostructured materials," Sensors Actuators B Chem., vol. 122, no. 2, pp. 659–671, Mar. 2007.

209. J. Brugger, "Nanotechnology impact on sensors.," Nanotechnology, vol. 20, no. 43, p. 430206, Oct. 2009.

210. S. Baruah and J. Dutta, "Nanotechnology applications in pollution sensing and degradation in agriculture: a review," Environ. Chem. Lett., vol. 7, no. 3, pp. 191–204, Jul. 2009.

211. T. Zhang, S. Mubeen, N. V Myung, and M. a Deshusses, "Recent progress in carbon nanotube-based gas sensors.," Nanotechnology, vol. 19, no. 33, p. 332001, Aug. 2008.

212. B. Lee, "Review of the present status of optical fiber sensors," Opt. Fiber Technol., vol. 9, no. 2, pp. 57–79, Apr. 2003.

213. H.-N. Kim, W. Xiu Ren, J. S. Kim, and J. Yoon, "Fluorescent and colorimetric sensors for detection of lead, cadmium, and mercury ions," Chem. Soc. Rev., vol. 41, no. 8, pp. 3210–3244, 2012.

214. J. R. Askim, M. Mahmoudi, and K. S. Suslick, "Optical sensor arrays for chemical sensing: the optoelectronic nose," Chem. Soc. Rev., vol. 42, no. 22, pp. 8649–8682, 2013.

215. A. K. Sharma, M. S. Gaur, P. Sharma, R. K. Tiwari, and S. Bhadoria, "Development of colorimetric sensor instrument for quantitative analysis of methyl parathion," Sens. Rev., vol. 29, no. 1, pp. 70–74, 2009.

216. X. Chen, Y. Zhou, X. Peng, and J. Yoon, "Fluorescent and Colorimetric Probes for Detection of Thiols," Chem. Soc. Rev., vol. 39, no. 6, pp. 2120–2135, 2010.

217. H.-A. Ho, M. Boissinot, M. G. Bergeron, G. Corbeil, K. Doré, D. Boudreau, and M. Leclerc, "Colorimetric and fluorometric detection of nucleic acids using cationic polythiophene derivatives.," Angew. Chem. Int. Ed. Engl., vol. 41, no. 9, pp. 1548–51, May 2002.

218. U. Tu, J. Homola, S. S. Yee, and G. Gauglitz, "Surface plasmon resonance sensors: review," Sensors Actuators B Chem., vol. 54, pp. 3–15, 1999.

219. Y. Chen and H. Ming, "Review of surface plasmon resonance and localized surface

plasmon resonance sensor," Photonic Sensors, vol. 2, no. 1, pp. 37–49, Jan. 2012.

220. X. D. Hoa, a G. Kirk, and M. Tabrizian, "Towards integrated and sensitive surface plasmon resonance biosensors: a review of recent progress.," Biosens. Bioelectron., vol. 23, no. 2, pp. 151–60, Sep. 2007.

221. E. Udd and W. B. Spillman, Eds., Fiber Optic Sensors: An Introduction for Engineers and Scientists, 2nd ed. Wiley, 2011.

222. S. Yin, P. B. Ruffin, and Y. F. R. S., Eds., Fiber Optic Sensors. CRC Press, 2008.

223. X.-D. Wang and O. S. Wolfbeis, "Fiber-optic chemical sensors and biosensors," Anal. Chem., vol. 85, no. 2, pp. 487–508, Jan. 2013.

224. K. T. V. Grattan and T. Sun, "Fiber optic sensor technology: an overview," Sensors Actuators A Phys., vol. 82, no. 1–3, pp. 40–61, May 2000.

225. A. D. Kersey, "A Review of Recent Developments in Fiber Optic Sensor Technology," Opt. Fiber Technol., vol. 2, no. 3, pp. 291–317, 1996.

226. T. L. Yeo, T. Sun, and K. T. V. Grattan, "Fibre-optic sensor technologies for humidity and moisture measurement," Sensors Actuators A Phys., vol. 144, no. 2, pp. 280–295, Jun. 2008.

227. M.-S. Kwon and W. H. Steier, "Microring-resonator-based sensor measuring both the concentration and temperature of a solution.," Opt. Express, vol. 16, no. 13, pp. 9372–7, Jun. 2008.

228. V. M. N. Passaro, F. Dell'Olio, and F. De Leonardis, "Ammonia Optical Sensing by Microring Resonators," Sensors, vol. 7, no. 11, pp. 2741–2749, Nov. 2007.

229. I. M. White, H. Oveys, and X. Fan, "Liquid-core optical ring-resonator sensors.," Opt. Lett., vol. 31, no. 9, pp. 1319–21, May 2006.

230. B. Troia, A. Paolicelli, F. De Leonardis, and V. M. N. Passaro, "Photonic Crystals for Optical Sensing: A Review," in Advances in Photonic Crystals, V. M. N. Passaro, Ed. InTech, 2013, pp. 241–295.

231. Y. Liu and H. W. M. Salemink, "Photonic crystal-based all-optical on-chip sensor.," Opt. Express, vol. 20, no. 18, pp. 19912–20, Aug. 2012.

232. M. Lončar, A. Scherer, and Y. Qiu, "Photonic crystal laser sources for chemical detection," Appl. Phys. Lett., vol. 82, no. 26, p. 4648, 2003.

233. S. a Asher, V. L. Alexeev, A. V Goponenko, A. C. Sharma, I. K. Lednev, C. S. Wilcox, and D. N. Finegold, "Photonic crystal carbohydrate sensors: low ionic strength sugar sensing.," J. Am. Chem. Soc., vol. 125, no. 11, pp. 3322–9, Mar. 2003.

234. J. Hodgkinson and R. P. Tatam, "Optical gas sensing: a review," Meas. Sci. Technol., vol. 24, no. 1, p. 012004, Jan. 2013.

235. M. Lackner, "Tunable Diode Laser Absortpion Spectroscopy (TDLAS) in the Process Industries - A Review," Rev. Chem. Eng., vol. 23, no. 2, pp. 65–147, 2011.

236. M. G. Allen, "Diode laser absorption sensors for gas-dynamic and combustion flows.,"

Meas. Sci. Technol., vol. 9, no. 4, pp. 545–62, Apr. 1998.

237. K. Reddy, Y. Guo, J. Liu, W. Lee, M. K. Khaing Oo, and X. Fan, “On-chip Fabry–Pérot interferometric sensors for micro-gas chromatography detection,” Sensors Actuators B Chem., vol. 159, no. 1, pp. 60–65, Nov. 2011.
238. A. Brandenburg, R. Krauter, C. Künzel, M. Stefan, and H. Schulte, “Interferometric sensor for detection of surface-bound bioreactions.,” Appl. Opt., vol. 39, no. 34, pp. 6396–405, Dec. 2000.
239. A. Ymeti, J. S. Kanger, J. Greve, P. V Lambeck, R. Wijn, and R. G. Heideman, “Realization of a multichannel integrated Young interferometer chemical sensor.,” Appl. Opt., vol. 42, no. 28, pp. 5649–60, Oct. 2003.
240. R. M. Measures, Laser Remote Sensing: Fundamentals and Applications. Krieger, 1992.
241. M. C. Roggermann, B. M. Welsh, and B. R. Hunt, Imaging Through Turbulence. CRC Press, 1996.
242. E. Masciadri and M. Sarazin, Optical Turbulence, Astronomy Meets Meteorology: Proccedings of the Optical Turbulence Characterization for Astronomical Applications, Sardinia, Italy, 15-18 September 2008. Imperial College Press, 2009.
243. W. Hong-shuai, Y. Yong-qiang, Q. Xuan, L. Li-yong, W. Yi-ping, and L. Jun-rong, “Method of Modeling Atmospheric Optical Turbulence,” Chinese Astron. Astrophys., vol. 37, no. 3, pp. 345–356, Jul. 2013.
244. O. S. Heavens, Optical Properties of Thin Solid Films. Dover, 1995.
245. B. Timmer, W. Olthuis, and A. Van Den Berg, “Ammonia sensors and their applications—a review,” Sensors Actuators B Chem., vol. 107, no. 2, pp. 666–677, Jun. 2005.
246. M. Appl, “Ammonia,” in Ullmann’s Encyclopedia of Industrial Chemistry, Wiley-VCH, 2000.
247. “Council Directive 67/548/EEC of 27 June 1967 on the approximation of laws, regulations and administrative provisions relating to the classification, packaging and labelling of dangerous substances.” Amended various time the directive will be replaced by the “Classification, Labelling and Packaging” (CLP) Regulation starting in 2016.
248. “Ammonia health effects descriptions and precautions under the ‘Managing Hazardous Materials Incidents’ guidelines of the Agency for Toxic Substances and Disease Registry (ATSDDR) of the U.S. Department of Health and Human Services.”
249. “Toxic FAQ Sheet for Ammonia.” Agency for Toxic Substances and Disease Registry (ATSDR), 2004.
250. “U.S. Department of Health and Human Services, Public Health Service, Agency for Toxic Subastances and Disease Registry, ‘Toxicological Profile for Ammonia.’”Available online: http://www.atsdr.cdc.gov/toxprofiles/tp126.pdf.
251. “U.S. Department of Health and Human Services, Public Health Service, Agency

for Toxic Subastances and Disease Registry, ‘Public Health Statement. Ammonia.’” Available online: http://www.atsdr.cdc.gov/toxprofiles/tp126-c1-b.pdf.

252. “Internation Programme on Chemical Safety (joint venture of the United Nαtions Environment Programme, the International Labour Organisation, and the World Health Organization, Environmental Health Criteria 54, Ammonia report.” Available online: http://www.inchem.org/documents/ehc/ehc/ehc54.htm.
253. H. J. Levinson, Principles of Lithography, 3rd ed. SPIE Press Monograph, 2011.
254. C. Mack, Fundamental Principles of Optical Lithography: The Science of Microfabrication. Wiley, 2007.
255. C. Mack, Field Guide to Optical Lithography. SPIE Publications, 2006.
256. B. J. Lin, Optical Lithography: Here is Why. SPIE Press Monograph, 2010.
257. A. Tsigara, G. Mountrichas, K. Gatsouli, a. Nichelatti, S. Pispas, N. Madamopoulos, N. A. Vainos, H. L. Du, and F. Roubani-Kalantzopoulou, “Hybrid polymer/cobalt chloride humidity sensors based on optical diffraction,” Sensors Actuators B Chem., vol. 120, no. 2, pp. 481–486, Jan. 2007.
258. E. Kim, Y. Xia, and G. M. Whitesides, “Micromolding in Capillaries : Applications in Materials Science,” J. Am. Chem. Soc., vol. 118, pp. 5722–5731, 1996.
259. X. Zhao, Y. Xia, and G. M. Whitesides, “Fabrication of Three-Dimensional Micro-Stuctures: Microtranfer Molding,” Adv. Mater., vol. 8, no. 10, pp. 837–840, 1996.
260. E. Kin, Y. Xia, and G. M. Whitesides, “Polymer microstructures formed by moulding in capillaries,” Nature, vol. 376, pp. 581–584, 1995.
261. L. Athanasekos, S. Pispas, and C. Riziotis, “Novel block copolymers for multi-agent detection using polymer optical fibers,” in Microstructured and Specialty Optical Fibres, 2012, pp. 842615–842622.
262. M. G. Moharam and T. K. Gaylord, “Rigorous coupled-wave analysis of planar-grating diffraction,” J. Opt. Soc. Am., vol. 71, no. 7, p. 811, Jul. 1981.
263. M. G. Moharam and T. K. Gaylord, “Rigorous coupled-wave analysis of metallic surface-relief gratings,” J. Opt. Soc. Am. A, vol. 3, no. 11, p. 1780, Nov. 1986.
264. L. Li, “New formulation of the Fourier modal method for crossed surface-relief gratings,” J. Opt. Soc. Am. A, vol. 14, no. 10, p. 2758, Oct. 1997.
265. C. Shakher, H. Yadav, “Dependence of diffraction efficiency of holographic concentrators on angle of illumination, hologram-thickness and wavelength of illuminating light,” J. Opt., vol. 21, no. 6, pp. 267–272, 1990.
266. B. L. J. Guo, “Nanoimprint Lithography : Methods and Material Requirements,” Adv. Mater., vol. 19, pp. 495–513, 2007.
267. W. Zhou, G. Min, J. Zhang, and Y. Liu, “Nanoimprint Lithography : A Processing Technique for Nanofabrication Advancement,” Nano-Micro Lett. Rev., vol. 3, no. 2, pp. 135–140, 2011.

268. H. Schift, "Nanoimprint lithography: An old story in modern times? A review," J. Vac. Sci. Technol. B Microelectron. Nanom. Struct., vol. 26, no. 2, p. 458, 2008.

269. S. Y. Chou, P. R. Krauss, and P. J. Renstrom, "Nanoimprint lithography," vol. 14, no. June, pp. 4129–4133, 1996.

270. V. Reboud, N. Kehagias, M. Zelsmann, M. Striccoli, M. Tamborra, and M. L. Curri, "Nanoimprinted photonic crystals for the modification of the (CdSe) ZnS nanocrystals light emission," vol. 84, no. 0167, pp. 1574–1577, 2007.

271. B. D. Gates, "Nanofabrication with molds & stamps," Mater. today, no. Februay 2005, pp. 44–49.

272. L. Yang, I. Akhatov, M. Mahinfalah, and B. Z. Jang, "Nano-fabrication: A review," J. Chinese Inst. Eng., vol. 30, no. 3, pp. 441–446, Apr. 2007.

273. W. Zhou, Nanoimprint Lithography: An Enabling Process for Nanofabrication. Springer, 2013.

274. F. C. Krebs, S. a. Gevorgyan, and J. Alstrup, "A roll-to-roll process to flexible polymer solar cells: model studies, manufacture and operational stability studies," J. Mater. Chem., vol. 19, no. 30, p. 5442, 2009.

275. H. Tan, "Roller nanoimprint lithography," J. Vac. Sci. Technol. B Microelectron. Nanom. Struct., vol. 16, no. 6, p. 3926, Nov. 1998.

276. J. J. Dumond and H. Yee Low, "Recent developments and design challenges in continuous roller micro- and nanoimprinting," J. Vac. Sci. Technol. B Microelectron. Nanom. Struct., vol. 30, no. 1, p. 010801, 2012.

277. S. H. Ahn and L. J. Guo, "High-Speed Roll-to-Roll Nanoimprint Lithography on Flexible Plastic Substrates," Adv. Mater., vol. 20, no. 11, pp. 2044–2049, Jun. 2008.

278. P. Calvert, "Inkjet Printing for Materials and Devices," Chem. Mater., vol. 13, no. 10, pp. 3299–3305, 2001.

279. B.-J. de Gans and U. S. Schubert, "Inkjet Printing of Well-Defined Polymer Dots and Arrays," Langmuir, vol. 20, no. 18, pp. 7789–7793, Jul. 2004.

280. M. Singh, H. M. Haverinen, P. Dhagat, and G. E. Jabbour, "Inkjet printing-process and its applications.," Adv. Mater., vol. 22, no. 6, pp. 673–85, Feb. 2010.

281. H. Sirringhaus, "High-Resolution Inkjet Printing of All-Polymer Transistor Circuits," Science, vol. 290, pp. 2123–2126, Dec. 2000.

282. C. E. Shannon, "A mathematical theory of communication," Bell Syst. Tech. J., vol. 27, pp. 379–423, 1948.

283. J. Davies, The Physics of Low-dimensional Semiconductors: An Introduction. Cambridge University Press, 1997.

284. N. N. Ledentsov, M. Grundmann, F. Heinrichsdorff, D. Bimberg, V. M. Ustinov, A. E. Zhukov, M. V Maximov, Z. I. Alferov, and J. A. Lott, "Quantum-Dot Heterostructure Lasers," J. Sel. Top. Quantum Electron., vol. 6, no. 3, pp. 439–451, 2000.

285. D. Bimberg, N. Ledentsov, and C. Ribbat, “Quantum dots: lasers and amplifiers,” J. Phys. Condens. Matter, vol. 15, no. 24, pp. R1063–R1076, Jun. 2003.

286. M. V. Maximov and N. Ledentsov, Quantum dots lasers. Dekker Encyclopedia of Nanoscience and Nanotechnology, 2004.

287. D. Bimberg, P. Hawrylak, and A. Wojs, Quantum Dot Heterostructures. Wiley, 2001.

288. M. Sugawara, Ed., Self-Assembled InGaAs/GaAs Quantum Dots. Academic Press, 1999.

289. H. Schweizer, M. Jetter, and F. Scholz, “Quantum-Dot Lasers,” vol. 237, pp. 185–237, 2003.

290. P. Bhattacharya, S. Ghosh, and A. D. Stiff-Roberts, “Quantum Dot Opto-Electronic Devices,” Annu. Rev. Mater. Res., vol. 34, no. 1, pp. 1–40, Aug. 2004.

291. M. Sugawara, N. Hatori, H. Ebe, and M. Ishida, “InAs / GaAs quantum-dot lasers : Homogeneous broadening of optical gain under current injection,” pp. 1–8, 2005.

292. M. Sugawara, T. Akiyama, N. Hatori, Y. Nakata, H. Ebe, and H. Ishikawa, “Quantum-dot semiconductor optical amplifiers for high-bit-rate signal processing up to 160 Gb s -1 and a new scheme of 3R regenerators,” Meas. Sci. Technol., vol. 13, no. 11, pp. 1683–1691, Nov. 2002.

293. D. L. Huffaker, H. Deng, D. G. Deppe, and S. Member, “Vertical-Cavity Surface-Emitting Laser,” vol. 10, no. 2, pp. 185–187, 1998.

294. K. Iga, “Vertical-Cavity Surface-Emitting Laser: Its Conception and Evolution,” Jpn. J. Appl. Phys., vol. 47, no. 1, pp. 1–10, Jan. 2008.

295. C. W. Wilmsen, H. Temkin, and L. a. Coldren, Vertical-Cavity Surface-Emitting Lasers: Design, Fabrication, Characterization, and Applications. Cambridge University Press, 2002.

296. R. Michalzik, VCSELs: Fundamentals, Technology and Applications of Vertical-Cavity Surface-Emitting Lasers. Springer, 2013.

297. J. Piprek, S. Bjorlin, and J. Bowers, “Design and analysis of vertical-cavity semiconductor optical amplifiers,” Quantum Electron. IEEE …, vol. 37, no. 1, pp. 127–134, 2001.

298. A. Karim, S. Member, S. Björlin, J. Piprek, S. Member, and J. E. Bowers, “Long-Wavelength Vertical-Cavity Lasers and Amplifiers,” vol. 6, no. 6, pp. 1244–1253, 2000.

299. M. J. Adams, J. V. Collins, and I. D. Henning, “Analysis of semiconductor laser optical amplifiers,” IEE Proc., vol. 132, no. 1, pp. 58–63, 1985.

300. D. Alexandropoulos and M. J. Adams, “Theoretical Study of GaInNAs – GaAs-Based Semiconductor Optical Amplifiers,” IEEE J. Quantum Electron., vol. 39, no. 5, pp. 647–655, 2003.

301. G. O. I. A. Gaas and R. P. Sarzala, “Modeling of the Threshold Operation of 1.3 µm Surface-Emitting Lasers,” vol. 40, no. 6, pp. 629–639, 2004.

302. S. A. Blokhin, N. A. Maleev, A. G. Kuzmenkov, A. V Sakharov, M. M. Kulagina, Y. M. Shernyakov, I. I. Novikov, M. V Maximov, V. M. Ustinov, A. R. Kovsh, S. S. Mikhrin, N. N. Ledentsov, G. Lin, J. Y. Chi, S. Member, and A. Molecular, “Vertical-Cavity Surface-

Emitting Lasers Based on Submonolayer InGaAs Quantum Dots," IEEE J. Quantum Electron., vol. 42, no. 9, pp. 851–858, 2006.

303. H. Saito, K. Nishi, I. Ogura, S. Sugou, and Y. Sugimoto, "Room-temperature lasing operation of a quantum-dot vertical-cavity surface-emitting laser," Appl. Phys. Lett., vol. 69, no. November, pp. 3140–3142, 1996.

304. F. Hopfer, I. Kaiander, a. Lochmann, a. Mutig, S. Bognar, M. Kuntz, U. W. Pohl, V. a. Haisler, and D. Bimberg, "Vertical-cavity surface-emitting quantum-dot laser with low threshold current grown by metal-organic vapor phase epitaxy," Appl. Phys. Lett., vol. 89, no. 6, p. 061105, 2006.

305. F. Hopfer, a. Mutig, M. Kuntz, G. Fiol, D. Bimberg, N. N. Ledentsov, V. a. Shchukin, S. S. Mikhrin, D. L. Livshits, I. L. Krestnikov, a. R. Kovsh, N. D. Zakharov, and P. Werner, "Single-mode submonolayer quantum-dot vertical-cavity surface-emitting lasers with high modulation bandwidth," Appl. Phys. Lett., vol. 89, no. 14, p. 141106, 2006.

306. D. L. Huffaker, O. Baklenov, L. A. Graham, B. G. Streetman, and D. G. Deppe, "Quantum dot vertical-cavity surface-emitting laser with a dielectric aperture," Appl. Phys. Lett., vol. 70, no. 18, p. 2356, 1997.

307. N. N. Ledentsov, F. Hopfer, and D. Bimberg, "High-Speed Quantum-Dot Vertical-Cavity Surface-Emitting Lasers," Proc. IEEE, vol. 95, no. 9, pp. 1741–1756, Sep. 2007.

308. C. Tombling, T. Saitoh, and T. Mukai, "Performance predictions for vertical-cavity semiconductor laser amplifiers," IEEE J. Quantum Electron., vol. 30, no. 11, pp. 2491–2499, 1994.

309. J. Piprek, S. Member, and J. E. Bowers, "Design and Analysis of Vertical-Cavity Semiconductor Optical Amplifiers," vol. 37, no. 1, pp. 127–134, 2001.

310. A. V Uskov, T. W. Berg, and J. Mørk, "Theory of Pulse-Train Amplification Without Patterning Effects in Quantum-Dot Semiconductor Optical Amplifiers," vol. 40, no. 3, pp. 306–320, 2004.

311. D. I. Babic and S. W. Corzine, "Analytic expressions for the reflection delay, penetration depth, and absorptance of quarter-wave dielectric mirrors," IEEE J. Quantum Electron., vol. 28, no. 2, pp. 514–524, 1992.

312. A. V. Uskov, E. P. O'Reilly, D. McPeake, N. N. Ledentsov, D. Bimberg, and G. Huyet, "Carrier-induced refractive index in quantum dot structures due to transitions from discrete quantum dot levels to continuum states," Appl. Phys. Lett., vol. 84, no. 2, p. 272, 2004.

313. S. W. Corzine, R. H. Yan, and L. A. Coldren, "A tanh substitution technique for the analysis of abrupt and graded interface multilayer dielectric stacks," IEEE J. Quantum Electron., vol. 27, no. 9, pp. 2086–2090, 1991.

314. J. Piprek, S. Member, and J. E. Bowers, "Design and Analysis of Vertical-Cavity Semiconductor Optical Amplifiers," vol. 37, no. 1, pp. 127–134, 2001.

315. S. W. Corzine, R. S. Geels, J. W. Scott, R.-H. Yan, and L. A. Coldren, "Design of Fabry-Perot

surface-emitting lasers with a periodic gain structure," IEEE J. Quantum Electron., vol. 25, no. 6, pp. 1513–1524, Jun. 1989.

316. M. Sugawara, H. Ebe, N. Hatori, M. Ishida, Y. Arakawa, T. Akiyama, K. Otsubo, and Y. Nakata, "Theory of optical signal amplification and processing by quantum-dot semiconductor optical amplifiers," Phys. Rev. B, vol. 69, no. 23, p. 235332, Jun. 2004.

317. T. W. Berg and J. Mork, "Saturation and noise properties of quantum-dot optical amplifiers," IEEE J. Quantum Electron., vol. 40, no. 11, pp. 1527–1539, Nov. 2004.

318. T. W. Berg and J. Mørk, "Quantum dot amplifiers with high output power and low noise," Appl. Phys. Lett., vol. 82, no. 18, p. 3083, 2003.

319. T. W. Berg, S. Bischoff, I. Magnusdottir, and J. Mørk, "Ultrafast Gain Recovery and Modulation Limitations in Self-Assembled Quantum-Dot Devices," IEEE J. Quantum Electron., vol. 13, no. 6, pp. 541–543, 2001.

320. H. C. Wong, G. B. Ren, and J. M. Rorison, "Mode Amplification in Inhomogeneous QD Semiconductor Optical Amplifiers," Opt. Quantum Electron., vol. 38, no. 4–6, pp. 395–409, Mar. 2006.

321. P. Royo, R. Koda, and L. a. L. A. Coldren, "Rate equations of vertical-cavity semiconductor optical amplifiers," Appl. Phys. Lett., vol. 80, no. 17, pp. 3057–3059, 2002.

322. V. Cesari, W. Langbein, P. Borri, M. Rossetti, A. Fiore, S. Mikhrin, I. Krestnikov, and a. Kovsh, "Ultrafast gain dynamics in 1.3 μm InAs⁄GaAs quantum-dot optical amplifiers: The effect of p doping," Appl. Phys. Lett., vol. 90, no. 20, p. 201103, 2007.

323. E. Le Ru, P. Howe, T. Jones, and R. Murray, "Strain-engineered InAs/GaAs quantum dots for long-wavelength emission," Phys. Rev. B, vol. 67, no. 16, p. 165303, Apr. 2003.

324. D. Bimberg, M. Grundmann, F. Heinrichsdorff, N. N. Ledentsov, and V. M. Ustinov, "Quantum dot lasers : breakthrough in optoelectronics," vol. 367, pp. 235–249, 2000.

325. J. He, B. Xu, Z. G. Wang, S. C. Qu, F. Q. Liu, T. W. Zhu, X. L. Ye, F. A. Zhao, and X. Q. Meng, "Structure and optical properties of self-assembled InAs/GaAs quantum dots with In0.15Ga0.85As underlying layer," J. cry, vol. 240, pp. 395–400, 2002.

326. K. Leifer, E. Pelucchi, S. Watanabe, F. Michelini, B. Dwir, and E. Kapon, "Narrow (≈4 meV) inhomogeneous broadening and its correlation with confinement potential of pyramidal quantum dot arrays," Appl. Phys. Lett., vol. 91, no. 8, p. 081106, 2007.

327. J. He, X.-D. Wang, B. Xu, Z.-G. Wang, and S.-C. Qu, "Structure and Photoluminescence Study of InGaAs/GaAs Quantum Dots Grown via Cycled (InAs)n/(GaAs)n Monolayer Deposition," Jpn. J. Appl. Phys., vol. 42, no. Part 1, No. 3, pp. 1154–1157, Mar. 2003.

328. D. Alexandropoulos and M. J. Adams, "GaInNAs-based vertical cavity semiconductor optical amplifiers," J. Phys. Condens. Matter, vol. 16, no. 31, pp. S3345–S3354, Aug. 2004.

329. J. Piprek, S. Bjorlin, and J. E. Bowers, "Design and Analysis of Vertical-Cavity Semiconductor

Optical Amplifiers," IEEE J. Quantum Electron., vol. 37, no. 1, pp. 127–134, 2001.

330. X. Li, M. J. Adams, D. Alexandropoulos, and I. F. Lealman, "Gain recovery in semiconductor optical amplifiers," Opt. Commun., vol. 281, no. 13, pp. 3466–3470, Jul. 2008.

331. I. Henning, M. J. Adams, and J. V. Collins, "Performance predictions from a new optical amplifier model," IEEE J. Quantum Electron., vol. 21, no. 6, pp. 609–613, Jun. 1985.

332. M. J. Adams, J. V. Collins, and I. V. Henning, "Analysis of semiconductor laser optical amplifiers," IEE Procceding, vol. 132, no. 1, pp. 58–63.

333. P. Wen, M. Sanchez, M. Gross, and S. Esener, "Optical bistability in a Vertical-Cavity Semiconductor Optical Amplifier (VCSOA): pulsed input," Opt. Process. Comput., vol. 90, pp. 75–77, 2003.

334. D. Alexandropoulos, H. Simos, M. J. Adams, and D. Syvridis, "Optical Bistability in Active Semiconductor Microring Structures," IEEE J. Sel. Top. Quantum Electron., vol. 14, no. 3, pp. 918–926, 2008.

LIST OF PUBLICATIONS

Scientific Journals

1. A. Meristoudi, L. Athanasekos, M. Vasileiadis, S. Pispas, G. Mousdis, E.Karoutsos, D. Alexandropoulos, H. Du, A. Tsigara, K. Kibasi, A. Perrone and N. A. Vainos,
   "Nanocomposite hybrid photonic media for remote point sensors",
   J. Opt. A: Pure Appl. Opt. 11, 034005, 2009.

2. M. Vasileiadis, L. Athanasekos, A. Meristoudi, D. Alexandropoulos, G. Mousdis, E. Karoutsos, A. Botsialas, and N. Vainos
   "Diffractive Optic Sensor for Remote Point Detection of Ammonia"
   Optics Letters vol. 35, no. 9, pp. 1476–1478, May 1, 2010

3. M. Vasileiadis, D Alexandropoulos, V Karoutsos, L Athanasekos. M Sigalas and N A Vainos,
   "Optimized design of remote point diffractive optical sensors",
   J. Opt. 12, 124016, 2010.

4. L Athanasekos, Z Kollia, M. Vasileiadis, N Aspiotis, D Alexandropoulos, A Meristoudi, V Karoutsos and E Sarantopoulou,
   "Effect of 193 and 157 nm laser light illumination on the surface properties TMOS-NiCl2 sol-gel derived material"
   J. Opt. 12, 124015, 2010.

5. N. Aspiotis, A. El Sachat, L. Athanasekos, M. Vasileiadis, G. Mousdis, N. Vainos, and C. Riziotis, "Diffractive Ammonia Sensors Based on Sol-Gel Nanocomposites Materials" Sensor Letters, vol. 11, no. 8, pp. 1415–1419, August 2013

6. N. Aspiotis, A. El Sachat, L. Athanasekos, M. Vasileiadis, G. Mousdis, S. Pispas, N. Vainos, and C. Riziotis
"Ultra-low cost rapid prototyping of diffraction grating remote point gas sensors", Key Engineering Materials, vol. 543, pp 377-380, March 2013

7. L. Athanasekos, M. Vasileiadis, N. Vainos, and C. Riziotis,
"Study on ArF excimer laser micromachining on Polymer Optical Fibers"
Submitted for publication in Journal of Optics

Conference Proceedings

8. M. Vasileiadis, L. Athanasekos, D. Alexandropoulos, A. Meristoudi, V. Karoutsos, A. Botsialas, G. Mousdis, I. Koutselas, M. Sigalas, and N. Vainos
"Optical Sensor Sensitivity Enhancement by Use of Diffraction Gratings",
AIP Conference Proceedings 1288 , Issue 1, p192, October 11, 2010

9. N. Aspiotis, A. El Sachat, L. Athanasekos, M. Vasileiadis, G. Mousdis, S. Pispas, N. Vainos, and C. Riziotis.
"Ultra Low Cost Rapid Prototyping of Diffraction Grating Remote Point Gas Sensors"
IC-MAST Conference Proceedings, pp.377-380 2012

Presentation in Conferences

10. L. Athanasekos*, M. Vasileiadis, A. Meristoudi, S. Pispas, G. Mousdis, A. Tsigara, V. Karoutsos, and N. A. Vainos, "Diffractive Optic Nanocomposite Sensors", 5th International Conference on Nanosciences & Nanotechnologies - NN08, 14-16 July 2008, Thessaloniki, Greece

11. M. Vasileiadis*, L. Athanasekos, A. Meristoudi, S. Pispas, G. Mousdis, A. Tsigara, and N. A. Vainos, "Hybrid materials photonic sensors", XXIV Panhellenic Conference on Solid State Physics & Materials Science, September 21-24, 2008, Heraklion, Crete, Greece.

.

12. N. A. Vainos*, L. Athanasekos, M. Vasileiadis, A. Meristoudi, Ch. Mantzaridis, V. Karoutsos, D. Alexandropoulos, S. Pispas and M. Sigalas
"Photonic interfaces: Laser tailoring of nanocomposites for sensors and other applications"
7th International Conference on Nanosciences & Nanotechnologies – NN10
11-14 July 2010, Ouranoupolis, Halkidiki, Greece.

13. N. A. Vainos*, L. Athanasekos, M. Vasileiadis, D. Alexandropoulos, V. Karoutsos, M. Sigalas
"Photonic interfacing by laser light: structures and applications",
XXVI PanHellenic Conference on Solid State Physics and Materials Science, Ioannina, September 26-29, 2010.

14. M. Vasileiadis*, D. Alexandropoulos, C. (T.) Politi, A. Stavdas and N. A. Vainos
"A comparative study of quantum well and quantum dot vertical cavity semiconductor optical amplifiers (VCSOAs)"
2nd Mediterranean Photonics Conference, November 29 – December 2 2010, Eilat, Israel

15. N. Aspiotis, M. Vasileiadis, A. El Sachat, L. Athanasekos, S. Pispas, N. Vainos, C. Riziotis*,
"Ultra–Low Cost Rapid Prototyping of Diffraction Grating Remote Point Sensors",
International Conference on Materials and Applications for Sensors and Transducers, May 24-28, 2012, Budapest, Hungary

16. M. Vasileiadis*, L. Athanasekos, D. Alexandropoulos, V. Karoutsos, I. Koutselas, S. Pispas, and N. A. Vainos,
"Advanced Photonic Structures via 193 nm excimer laser microfabrication",
10th International Conference on Nanosciences & Nanotechnologies (NN13), 9-12 July 2013, Thessaloniki, Greece

17. M. Vasileiadis*, I. Koutselas, D. Alexandropoulos, N. Kehagias, K. Dimos, M. Karakassides, L'uboš Jankovic, R. Zboril, Peter Komadel, and N. Vainos
"Chemical Synthesis and Characterization of GaN Quantum Dots Incorporated in Simple Photonic Devices,"
Novel Gain Materials and Devices Based on III-V-N/Bi Compounds, 24-26 September 2013, Istanbul University, Istanbul, Turkey

18. A. El Sachat, N. Aspiotis, L. Athanasekos, M. Vasileiadis, G. Mousdis*, S. Pispas, N. Vainos and C. Riziotis
"Diffraction Grating Remote Point Gas Sensor,"
Invited paper, NATO Advanced Research, Nanotechnology in the Security Systems (NSS), 29 September – 3 October 2013, Yalta, Ukraine

Poster Session in Conferences

19. M. Vasileiadis, D. Alexandropoulos, M. J. Adams, and N. A. Vainos, "The Potential of Quantum Dots in High-Q Resonator Structures for Practical Applications", 5th International Conference on Nanosciences & Nanotechnologies - NN08, 14-16 July 2008, Thessaloniki, Greece

20. L. Athanasekos, D. Alexandropoulos, M. Vasileiadis, E. Karoutsos, S. Pispas, G. Mousdis, A. Meristoudi, A. Botsialas και N. A. Vainos, "Hybrid materials photonic sensors", XXIV Panhellenic Conference on Solid State Physics & Materials Science, September 21-24, 2008, Heraklion, Crete, Greece

21. M. Vasileiadis, D. Alexandropoulos, C. (T.) Politi, M. Adams, and N. Vainos, "Dynamic Response of GaInNAs based VCSOAs", Cost Action MP0805 - Novel Gain Materials And Devices Based On III-V-N Compounds - Essex scientific meeting, May 24, 2009, Colchester, UK

22. D. Alexandropoulos, C(T) Politi, M. Vasileiadis, A. Stavdas and N. Vainos, "Performance evaluation of GaInNAs- based semiconductor optical amplifiers", ICO - Emerging Trends and Novel Materials in Photonics - October 7-9, 2009, Delphi, Greece

23. M. Vasileiadis, D. Alexandropoulos, M. J. Adams and N. Vainos, "Performance Characteristics of Quantum Dot Micro-ring Amplifiers under Steady State Operation", ICO - Emerging Trends and Novel Materials in Photonics - October 7-9, 2009, Delphi, Greece

24. M. Vasileiadis, L. Athanasekos, D. Alexandropoulos, A. Meristoudi, A. Botsialas, G. Mousdis, and N. Vainos, "Optical Sensor Sensitivity Enhancement by Use of Diffraction Gratings", ICO - Emerging Trends and Novel Materials in Photonics - October 7-9, 2009, Delphi, Greece

25. E. Sarantopoulou, Z. Kollia, L. Athanasekos, M. Vasileiadis, N. Aspiotis, D. Alexandropoulos, "Surface modification properties of sol-gel and PDMS materials upon 193 nm and 157 nm laser light illumination", ICO - Emerging Trends and Novel Materials in Photonics - October 7-9, 2009, Delphi, Greece

26. M. Vasileiadis*, L. Athanasekos, D. Alexandropoulos, A. Meristoudi, A. Botsialas, G. Mousdis, V. Karoutsos, and N. Vainos
"Sensitivity Enhancement of Ammonia Photonic Sensor by Surface Relief Modulation", 2nd Mediterranean Conference on Nano-Photonics Medinano 2, October 26-27, 2009, Athens, Greece.

27. M. Vasileiadis, L. Athanasekos, D. Alexandropoulos, A. Meristoudi, V. Karoutsos, M. Sigalas and N. Vainos, "Diffraction Grating Thin Film Sensors Operating Under The Remote Point Optical Sensing Scheme"
XXVI PanHellenic Conference on Solid State Physics and Materials Science, Ioannina, September 26-29, 2010

28. M. Vasilieadis*, N. Aspiotis, L. Athanasekos, A. Meristoudi, V. Karoutsos, M. Sigalas, D. Alexandropoulos, and N.Vainos
"UV Laser Microetching and Soft Lithography for Diffractive Optic Sensors"
8th International Conference on Nanosciences & Nanotechnologies, 12-15 July 2011, Thessaloniki, Greece

29. V. Karoutsos*, D. Alexandropoulos, M. Vasileiadis, N. Leventis and N. Vainos,
"Laser microprocessing of aerogels"
8th International Conference on Nanosciences & Nanotechnologies, 12-15 July 2011, Thessaloniki, Greece

30. Y. Orphanos*, S. Brezas, M. Bakarezos, M.Vasileiadis, D. Alexandropoulos, L. Athanasekos, M. Tatarakis, N. Vainos and N.A. Papadogiannis,
"3D-detection of nanosecond laser generated high frequency micro-elastic waves in surface",
8th International Conference on Nanosciences & Nanotechnologies, 12-15 July 2011, Thessaloniki, Greece

31. L. Athanasekos*, C. Riziotis, M. Vasileiadis, D. Dimas, S. Pispas and N. Vainos,
"Laser Microstructured Polymer Optical Fibers for optimized sensing devices",
20th International Conference on Plastic Optical Fibers – POF 2011, September 14-16 2011, Bilbao, Spain

32. M. Vasileiadis*, D. Alexandropoulos, and N. A. Vainos,
"High Speed Operation of Threshold-less Quantum Dot Based Semiconductor Optical Amplifier Structures in Highly Resonance Structures",
10th International Conference on Nanosciences & Nanotechnologies (NN13), 9-12 July 2013, Thessaloniki, Greece

33. M. Vasileiadis*, L. Athanasekos, D. Alexandropoulos, V. Karoutsos, I. Koutselas, S. Pispas, and N. A. Vainos,
“Design, Synthesis and evaluation of polymer/quantum dot nanocomposites for integrated photonics circuits”,
10th International Conference on Nanosciences & Nanotechnologies (NN13), 9-12 July 2013, Thessaloniki, Greece

34. L. Athanasekos*, M. Vasileiadis, A. El Sachat, C. Riziotis, and N. A. Vainos,
“Study on ArF excimer laser micromachining on Polymer Optical Fibers for Photonic Sensor Applications,”
10th International Conference on Nanosciences & Nanotechnologies (NN13), 9-12 July 2013, Thessaloniki, Greece

35. M. Vasileiadis*, D. Alexandropoulos , C.(T) Politi, N. Vainos
“Performance Prediction of Quantum Dots Based Highly Resonant Optical Amplifiers,”
Novel Gain Materials and Devices Based on III-V-N/Bi Compounds, 24-26 September 2013, Istanbul University, Istanbul, Turkey

Other Presentations

36. M. Vasileiadis, L. Athanasekos, A. Meristoudi, S. Pispas, G. Mousdis, A. Tsigara, V. Karoutsos, and N. A. Vainos (oral),
“Photonic Methods and Materials for remote point etching”,
COST Training School (COST ACTION MP0604), September 2-5, 2008, Ischia (Naples), Italy.

37. L. Athanasekos, M. Vasileiadis, A. Meristoudi, S. Pispas, G. Mousdis, D. Alexandropoulos, V. Karoutsos, and N. A. Vainos,
“Diffractive Optical Elements and Novel microstructures for photonic applications”,
COST Training School (COST ACTION MP0604), September 2-5, 2008, Ischia (Naples), Italy.

38. M. Vasileiadis, L. Athanasekos, D. Alexandropoulos¬, V. Karoutsos, M. Sigalas, and N. Vainos,
“Theoretical study and experimental demonstration of diffraction grating sensors sensitivity enhancement”
COST Training School (COST ACTION MP0604), October 5-8, 2010, Visegrád, Hungary.